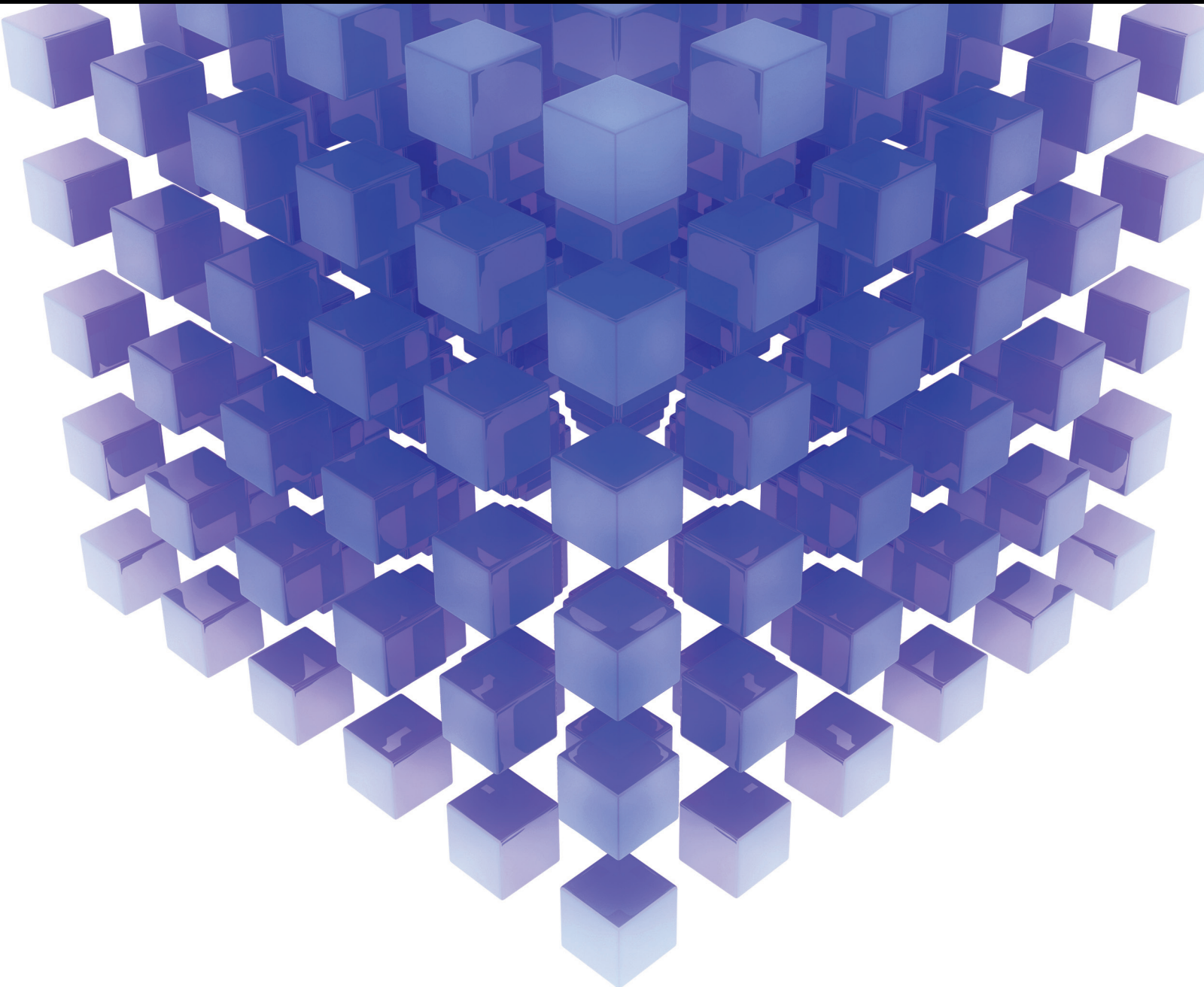


Mathematical Problems in Engineering

# Fault Detection, Isolation, Estimation, and Accommodation of Dynamic Systems

Guest Editors: Ke Zhang, Peng Shi, Vincent Cocquempot, and Bin Jiang





---

**Fault Detection, Isolation, Estimation,  
and Accommodation of Dynamic Systems**

Mathematical Problems in Engineering

---

**Fault Detection, Isolation, Estimation,  
and Accommodation of Dynamic Systems**

Guest Editors: Ke Zhang, Peng Shi, Vincent Cocquempot,  
and Bin Jiang



---

Copyright © 2015 Hindawi Publishing Corporation. All rights reserved.

This is a special issue published in “Mathematical Problems in Engineering.” All articles are open access articles distributed under the Creative Commons Attribution License, which permits unrestricted use, distribution, and reproduction in any medium, provided the original work is properly cited.

## Editorial Board

- Mohamed Abd El Aziz, Egypt  
Farid Abed-Meraim, France  
Silvia Abraho, Spain  
Paolo Adesso, Italy  
Claudia Adduce, Italy  
Ramesh Agarwal, USA  
Juan C. Agüero, Australia  
Ricardo Aguilar-López, Mexico  
Tarek Ahmed-Ali, France  
Hamid Akbarzadeh, Canada  
Muhammad N. Akram, Norway  
Mohammad-Reza Alam, USA  
Salvatore Alfonzetti, Italy  
Francisco Alhama, Spain  
Juan A. Almendral, Spain  
Saiied Aminossadati, Australia  
Lionel Amodeo, France  
Igor Andrianov, Germany  
Sebastian Anita, Romania  
Renata Archetti, Italy  
Felice Arena, Italy  
Sabri Arik, Turkey  
Fumihiko Ashida, Japan  
Hassan Askari, Canada  
Mohsen Asle Zaeem, USA  
Francesco Aymerich, Italy  
Seungik Baek, USA  
Khaled Bahlali, France  
Laurent Bako, France  
Stefan Balint, Romania  
Alfonso Banos, Spain  
Roberto Baratti, Italy  
Martino Bardi, Italy  
Azeddine Beghdadi, France  
Abdel-Hakim Bendada, Canada  
Ivano Benedetti, Italy  
Elena Benvenuti, Italy  
Jamal Berakdar, Germany  
Enrique Berjano, Spain  
Jean-Charles Beugnot, France  
Simone Bianco, Italy  
David Bigaud, France  
Jonathan N. Blakely, USA  
Paul Bogdan, USA  
Daniela Boso, Italy
- Abdel-Ouahab Boudraa, France  
Francesco Braghin, Italy  
Michael J. Brennan, UK  
Maurizio Brocchini, Italy  
Julien Bruchon, France  
Javier Bulduf, Spain  
Tito Busani, USA  
Pierfrancesco Cacciola, UK  
Salvatore Caddemi, Italy  
Jose E. Capilla, Spain  
Ana Carpio, Spain  
Miguel E. Cerrolaza, Spain  
Mohammed Chadli, France  
Gregory Chagnon, France  
Ching-Ter Chang, Taiwan  
Michael J. Chappell, UK  
Kacem Chehdi, France  
Xinkai Chen, Japan  
Chunlin Chen, China  
Francisco Chicano, Spain  
Hung-Yuan Chung, Taiwan  
Joaquim Ciurana, Spain  
John D. Clayton, USA  
Carlo Cosentino, Italy  
Paolo Crippa, Italy  
Erik Cuevas, Mexico  
Peter Dabnichki, Australia  
Luca D'Acerno, Italy  
Weizhong Dai, USA  
Purushothaman Damodaran, USA  
Farhang Daneshmand, Canada  
Fabio De Angelis, Italy  
Stefano de Miranda, Italy  
Filippo de Monte, Italy  
Xavier Delorme, France  
Luca Deseri, USA  
Yannis Dimakopoulos, Greece  
Zhengtao Ding, UK  
Ralph B. Dinwiddie, USA  
Mohamed Djemai, France  
Alexandre B. Dolgui, France  
George S. Dulikravich, USA  
Bogdan Dumitrescu, Finland  
Horst Ecker, Austria  
Karen Egizarian, Finland
- Ahmed El Hajjaji, France  
Fouad Erchiqui, Canada  
Anders Eriksson, Sweden  
Giovanni Falsone, Italy  
Hua Fan, China  
Yann Favennec, France  
Roberto Fedele, Italy  
Giuseppe Fedele, Italy  
Jacques Ferland, Canada  
Jose R. Fernandez, Spain  
Simme Douwe Flapper, The Netherlands  
Thierry Floquet, France  
Eric Florentin, France  
Francesco Franco, Italy  
Tomonari Furukawa, USA  
Mohamed Gadala, Canada  
Matteo Gaeta, Italy  
Zoran Gajic, USA  
Ciprian G. Gal, USA  
Ugo Galvanetto, Italy  
Akemi Glvez, Spain  
Rita Gamberini, Italy  
Maria Gandarias, Spain  
Arman Ganji, Canada  
Zhong-Ke Gao, China  
Xin-Lin Gao, USA  
Giovanni Garcea, Italy  
Fernando Garca, Spain  
Laura Gardini, Italy  
Alessandro Gasparetto, Italy  
Vincenzo Gattulli, Italy  
Jürgen Geiser, Germany  
Oleg V. Gendelman, Israel  
Mergen H. Ghayesh, Australia  
Anna M. Gil-Lafuente, Spain  
Hector Gómez, Spain  
Rama S. R. Gorla, USA  
Oded Gottlieb, Israel  
Antoine Grall, France  
Jason Gu, Canada  
Quang Phuc Ha, Australia  
Ofer Hadar, Israel  
Masoud Hajarian, Iran  
Frédéric Hamelin, France  
Zhen-Lai Han, China

Thomas Hanne, Switzerland  
Takashi Hasuike, Japan  
Xiao-Qiao He, China  
Mara I. Herreros, Spain  
Vincent Hilaire, France  
Eckhard Hitzer, Japan  
Jaromir Horacek, Czech Republic  
Muneo Hori, Japan  
András Horváth, Italy  
Gordon Huang, Canada  
Sajid Hussain, Canada  
Asier Ibeas, Spain  
Giacomo Innocenti, Italy  
Emilio Insfran, Spain  
Nazrul Islam, USA  
Payman Jalali, Finland  
Reza Jazar, Australia  
Khalide Jbilou, France  
Linni Jian, China  
Zhongping Jiang, USA  
Bin Jiang, China  
Ningde Jin, China  
Grand R. Joldes, Australia  
Joaquim Joao Judice, Portugal  
Tadeusz Kaczorek, Poland  
Tamas Kalmar-Nagy, Hungary  
Tomasz Kapitaniak, Poland  
Haranath Kar, India  
Konstantinos Karamanos, Belgium  
C. Masood Khaliq, South Africa  
Nam-Il Kim, Republic of Korea  
Do Wan Kim, Republic of Korea  
Oleg Kirillov, Germany  
Manfred Krafczyk, Germany  
Frederic Kratz, France  
Jurgen Kurths, Germany  
Kyandoghere Kyamakya, Austria  
Davide La Torre, Italy  
Risto Lahdelma, Finland  
Hak-Keung Lam, UK  
Antonino Laudani, Italy  
Aime' Lay-Ekuakille, Italy  
Marek Lefik, Poland  
Yaguo Lei, China  
Thibault Lemaire, France  
Stefano Lenci, Italy  
Roman Lewandowski, Poland  
Qing Q. Liang, Australia  
Panos Liatsis, UK  
Wanquan Liu, Australia  
Yan-Jun Liu, China  
Peide Liu, China  
Peter Liu, Taiwan  
Jean J. Loiseau, France  
Paolo Lonetti, Italy  
Luis M. López-Ochoa, Spain  
Vassilios C. Loukopoulos, Greece  
Valentin Lychagin, Norway  
Fazal M. Mahomed, South Africa  
Yassir T. Makkawi, UK  
Noureddine Manamanni, France  
Didier Maquin, France  
Paolo Maria Mariano, Italy  
Benoit Marx, France  
Gefhrard A. Maugin, France  
Driss Mehdi, France  
Roderick Melnik, Canada  
Pasquale Memmolo, Italy  
Xiangyu Meng, Canada  
Jose Merodio, Spain  
Luciano Mescia, Italy  
Laurent Mevel, France  
Y. V. Mikhlin, Ukraine  
Aki Mikkola, Finland  
Hiroyuki Mino, Japan  
Pablo Mira, Spain  
Vito Mocella, Italy  
Roberto Montanini, Italy  
Gisele Mophou, France  
Rafael Morales, Spain  
Aziz Moukrim, France  
Emiliano Mucchi, Italy  
Domenico Mundo, Italy  
Jose J. Muñoz, Spain  
Giuseppe Muscolino, Italy  
Marco Mussetta, Italy  
Hakim Naceur, France  
Hassane Naji, France  
Dong Ngoduy, UK  
Tatsushi Nishi, Japan  
Ben T. Nohara, Japan  
Mohammed Nouari, France  
Mustapha Nourelfath, Canada  
Sotiris K. Ntouyas, Greece  
Roger Ohayon, France  
Mitsuhiro Okayasu, Japan  
Eva Onaindia, Spain  
Javier Ortega-Garcia, Spain  
Alejandro Ortega-Moñux, Spain  
Naohisa Otsuka, Japan  
Erika Ottaviano, Italy  
Alkiviadis Paipetis, Greece  
Alessandro Palmeri, UK  
Anna Pandolfi, Italy  
Elena Panteley, France  
Manuel Pastor, Spain  
Pubudu N. Pathirana, Australia  
Francesco Pellicano, Italy  
Haipeng Peng, China  
Mingshu Peng, China  
Zhike Peng, China  
Marzio Pennisi, Italy  
Matjaz Perc, Slovenia  
Francesco Pesavento, Italy  
Maria do Rosário Pinho, Portugal  
Antonina Pirrotta, Italy  
Vicent Pla, Spain  
Javier Plaza, Spain  
Jean-Christophe Ponsart, France  
Mauro Pontani, Italy  
Stanislav Potapenko, Canada  
Sergio Preidikman, USA  
Christopher Pretty, New Zealand  
Carsten Proppe, Germany  
Luca Pugi, Italy  
Yuming Qin, China  
Dane Quinn, USA  
Jose Ragot, France  
Kumbakonam Ramamani Rajagopal, USA  
Gianluca Ranzi, Australia  
Sivaguru Ravindran, USA  
Alessandro Reali, Italy  
Giuseppe Rega, Italy  
Oscar Reinoso, Spain  
Nidhal Rezg, France  
Ricardo Riaza, Spain  
Gerasimos Rigatos, Greece  
José Rodellar, Spain  
Rosana Rodriguez-Lopez, Spain  
Ignacio Rojas, Spain  
Carla Roque, Portugal  
Aline Roumy, France  
Debasish Roy, India  
Rubén Ruiz García, Spain

Antonio Ruiz-Cortes, Spain  
Ivan D. Rukhlenko, Australia  
Mazen Saad, France  
Kishin Sadarangani, Spain  
Mehrdad Saif, Canada  
Miguel A. Salido, Spain  
Roque J. Saltarén, Spain  
Francisco J. Salvador, Spain  
Alessandro Salvini, Italy  
Maura Sandri, Italy  
Miguel A. F. Sanjuan, Spain  
Juan F. San-Juan, Spain  
Roberta Santoro, Italy  
Ilmar Ferreira Santos, Denmark  
José A. Sanz-Herrera, Spain  
Nickolas S. Sapidis, Greece  
Evangelos J. Sapountzakis, Greece  
Themistoklis P. Sapsis, USA  
Andrey V. Savkin, Australia  
Valery Sbitnev, Russia  
Thomas Schuster, Germany  
Mohammed Seaid, UK  
Lotfi Senhadji, France  
Joan Serra-Sagrasta, Spain  
Leonid Shaikhet, Ukraine  
Hassan M. Shanechi, USA  
Sanjay K. Sharma, India  
Bo Shen, Germany  
Babak Shotorban, USA  
Zhan Shu, UK  
Dan Simon, USA  
Luciano Simoni, Italy  
Christos H. Skiadas, Greece  
Michael Small, Australia

Francesco Soldovieri, Italy  
Raffaele Solimene, Italy  
Ruben Specogna, Italy  
Sri Sridharan, USA  
Ivanka Stamova, USA  
Yakov Strelniker, Israel  
Sergey A. Suslov, Australia  
Thomas Svensson, Sweden  
Andrzej Swierniak, Poland  
Yang Tang, Germany  
Sergio Teggi, Italy  
Roger Temam, USA  
Alexander Timokha, Norway  
Rafael Toledo, Spain  
Gisella Tomasini, Italy  
Francesco Tornabene, Italy  
Antonio Tornambe, Italy  
Fernando Torres, Spain  
Fabio Tramontana, Italy  
Sébastien Tremblay, Canada  
Irina N. Trendafilova, UK  
George Tsiatas, Greece  
Antonios Tsourdos, UK  
Vladimir Turetsky, Israel  
Mustafa Tutar, Spain  
Efstratios Tzirtzilakis, Greece  
Filippo Ubertini, Italy  
Francesco Ubertini, Italy  
Hassan Ugail, UK  
Giuseppe Vairo, Italy  
Kuppalapalle Vajravelu, USA  
Robertt A. Valente, Portugal  
Raoul van Loon, UK  
Pandian Vasant, Malaysia

Miguel E. Vázquez-Méndez, Spain  
Josep Vehi, Spain  
Kalyana C. Veluvolu, Republic of Korea  
Fons J. Verbeek, The Netherlands  
Franck J. Vernerey, USA  
Georgios Veronis, USA  
Anna Vila, Spain  
R.-J. Villanueva, Spain  
Uchechukwu E. Vincent, UK  
Mirko Viroli, Italy  
Michael Vynnycky, Sweden  
Junwu Wang, China  
Shuming Wang, Singapore  
Yan-Wu Wang, China  
Yongqi Wang, Germany  
Jeroen A. S. Witteveen, The Netherlands  
Yuqiang Wu, China  
Dash Desheng Wu, Canada  
Xuejun Xie, China  
Guangming Xie, China  
Gen Qi Xu, China  
Hang Xu, China  
Xinggong Yan, UK  
Luis J. Yebra, Spain  
Peng-Yeng Yin, Taiwan  
Ibrahim Zeid, USA  
Qingling Zhang, China  
Huaguang Zhang, China  
Jian Guo Zhou, UK  
Quanxin Zhu, China  
Mustapha Zidi, France  
Alessandro Zona, Italy

# Contents

**Fault Detection, Isolation, Estimation, and Accommodation of Dynamic Systems**, Ke Zhang, Peng Shi, Vincent Cocquempot, and Bin Jiang  
Volume 2015, Article ID 798563, 2 pages

**Robust Fault Reconstruction in Discrete-Time Lipschitz Nonlinear Systems via Euler-Approximate Proportional Integral Observers**, Qingxian Jia, Wen Chen, Yingchun Zhang, and Yu Jiang  
Volume 2015, Article ID 741702, 14 pages

**Simultaneous Fault Detection and Control for Discrete-Time Systems via a Switched Scheme**, Jian Li and Xingze Dai  
Volume 2015, Article ID 841031, 13 pages

**SINS/CNS Nonlinear Integrated Navigation Algorithm for Hypersonic Vehicle**, Yong-jun Yu, Jin-fa Xu, and Zhi Xiong  
Volume 2015, Article ID 903054, 6 pages

**Sensor Fault Tolerant Control of a Fast Steering Mirror System Using Adaptive PI-Based Sliding Mode Observer and Hardware Redundancy**, Hongju Wang, Qiliang Bao, Wenshu Yang, Zidong Liu, and Jing Tian  
Volume 2015, Article ID 918456, 14 pages

**Robust Fault Diagnosis Design for Linear Multiagent Systems with Incipient Faults**, Jingping Xia, Bin Jiang, Ke Zhang, and Jinfa Xu  
Volume 2015, Article ID 436935, 7 pages

**Bayesian Network Based Fault Prognosis via Bond Graph Modeling of High-Speed Railway Traction Device**, Yunkai Wu, Bin Jiang, Ningyun Lu, and Yang Zhou  
Volume 2015, Article ID 321872, 11 pages

**Fault Tolerant Control for Uncertain Time-Delay Systems with a Trajectory Tracking Approach**, ShiLei Zhao, Hong Guo, and YuPeng Liu  
Volume 2015, Article ID 297985, 10 pages

**Actuator Fault Diagnosis with Application to a Diesel Engine Testbed**, Boulaïd Boulkroune, Abdel Aitouche, Vincent Cocquempot, Li Cheng, and Zhijun Peng  
Volume 2015, Article ID 189860, 15 pages

**Joint Feature and Model Selection for SVM Fault Diagnosis in Solid Oxide Fuel Cell Systems**, Gabriele Moser, Paola Costamagna, Andrea De Giorgi, Andrea Greco, Loredana Magistri, Lissy Pellaco, and Andrea Trucco  
Volume 2015, Article ID 282547, 12 pages

**Vacuum Large Current Parallel Transfer Numerical Analysis**, Enyuan Dong, Shengkai Hou, Xiang Zheng, Taotao Qin, Guixin Liu, and Bing Zhao  
Volume 2014, Article ID 384790, 7 pages

## Editorial

# Fault Detection, Isolation, Estimation, and Accommodation of Dynamic Systems

**Ke Zhang,<sup>1</sup> Peng Shi,<sup>2,3</sup> Vincent Cocquempot,<sup>4</sup> and Bin Jiang<sup>1</sup>**

<sup>1</sup>College of Automation Engineering, Nanjing University of Aeronautics and Astronautics, 29 Yudao Street, Nanjing 210016, China

<sup>2</sup>College of Automation, Harbin Engineering University, Harbin, Heilongjiang 150001, China

<sup>3</sup>College of Engineering and Science, Victoria University, Melbourne, VIC 8001, Australia

<sup>4</sup>CRISTAL Laboratory, UMR CNRS 9189, Lille 1 University of Sciences and Technologies, 59655 Villeneuve-d'Ascq Cedex, France

Correspondence should be addressed to Ke Zhang; kezhang@nuaa.edu.cn

Received 11 March 2015; Accepted 11 March 2015

Copyright © 2015 Ke Zhang et al. This is an open access article distributed under the Creative Commons Attribution License, which permits unrestricted use, distribution, and reproduction in any medium, provided the original work is properly cited.

Fault detection, isolation, estimation, and accommodation of dynamic systems play important roles to improve system reliability and stability. Hence, it is important to develop novel theories and methods to investigate fault diagnosis and fault tolerant control or related topics. The papers selected for this special issue represent a good panel for addressing this challenge. Of course, the selected topic and the papers are not an exhaustive representation of the area of fault detection, isolation, estimation, and accommodation of dynamic systems. Nonetheless, they represent the rich and many-facet knowledge, which we have the pleasure of sharing with the readers.

The special issue contains eleven papers, where one paper is about fault detection of discrete-time systems, two papers are related to the observer-based fault estimation, and two papers are regarding fault tolerant control of dynamical systems. Finally, six papers introduce the application of fault detection and fault tolerant control in practical systems.

In a paper entitled “Simultaneous Fault Detection and Control for Discrete-Time Systems via a Switched Scheme,” J. Li and X. Dai study the problem of simultaneous fault detection and control for linear systems with a switched scheme. The switched detector/controller is designed simultaneously. When the faults are detected, the detector/controller is switched to reduce the effect of the faults.

In a paper entitled “Robust Fault Reconstruction in Discrete-Time Lipschitz Nonlinear Systems via Euler-Approximate Proportional Integral Observers,” Q. Jia et al.

investigate the problem of observer-based robust fault reconstruction for a class of nonlinear sampled-data systems. A discrete-time Lipschitz nonlinear system is first established, and its Euler-approximate model is described; then, an Euler-approximate proportional integral observer is constructed. Finally, a single-link flexible robot is employed to verify the effectiveness of the proposed fault-reconstructing method.

In a paper entitled “Robust Fault Diagnosis Design for Linear Multiagent Systems with Incipient Faults,” J. Xia et al. investigate the design of a robust fault estimation observer for linear multiagent systems subject to incipient faults. By considering the fact that incipient faults are in low frequency domain, the fault estimation of such faults is proposed for discrete-time multiagent systems based on finite frequency technique.

In a paper entitled “Sensor Fault Tolerant Control of a Fast Steering Mirror System Using Adaptive PI-Based Sliding Mode Observer and Hardware Redundancy,” H. Wang et al. consider a sensor fault tolerant control scheme for a two-axis fast steering mirror system with minimum power consumption and without changing the controller structure. An adaptive PI-based sliding mode observer is adopted to estimate the fault signal. The estimation is then used by the fault isolation logic to identify the fault.

In a paper entitled “Fault Tolerant Control for Uncertain Time-Delay Systems with a Trajectory Tracking Approach,” S. Zhao et al. investigate the problem of fault tolerant control by trajectory tracking for a class of linear time-delay systems.

Based on Lyapunov-Krasovskii functional approach, stability problems of the descriptor system are easily solved in terms of the linear matrix inequalities.

In a paper entitled “Bayesian Network Based Fault Prognosis via Bond Graph Modeling of High-Speed Railway Traction Device,” Y. Wu et al. first introduce a bond graph modeling of CRH5 high-speed train traction device, based on which a multilayer Bayesian network is developed. Later, two different parameter learning algorithms such as Bayesian estimation and expectation maximization algorithm are adopted to determine the conditional probability table of the Bayesian network. Finally, Pearl’s polytree propagation algorithm for joint probability reasoning is used for failure prediction.

In a paper entitled “Actuator Fault Diagnosis with Application to a Diesel Engine Testbed,” B. Boulkroune et al. study the issues of actuator fault detection and isolation for diesel engines. They are particularly interested in faults affecting the exhaust gas recirculation and the variable geometry turbocharger actuator valves. A bank of observer-based residuals is designed using a nonlinear mean value model of diesel engines.

In a paper entitled “Joint Feature and Model Selection for SVM Fault Diagnosis in Solid Oxide Fuel Cell Systems,” G. Moser et al. investigate an original technique for the joint feature and model selection in the context of support vector machine classification applied as a diagnosis strategy in model-based fault detection and isolation.

In a paper entitled “Vacuum Large Current Parallel Transfer Numerical Analysis,” E. Dong et al. analyze the transfer current’s experiments and the real vacuum arc resistance and precise correctional model in the large transfer current’s process are obtained.

In a paper entitled “Relationship-Oriented Software Defined AS-Level Fast Rerouting for Multiple Link Failures,” C. Li et al. study a local fast reroute approach to effectively recover from multiple link failures in one administrative domain. It can handle various types of multiple link failures that distribute in a vast scope of space and time.

In a paper entitled “SINS/CNS Nonlinear Integrated Navigation Algorithm for Hypersonic Vehicle,” Y. Yu et al. design the model of altitude azimuth, platform error angles, and horizontal position. The SINS/CNS tightly integrated algorithm. Gaussian particle filter is introduced to solve the problem of nonlinear filtering.

## Acknowledgments

We would like to thank the authors for their excellent contributions and patience in assisting us. Finally, the fundamental work of all the reviewers of these papers is also very warmly acknowledged.

*Ke Zhang*  
*Peng Shi*  
*Vincent Cocquempot*  
*Bin Jiang*

## Research Article

# Robust Fault Reconstruction in Discrete-Time Lipschitz Nonlinear Systems via Euler-Approximate Proportional Integral Observers

Qingxian Jia,<sup>1</sup> Wen Chen,<sup>2</sup> Yingchun Zhang,<sup>1,3</sup> and Yu Jiang<sup>1</sup>

<sup>1</sup>Research Center of Satellite Technology, Harbin Institute of Technology, Harbin 150001, China

<sup>2</sup>Division of Engineering Technology, Wayne State University, Detroit, MI 48202, USA

<sup>3</sup>Shenzhen Aerospace Dongfanghong HIT Satellite Company Ltd., Shenzhen 518057, China

Correspondence should be addressed to Yingchun Zhang; zhang@hit.edu.cn

Received 8 August 2014; Accepted 15 October 2014

Academic Editor: Ke Zhang

Copyright © 2015 Qingxian Jia et al. This is an open access article distributed under the Creative Commons Attribution License, which permits unrestricted use, distribution, and reproduction in any medium, provided the original work is properly cited.

The problem of observer-based robust fault reconstruction for a class of nonlinear sampled-data systems is investigated. A discrete-time Lipschitz nonlinear system is first established, and its Euler-approximate model is described; then, an Euler-approximate proportional integral observer (EPIO) is constructed such that simultaneous reconstruction of system states and actuator faults are guaranteed. The presented EPIO possesses the disturbance-decoupling ability because its architecture is similar to that of a nonlinear unknown input observer. The robust stability of the EPIO and convergence of fault-reconstructing errors are proved using Lyapunov stability theory together with  $H_\infty$  techniques. The design of the EPIO is reformulated into convex optimization problem involving linear matrix inequalities (LMIs) such that its gain matrices can be conveniently calculated using standard LMI tools. In addition, to guarantee the implementation of the EPIO on the exact model, sufficient conditions of its semiglobal practical convergence are provided explicitly. Finally, a single-link flexible robot is employed to verify the effectiveness of the proposed fault-reconstructing method.

## 1. Introduction

Increasing complexity of modern engineering systems and higher demand for system performance, particularly in safety-critical systems, will correspondingly raise the probability of system faults and/or failures. As a response to the requirement for system safety, reliability, and survivability, fault diagnosis of dynamic systems has been an attractive subject during the past few decades. In general, fault-diagnostic module consists of three essential tasks: fault detection, isolation, and reconstruction (also known as fault estimation or fault identification) [1–3]. In literature, fault detection and isolation (FDI) schemes are considered to be the most important and are of main focuses; nevertheless, fault reconstruction is an indispensable component in active fault-tolerant control (FTC) systems where faults can be effectively accommodated utilizing reconfigurable

fault-tolerant controller with reconstructed fault information in real time.

During the past decade, observer-based methods for fault reconstruction have been increasingly attracting the attention of many researchers and different categories of fault reconstruction observers have been developed, such as adaptive observers [4, 5], sliding mode observers (SMOs) [6, 7], learning observers [8, 9], and proportional integral observers (PIOs) [10, 11], to name just a few. It is worth noting that most of existing observers are mainly applicable to continuous-time systems. On the other hand, it is well known that fault reconstruction for nonlinear discrete-time systems is considerably practical and challenging because the nonlinearities inherently exist in nature, and most continuous-time systems are implemented digitally in practical applications. Under the assumption that nonlinear discrete-time models are accurate, numerous fault-reconstructing strategies have

been reported [12–15]. However, the availability of the exact models, originated from discretization of a continuous-time plant, is usually unrealistic. A practical solution to this difficult situation is to employ approximate discrete-time models, especially Euler-approximate models, instead of exact models.

More recently, many researchers have paid much attention to observer design and observer-based fault reconstruction for nonlinear discrete-time systems with Euler-approximate models. Reference [16] proposes a general framework for nonlinear observer design via the approximate discrete models. For Lipschitz nonlinear systems, the authors in [17] suggest a robust  $H_\infty$  observer whose main advantage is that maximum admissible Lipschitz constant and robustness can be solved using LMI optimization techniques. Based on [16, 17], a Euler-approximate observer (EAO) is presented for fault reconstruction and active FTC in [18]; however, the robustness is not well guaranteed. For nonlinear networked control systems, an SMO-based fault reconstruction approach is investigated in [19] where the chattering phenomenon resulting from the signum function in the SMO is inevitable. In [20], a Euler-approximate unknown input observer- (UIO-) based robust fault detection strategy is developed. However, to the best of our knowledge, few results have been reported on observer-based robust fault reconstruction for nonlinear discrete-time systems via Euler-approximate models. In addition, how to solve the error problem caused by the approximate models such that the observer designed under Euler-approximate models can be implemented on the exact models has still been an interesting and challenging issue. All of these motivate us to pursue this investigation.

The main objective of this work is to design and analyze an observer-based robust fault-reconstructing strategy for a class of nonlinear discrete-time systems using Euler-approximate models. First, a sampled-data nonlinear system, satisfying the Lipschitz condition, is formulated into a Euler-approximate model; then, on the basis of our previous results in [20], a discrete-time Euler-approximate proportional integral observer (EPIO) is constructed to simultaneously reconstruct system states and actuator faults. The EPIO has an architecture similar to that of a nonlinear UIO. Compared with the EAO proposed in [18], the designed EPIO is able to partially decouple external disturbances and is robust to the reminding part of external disturbances and measurement noises. As a result, the accuracy of the EPIO-based fault reconstruction can be guaranteed. In addition, to guarantee implementation of the EPIO on the exact models, sufficient conditions for *semiglobal practical convergence*, which is defined in [16], are explicitly provided. Besides, systematic observer synthesis with an  $H_\infty$  technique is effectively solved using LMI optimization techniques. Simulation results on a single-link flexible robot are also presented to verify the effectiveness of the proposed fault-reconstructing method.

The rest of this paper is organized as follows. In Section 2, an Euler-approximate model of a Lipschitz nonlinear system is described, and main problems are formulated. In Section 3, a discrete-time EPIO is constructed, and robust stability and semiglobal practical convergence of the proposed observer

are analyzed. Simulation studies are reported in Section 4, and conclusions are drawn in the last section.

## 2. System Description and Problem Formulation

A continuous-time nonlinear system subject to actuator faults, external disturbances, and measurement noises is described as

$$\dot{x}(t) = Ax(t) + \Phi(x(t), t) + Bu(t) + D_1d_1(t) + Ff(t), \quad (1a)$$

$$y(t) = Cx(t) + D_2d_2(t), \quad (1b)$$

where  $x(t) \in \mathbb{R}^n$ ,  $u(t) \in \mathbb{R}^m$ , and  $y(t) \in \mathbb{R}^p$ , representing system state vector, control input vector and measurable output vector, respectively. Variable  $f(t)$  denotes actuator faults with  $f(t) \in \mathbb{R}^m$ . Vectors  $d_1 \in \mathbb{R}^d$  and  $d_2 \in \mathbb{R}^s$ , representing external disturbances and measurement noises, respectively. Without loss of generality, matrices  $D_1$  and  $C$  are assumed to be of full column rank and of full row rank, respectively. The symbol  $\Phi(x(t), t)$  is a continuous nonlinear function that is assumed to satisfy the Lipschitz condition (at least local), that is,  $\|\Phi(x(t), t) - \Phi(\hat{x}(t), t)\| \leq L_g \|x(t) - \hat{x}(t)\|$ , where  $L_g$  is a Lipschitz constant.

Herein, system control input  $u(t)$  is taken to be a piecewise constant signal as  $u(k)$  during the sampling intervals  $[k\tau, (k+1)\tau)$  with a zero-order hold, where  $\tau$  is the sampling period. Therefore, the Euler-approximate discrete model of continuous-time system ((1a), (1b)) can be formulated as

$$x(k+1) = (I_n + \tau A)x(k) + \tau\Phi(x(k), k) + \tau Bu(k) + \tau D_1d_1(k) + \tau Ff(k), \quad (2a)$$

$$y(k) = Cx(k) + D_2d_2(k), \quad (2b)$$

where discrete nonlinear term  $\|\Phi(x(k), k)\|$  still satisfies Lipschitz constraint, namely,

$$\|\Phi(x(k), k) - \Phi(\hat{x}(k), k)\| \leq L_g \|x(k) - \hat{x}(k)\|. \quad (3)$$

Before finishing this section, the following lemma is provided for proof of theorems in the latter section.

**Lemma 1.** *For any positive scalar  $\delta$ , there exists a positive-definite symmetric matrix  $N$  such that the following inequality holds:*

$$2a^T N b \leq \delta a^T N a + \frac{1}{\delta} b^T N b, \quad \forall (a, b) \in \mathbb{R}^n. \quad (4)$$

Throughout the paper,  $A > 0$  ( $A < 0$ ) denotes that  $A$  is positive (negative) definite,  $\lambda_{\min}(A)$  and  $\lambda_{\max}(A)$  are the minimum and maximum eigenvalues of  $A$ ,  $\bar{\sigma}(A)$  represents the maximum singular value of matrix  $A$ ,  $\|\cdot\|$  and  $\|\cdot\|_\infty$  represent Euclidean norm and infinity norm of a vector or matrix,  $*$  means symmetric term,  $I_n$  is an identity matrix of size  $n$ ,  $0_n$  is a zero matrix of size  $n$ ,  $\dagger$  represents a pseudoinverse of a matrix, and  $\mathbb{C}$  denotes the set of all complex numbers.

### 3. Fault Reconstruction via Euler-Approximate Proportional Integral Observers

In this section, we will construct a discrete-time EPIO to achieve robust actuator-fault reconstruction; then, robust stability and semiglobal practical convergence of the presented EPIO will be discussed in detail.

*3.1. Design of a Euler-Approximate Proportional Integral Observer.* In order to perform fault reconstruction for actuators in Lipschitz nonlinear system ((1a), (1b)), a discrete-time nonlinear EPIO is established for the Euler-approximate model ((2a), (2b)) as follows:

$$z(k+1) = T(I_n + \tau A)\hat{x}(k) + \tau T\Phi(\hat{x}(k), k) + \tau T B u(k) + L(y(k) - \hat{y}(k)) + \tau T F \hat{f}(k), \quad (5a)$$

$$\hat{x}(k) = z(k) + H y(k), \quad (5b)$$

$$\hat{y}(k) = C \hat{x}(k), \quad (5c)$$

$$\hat{f}(k+1) = \hat{f}(k) + K(y(k) - \hat{y}(k)), \quad (5d)$$

where  $z(k) \in \mathbb{R}^n$ ,  $\hat{x}(k) \in \mathbb{R}^n$ , and  $\hat{y}(k) \in \mathbb{R}^p$ ; they represent the observer state vector, the estimated state vector, and measurement output vector, respectively. Fault reconstruction signal  $\hat{f}(k)$  is recursively updated by both itself and output estimation errors at the sampling time  $k-1$ . Here,  $T$ ,  $H$ ,  $L$ , and  $K$  are gain matrices with appropriate dimensions to be determined later.

Defining  $e_x(k) := x(k) - \hat{x}(k)$ ,  $e_y(k) := y(k) - \hat{y}(k)$ , and  $e_f(k) := f(k) - \hat{f}(k)$  and letting  $T + HC = I_n$ , estimation error dynamics can be easily obtained as

$$e_x(k+1) = (T(I_n + \tau A) - LC)e_x(k) + \tau T \Delta \Phi(k) + \tau T D_1 d_1(k) - L D_2 d_2(k) \quad (6a)$$

$$- H D_2 d_2(k+1) + \tau T F e_f(k) \\ e_y(k) = C e_x(k) + D_2 d_2(k), \quad (6b)$$

where  $\Delta \Phi(k) = \Phi(x(k), k) - \Phi(\hat{x}(k), k)$ .

Since the nonlinear function  $\Phi(x(k), k)$  satisfies the Lipschitz condition, then

$$\Delta \Phi^T(k) \Delta \Phi(k) - L_g^2 e_x^T(k) e_x(k) \leq 0. \quad (7)$$

Inspired by disturbance-decoupling principle of UIOs [20, 21], we will design gain matrix  $T$  such that state estimation error can be partially decoupled from external disturbances. As such, state error dynamics (6a) can be reorganized as

$$e_x(k+1) = (T(I_n + \tau A) - LC)e_x(k) + \tau T \Delta \Phi(k) + \tau T \underbrace{\begin{bmatrix} D_{11} & D_{12} \end{bmatrix}}_{D_1} \times \underbrace{\begin{bmatrix} d_{11}^T(k) & d_{12}^T(k) \end{bmatrix}}_{d_1(k)}^T \\ - L D_2 d_2(k) - H D_2 d_2(k+1) + \tau T F e_f(k), \quad (8)$$

where  $d_{11} \in \mathbb{R}^q$  and  $q$  is the maximum number of columns of the matrix  $D_1$  for which the condition,  $\text{rank}(C D_{11}) = \text{rank}(D_{11})$ , is satisfied. Matrix  $D_{11}$  is composed of  $q$  columns of the matrix  $D_1$  while matrix  $D_{12}$  represents the remaining part of the matrix  $D_1$ .

Matrix  $T$  is selected such that the condition,  $T D_{11} = 0$ , holds. Herein, we define matrix  $E$  as  $\begin{bmatrix} 0_q & D_{12} \end{bmatrix}$ . Hence, state error dynamics (6a) can be further manipulated as

$$e_x(k+1) = (T(I_n + \tau A) - LC)e_x(k) + \tau T \Delta \Phi(k) + \tau T E d_1(k) - L D_2 d_2(k) - H D_2 d_2(k+1) + \tau T F e_f(k). \quad (9)$$

Considering (5d), fault-reconstructing errors  $e_f(k)$  can be expressed in the following equation:

$$e_f(k+1) = e_f(k) - K C e_x(k) - K D_2 d_2(k) + \Delta f(k), \quad (10)$$

where fault variation vector  $\Delta f(k) := f(k+1) - f(k)$ . If constant actuator faults are considered in system ((1a), (1b)), then  $\Delta f(k) \equiv 0$ . Therefore, one obtains

$$e_f(k+1) = e_f(k) - K C e_x(k) - K D_2 d_2(k). \quad (11)$$

*Remark 2.* Equations (8) and (9) display that the designed EPIO is only partially decoupled from external disturbance  $d_1(k)$ . It is because either the number of measurement outputs is not greater than that of external disturbances or fault-reconstructing ability of the presented EPIO should be guaranteed when coupling problem exists between external disturbances and actuator faults. To tackle the above disturbance-decoupling problem, gain matrices  $T$  and  $H$  should be designed such that matrix equations,  $T + HC = I_n$ , and  $T D_{11} = 0$ , are satisfied simultaneously. Augmented matrix equation composing of these two constraints can be written as

$$\begin{bmatrix} T & H \end{bmatrix} \begin{bmatrix} I_n & D_{11} \\ C & 0 \end{bmatrix} = \begin{bmatrix} I_n & 0 \end{bmatrix}. \quad (12)$$

Therefore, a general solution of (12) can be determined by

$$\begin{bmatrix} T & H \end{bmatrix} = \begin{bmatrix} I_n & 0 \end{bmatrix} \begin{bmatrix} I_n & D_{11} \\ C & 0 \end{bmatrix}^\dagger. \quad (13)$$

In addition, to guarantee actuator-fault detectability by the proposed EPIO, the constraint,  $\text{rank}(TF) = \text{rank}(F)$ , should be also satisfied.

According to (9) and (10), the following augmented error dynamics can be constructed as

$$\begin{bmatrix} e_x(k+1) \\ e_f(k+1) \end{bmatrix} = \begin{bmatrix} T(I_n + \tau A) - LC & \tau T F \\ -KC & I_m \end{bmatrix} \begin{bmatrix} e_x(k) \\ e_f(k) \end{bmatrix} + \tau T \begin{bmatrix} \Delta \Phi(k) \\ 0 \end{bmatrix} + \begin{bmatrix} \tau T E & -L D_2 & -H D_2 & 0 \\ 0 & -K D_2 & 0 & I_m \end{bmatrix} \begin{bmatrix} d_1(k) \\ d_2(k) \\ d_2(k+1) \\ \Delta f(k) \end{bmatrix}. \quad (14)$$

Denote

$$\begin{aligned}\bar{e}(k) &= \begin{bmatrix} e_x(k) \\ e_f(k) \end{bmatrix}, & \omega(k) &= \begin{bmatrix} d_1(k) \\ d_2(k) \\ d_2(k+1) \\ \Delta f(k) \end{bmatrix}, \\ \bar{T} &= \begin{bmatrix} T & 0 \\ 0 & I_m \end{bmatrix}, & \bar{A} &= \begin{bmatrix} I_n + \tau A & \tau F \\ 0 & I_m \end{bmatrix}, \\ \Delta\bar{\Phi}(k) &= \begin{bmatrix} \Delta\Phi(k) \\ 0 \end{bmatrix}, & \bar{D}_1 &= \begin{bmatrix} -\tau TE & 0 & HD_2 & 0 \\ 0 & 0 & 0 & -I_m \end{bmatrix}, \\ \bar{L} &= \begin{bmatrix} L \\ K \end{bmatrix}, & \bar{C} &= [C \ 0], & \bar{D}_2 &= [0 \ -D_2 \ 0 \ 0].\end{aligned}\quad (15)$$

Further, augmented error dynamics (14) can be reorganized into a compact form

$$\begin{aligned}\bar{e}(k+1) &= (\bar{T}\bar{A} - \bar{L}\bar{C})\bar{e}(k) + \tau\bar{T}\Delta\bar{\Phi}(k) \\ &\quad + (\bar{L}\bar{D}_2 - \bar{D}_1)\omega(k) \\ e_y(k) &= \bar{C}\bar{e}(k) - \bar{D}_2\omega(k).\end{aligned}\quad (16)$$

Besides, fault reconstruction error  $e_f(k) = C_f\bar{e}(k)$ , where  $C_f = [0 \ I_m]$ .

For nonlinear function  $\Delta\bar{\Phi}(k)$ , the following inequality holds:

$$\Gamma = \Delta\bar{\Phi}^T(k)\Delta\bar{\Phi}(k) - \bar{e}^T(k)\bar{L}_g^T\bar{L}_g\bar{e}(k) \leq 0, \quad (17)$$

where  $\bar{L}_g = \begin{bmatrix} L_g I_n & 0 \\ 0 & 0_m \end{bmatrix}$ .

It is noticed that augmented error system (16) can be treated as an observation-error equation of the following nonlinear system:

$$\begin{aligned}\bar{x}(k+1) &= \bar{T}\bar{A}\bar{x}(k) + \tau\bar{T}\bar{\Phi}(\bar{x}(k), k) + \bar{D}_1\omega(k) \\ y(k) &= \bar{C}\bar{x}(k) - \bar{D}_2\omega(k),\end{aligned}\quad (18)$$

where

$$\begin{aligned}\bar{x}(k) &= [x^T(k) \ f^T(k)]^T, \\ \bar{\Phi}(\bar{x}(k), k) &= [\Phi^T(x(k), k) \ 0]^T.\end{aligned}\quad (19)$$

An augmented state observer can be established for (18) as follows:

$$\begin{aligned}\hat{\bar{x}}(k+1) &= \bar{T}\bar{A}\hat{\bar{x}}(k) + \tau\bar{T}\bar{\Phi}(\hat{\bar{x}}(k), k) + \bar{L}(y(k) - \hat{y}(k)), \\ \hat{y}(k) &= \bar{C}\hat{\bar{x}}(k).\end{aligned}\quad (20)$$

*Remark 3.* If both the nonlinear term  $\Delta\bar{\Phi}(k)$  and augmented disturbance  $\omega(k)$  are not considered in (16), we can obtain

$$\begin{aligned}\bar{e}(k+1) &= (\bar{T}\bar{A} - \bar{L}\bar{C})\bar{e}(k), \\ e_y(k) &= \bar{C}\bar{e}(k).\end{aligned}\quad (21)$$

The linear error dynamics (21) is asymptotically stable if and only if the pair  $(\bar{T}\bar{A}, \bar{C})$  is detectable. It is equivalent to

$$\text{rank} \begin{bmatrix} zI_{n+m} - \bar{T}\bar{A} \\ \bar{C} \end{bmatrix} = n + m, \quad \forall z \in \mathbb{C}, |z| \geq 1, \quad (22)$$

and one obtains

$$\begin{aligned}\text{rank} \begin{bmatrix} zI_{n+m} - \bar{T}\bar{A} \\ \bar{C} \end{bmatrix} \\ = \text{rank} \begin{bmatrix} zI_n - T(I_n + \tau A) & -\tau TF \\ 0 & (z-1)I_m \\ C & 0 \end{bmatrix}.\end{aligned}\quad (23)$$

(1) If  $z = 1$ ,

$$\begin{aligned}\text{rank} \begin{bmatrix} zI_n - T(I_n + \tau A) & -\tau TF \\ 0 & (z-1)I_m \\ C & 0 \end{bmatrix} \\ = \text{rank} \begin{bmatrix} I_n - T(I_n + \tau A) & -\tau TF \\ C & 0 \end{bmatrix} \\ = \text{rank} \begin{bmatrix} I_n - (I_n - HC)(I_n + \tau A) & -\tau TF \\ C & 0 \end{bmatrix} \\ = \text{rank} \begin{bmatrix} A & TF \\ C & 0 \end{bmatrix}.\end{aligned}\quad (24)$$

(2) If  $z \neq 1$ ,

$$\begin{aligned}\text{rank} \begin{bmatrix} zI_n - T(I_n + \tau A) & -\tau TF \\ 0 & (z-1)I_m \\ C & 0 \end{bmatrix} \\ = \text{rank} \begin{bmatrix} zI_n - T(I_n + \tau A) \\ C \end{bmatrix} + m \\ = \text{rank} \begin{bmatrix} zI_n - (I_n - HC)(I_n + \tau A) \\ C \end{bmatrix} + m \\ = \text{rank} \begin{bmatrix} zI_n - (I_n + \tau A) \\ C \end{bmatrix} + m.\end{aligned}\quad (25)$$

Thus, the pair  $(\bar{T}\bar{A}, \bar{C})$  is detectable if and only if

$$\begin{aligned}\text{rank} \begin{bmatrix} A & TF \\ C & 0 \end{bmatrix} &= n + m, \\ \text{rank} \begin{bmatrix} zI_n - (I_n + \tau A) \\ C \end{bmatrix} &= n\end{aligned}\quad (26)$$

when  $z = -1$  and  $|z| > 1$ . Therefore, the above two conditions can be regarded as necessary conditions for existence of the proposed nonlinear EPIO ((5a), (5b), (5c), and (5d)).

*Remark 4.* Equations (14)–(20) imply that the design of the proposed nonlinear EPIO is now converted into the analysis of robust stability of the augmented error dynamics (16),

that is, the design of robust observer (20) for the augmented nonlinear system (18). Therefore, to guarantee the robustness of the proposed EPIO against the remaining part of external disturbance  $d_1(k)$  and measurement noise  $d_2(k)$ , we shall design augmented matrix  $\bar{L}$ , which is composed of two unknown matrices  $L$  and  $K$ , such that the robust stability of the augmented error dynamics (16) is guaranteed with a prescribed  $H_\infty$  performance specification.

**3.2. Robust Stability Analysis of the Euler-Approximate Proportional Integral Observer.** In this subsection, we will focus on the robust stability analysis of the proposed nonlinear EPIO ((5a), (5b), (5c), and (5d)). Equation (14) shows that different components of the augmented disturbance  $\omega(k)$  have different influences on fault reconstruction performance. To guarantee better robustness of the designed nonlinear EPIO against external disturbance  $d_1(k)$ , measurement noise  $d_2(k)$ ,

and fault variation vector  $\Delta f(k)$ , multiple attenuation levels in an  $H_\infty$  performance specification will be adopted in the EPIO synthesis. In what follows, a theorem is presented to characterize the robust stability of the proposed EPIO ((5a), (5b), (5c), and (5d)).

**Theorem 5.** Consider the Euler-approximate discrete model ((2a), (2b)). For a given positive scalar  $\gamma_i$ ,  $i = \{1, 2, 3, 4\}$ , if there exist a positive-definite symmetric matrix  $\bar{P} \in \mathbb{R}^{(n+m) \times (n+m)}$ , a matrix  $\bar{Y} \in \mathbb{R}^{(n+m) \times p}$ , and positive scalars  $\delta_i$ ,  $i = \{1, 2, 3, 4\}$  such that

$$\begin{bmatrix} -\bar{P} & \sqrt{1+\delta_1}(\bar{P}\bar{T}\bar{A}-\bar{Y}\bar{C}) & \tau\sqrt{1+\delta_2}\bar{P}\bar{T} \\ * & -\bar{P}+\delta_3\bar{L}_g^T\bar{L}_g & 0 \\ * & * & -\delta_3I_{n+m} \end{bmatrix} < 0, \quad (27)$$

$$\begin{bmatrix} -\bar{P} & \bar{P}\bar{T}\bar{A}-\bar{Y}\bar{C} & \tau\bar{P}\bar{T} & \tau\bar{P}\bar{T}\bar{E} & -\bar{Y}\bar{D}_2 & -\bar{P}\bar{D}_h & \bar{P}\bar{I}_m \\ * & -\bar{P}+\delta_4\bar{L}_g^T\bar{L}_g+C_f^TC_f & 0 & 0 & 0 & 0 & 0 \\ * & * & -\delta_4I_{n+m} & 0 & 0 & 0 & 0 \\ * & * & * & -\gamma_1^2I_d & 0 & 0 & 0 \\ * & * & * & * & -\gamma_2^2I_s & 0 & 0 \\ * & * & * & * & * & -\gamma_3^2I_s & 0 \\ * & * & * & * & * & 0 & -\gamma_4^2I_m \end{bmatrix} < 0, \quad (28)$$

where  $\bar{L}_g = \begin{bmatrix} L_g I_n & 0 \\ 0 & 0_m \end{bmatrix}$ ,  $\bar{E} = \begin{bmatrix} E \\ 0 \end{bmatrix}$ ,  $\bar{D}_h = \begin{bmatrix} HD_2 \\ 0 \end{bmatrix}$ , and  $\bar{I}_m = \begin{bmatrix} 0 \\ I_m \end{bmatrix}$ , then the proposed nonlinear EPIO ((5a), (5b), (5c), and (5d)) can realize uniform ultimate boundedness of state-estimating error  $e_x(k)$  and fault-reconstructing error  $e_f(k)$  with an  $H_\infty$  performance criterion:

$$\begin{aligned} \|e_f(k)\|^2 &\leq \gamma_1^2 \|d_1(k)\|^2 \\ &+ (\gamma_2^2 + \gamma_3^2) \|d_2(k)\|^2 + \gamma_4^2 \|\Delta f(k)\|^2. \end{aligned} \quad (29)$$

Moreover, augmented matrix  $\bar{L}$  can be determined by  $\bar{L} = \bar{P}^{-1}\bar{Y}$ .

*Proof.* Consider the Lyapunov function candidate  $V(k) = \bar{e}^T(k)\bar{P}\bar{e}(k)$ . The external disturbance  $d_1(k)$  and measurement noise  $d_2(k)$  are temporarily dropped; then, the difference  $\Delta V(k) = V(k+1) - V(k)$  is derived as

$$\begin{aligned} \Delta V(k) &= \begin{bmatrix} \bar{e}(k) \\ \Delta\bar{\Phi}(k) \end{bmatrix}^T \begin{bmatrix} R & \tau(\bar{T}\bar{A}-\bar{L}\bar{C})^T\bar{P}\bar{T} \\ * & \tau^2\bar{T}^T\bar{P}\bar{T} \end{bmatrix} \begin{bmatrix} \bar{e}(k) \\ \Delta\bar{\Phi}(k) \end{bmatrix} \\ &+ 2\bar{e}^T(k)(\bar{T}\bar{A}-\bar{L}\bar{C})^T\bar{P}\bar{I}_m\Delta f(k) \\ &+ 2\tau\Delta\bar{\Phi}^T(k)\bar{T}^T\bar{P}\bar{I}_m\Delta f(k) \\ &+ \Delta f^T(k)\bar{I}_m^T\bar{P}\bar{I}_m\Delta f(k), \end{aligned} \quad (30)$$

where  $R = (\bar{T}\bar{A}-\bar{L}\bar{C})^T\bar{P}(\bar{T}\bar{A}-\bar{L}\bar{C}) - \bar{P}$ .

Considering Lemma 1, the following inequalities hold:

$$\begin{aligned} &2\bar{e}^T(k)(\bar{T}\bar{A}-\bar{L}\bar{C})^T\bar{P}\bar{I}_m\Delta f(k) \\ &\leq \delta_1\bar{e}^T(k)(\bar{T}\bar{A}-\bar{L}\bar{C})^T\bar{P}(\bar{T}\bar{A}-\bar{L}\bar{C})\bar{e}(k) \\ &\quad + \frac{1}{\delta_1}\Delta f^T(k)\bar{I}_m^T\bar{P}\bar{I}_m\Delta f(k), \\ &2\tau\Delta\bar{\Phi}^T(k)\bar{T}^T\bar{P}\bar{I}_m\Delta f(k) \\ &\leq \delta_2\tau^2\Delta\bar{\Phi}^T(k)\bar{T}^T\bar{P}\bar{T}\Delta\bar{\Phi}(k) \\ &\quad + \frac{1}{\delta_2}\Delta f^T(k)\bar{I}_m^T\bar{P}\bar{I}_m\Delta f(k), \end{aligned} \quad (31)$$

where  $\delta_1 > 0$  and  $\delta_2 > 0$ .

Substituting (17), (31) into (30) leads to

$$\begin{aligned} \Delta V(k) &\leq \begin{bmatrix} \bar{e}(k) \\ \Delta\bar{\Phi}(k) \end{bmatrix}^T \begin{bmatrix} R & \tau(\bar{T}\bar{A}-\bar{L}\bar{C})^T\bar{P}\bar{T} \\ * & \tau^2\bar{T}^T\bar{P}\bar{T} \end{bmatrix} \begin{bmatrix} \bar{e}(k) \\ \Delta\bar{\Phi}(k) \end{bmatrix} \\ &\quad - \delta_3\Gamma + \delta_1\bar{e}^T(k)(\bar{T}\bar{A}-\bar{L}\bar{C})^T\bar{P}(\bar{T}\bar{A}-\bar{L}\bar{C})\bar{e}(k) \\ &\quad + \frac{1}{\delta_1}\Delta f^T(k)\bar{I}_m^T\bar{P}\bar{I}_m\Delta f(k) \end{aligned}$$

$$\begin{aligned}
& + \delta_2 \tau^2 \Delta \bar{\Phi}^T(k) \bar{T}^T \bar{P} \bar{T} \Delta \bar{\Phi}(k) \\
& + \frac{1}{\delta_2} \Delta f^T(k) \bar{I}_m^T \bar{P} \bar{I}_m \Delta f(k) + \Delta f^T(k) \bar{I}_m^T \bar{P} \bar{I}_m \Delta f(k) \\
& \leq \begin{bmatrix} \bar{e}(k) \\ \Delta \bar{\Phi}(k) \end{bmatrix}^T \begin{bmatrix} R_1 + \delta_3 \bar{L}_g^T \bar{L}_g & \tau (\bar{T} \bar{A} - \bar{L} \bar{C})^T \bar{P} \bar{T} \\ * & (1 + \delta_2) \tau^2 \bar{T}^T \bar{P} \bar{T} - \delta_3 I_{n+m} \end{bmatrix} \\
& \times \begin{bmatrix} \bar{e}(k) \\ \Delta \bar{\Phi}(k) \end{bmatrix} + \left(1 + \frac{1}{\delta_1} + \frac{1}{\delta_2}\right) \Delta f^T(k) \bar{I}_m^T \bar{P} \bar{I}_m \Delta f(k) \\
& \leq \xi^T(k) \Omega \xi(k) + \left(1 + \frac{1}{\delta_1} + \frac{1}{\delta_2}\right) \Delta f^T(k) \bar{I}_m^T \bar{P} \bar{I}_m \Delta f(k), \tag{32}
\end{aligned}$$

where  $\xi(k) = \begin{bmatrix} \bar{e}(k) \\ \Delta \bar{\Phi}(k) \end{bmatrix}$  and  $\Omega = \begin{bmatrix} R_1 + \delta_3 \bar{L}_g^T \bar{L}_g & \tau (\bar{T} \bar{A} - \bar{L} \bar{C})^T \bar{P} \bar{T} \\ * & (1 + \delta_2) \tau^2 \bar{T}^T \bar{P} \bar{T} - \delta_3 I_{n+m} \end{bmatrix}$   
with  $R_1 = (1 + \delta_1) (\bar{T} \bar{A} - \bar{L} \bar{C})^T \bar{P} (\bar{T} \bar{A} - \bar{L} \bar{C}) - \bar{P}$  and  $\delta_3 > 0$ .  
If  $\Omega < 0$ , then we have

$$\Delta V(k) \leq -\epsilon \|\bar{e}(k)\|^2 + \nu, \tag{33}$$

where  $\epsilon = \lambda_{\min}(-\Omega)$  and  $\nu = (1 + (1/\delta_1) + (1/\delta_2)) \lambda_{\max}(P) \|\Delta f(k)\|_{\infty}$ .

Further, the condition  $\Omega < 0$  can be rewritten as

$$\begin{aligned}
& \begin{bmatrix} \sqrt{1 + \delta_1} (\bar{T} \bar{A} - \bar{L} \bar{C})^T \bar{P} \\ \tau \sqrt{1 + \delta_2} \bar{T}^T \bar{P} \end{bmatrix} \bar{P}^{-1} \begin{bmatrix} \sqrt{1 + \delta_1} (\bar{T} \bar{A} - \bar{L} \bar{C})^T \bar{P} \\ \tau \sqrt{1 + \delta_2} \bar{T}^T \bar{P} \end{bmatrix}^T \\
& + \begin{bmatrix} -P + \delta_3 \bar{L}_g^T \bar{L}_g & 0 \\ * & -\delta_3 I_{n+m} \end{bmatrix} < 0. \tag{34}
\end{aligned}$$

By the Scular complement lemma [22], (34) is equivalent to (27).

Therefore, if (27) holds, then  $\Delta V(k) < 0$  for  $\epsilon \|\bar{e}(k)\|^2 > \nu$ , which means that the trajectory of  $\bar{e}(k)$  that is outside of the set  $\Phi = \{\bar{e}(k) \mid \|\bar{e}(k)\|^2 \leq \nu/\epsilon\}$  will converge to the set  $\Phi$  according to the Lyapunov stability theory. Therefore, the uniform ultimate boundedness of the state-estimating error  $e_x(k)$  and the fault-reconstructing error  $e_f(k)$  can be guaranteed.

To guarantee that the proposed nonlinear EPIO ((5a), (5b), (5c), and (5d)) is robust to  $d_1(k)$ ,  $d_2(k)$ , and  $\Delta f(k)$ , an  $H_{\infty}$  performance index function is chosen as [23]

$$\begin{aligned}
J = \sum_{k=0}^{\infty} & \left[ e_f^T(k) e_f(k) - \gamma_1^2 d_1^T(k) d_1(k) - \gamma_2^2 d_2^T(k) d_2(k) \right. \\
& \left. - \gamma_3^2 d_2^T(k+1) d_2(k+1) - \gamma_4^2 \Delta f^T(k) \Delta f(k) \right]. \tag{35}
\end{aligned}$$

Under zero-initial conditions, the following is obtained:

$$\begin{aligned}
J \leq \sum_{k=0}^{\infty} & \left[ \Delta V(k) + e_f^T(k) e_f(k) - \gamma_1^2 d_1^T(k) d_1(k) \right. \\
& \left. - \gamma_2^2 d_2^T(k) d_2(k) - \gamma_3^2 d_2^T(k+1) \right. \\
& \left. \times d_2(k+1) - \gamma_4^2 \Delta f^T(k) \Delta f(k) \right]. \tag{36}
\end{aligned}$$

Considering external disturbance  $d_1(k)$  and measurement noise  $d_2(k)$ , it follows from (17), (30), and (36) that

$$\begin{aligned}
\Delta V(k) + e_f^T(k) e_f(k) - \gamma_1^2 d_1^T(k) d_1(k) - \gamma_2^2 d_2^T(k) d_2(k) \\
- \gamma_3^2 d_2^T(k+1) d_2(k+1) - \gamma_4^2 \Delta f^T(k) \Delta f(k) \\
\leq \begin{bmatrix} \bar{e}(k) \\ \Delta \bar{\Phi}(k) \end{bmatrix}^T \begin{bmatrix} R + \delta_4 \bar{L}_g^T \bar{L}_g & \tau (\bar{T} \bar{A} - \bar{L} \bar{C})^T \bar{P} \bar{T} \\ * & \tau^2 \bar{T}^T \bar{P} \bar{T} - \delta_4 I_{n+m} \end{bmatrix} \begin{bmatrix} \bar{e}(k) \\ \Delta \bar{\Phi}(k) \end{bmatrix} \\
+ 2\tau \bar{e}^T(k) (\bar{T} \bar{A} - \bar{L} \bar{C})^T \bar{P} \bar{T} \bar{E} d_1(k) \\
- 2\bar{e}^T(k) (\bar{T} \bar{A} - \bar{L} \bar{C})^T \bar{P} \bar{L} D_2 d_2(k) \\
- 2\bar{e}^T(k) (\bar{T} \bar{A} - \bar{L} \bar{C})^T \bar{P} H \bar{D}_h d_2(k+1) \\
+ 2\bar{e}^T(k) (\bar{T} \bar{A} - \bar{L} \bar{C})^T \bar{P} \bar{I}_m \Delta f(k) \\
+ 2\tau^2 \Delta \bar{\Phi}^T(k) \bar{T}^T \bar{P} \bar{T} \bar{E} d_1(k) \\
- 2\tau \Delta \bar{\Phi}^T(k) \bar{T}^T \bar{P} \bar{L} D_2 d_2(k) \\
- 2\tau \Delta \bar{\Phi}^T(k) \bar{T}^T \bar{P} H \bar{D}_h d_2(k+1) \\
+ 2\tau \Delta \bar{\Phi}^T(k) \bar{T}^T \bar{P} \bar{I}_m \Delta f(k) + \tau^2 d_1^T(k) (\bar{T} \bar{E})^T \bar{P} \bar{T} \bar{E} d_1(k) \\
- 2\tau d_1^T(k) (\bar{T} \bar{E})^T \bar{P} \bar{L} D_2 d_2(k) \\
- 2\tau d_1^T(k) (\bar{T} \bar{E})^T \bar{P} H \bar{D}_h d_2(k+1) \\
+ 2\tau d_1^T(k) (\bar{T} \bar{E})^T \bar{P} \bar{I}_m \Delta f(k) \\
+ d_2^T(k) (\bar{L} D_2)^T \bar{P} \bar{L} D_2 d_2(k) \\
+ 2d_2^T(k) (\bar{L} D_2)^T \bar{P} H \bar{D}_h d_2(k+1) \\
- 2d_2^T(k) (\bar{L} D_2)^T \bar{P} \bar{I}_m \Delta f(k) \\
+ d_2^T(k+1) (H \bar{D}_h)^T \bar{P} H \bar{D}_h d_2(k+1) \\
- 2d_2^T(k+1) (H \bar{D}_h)^T \bar{P} \bar{I}_m \Delta f(k) \\
+ \Delta f^T(k) \bar{I}_m^T \bar{P} \bar{I}_m \Delta f(k) \\
- \gamma_1^2 d_1^T(k) d_1(k) - \gamma_2^2 d_2^T(k) d_2(k) \\
- \gamma_3^2 d_2^T(k+1) d_2(k+1) \\
- \gamma_4^2 \Delta f^T(k) \Delta f(k) \\
= \begin{bmatrix} \bar{e}(k) \\ \Delta \bar{\Phi}(k) \\ d_1(k) \\ d_2(k) \\ d_2(k+1) \\ \Delta f(k) \end{bmatrix}^T \begin{bmatrix} \Pi_{11} & \Pi_{12} & \Pi_{13} & \Pi_{14} & \Pi_{15} & \Pi_{16} \\ * & \Pi_{22} & \Pi_{23} & \Pi_{24} & \Pi_{25} & \Pi_{26} \\ * & * & \Pi_{33} & \Pi_{34} & \Pi_{35} & \Pi_{36} \\ * & * & * & \Pi_{44} & \Pi_{45} & \Pi_{46} \\ * & * & * & * & \Pi_{55} & \Pi_{56} \\ * & * & * & * & * & \Pi_{66} \end{bmatrix} \\
\times \begin{bmatrix} \bar{e}(k) \\ \Delta \bar{\Phi}(k) \\ d_1(k) \\ d_2(k) \\ d_2(k+1) \\ \Delta f(k) \end{bmatrix} = \zeta^T(k) \Pi \zeta(k), \tag{37}
\end{aligned}$$

where

$\zeta(k)$

$$= \left[ \bar{e}^T(k) \quad \Delta \bar{\Phi}^T(k) \quad d_1^T(k) \quad d_2^T(k) \quad d_2^T(k+1) \quad \Delta f^T(k) \right]^T,$$

$$\Pi = \begin{bmatrix} \Pi_{11} & \Pi_{12} & \Pi_{13} & \Pi_{14} & \Pi_{15} & \Pi_{16} \\ * & \Pi_{22} & \Pi_{23} & \Pi_{24} & \Pi_{25} & \Pi_{26} \\ * & * & \Pi_{33} & \Pi_{34} & \Pi_{35} & \Pi_{36} \\ * & * & * & \Pi_{44} & \Pi_{45} & \Pi_{46} \\ * & * & * & * & \Pi_{55} & \Pi_{56} \\ * & * & * & * & * & \Pi_{66} \end{bmatrix} \quad (38)$$

with  $\Pi_{11} = R + \delta_4 \bar{L}_g^T \bar{L}_g + C_f^T C_f$ ,  $\Pi_{12} = \tau(\bar{T} \bar{A} - \bar{L} \bar{C})^T \bar{P} \bar{T}$ ,  $\Pi_{13} = \tau(\bar{T} \bar{A} - \bar{L} \bar{C})^T \bar{P} \bar{T} \bar{E}$ ,  $\Pi_{14} = -(\bar{T} \bar{A} - \bar{L} \bar{C})^T \bar{P} \bar{L} \bar{D}_2$ ,  $\Pi_{15} = -(\bar{T} \bar{A} - \bar{L} \bar{C})^T \bar{P} \bar{H} \bar{D}_h$ ,  $\Pi_{16} = (\bar{T} \bar{A} - \bar{L} \bar{C})^T \bar{P} \bar{I}_m$ ,  $\Pi_{22} = \tau^2 \bar{T}^T \bar{P} \bar{T} - \delta_4 I_{n+m}$ ,  $\Pi_{23} = \tau^2 \bar{T}^T \bar{P} \bar{T} \bar{E}$ ,  $\Pi_{24} = -\tau \bar{T}^T \bar{P} \bar{L} \bar{D}_2$ ,  $\Pi_{25} = -\tau \bar{T}^T \bar{P} \bar{H} \bar{D}_h$ ,  $\Pi_{26} = \tau \bar{T}^T \bar{P} \bar{I}_m$ ,  $\Pi_{33} = \tau^2 (\bar{T} \bar{E})^T \bar{P} \bar{T} \bar{E} - \gamma_1^2 I_d$ ,  $\Pi_{34} = -\tau (\bar{T} \bar{E})^T \bar{P} \bar{L} \bar{D}_2$ ,  $\Pi_{35} = -\tau (\bar{T} \bar{E})^T \bar{P} \bar{H} \bar{D}_h$ ,  $\Pi_{36} = \tau (\bar{T} \bar{E})^T \bar{P} \bar{I}_m$ ,  $\Pi_{44} = (\bar{L} \bar{D}_2)^T \bar{P} \bar{L} \bar{D}_2 - \gamma_2^2 I_s$ ,  $\Pi_{45} = (\bar{L} \bar{D}_2)^T \bar{P} \bar{H} \bar{D}_h$ ,  $\Pi_{46} = -(\bar{L} \bar{D}_2)^T \bar{P} \bar{I}_m$ ,  $\Pi_{55} = (\bar{H} \bar{D}_h)^T \bar{P} \bar{H} \bar{D}_h - \gamma_3^2 I_s$ ,  $\Pi_{56} = -(\bar{H} \bar{D}_h)^T \bar{P} \bar{I}_m$ , and  $\Pi_{66} = \bar{I}_m^T \bar{P} \bar{I}_m - \gamma_4^2 I_m$ .

Further, the inequality,  $\Pi < 0$ , can be transformed into

$$\begin{bmatrix} (\bar{T} \bar{A} - \bar{L} \bar{C})^T \bar{P} \\ \tau \bar{T}^T \bar{P} \\ \tau (\bar{T} \bar{E})^T \bar{P} \\ \bar{L}^T \bar{P} \\ (\bar{H} \bar{D}_h)^T \bar{P} \\ \bar{I}_m^T \bar{P} \end{bmatrix} \bar{P}^{-1} \begin{bmatrix} (\bar{T} \bar{A} - \bar{L} \bar{C})^T \bar{P} \\ \tau \bar{T}^T \bar{P} \\ \tau (\bar{T} \bar{E})^T \bar{P} \\ \bar{L}^T \bar{P} \\ (\bar{H} \bar{D}_h)^T \bar{P} \\ \bar{I}_m^T \bar{P} \end{bmatrix} + \begin{bmatrix} -\bar{P} + \delta_4 \bar{L}_g^T \bar{L}_g + C_f^T C_f & 0 & 0 & 0 & 0 & 0 \\ * & -\delta_4 I_{n+m} & 0 & 0 & 0 & 0 \\ * & * & -\gamma_1^2 I_d & 0 & 0 & 0 \\ * & * & * & -\gamma_2^2 I_s & 0 & 0 \\ * & * & * & * & -\gamma_3^2 I_s & 0 \\ * & * & * & * & * & -\gamma_4^2 I_m \end{bmatrix} < 0. \quad (39)$$

Using the Schur complement lemma again, (39) is equivalent to (28), which means that, for all nonzero  $d_1(k) \in L_2[0, \infty)$ ,  $d_2(k) \in L_2[0, \infty)$ , and  $\Delta f(k) \in L_2[0, \infty)$ , one obtains  $J < 0$ . Therefore, we can conclude from (35) that the  $H_\infty$  performance criterion (29) is satisfied. This completes the proof.  $\square$

In Theorem 5, multiple attenuation levels in the  $H_\infty$  performance criterion (29) are prescribed for better restricting each component of the augmented disturbance  $\omega(k)$  on fault reconstruction performance. If only a single  $H_\infty$  attenuation level is considered for the augmented disturbance  $\omega(k)$ , the following corollary can be readily obtained based on Theorem 5.

**Corollary 6.** Consider the Euler-approximate discrete model ((2a), (2b)). For a given positive scalar  $\gamma$ , if there exist a positive-definite symmetric matrix  $\bar{P} \in \mathbb{R}^{(n+m) \times (n+m)}$ , a matrix  $\bar{Y} \in \mathbb{R}^{(n+m) \times p}$ , and positive scalars  $\delta_i$ ,  $i = \{1, 2, 3, 4\}$  satisfying (27) and

$$\begin{bmatrix} -\bar{P} & \bar{P} \bar{T} \bar{A} - \bar{Y} \bar{C} & \tau \bar{P} \bar{T} & \bar{Y} \bar{D}_2 - \bar{P} \bar{D}_1 \\ * & -\bar{P} + \delta_4 \bar{L}_g^T \bar{L}_g + C_f^T C_f & 0 & 0 \\ * & * & -\delta_4 I_{n+m} & 0 \\ * & * & * & -\gamma^2 I_{2s+d+m} \end{bmatrix} < 0, \quad (40)$$

then the proposed nonlinear EPIO ((5a), (5b), (5c), and (5d)) can realize the uniform ultimate boundedness of state-estimating error  $e_x(k)$  and fault-reconstructing error  $e_f(k)$  with an  $H_\infty$  performance criterion:  $\|e_f(k)\| \leq \gamma \|\omega(k)\|$ . Moreover, augmented matrix  $\bar{L}$  can be determined by  $\bar{L} = \bar{P}^{-1} \bar{Y}$ .

*Proof.* The proof of Corollary 6 is similar to that of Theorem 5; it is thus omitted here.  $\square$

*Remark 7.* In Corollary 6, the  $H_\infty$  performance criterion with an attenuation level  $\gamma$  is adopted such that the designed nonlinear EPIO is robust to the augmented disturbance  $\omega(k)$ . However, this design inevitably results in conservatism such that the EPIO has a limited robust performance. To obtain less conservative result in the EPIO design, the  $H_\infty$  criterion with attenuation levels  $\gamma_i$ ,  $\forall i \in \{1, 2, 3, 4\}$  is adopted in Theorem 5 such that the impact of  $d_1(k)$ ,  $d_2(k)$ , and  $\Delta f(k)$  on  $e_f(k)$  can be effectively attenuated. Therefore, Theorem 5 is more flexible than Corollary 6. Compared with Corollary 6, one may obtain smaller  $H_\infty$  attenuation levels using Theorem 5; that is,  $\gamma \geq \gamma_i$ ,  $\forall i \in \{1, 2, 3, 4\}$ . Additionally, to guarantee accurate reconstruction of time-varying faults, especially fast-varying faults, we can select a sufficiently small attenuation level  $\gamma_4$  to restrict variation vector  $\Delta f(k)$  at the expense of the robustness against external disturbance  $d_1(k)$  and measurement noise  $d_2(k)$ .

Considering constant actuator faults in the system ((1a), (1b)), the results proposed in Theorem 5 and in Corollary 6 can be readily particularized in the following corollaries.

**Corollary 8.** Consider the Euler-approximate discrete model ((2a), (2b)). For given positive scalars  $\gamma_1$ ,  $\gamma_2$ , and  $\gamma_3$ , if there exist a positive-definite symmetric matrix  $\bar{P} \in \mathbb{R}^{(n+m) \times (n+m)}$ , a matrix  $\bar{Y} \in \mathbb{R}^{(n+m) \times p}$ , and a positive scalar  $\delta$  such that the following LMI holds:

$$\begin{bmatrix} -\bar{P} & \bar{P}\bar{T}\bar{A} - \bar{Y}\bar{C} & \tau\bar{P}\bar{T} & \tau\bar{P}\bar{T}\bar{E} & -\bar{Y}D_2 & -\bar{P}\bar{D}_h \\ * & -\bar{P} + \delta\bar{L}_g^T\bar{L}_g + C_f^T C_f & 0 & 0 & 0 & 0 \\ * & * & -\delta I_{n+m} & 0 & 0 & 0 \\ * & * & * & -\gamma_1^2 I_d & 0 & 0 \\ * & * & * & * & -\gamma_2^2 I_s & 0 \\ * & * & * & * & * & -\gamma_3^2 I_s \end{bmatrix} < 0, \quad (41)$$

where  $\bar{L}_g = \begin{bmatrix} L_g I_n & 0 \\ 0 & 0_m \end{bmatrix}$ ,  $\bar{E} = \begin{bmatrix} E \\ 0 \end{bmatrix}$ , and  $\bar{D}_h = \begin{bmatrix} HD_2 \\ 0 \end{bmatrix}$ , then the proposed nonlinear EPIO ((5a), (5b), (5c), and (5d)) can asymptotically reconstruct constant actuator faults, and fault-reconstructing error  $e_f(k)$  satisfies the following inequality:

$$\|e_f(k)\|^2 \leq \gamma_1^2 \|d_1(k)\|^2 + (\gamma_2^2 + \gamma_3^2) \|d_2(k)\|^2. \quad (42)$$

Moreover, augmented matrix  $\bar{L}$  can be determined by  $\bar{L} = \bar{P}^{-1}\bar{Y}$ .

**Corollary 9.** Consider the Euler-approximate model ((2a), (2b)). For a given positive scalar  $\gamma$ , if there exist a positive-definite symmetric matrix  $\bar{P} \in \mathbb{R}^{(n+m) \times (n+m)}$ , a matrix  $\bar{Y} \in \mathbb{R}^{(n+m) \times p}$ , and a positive scalar  $\delta$  such that the following LMI holds:

$$\begin{bmatrix} -\bar{P} & \bar{P}\bar{T}\bar{A} - \bar{Y}\bar{C} & \tau\bar{P}\bar{T} & \bar{Y}\bar{D}_{23} - \bar{P}\bar{D}_{13} \\ * & -\bar{P} + \delta\bar{L}_g^T\bar{L}_g + C_f^T C_f & 0 & 0 \\ * & * & -\delta I_{n+m} & 0 \\ * & * & * & -\gamma^2 I_{2s+d} \end{bmatrix} < 0, \quad (43)$$

where  $\bar{L}_g = \begin{bmatrix} L_g I_n & 0 \\ 0 & 0_m \end{bmatrix}$ ,  $\bar{D}_{13} = \begin{bmatrix} -\tau TE & 0 & HD_2 \\ 0 & 0 & 0 \end{bmatrix}$ , and  $\bar{D}_{23} = \begin{bmatrix} 0 & -D_2 & 0 \end{bmatrix}$ , then the proposed nonlinear EPIO ((5a), (5b), (5c), and (5d)) can asymptotically reconstruct constant actuator faults, and fault reconstruction error  $e_f(k)$  satisfies that  $\|e_f(k)\| \leq \gamma \|\omega_d(k)\|$ , where  $\omega_d(k) = \begin{bmatrix} d_1^T(k) & d_2^T(k) & d_2^T(k+1) \end{bmatrix}^T$ . Moreover, augmented matrix  $\bar{L}$  can be determined by  $\bar{L} = \bar{P}^{-1}\bar{Y}$ .

**Remark 10.** Theorem 5 and Corollary 6 can guarantee the uniform ultimate boundedness of state estimation error  $e_x(k)$  and fault reconstruction error  $e_f(k)$  such that the designed EPIO can achieve accurate reconstruction of constant and time-varying actuator faults. If constant actuator faults are considered in the system 1, then one obtains  $\Delta f(k) \equiv 0$ .

Therefore, using Corollaries 8 and 9, the designed EPIO can asymptotically reconstruct constant actuator faults.

*Remark 11.* Since the Lipschitz condition (32) is introduced in the proof of Theorem 5, there may be no feasible solution for (27) and (28), especially for a large Lipschitz constant. However, the condition (17) is not overly restrictive because the Lipschitz constant might be reduced via coordinate transformation techniques, as discussed in [14, 17, 24]. For multiobjective observer design, the increased number of LMI constraints inevitably results in conservatism. It is worth noting that slack matrix variable technique can be adopted to reduce this conservatism; the interested readers can be referred to [14, 25, 26] for detailed information.

According to Theorem 5, the design procedure of the proposed EPIO will be summarized as follows:

*Step 1.* Find the maximum number of columns  $q$  of matrix  $D_1$  for which the condition  $\text{rank}(CD_{11}) = \text{rank}(D_{11})$  is satisfied.

*Step 2.* Solve (13) to obtain  $T$  and  $H$ , and verify that  $\text{rank}(TF) = \text{rank}(F)$ .

*Step 3.* Choose appropriate scalars  $\delta_i$ ,  $i = \{1, 2, 3, 4\}$ ; then, based on (27) and (40),  $H_\infty$  performance level  $\gamma$  is computed using the Solver *mincx* in the LMI toolbox of Matlab.

*Step 4.* Choose  $\gamma_i \leq \gamma$ ,  $i = \{1, 2, 3, 4\}$ ; then, solving (27) and (28) using the Solver *feasp* in the LMI toolbox of Matlab, matrices  $\bar{P}$  and  $\bar{Y}$  can be obtained.

*Step 5.* Compute  $\bar{L} = \bar{P}^{-1}\bar{Y}$ , then obtain gain matrices  $L$  and  $K$ .

*Step 6.* Construct the EPIO based on the above calculated matrices.

Using the above theorem and corollaries, we can design observer gain matrices such that the stability and convergence of the state estimation error and fault reconstruction error between the nonlinear EPIO and the Euler-approximate model are guaranteed. However, it might be impossible for the EPIO designed under the Euler-approximate model to be implemented on the exact system models. To solve this problem, the EPIO will be required to satisfy semiglobal practical convergence property introduced by [16] such that the EPIO can track actuator faults with satisfactory accuracy. This is what we shall address in next subsection.

**3.3. Semiglobal Practical Convergence Analysis.** In this subsection, we will derive sufficient conditions for existence of observer gain matrices and the sampling interval  $\tau$  to achieve semiglobal practical convergence under the Euler-approximate model without considering external disturbances and measurement noises. The definition of semiglobal practical convergence [16] is given as follows.

**Definition 12.** An observer is said to be semiglobal practical in the sampling period  $\tau$  if there exists a class- $\mathcal{KL}$  function

$\beta(\cdot, \cdot)$  such that, for any  $D > d > 0$  and compact sets  $\mathcal{X} \subset \mathbb{R}^n$ ,  $\mathcal{U} \subset \mathbb{R}^m$ , we can find a number  $\tau^* > 0$  with the property that, for all  $\tau \in (0, \tau^*]$ ,

$$\begin{aligned} \|\widehat{x}(0) - x(0)\| &\leq D, \\ x(k) \in \mathcal{X}, \quad u(k) \in \mathcal{U}, \quad \forall k \geq 0 \end{aligned} \quad (44)$$

imply

$$\|\widehat{x}(k) - x(k)\| \leq \beta(\|\widehat{x}(0) - x(0)\|, k\tau) + d. \quad (45)$$

In reference to the method proposed by [16], the following theorem presents the semiglobal practical convergence of the EPIO ((5a), (5b), (5c), and (5d)).

**Theorem 13.** *The proposed nonlinear EPIO under the Euler-approximate model ((2a), (2b)) is semiglobal practical in the sampling period  $\tau$  if there exist a positive scalar  $\sigma_1 > 1$ , a fixed positive-definite symmetric matrix  $Q_1 \in \mathbb{R}^{n \times n}$ , and a positive-definite symmetric matrix  $P_1 \in \mathbb{R}^{n \times n}$  such that*

$$\sigma_1 (T(I_n + \tau A) - LC)^T P_1 (T(I_n + \tau A) - LC) - P_1 = -Q_1, \quad (46)$$

$$\lambda_{\min}(Q_1) = \tau. \quad (47)$$

*Proof.* Consider the Lyapunov function candidate,  $V(k) = e_x^T(k)P_1e_x(k)$ ; then,

$$\begin{aligned} \|V(k_1) - V(k_2)\| &= \|e_x^T(k_1)P_1e_x(k_1) - e_x^T(k_2)P_1e_x(k_2)\| \\ &= \|[e_x(k_1) + e_x(k_2)]^T P_1 [e_x(k_1) - e_x(k_2)]\| \\ &\leq \lambda_{\max}(P_1) \|e_x(k_1) + e_x(k_2)\| \|e_x(k_1) - e_x(k_2)\|. \end{aligned} \quad (48)$$

Since the convergence of the proposed nonlinear EPIO ((5a), (5b), (5c), and (5d)) to the Euler-approximate model has been established using the aforementioned theorem and corollaries, then one obtains

$$\exists M \in (0, \infty), \quad \lambda_{\max}(P_1) \|e_x(k_1) + e_x(k_2)\| \leq M. \quad (49)$$

Thus,

$$\|V(k_1) - V(k_2)\| \leq M \|e_x(k_1) - e_x(k_2)\|, \quad (50)$$

$$\begin{aligned} \Delta V(k) &\leq e_x^T(k) (T(I_n + \tau A) - LC)^T \\ &\quad \times P_1 (T(I_n + \tau A) - LC) e_x(k) - e_x^T(k) P_1 e_x(k) \\ &\quad + 2\tau e_x^T(k) (T(I_n + \tau A) - LC)^T P_1 T \Delta \Phi(k) \\ &\quad + 2\tau e_x^T(k) (T(I_n + \tau A) - LC)^T P_1 T F e_f(k) \\ &\quad + \tau^2 \Delta \Phi^T(k) T^T P_1 T \Delta \Phi(k) + 2\tau^2 \Delta \Phi^T(k) T^T P_1 T F e_f(k) \\ &\quad + \tau^2 e_f^T(k) (TF)^T P_1 (TF) e_f(k). \end{aligned} \quad (51)$$

With the help of Lemma 1, the following inequalities can be easily derived:

$$\begin{aligned} 2\tau e_x^T(k) (T(I_n + \tau A) - LC)^T P_1 T \Delta \Phi(k) &\leq \epsilon_1 e_x^T(k) (T(I_n + \tau A) - LC)^T \\ &\quad \times P_1 (T(I_n + \tau A) - LC) e_x(k) \\ &\quad + \frac{\tau^2}{\epsilon_1} \Delta \Phi^T(k) T^T P_1 T \Delta \Phi(k), \end{aligned} \quad (52)$$

where  $\epsilon_1 > 0$ ,

$$\begin{aligned} 2\tau e_x^T(k) (T(I_n + \tau A) - LC)^T P_1 T F e_f(k) &\leq \epsilon_2 e_x^T(k) (T(I_n + \tau A) - LC)^T \\ &\quad \times P_1 (T(I_n + \tau A) - LC) e_x(k) \\ &\quad + \frac{\tau^2}{\epsilon_2} e_f^T(k) (TF)^T P_1 T F e_f(k), \end{aligned} \quad (53)$$

where  $\epsilon_2 > 0$ , and

$$\begin{aligned} 2\tau \Delta \Phi^T(k) T^T P_1 T F e_f(k) &\leq \epsilon_3 \Delta \Phi^T(k) T^T P_1 T \Delta \Phi(k) \\ &\quad + \frac{\tau^2}{\epsilon_3} e_f^T(k) (TF)^T P_1 T F e_f(k), \end{aligned} \quad (54)$$

where  $\epsilon_3 > 0$ .

Substituting (52)–(54) into (51) leads to

$$\begin{aligned} \Delta V(k) &\leq e_x^T(k) \\ &\quad \times (\sigma_1 (T(I_n + \tau A) - LC)^T P_1 (T(I_n + \tau A) - LC) - P_1) \\ &\quad \times e_x(k) + \sigma_2 \tau^2 \Delta \Phi^T(k) T^T P_1 T \Delta \Phi(k) \\ &\quad + \sigma_3 \tau^2 e_f^T(k) (TF)^T P_1 T F e_f(k) \\ &\leq e_x^T(k) \\ &\quad \times (\sigma_1 (T(I_n + \tau A) - LC)^T P_1 (T(I_n + \tau A) - LC) - P_1) \\ &\quad \times e_x(k) + \sigma_2 \tau^2 L_g^2 \bar{\sigma}^2(T) \lambda_{\max}(P_1) \|e_x(k)\|^2 \\ &\quad + \sigma_3 \tau^2 \bar{\sigma}^2(TF) \lambda_{\max}(P_1) \|e_f(k)\|^2, \end{aligned} \quad (55)$$

where  $\sigma_1 = 1 + \epsilon_1 + \epsilon_2$ ,  $\sigma_2 = 1 + (1/\epsilon_1) + \epsilon_3$ , and  $\sigma_3 = 1 + (1/\epsilon_2) + (1/\epsilon_3)$  with  $\epsilon_i > 0$ ,  $i = 1, 2, 3$ .

According to (46) and (47), (55) can be reorganized and simplified

$$\begin{aligned} \frac{\Delta V(k)}{\tau} &\leq -\|e_x(k)\|^2 \\ &+ \sigma_2 \tau L_g^2 \bar{\sigma}^2(T) \lambda_{\max}(P_1) \|e_x(k)\|^2 \\ &+ \sigma_3 \tau \bar{\sigma}^2(TF) \lambda_{\max}(P_1) \|e_f(k)\|^2. \end{aligned} \quad (56)$$

In addition, the following functions are defined:

$$\begin{aligned} \alpha_1(\|e_x(k)\|) &\triangleq \lambda_{\min}(P_1) \|e_x(k)\|^2, \\ \alpha_2(\|e_x(k)\|) &\triangleq \lambda_{\max}(P_1) \|e_x(k)\|^2, \\ \alpha_3(\|e_x(k)\|) &\triangleq \|e_x(k)\|^2, \quad \rho_0(\tau) \triangleq \tau, \\ \nu_0(\|e_x(k)\|) &\triangleq \sigma_2 \tau^2 L_g^2 \bar{\sigma}^2(T) \lambda_{\max}(P_1) \|e_x(k)\|^2, \\ \nu_1(\|x(k)\|) &\triangleq 0, \quad \nu_2(\|u(k)\|) \triangleq 0, \\ \nu_3(\|e_f(k)\|) &= \sigma_3 \tau \bar{\sigma}^2(TF) \lambda_{\max}(P_1) \|e_f(k)\|^2. \end{aligned} \quad (57)$$

Therefore, the following results can be derived:

$$\begin{aligned} \alpha_1(\|e_x(k)\|) &\leq V(k) \leq \alpha_2(\|e_x(k)\|), \\ \frac{V(k+1) - V(k)}{\tau} &\leq -\alpha_3(\|e_x(k)\|) \\ &+ \rho_0(\tau) [\nu_0(\|e_x(k)\|) + \nu_1(\|x(k)\|) \\ &+ \nu_2(\|u(k)\|) + \nu_3(\|e_f(k)\|)], \end{aligned} \quad (58)$$

where  $\alpha_1(\cdot), \alpha_2(\cdot), \alpha_3(\cdot)$ , and  $\rho_0(\cdot)$  are in class- $\mathcal{H}_\infty$  and  $\nu_0(\cdot), \nu_1(\cdot), \nu_2(\cdot)$ , and  $\nu_3(\cdot)$  are nondecreasing functions.

Based on the theorem and corollaries discussed in Subsection 3.2, it can be known that fault reconstruction error  $e_f(k)$  are uniformly bounded; herein, they are considered as the external disturbances. According to [17, 27], the Euler-approximate model is consistent with the exact discrete-time model. Conditions (50), (58) together display that all the conditions for semiglobal practical convergence as required by [16] are satisfied; hence, the designed nonlinear EPIO is semiglobal practical convergence in the sampling time in  $\tau$ . This completes the proof.  $\square$

Motivated by [18], we will present another sufficient conditions for semiglobal practical convergence of the proposed nonlinear EPIO ((5a), (5b), (5c) and (5d)).

**Theorem 14.** *The proposed nonlinear EPIO ((5a), (5b), (5c) and (5d)) designed under the Euler-approximate model ((2a), (2b)) is semiglobal practical in the sampling period  $\tau$  if there*

*exist positive-definite symmetric matrices  $P_2 \in \mathbb{R}^{n \times n}$  and  $Q_2 \in \mathbb{R}^{n \times n}$ , a matrix  $L \in \mathbb{R}^{n \times p}$ , and a positive scalar  $\epsilon_4$ , such that*

$$(T(I_n + \tau A) - LC)^T P_2 (T(I_n + \tau A) - LC) - P_2 = -Q_2, \quad (59)$$

$$\tau \leq \tau^* = \frac{\lambda_{\max}(Q_2) - \epsilon_4 [\lambda_{\max}(P_2) + \lambda_{\max}(Q_2)]}{2L_g \bar{\sigma}(T) \lambda_{\max}(P_2) \sqrt{1 + (\lambda_{\max}(Q_2) / \lambda_{\max}(P_2))}}. \quad (60)$$

*Proof.* The proof of Theorem 14 is similar to that of Theorem 2 in [18]; it is thus omitted here.  $\square$

*Remark 15.* Theorem 5 and Corollaries 6–9 imply that observer gain matrices  $L$  and  $K$  can be conveniently calculated using standard LMI optimization technique; furthermore, using Theorem 13 or Theorem 14, whether or not semiglobal practical convergence property of the designed EPIO can be guaranteed can be checked. If yes, the EPIO designed under Euler-approximate models can be implemented on the exact discrete-time models.

## 4. Simulation Studies

In this section, a single-link robot with a flexible joint borrowed from [28] is employed to illustrate the effectiveness of the proposed fault-reconstructing method. The considered system dynamics is described in a form of (1a), (1b) with

$$\begin{aligned} A &= \begin{bmatrix} 0 & 1 & 0 & 0 \\ -48.6 & -1.25 & 48.6 & 0 \\ 0 & 0 & 0 & 1 \\ 19.5 & 0 & -19.5 & -1.325 \end{bmatrix}, \\ \Phi(x(t), t) &= \begin{bmatrix} 0 \\ 0 \\ 0 \\ -0.333 \sin(x_3(t)) \end{bmatrix}, \quad B = \begin{bmatrix} 0 \\ 21.60 \\ 0 \\ 0 \end{bmatrix}, \\ C &= \begin{bmatrix} 1 & 0 & 0 & 0 \\ 0 & 1 & 0 & 0 \\ 0 & 0 & 1 & 0 \end{bmatrix}, \quad D_1 = \begin{bmatrix} 0.1 & 0 \\ 0 & 0.1 \\ 0 & 0 \\ 0 & 0 \end{bmatrix}, \\ D_2 &= 0.1I_3, \end{aligned} \quad (61)$$

where system states are the motor position, link position, and velocities. Measurement outputs are the first three system states. In this work, we consider actuator faults that usually occur in input channels. Therefore, it is reasonable to assume that fault distribution matrix  $F = B$ .

The Lipschitz constant  $L_g$  for the system ((1a), (1b)) is selected as 0.333 and the sampling period  $\tau$  is selected as 0.01 s. Therefore, an Euler-approximate model of the considered system ((1a), (1b)) can be established for the flexible-joint robot.

In order to achieve robust actuator-fault reconstruction, observer gain matrices  $T$  and  $H$  are chosen as follows:

$$T = \begin{bmatrix} 0 & 0 & 0 & 0 \\ 0 & 0.5 & 0 & 0 \\ 0 & 0 & 0.5 & 0 \\ 0 & 0 & 0 & 1.0 \end{bmatrix}, \quad H = \begin{bmatrix} 1.0 & 0 & 0 \\ 0 & 0.5 & 0 \\ 0 & 0 & 0.5 \\ 0 & 0 & 0 \end{bmatrix}. \quad (62)$$

Letting  $\delta_i = 0.1$ ,  $\forall i = \{1, 2, 3, 4\}$ , and solving (27) and (40) in Corollary 6 using the Solver *mincx* in the LMI toolbox of Matlab, one can obtain the  $H_\infty$  attenuation level  $\gamma = 2.0230$ . Further, choosing  $\gamma_1 = 0.5$ ,  $\gamma_2 = 2.0230$ ,  $\gamma_3 = 2.0230$ , and  $\gamma_4 = 2.0230$  and solving (27) and (28) in Theorem 5 using the LMI toolbox of Matlab, a feasible solution for gain matrices  $L$  and  $K$  can be obtained as

$$L = \begin{bmatrix} 0.0174 & 0.0014 & 0.1951 \\ 0.0014 & 1.6401 & 0.0359 \\ 0.0358 & -0.0030 & 0.3299 \\ 1.3353 & -0.2860 & 8.8951 \end{bmatrix}, \quad K = \begin{bmatrix} -0.0067 \\ 10.6257 \\ -0.4187 \end{bmatrix}^T. \quad (63)$$

Therefore, the EPIO designed using Theorem 5 has better robustness against external disturbances and measurement noises.

Choosing  $Q_1 = 0.01I_4$  and  $\sigma_1 = 1.01$ , matrix  $P_1$  can be obtained by solving (46):

$$P_1 = \begin{bmatrix} 0.0961 & -0.0119 & 1.0957 & -0.0976 \\ -0.0119 & 0.0020 & -0.1611 & 0.0164 \\ 1.0957 & -0.1611 & 15.0770 & -1.3221 \\ -0.0976 & 0.0164 & -1.3221 & 0.1317 \end{bmatrix}. \quad (64)$$

Further, choosing  $\epsilon_4 = 0.01$  and solving (59) lead to

$$P_2 = 10^2 \times \begin{bmatrix} 3.5324 & -0.0081 & 0.2805 & -0.0369 \\ -0.0081 & 0.0006 & -0.0374 & 0.0047 \\ 0.2805 & -0.0374 & 6.6747 & -0.3458 \\ -0.0369 & 0.0047 & -0.3458 & 0.0376 \end{bmatrix}, \quad (65)$$

$$Q_2 = 10^2 \times \begin{bmatrix} 3.5024 & -0.0044 & -0.0268 & -0.0077 \\ -0.0044 & 0.0001 & 0.0069 & 0.0006 \\ -0.0268 & 0.0069 & 2.3426 & 0.0201 \\ -0.0077 & 0.0006 & 0.0201 & 0.0042 \end{bmatrix},$$

and  $\tau^* = 0.6162$  s, which is greater than 0.01 s. We can now check that the designed observer gain matrices and the sampling period 0.01 s can make the Theorems 13 and 14 hold. Hence, it is concluded that the designed EPIO ((5a), (5b), (5c), and (5d)) is semiglobal practical convergent in the sampling period 0.01 s.

According to Corollary 9, let  $\delta = 0.1$ ; then, (43) can be solved to obtain  $\gamma = 1.3007$ . Further, choosing  $\gamma_1 = 0.3$ ,  $\gamma_2 = 1.3007$ , and  $\gamma_3 = 1.3007$ , and solving (41) in Corollary 8 leads to

$$L = \begin{bmatrix} -0.0167 & -0.1111 & -0.0104 \\ -0.1134 & 0.3838 & 0.0023 \\ 0.02766 & 0.1753 & 0.5899 \\ 0.4578 & 1.5168 & 14.4412 \end{bmatrix}, \quad K = \begin{bmatrix} 0.0121 \\ 0.6371 \\ -0.1017 \end{bmatrix}^T. \quad (66)$$

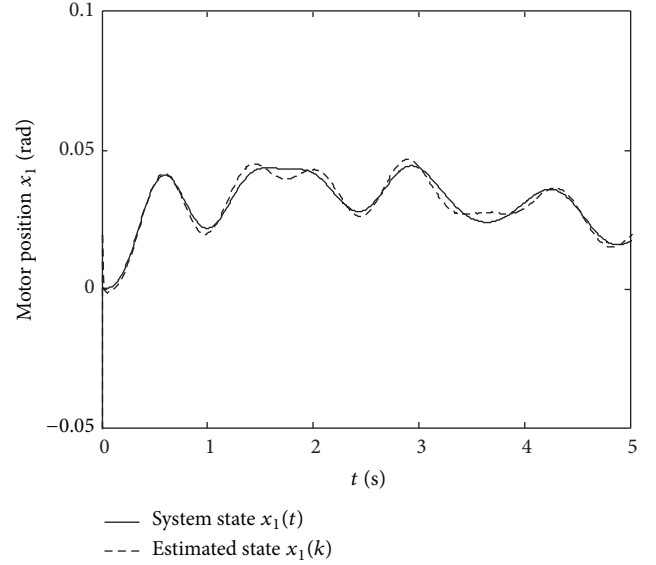


FIGURE 1: Actual system state  $x_1(t)$  and its estimate.

Using Theorems 13 and 14, it is easily checked that the EPIO designed using Corollary 8 is also semiglobal practical convergent in 0.01 s.

In the simulation, the control input signal is assigned as  $u(k) = 0.05 \sin 5k$ ; the initial values of the estimated states are assumed as  $\hat{x}(0) = [-0.1 \ 0.5 \ -0.1 \ 0.2]^T$ ; external disturbance  $d_1(k)$  and measurement noise  $d_2(k)$  are chosen as  $0.001 \sin(10k)$  and a Gaussian-distributed random signal with zero mean and variance of  $10^{-5}$ , respectively. Additionally, actuator faults are assumed to be changes of bus voltage, and two fault scenarios are employed as

- (1) a constant fault that is described as

$$f(k) = \begin{cases} 0.2 & 2 \text{ s} \leq k\tau \leq 6 \text{ s} \\ 0 & \text{others.} \end{cases} \quad (67)$$

- (2) a time-varying fault that is described as

$$f(k) = \begin{cases} 0.05 \sin(5k\tau) + 0.05 \sin(3k\tau) \\ + 0.06 \sin(2k\tau) + 0.2, & k\tau \geq 2 \text{ s} \\ 0 & \text{others.} \end{cases} \quad (68)$$

Using the designed EPIO via Theorem 5, the estimated system states in fault-free conditions are exhibited in Figures 1, 2, 3, and 4 where the estimated states can track the original states of system ((1a), (1b)) with satisfactory accuracy. Further, reconstruction signals for the constant and time-varying faults obtained by the EPIO designed using Theorem 5 are demonstrated in Figures 5 and 6 while constant-fault reconstruction signal by the EPIO designed using Corollary 8 is illustrated in Figure 7. The above figures reveal that the proposed EPIO can accurately reconstruct actuator faults. All of simulation results claim that the EPIO-based fault-reconstructing method is effective for Lipschitz nonlinear systems with Euler-approximate models.

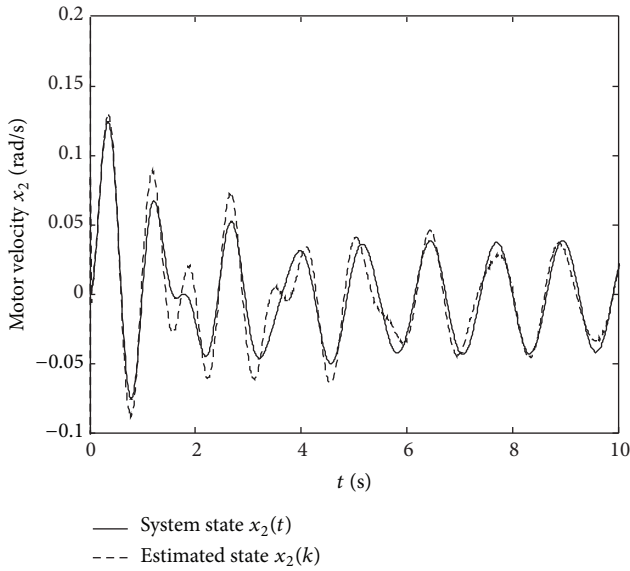
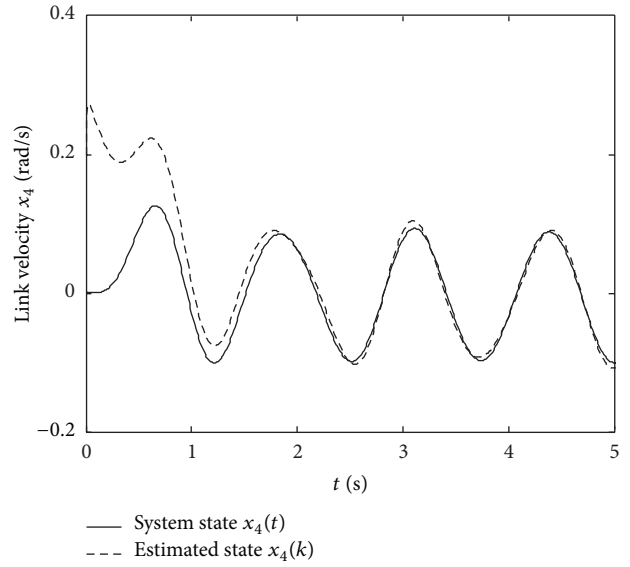
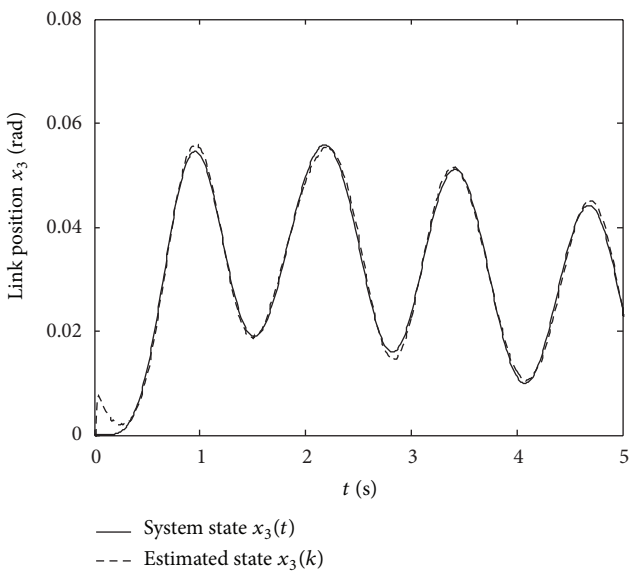
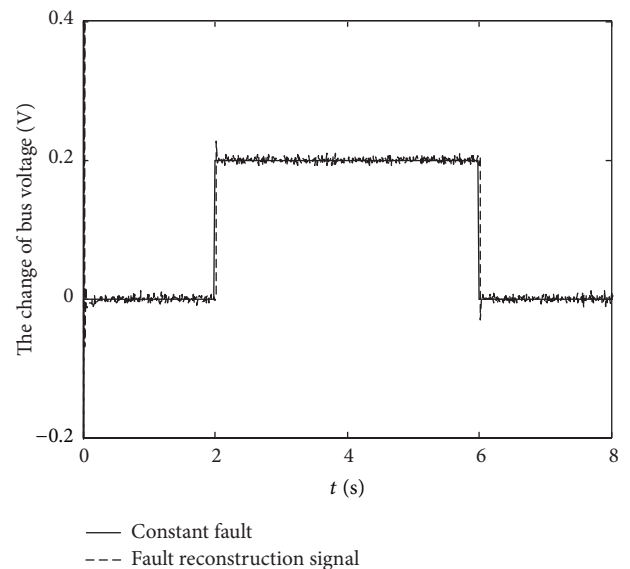
FIGURE 2: Actual system state  $x_2(t)$  and its estimate.FIGURE 4: Actual system state  $x_4(t)$  and its estimate.FIGURE 3: Actual system state  $x_3(t)$  and its estimate.

FIGURE 5: Reconstruction signal of a constant fault via the EPIO designed using Theorem 5.

## 5. Conclusions

In this paper, a robust fault-reconstructing scheme for Lipschitz nonlinear systems with Euler-approximate models is investigated. A new discrete-time EPIO is constructed to achieve robust actuator-fault reconstruction. An important advantage of the newly designed EPIO is its disturbance-decoupling ability such that the accuracy of the reconstructed faults can be guaranteed. To ensure convergence of the estimated states to the system states of the continuous-time model, semiglobal practical convergence of the EPIO is proved. Another advantage of the proposed approach is that a systematic observer synthesis with  $H_\infty$  techniques is effectively solved using a standard LMI tool. Simulated

results on a flexible-joint robot have clearly verified the effectiveness of the proposed fault-reconstruction method. With mismatching errors caused by approximate discrete models and reconstructed fault signals, active FTC for Lipschitz nonlinear systems with Euler-approximate models will be our future research target.

## Conflict of Interests

The authors declare that there is no conflict of interests regarding the publication of this paper.

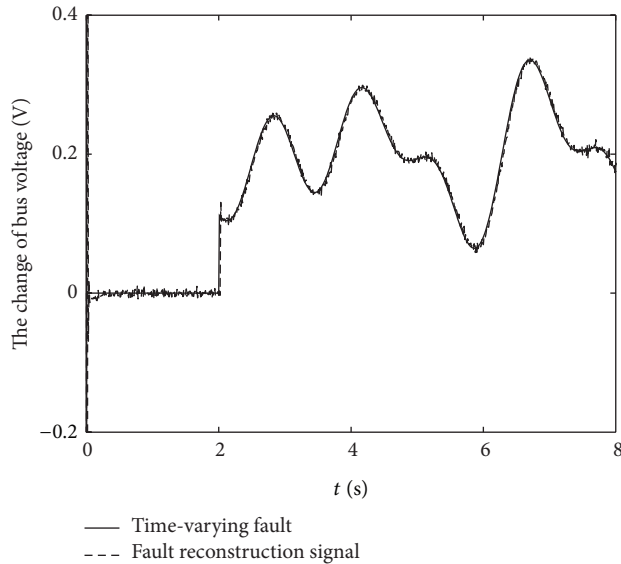


FIGURE 6: Reconstruction signal of a time-varying fault via the EPIO designed using Theorem 5.

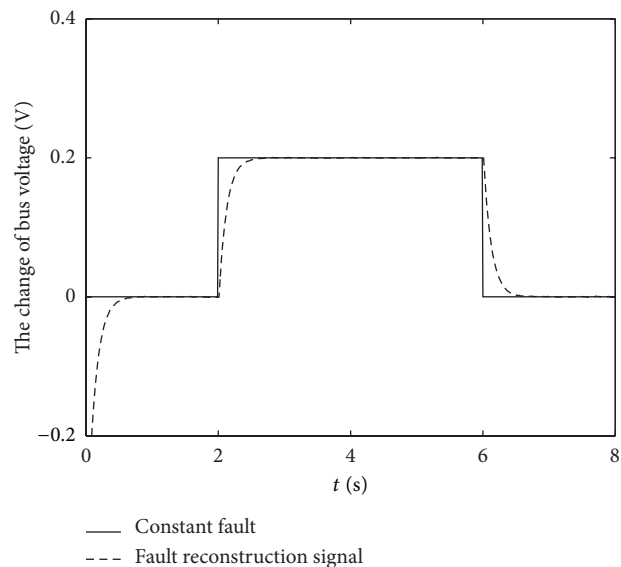


FIGURE 7: Reconstruction signal of a constant fault via the EPIO designed using Corollary 8.

## Acknowledgments

This work is partially supported by National Natural Science Foundation of China (Grant no. 61203185) and Open Funding for National Defense Key Subject Laboratory of Micro- and Small Spacecraft Technology (Grant no. 20090450126).

## References

- [1] S. X. Ding, *Model-Based Fault Diagnosis Techniques-Design Schemes, Algorithms, and Tools*, Springer, 2008.
- [2] J. Chen and R. Patton, *Robust Model-Based Fault Diagnosis for Dynamic Systems*, Springer, London, UK, 2012.
- [3] I. Hwang, S. Kim, Y. Kim, and C. E. Seah, "A survey of fault detection, isolation, and reconfiguration methods," *IEEE Transactions on Control Systems Technology*, vol. 18, no. 3, pp. 636–653, 2010.
- [4] K. Zhang, B. Jiang, and V. Cocquempot, "Adaptive observer-based fast fault estimation," *International Journal of Control, Automation and Systems*, vol. 6, no. 3, pp. 320–326, 2008.
- [5] J. H. Fan, Y. M. Zhang, and Z. Q. Zheng, "Adaptive observer-based integrated fault diagnosis and fault-tolerant control systems against actuator faults and saturation," *Journal of Dynamic Systems, Measurement and Control*, vol. 135, no. 4, Article ID 041008, 13 pages, 2013.
- [6] H. Alwi, C. Edwards, and A. Marcos, "Fault reconstruction using a LPV sliding mode observer for a class of LPV systems," *Journal of the Franklin Institute*, vol. 349, no. 2, pp. 510–530, 2012.
- [7] M. Liu and P. Shi, "Sensor fault estimation and tolerant control for Itô stochastic systems with a descriptor sliding mode approach," *Automatica*, vol. 49, no. 5, pp. 1242–1250, 2013.
- [8] W. Chen and M. Saif, "An iterative learning observer for fault detection and accommodation in nonlinear time-delay systems," *International Journal of Robust and Nonlinear Control*, vol. 16, no. 1, pp. 1–19, 2006.
- [9] Q. X. Jia, W. Chen, Y. C. Zhang, and X. Q. Chen, "Robust fault reconstruction via learning observers in linear parameter-varying systems subject to loss of actuator effectiveness," *IET Control Theory and Applications*, vol. 8, no. 1, pp. 42–50, 2014.
- [10] D. Koenig, "Unknown input proportional multiple-integral observer design for linear descriptor systems: application to state and fault estimation," *IEEE Transactions on Automatic Control*, vol. 50, no. 2, pp. 212–217, 2005.
- [11] H. Hamdi, M. Rodrigues, C. Mechmeche, D. Theilliol, and N. B. Braiek, "Fault detection and isolation in linear parameter-varying descriptor systems via proportional integral observer," *International Journal of Adaptive Control and Signal Processing*, vol. 26, no. 3, pp. 224–240, 2012.
- [12] F. Caccavale, F. Pierri, and L. Villani, "Adaptive observer for fault diagnosis in nonlinear discrete-time systems," *Journal of Dynamic Systems, Measurement and Control*, vol. 130, no. 2, Article ID 021005, 2008.
- [13] X. D. Zhang, M. M. Polycarpou, and T. Parisini, "Fault diagnosis of a class of nonlinear uncertain systems with Lipschitz nonlinearities using adaptive estimation," *Automatica*, vol. 46, no. 2, pp. 290–299, 2010.
- [14] K. Zhang, B. Jiang, and P. Shi, "Observer-based integrated robust fault estimation and accommodation design for discrete-time systems," *International Journal of Control*, vol. 83, no. 6, pp. 1167–1181, 2010.
- [15] S. M. Tabatabaeipour and T. Bak, "Robust observer-based fault estimation and accommodation of discrete-time piecewise linear systems," *Journal of the Franklin Institute*, vol. 351, no. 1, pp. 277–295, 2014.
- [16] M. Arcak and D. Nešić, "A framework for nonlinear sampled-data observer design via approximate discrete-time models and emulation," *Automatica*, vol. 40, no. 11, pp. 1931–1938, 2004.
- [17] M. Abbaszadeh and H. J. Marquez, "Robust  $H_\infty$  observer design for sampled-data Lipschitz nonlinear systems with exact and Euler approximate models," *Automatica*, vol. 44, no. 3, pp. 799–806, 2008.
- [18] Z. Mao, B. Jiang, and P. Shi, "Fault-tolerant control for a class of nonlinear sampled-data systems via a Euler approximate observer," *Automatica*, vol. 46, no. 11, pp. 1852–1859, 2010.

- [19] B. Jiang, P. Shi, and Z. Mao, "Sliding mode observer-based fault estimation for nonlinear networked control systems," *Circuits, Systems, and Signal Processing*, vol. 30, no. 11, pp. 1–16, 2011.
- [20] Q. X. Jia, Y. C. Zhang, W. Chen, and Y. H. Geng, "Design of novel observers for robust fault detection in discrete-time Lipschitz nonlinear systems with Euler-approximate models," *International Journal of Automation and Control*, vol. 8, no. 3, pp. 191–210, 2014.
- [21] F. Amato, C. Cosentino, M. Mattei, and G. Paviglianiti, "A direct/functional redundancy scheme for fault detection and isolation on an aircraft," *Aerospace Science and Technology*, vol. 10, no. 4, pp. 338–345, 2006.
- [22] S. Boyd, L. El Ghaoui, E. Feron, and V. Balakrishnan, *Linear Matrix Inequalities in Systems and Control Theory*, Philadelphia, Pa, USA, Society for Industrial and Applied Mathematics (SIAM), Philadelphia, PA, 1994.
- [23] Z. Wang, M. Rodrigues, D. Theilliol, and Y. Shen, "Actuator fault estimation observer design for discrete-time linear parameter-varying descriptor systems," *International Journal of Adaptive Control and Signal Processing*, 2014.
- [24] F. Zhu and Z. Han, "A note on observers for Lipschitz nonlinear systems," *IEEE Transactions on Automatic Control*, vol. 47, no. 10, pp. 1751–1754, 2002.
- [25] W. Xie, "Multi-objective  $H_\infty/\alpha$ -stability controller synthesis of LTI systems," *IET Control Theory and Applications*, vol. 2, no. 1, pp. 51–55, 2008.
- [26] K. Zhang, B. Jiang, P. Shi, and J. Xu, "Multi-constrained fault estimation observer design with finite frequency specifications for continuous-time systems," *International Journal of Control*, vol. 87, no. 8, pp. 1635–1645, 2014.
- [27] D. Nesic, A. R. Teel, and P. V. Kokotovic, "Sufficient conditions for stabilization of sampled-data nonlinear systems via discrete-time approximations," *Systems and Control Letters*, vol. 38, no. 4-5, pp. 259–270, 1999.
- [28] K. Vijayaraghavan, R. Rajamani, and J. Bokor, "Quantitative fault estimation for a class of non-linear systems," *International Journal of Control*, vol. 80, no. 1, pp. 64–74, 2007.

## Research Article

# Simultaneous Fault Detection and Control for Discrete-Time Systems via a Switched Scheme

**Jian Li and Xingze Dai**

*School of Automation Engineering, Northeast Dianli University, Jilin 132012, China*

Correspondence should be addressed to Jian Li; [lijianphd@yeah.net](mailto:lijianphd@yeah.net)

Received 11 April 2014; Accepted 13 July 2014

Academic Editor: Ke Zhang

Copyright © 2015 J. Li and X. Dai. This is an open access article distributed under the Creative Commons Attribution License, which permits unrestricted use, distribution, and reproduction in any medium, provided the original work is properly cited.

This paper is concerned with the problem of simultaneous fault detection and control for linear systems with a switched scheme. The switched detector/controller is designed simultaneously and generates two signals such that it provides fault tolerance, especially including “destabilizing failure” meanwhile, it generates the residual signal to alarm the fault. When the faults are detected, the detector/controller is switched to reduce the effect of the faults. When the faults are removed, the detector/controller is switched to the original detector/controller to guarantee the control objective. In addition, it has time delay in detection of the faults; then the time-driven switching strategy for asynchronous case is included. Thus a mixed switching strategy is proposed. A two-step procedure is adopted to obtain the solutions through satisfying a set of linear matrix inequalities. Finally, an example is provided to demonstrate the effectiveness of the proposed design method.

## 1. Introduction

The problem of designing reliable control systems has attracted strong interest and intensive research activities recently. The objective of this research is focused on designing an appropriate controller such that the closed-loop system can guarantee system stability. During the past decades, there were many results that investigated this important issue. The problem of the reliable control and the reliable filter has been thoroughly investigated in [1–5]. Meanwhile, the simultaneous fault detection and control problem also has attracted a lot of attention in the last two decades. The attention of this study is to unify the control and detection units into a single unit; then it ensures that the reliable control is feasible, and the information of the fault is got. The advantage of this method is far less overall complexity than the design method where the two units are designed separately. Thus, the simultaneous fault detection and control problem has been addressed by several researches, for example, [6–9].

On the other hand, there has been a great interest in switching control due to their significance both in theory and in applications [10–14]. The motivation of studying switched systems comes from the fact that many physical plants exhibit the switching feature during multimodels or multicontrollers,

and a suitable switching rule is needed to deal with some complex tasks or to overcome the shortcomings of the single controller. Several approaches have been proposed for the control problem or the filtering problem for switched systems [15–18]. In addition, when the faults have been detected, the switched scheme can be applied to the problem of fault detection and control; then the detected information of the fault is the switching signal. This problem has been studied by several researches, for example, [19, 20]. It should be pointed out, however, that there has been “destabilizing failure” in many practical systems; that is, the never-faulty actuator cannot stabilize the considered system. Then, the existing design approaches are not appropriate for these complicated cases; the new technique with the switched scheme should be considered to guarantee the norm of the states of the system to increase within the acceptable limits and then realize the reliable control.

In this paper, the detector/controller is designed as a switched scheme. When the actuator faults are detected, the detector/controller is switched to reduce the effect of the faults. When the faults are removed, the detector/controller is converted back to consider the control performance firstly. Meanwhile, the detector/controller is designed as a single unit and generates two signals: a detection signal and a

control signal, which are used to detect faults and guarantee fault tolerance, especially including “destabilizing failure,” respectively. The key idea is to view the information of the fault detection to preserve the overall system stability and use the switching strategy to provide fault tolerance, especially including “destabilizing failure.”

The contributions of this paper are in two respects. Firstly, the method takes into account the information of the faulty detection to control the system and improves the results in [21, 22], which only employ an average dwell-time switching strategy to stabilize the given system with actuators fault. Subsequently, it has time delay in detection of the faults; thus, the asynchronous case is considered in this switching strategy.

## 2. Problem Statement and Preliminaries

*2.1. System Model.* Consider the following discrete-time linear systems:

$$\begin{aligned} x(k+1) &= Ax(k) + B_1u(k) + B_2d(k), \\ y(k) &= Cx(k) + D_2d(k), \\ z(k) &= Ex(k) + F_1u(k) + F_2d(k), \end{aligned} \quad (1)$$

where  $x(k) \in R^n$  is the state,  $y(k) \in R^m$  is the measured output,  $z(k) \in R^{m_z}$  is the performance output,  $u(k) \in R^{n_u}$  is the control input, and  $d(k) \in R^{n_d}$  is the disturbance input which is assumed to belong to  $l_2[0, \infty)$ . The matrices  $A$ ,  $B_1$ ,  $B_2$ ,  $C$ ,  $D_2$ ,  $E$ ,  $F_1$ , and  $F_2$  of each subsystem have appropriate dimensions.

*2.2. Fault Model.* To formulate the fault detection and control problem in this paper, the following fault model type is adopted. The actuator stuck fault defined in [23] is described as follows:

$$u_f(k) = \rho_i u(k) + (I - \rho_i) f(k), \quad i = 0, \dots, N, \quad (2)$$

where index  $i$  denotes the  $i$ th fault mode and  $N$  denotes the number of the total fault modes. The diagonal matrices  $\rho_i$  is defined as

$$\rho_i = \text{diag} [\rho_{i1}, \dots, \rho_{ik}, \dots, \rho_{in_u}], \quad (3)$$

where  $\rho_i$ 's diagonal elements are either 1 or 0. Consider  $f(k) = [f_1, \dots, f_k, \dots, f_{n_u}]$ , where  $f_k(k = 1, \dots, n_u)$  is an unknown constant which means the value of the stuck fault for the  $k$ th actuator.

*Remark 1.* Each  $\rho_i$  corresponds to a fault mode. We assume that  $\rho_0 = I$ ; then it is fault free case and  $u_f(k) = u(k)$ . Note that when  $\rho_{ik} = 0$  and  $f_{ik} \neq 0$ , the  $k$ th actuator is stuck. If  $\rho_{ik} = 0$  and  $f_k = 0$ , (2) means that the  $k$ th actuator is outages. As [24], the fault  $f(k)$  is an intermittent fault, and it can be eliminated in a limited time.

Then system (1) with actuator faults (2) can be described as

$$\begin{aligned} x(k+1) &= \begin{cases} Ax(k) + B_1u(k) \\ \quad + B_2d(k), & \text{fault free case} \\ Ax(k) + B_1\rho_i u(k) + B_2d(k) \\ \quad + B_1(I - \rho_i)f(k), & \text{fault case,} \end{cases} \\ y(k) &= Cx(k) + D_2d(k), \\ z(k) &= \begin{cases} Ex(k) + F_1u(k) \\ \quad + F_2d(k), & \text{fault free case} \\ Ex(k) + F_1\rho_i u(k) + F_2d(k) \\ \quad + F_1(1 - \rho_i)f(k), & \text{fault case.} \end{cases} \end{aligned} \quad (4)$$

*Remark 2.* In this paper, the case that  $(A, B_1\rho_i)$  is not stabilizable is also included in this paper; then, all the results which are based on the common assumption are invalid.

To detect the fault and control system (4), design the detector/controller as the following form:

$$\begin{aligned} \hat{x}(k+1) &= \begin{cases} A_k \hat{x}(k) + B_k y(k), & \text{fault no-detected case} \\ \bar{A}_k \hat{x}(k) + \bar{B}_k y(k), & \text{fault detected case,} \end{cases} \\ u(k) &= \begin{cases} C_k \hat{x}(k), & \text{fault no-detected case} \\ \bar{C}_k \hat{x}(k), & \text{fault detected case,} \end{cases} \\ \hat{y}(k) &= C \hat{x}(k), \end{aligned} \quad (5)$$

where  $\hat{x}(k)$  is the detector/controller state vector and  $A_k, B_k, C_k, \bar{A}_k, \bar{B}_k$ , and  $\bar{C}_k$ , are real matrices of appropriate dimensions to be determined.

*Remark 3.* The detector/controller is switched between the fault no-detected case and the fault detected case, which can be seen as event-driven switching control.

For fault detection, we can formulate the fault as the weighted fault  $\hat{f}(k) = W_f(z)f(k)$  with a given stable weighted matrix. Assume  $A_w, B_w, C_w$ , and  $D_w$  are known constant matrices; then the minimal realization of  $W_f(z)$  is

$$\begin{aligned} x_w(k+1) &= A_w x_w(k) + B_w f(k), \\ \hat{f}(k) &= C_w x_w(k) + D_w f(k). \end{aligned} \quad (6)$$

Combining (4), (5), and (6), we have the following augmented model:

$$\begin{aligned} \tilde{x}(k+1) &= \begin{cases} \bar{A}\tilde{x}(k) + \bar{B}w(k), & \text{fault free case} \\ \bar{A}_1\tilde{x}(k) + \bar{B}_1w(k), & \text{fault no-detected case} \\ \bar{A}_2\tilde{x}(k) + \bar{B}_2w(k), & \text{fault detected case,} \end{cases} \\ r_e(k) &= \bar{C}\tilde{x}(k) + \bar{D}w(k), \end{aligned} \quad (7)$$

$$z(k) = \begin{cases} \bar{E}\tilde{x}(k) + \bar{F}w(k), & \text{fault free case} \\ \bar{E}_1\tilde{x}(k) + \bar{F}_1w(k), & \text{fault no-detected case} \\ \bar{E}_2\tilde{x}(k) + \bar{F}_2w(k), & \text{fault detected case,} \end{cases}$$

where  $r(k) = y(k) - \hat{y}(k)$  is the residual signal and  $r_e(k) = r(k) - \hat{f}(k)$  is the fault estimate error,  $\tilde{x}(k) = [x(k)^T \ \hat{x}(k)^T \ x_w(k)^T]^T$ ,  $w(k) = [d(k) \ f(k)]$ ,

$$\begin{bmatrix} \bar{A} & \bar{B} \\ \bar{A}_1 & \bar{B}_1 \\ \bar{A}_2 & \bar{B}_2 \\ \bar{C} & \bar{D} \\ \bar{E} & \bar{F} \\ \bar{E}_1 & \bar{F}_1 \\ \bar{E}_2 & \bar{F}_2 \end{bmatrix} = \begin{bmatrix} A & B_1C_k & 0 & B_2 & 0 \\ B_kC & A_k & 0 & B_kD_2 & 0 \\ 0 & 0 & A_w & 0 & B_w \\ \hline A & B_1\rho_iC_k & 0 & B_2 & B_1(I-\rho_i) \\ B_kC & A_k & 0 & B_kD_2 & 0 \\ 0 & 0 & A_w & 0 & B_w \\ \hline A & B_1\rho_i\bar{C}_k & 0 & B_2 & B_1(I-\rho_i) \\ \bar{B}_kC & \bar{A}_k & 0 & \bar{B}_kD_2 & 0 \\ 0 & 0 & A_w & 0 & B_w \\ \hline C & -C & -C_w & D_2 & -D_w \\ E & F_1C_k & 0 & F_2 & 0 \\ E & F_1\rho_iC_k & 0 & F_2 & F_1(I-\rho_i) \\ E & F_1\rho_i\bar{C}_k & 0 & F_2 & F_1(I-\rho_i) \end{bmatrix}. \quad (8)$$

*Remark 4.* Since the faults may not be detected instantaneously, but only after a time period, the detector/controller cannot be available in time to be switched to control the system when the faults occur. Hence, there exists mismatching case between the detector/controller and the system; then it is the asynchronous case.

**2.3. Problem Formulation.** The design problem of the detector/controller addressed in this paper can be expressed as follows.

The frameworks of the detector/controller: given system (1), we transform system (1) into system (4) which contains the faults. Based on model (4), detector/controller (5) is designed and generates two signals: a residual signal and a control signal. Meanwhile, augmented system (7) is asymptotically stable, and the disturbances and the faults affect the performance output  $z(k)$  and the fault estimate errors  $r_e(k)$  are both minimized. When the faults are detected, the controller is switched to reduce the effect of the faults. When

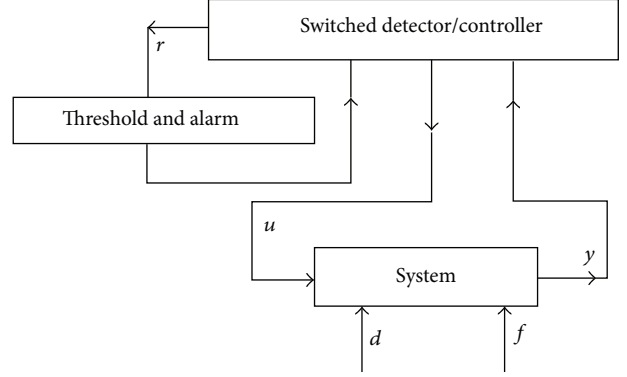


FIGURE 1: Evolution of the procedure.

the faults are removed, the detector/controller is switched to the original controller, and the residual evaluation function is reset. The proposed fault detection and control scheme is described in Figure 1.

To detect the faults and control system, our design objectives of the detector/controller can now be formulated as the following performance indices:

(i) for the fault detection objective

$$\sum_{k=0}^{\infty} (1-\varsigma)^k r_e(k)^T r_e(k) \leq \gamma_{s1}^2 \sum_{k=0}^{\infty} w(k)^T w(k), \quad (9)$$

(ii) for the control objective

$$\sum_{k=0}^{\infty} (1-\varsigma)^k z(k)^T z(k) \leq \gamma_{s2}^2 \sum_{k=0}^{\infty} w(k)^T w(k). \quad (10)$$

After designing detector/controller (5), the remaining important task is to evaluate the generated residual. One of the widely adopted residual evaluation functions  $J_r(k)$  can be chosen as [25]:

$$J_r(k) = \sqrt{\frac{1}{k} \sum_{l=1}^k r^T(l) r(l)}, \quad (11)$$

where  $k$  denotes the evaluation time step. We propose to use the following reasonable threshold for the residual evaluation functions and residual signal:

$$J_{th}(k) = \sup_{\substack{d(k) \in L_2[0, \infty) \\ f(k)=0}} J_r(k), \quad (12)$$

$$r_{th}(k) = \sup_{\substack{d(k) \in L_2[0, \infty) \\ f(k)=0}} r(k).$$

Consequently, the occurrence of faults can be detected by the following logical relationship:

$$\begin{cases} \|J_r(k)\| > \|J_{th}(k)\|, \\ \|r(k)\| > \|r_{th}(k)\|, \\ \text{others} \end{cases} \begin{cases} \text{the system with alarm,} \\ \text{and switching the controller,} \\ \text{the system no alarm.} \end{cases} \quad (13)$$

When the fault is removed, the residual evaluation function is reset.

### 3. The Fault Detection and Control Design

We let  $k_i, i \in \mathbb{N}^+$ , denote the starting time when the system resumes normal operations for the  $i$ th time and denote by the instants  $k_i^1$  and  $k_i^2$  the instant faults that happen and for faults that are detected during the interval  $[k_i, k_{i+1})$ , respectively. Moreover, denote  $\mathcal{T}_n(k_i, k_{i+1})$ ,  $\mathcal{T}_{nd}(k_i, k_{i+1})$ , and  $\mathcal{T}_d(k_i, k_{i+1})$  by the total activation time for fault free case, for fault no-detected case, and for fault detected case in the  $i$ th occurred fault, respectively. Then, we have the total time for fault free case  $\mathcal{T}_n(k_0, k) = \sum_{l=0}^{i-1} \mathcal{T}_n(k_l, k_{l+1}) + \mathcal{T}_n(k_i, k)$ , the total activation time for fault no-detected case  $\mathcal{T}_{nd}(k_1, k) = \sum_{l=0}^{i-1} \mathcal{T}_{nd}(k_l, k_{l+1}) + \mathcal{T}_{nd}(k_i, k)$ , the total activation time for fault detected case  $\mathcal{T}_d(k_1, k) = \sum_{l=0}^{i-1} \mathcal{T}_d(k_l, k_{l+1}) + \mathcal{T}_d(k_i, k)$ , and the total activation time for fault case  $\mathcal{T}_f(k_1, k) = \mathcal{T}_{nd}(k_1, k) + \mathcal{T}_d(k_1, k)$ . The time series of system operation is described in Figure 2.

In this paper, we focus our study of system (4) for simultaneous fault detection and control on the switching method. The following definition is first introduced.

**Definition 5.** For any  $k_0 < k_s < k_v$ , denote  $N_{\sigma(k)}(k_s, k_v)$  by the number for the operations returning to normal during  $(k_s, k_v)$ . If  $N_{\sigma(k)}(k_s, k_v) \leq N_0 + (k_v - k_s)/\tau_a$  for  $\tau_a > 0$  and  $N_0 \geq 0$ , then  $\tau_a$  and  $N_0$  are called the average dwell-time for resumed normal operations and the chatter bound, respectively.

**Remark 6.** The average dwell-time for resumed normal operations is defined as the average time for  $\mathcal{T}_n(k_i, k_{i+1}) + \mathcal{T}_{nd}(k_i, k_{i+1}) + \mathcal{T}_d(k_i, k_{i+1})$ .

Before the results are obtained, the simultaneous fault detection and control problem design can be solved starting from the weighted  $L_2$  performance and the conditions for augmented system (7) with the weighted  $L_2$  performance are obtained.

**Lemma 7.** Consider the discrete-time linear system

$$\begin{aligned} \tilde{x}(k+1) &= \begin{cases} \tilde{A}\tilde{x}(k) + \tilde{B}w(k), & \text{fault free case} \\ \tilde{A}_1\tilde{x}(k) + \tilde{B}_1w(k), & \text{fault no-detected case} \\ \tilde{A}_2\tilde{x}(k) + \tilde{B}_2w(k), & \text{fault detected case,} \end{cases} \\ \tilde{y}(k) &= \begin{cases} \tilde{C}\tilde{x}(k) + \tilde{D}w(k), & \text{fault free case} \\ \tilde{C}_1\tilde{x}(k) + \tilde{D}_1w(k), & \text{fault no-detected case} \\ \tilde{C}_2\tilde{x}(k) + \tilde{D}_2w(k), & \text{fault detected case} \end{cases} \end{aligned} \quad (14)$$

and let  $\alpha, \beta_1, \beta_2, \beta, \varsigma, \mu$ , and  $\gamma$  be some constants satisfying  $0 < \alpha < 1, \beta_1 > \beta > \beta_2 > 0, 0 < \varsigma < 1, \gamma > 0$ , and  $\mu \geq 1$ . If there exists Lyapunov-like functions candidate

$$V(\tilde{x}(k)) : \begin{cases} V_1(\tilde{x}(k)), & \text{fault free case,} \\ V_2(\tilde{x}(k)), & \text{fault no-detected case} \\ V_3(\tilde{x}(k)), & \text{fault detected case,} \end{cases} \quad (15)$$

satisfying the following inequalities

$$\Delta V_1(\tilde{x}(k)) < -\alpha V_1(\tilde{x}(k)) - \Gamma, \quad \text{fault free case,} \quad (16a)$$

$$\Delta V_2(\tilde{x}(k)) \leq \beta_1 V_2(\tilde{x}(k)) - \Gamma, \quad \text{fault no-detected case} \quad (16b)$$

$$\Delta V_3(\tilde{x}(k)) \leq \beta_2 V_3(\tilde{x}(k)) - \Gamma, \quad \text{fault detected case} \quad (16c)$$

$$V_g(\tilde{x}(k)) - \mu V_h(\tilde{x}(k)) \leq 0, \quad (16d)$$

where  $\Gamma(k) = \tilde{y}^T(k)\tilde{y}(k) - \gamma^2 w^T(k)w(k)$ ,  $g, h \in \{1, 2, 3\}$ , and  $g \neq h$ , then system (14) is asymptotically stable with the weighted  $L_2$ -gain  $\gamma_s = \mu\gamma$  for satisfying the following constraints:

$$\tau_a \geq \text{ceil} \left[ -\frac{3 \ln \mu}{\ln(1-\varsigma)} \right], \quad (17a)$$

$$\frac{\mathcal{T}_{nd}(k_0, k)}{\mathcal{T}_d(k_0, k)} \leq \frac{\ln(1+\beta) - \ln(1+\beta_2)}{\ln(1+\beta_1) - \ln(1+\beta)}, \quad (17b)$$

$$\frac{\mathcal{T}_n(k_0, k)}{\mathcal{T}_f(k_0, k)} \geq \frac{\ln(1+\beta) - \ln(1-\varsigma)}{\ln(1-\varsigma) - \ln(1-\alpha)}, \quad (17c)$$

where the function  $\text{ceil}(v)$  represents rounding real number  $v$  to the nearest integer greater than or equal to  $v$ .

*Proof.* Denote  $\bar{\alpha}_1 = (1-\alpha)$ ,  $\bar{\beta}_1 = (1+\beta_1)$ ,  $\bar{\beta}_2 = (1+\beta_2)$ ,  $\bar{\beta} = (1+\beta)$ , and  $\bar{\varsigma} = 1-\varsigma$ . Firstly, the stability of system (14) with  $d(k) = 0$  is considered. When the fault does not occur, that is,  $k \in \mathcal{T}_n(k_i, k_{i+1})$ ,  $i \in \mathbb{N}^+$ , it holds from (16a) that

$$V_1(\tilde{x}(k+1)) \leq \bar{\alpha} V_1(\tilde{x}(k)). \quad (18)$$

When the fault occurs, but the fault is not detected, that is,  $k \in \mathcal{T}_{nd}(k_i, k_{i+1})$ ,  $i \in \mathbb{N}^+$ , it holds from (16b) that

$$V_2(\tilde{x}(k+1)) \leq \bar{\beta}_1 V_2(\tilde{x}(k)). \quad (19)$$

When the fault is detected, that is,  $k \in \mathcal{T}_d(k_i, k_{i+1})$ ,  $i \in \mathbb{N}^+$ , it holds from (16c) that

$$V_3(\tilde{x}(k+1)) \leq \bar{\beta}_2 V_3(\tilde{x}(k)). \quad (20)$$

Thus, assuming  $k \in \mathcal{T}_n(k_i, k_{i+1})$ ,  $i \in \mathbb{N}^+$ , and according to (16d), (18), (19), (20), and Definition 5, we have

$$\begin{aligned} V_1(\tilde{x}(k)) &\leq \bar{\alpha}^{\mathcal{T}_n(k_i, k)} V_1(\tilde{x}(k_i)) \\ &\leq \mu \bar{\alpha}^{\mathcal{T}_n(k_i, k)} V_3(\tilde{x}(k_i^-)) \\ &\leq \dots \leq \\ &\leq \mu^{3N_{\sigma(k)}(k_0, k)} \bar{\beta}_1^{\mathcal{T}_{nd}(k_0^1, k_{i-1}^2)} \bar{\beta}_2^{\mathcal{T}_d(k_0^2, k_i)} \\ &\quad \times \bar{\alpha}^{\mathcal{T}_n(k_0, k)} V_1(\tilde{x}(k_0)). \end{aligned} \quad (21)$$

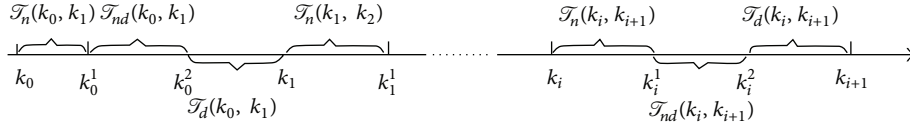


FIGURE 2: The time series of system operation.

According to (17b), (17c) and Definition 5 can be rewritten as

$$\begin{aligned} V_1(\tilde{x}(k)) &\leq \mu^{3N_{\sigma(k)}(k_0, k)} \bar{\beta}^{\mathcal{T}_f(k_0^1, k_1)} \bar{\alpha}^{\mathcal{T}_n(k_0, k)} V_1(\tilde{x}(k_0)) \\ &\leq \mu^{3N_{\sigma(k)}(k_0, k)} \bar{\zeta}^{k-k_0} V_1(\tilde{x}(k_0)) \\ &\leq \mu^{3N_0} (\bar{\zeta} \mu^{3/\tau_a})^{k-k_0} V_1(\tilde{x}(k_0)). \end{aligned} \quad (22)$$

If (17a) holds, then  $\bar{\zeta} \mu^{3/\tau_a} < \bar{\zeta} \mu^{-3 \ln \bar{\zeta} / 3 \ln(\mu)} = 1$ . Therefore, we conclude that  $V_1(\tilde{x}(k))$  converges to zero as  $k \rightarrow \infty$ . Then if (17a), (17b), and (17c) are satisfied, system (14) is stable.

Secondly, establish the weighted  $L_2$  performance for system (14). Let any nonzero  $w(k) \in l_2[0, \infty)$ , zero initial condition  $\tilde{x}(k_0)$ , and  $\Gamma(k) = \tilde{y}^T(k) \tilde{y}(k) - \gamma^2 w^T(k) w(k)$  and consider the Lyapunov-like functions for the fault free period, no-detected fault period, and detected fault period, respectively; then one can obtain that

$$\begin{aligned} V_1(\tilde{x}(k)) &\leq \mu^{3N_{\sigma(k)}(k_0, k)} \bar{\beta}_1^{\mathcal{T}_{nd}(k_0, k_{i-1}^1)} \bar{\beta}_2^{\mathcal{T}_d(k_0, k_i)} \\ &\quad \times \bar{\alpha}^{\mathcal{T}_n(k_0, k)} V_1(\tilde{x}(k_0)) \\ &\quad - \sum_{j=0}^{i-1} \sum_{l=k_j^1}^{k_j^2-1} \mu^{3N_{\sigma(k)}(l, k)-1} \bar{\alpha}^{\mathcal{T}_n(k_{j+1}, k-1)} \bar{\beta}_1^{\mathcal{T}_{nd}(l, k_{i-1}^2-1)} \\ &\quad \quad \times \bar{\beta}_2^{\mathcal{T}_d(k_j^2, k_i-1)} \Gamma(l) \\ &\quad - \sum_{j=0}^{i-1} \sum_{l=k_j^2}^{k_{j+1}^1-1} \mu^{3N_{\sigma(k)}(l, k)-2} \bar{\alpha}^{\mathcal{T}_n(k_{j+1}, k-1)} \bar{\beta}_1^{\mathcal{T}_{nd}(k_{j+1}^1, k_{i-1}^2-1)} \\ &\quad \quad \times \bar{\beta}_2^{\mathcal{T}_d(l, k_i-1)} \Gamma(l) \\ &\quad - \sum_{j=0}^i \sum_{l=k_j^1}^{k_j^2-1} \mu^{3N_{\sigma(k)}(l, k)} \bar{\alpha}^{\mathcal{T}_n(l, k-1)} \bar{\beta}_1^{\mathcal{T}_{nd}(k_j^1, k_{i-1}^2-1)} \\ &\quad \quad \times \bar{\beta}_2^{\mathcal{T}_d(k_j^2, k_i-1)} \Gamma(l). \end{aligned} \quad (23)$$

Due to the fact that  $V_1(\tilde{x}(k)) \geq 0$  and the zero initial condition, we have

$$\begin{aligned} &\sum_{j=0}^{i-1} \sum_{l=k_j^1}^{k_j^2-1} \mu^{3N_{\sigma(k)}(l, k)-1} \bar{\alpha}^{\mathcal{T}_n(k_{j+1}, k-1)} \bar{\beta}_1^{\mathcal{T}_{nd}(l, k_{i-1}^2-1)} \bar{\beta}_2^{\mathcal{T}_d(k_j^2, k_i-1)} \Gamma(l) \\ &+ \sum_{j=0}^{i-1} \sum_{l=k_j^2}^{k_{j+1}^1-1} \mu^{3N_{\sigma(k)}(l, k)-2} \bar{\alpha}^{\mathcal{T}_n(k_{j+1}, k-1)} \bar{\beta}_1^{\mathcal{T}_{nd}(k_{j+1}^1, k_{i-1}^2-1)} \\ &\quad \times \bar{\beta}_2^{\mathcal{T}_d(l, k_i-1)} \Gamma(l) \end{aligned}$$

$$\begin{aligned} &+ \sum_{j=0}^i \sum_{l=k_j^1}^{k_j^2-1} \mu^{3N_{\sigma(k)}(l, k)} \bar{\alpha}^{\mathcal{T}_n(l, k-1)} \bar{\beta}_1^{\mathcal{T}_{nd}(k_j^1, k_{i-1}^2-1)} \\ &\quad \times \bar{\beta}_2^{\mathcal{T}_d(k_j^2, k_i-1)} \Gamma(l) \leq 0. \end{aligned} \quad (24)$$

According to (17b) and (17c) and from  $\bar{\beta}_1 > 0$ ,  $\bar{\beta}_2 > 0$ ,  $\bar{\beta} > 0$ , and  $\bar{\alpha} > 0$ , we have

$$\begin{aligned} \bar{\beta}_1^{\mathcal{T}_{nd}(l, k_{i-1}^2-1)} \bar{\beta}_2^{\mathcal{T}_d(k_j^2, k_i-1)} &\leq \bar{\beta}^{\mathcal{T}_f(l, k_i-1)} \\ \bar{\alpha}^{\mathcal{T}_n(k_{j+1}, k-1)} \bar{\beta}^{\mathcal{T}_f(l, k_i-1)} &\leq \bar{\zeta}^{k-l-1}, \\ l &\in \mathcal{T}_{nd}(k_j^1, k_j^2-1), \\ \bar{\beta}_1^{\mathcal{T}_{nd}(k_{j+1}^1, k_{i-1}^2-1)} \bar{\beta}_2^{\mathcal{T}_d(l, k_i-1)} &\leq \bar{\beta}^{\mathcal{T}_f(l, k_i-1)}, \\ \bar{\alpha}^{\mathcal{T}_n(k_{j+1}, k-1)} \bar{\beta}^{\mathcal{T}_f(l, k_i-1)} &\leq \bar{\zeta}^{k-l-1}, \\ l &\in \mathcal{T}_d(k_j^2, k_{j+1}-1), \\ \bar{\beta}_1^{\mathcal{T}_{nd}(k_j^1, k_{i-1}^2-1)} \bar{\beta}_2^{\mathcal{T}_d(k_j^2, k_i-1)} &\leq \bar{\beta}^{\mathcal{T}_f(k_j^1, k_i-1)} \\ \bar{\alpha}^{\mathcal{T}_n(l, k-1)} \bar{\beta}^{\mathcal{T}_f(k_j^1, k_i-1)} &\leq \bar{\zeta}^{k-l-1} \\ l &\in \mathcal{T}_n(k_j, k_j^1-1). \end{aligned} \quad (25)$$

Then, we have

$$\begin{aligned} &\sum_{j=0}^{i-1} \sum_{l=k_j^1}^{k_j^2-1} \mu^{3N_{\sigma(k)}(l, k)-1} \bar{\zeta}^{k-l-1} \Gamma(l) \\ &+ \sum_{j=0}^{i-1} \sum_{l=k_j^2}^{k_{j+1}^1-1} \mu^{3N_{\sigma(k)}(l, k)-2} \bar{\zeta}^{k-l-1} \Gamma(l) \\ &+ \sum_{j=0}^i \sum_{l=k_j^1}^{k_j^2-1} \mu^{3N_{\sigma(k)}(l, k)} \bar{\zeta}^{k-l-1} \Gamma(l) \leq 0. \end{aligned} \quad (26)$$

Moreover, it has

$$\begin{aligned} &\sum_{j=0}^{i-1} \sum_{l=k_j^1}^{k_j^2-2} \mu^{3N_{\sigma(k)}(l, k)-1} \bar{\zeta}^{k-l-1} \tilde{y}^T(k) \tilde{y}(k) \\ &+ \sum_{j=0}^{i-1} \sum_{l=k_j^2}^{k_{j+1}^1-1} \mu^{3N_{\sigma(k)}(l, k)-2} \bar{\zeta}^{k-l-1} \tilde{y}^T(k) \tilde{y}(k) \end{aligned}$$

$$\begin{aligned}
& + \sum_{j=0}^i \sum_{l=k_j}^{k_j^1-1} \mu^{3N_{\sigma(k)}(l,k)} \bar{\zeta}^{k-l-1} \check{y}^T(k) \check{y}(k) \\
& \leq \sum_{j=0}^{i-1} \sum_{l=k_j^1}^{k_j^2-1} \mu^{3N_{\sigma(k)}(l,k)-1} \bar{\zeta}^{k-l-1} \gamma^2 w^T(k) w(k) \\
& \quad + \sum_{j=0}^{i-1} \sum_{l=k_j^2}^{k_{j+1}^1-1} \mu^{3N_{\sigma(k)}(l,k)-2} \bar{\zeta}^{k-l-1} \gamma^2 w^T(k) w(k) \\
& \quad + \sum_{j=0}^i \sum_{l=k_j}^{k_j^1-1} \mu^{3N_{\sigma(k)}(l,k)} \bar{\zeta}^{k-l-1} \gamma^2 w^T(k) w(k). \tag{27}
\end{aligned}$$

Thus, from  $\mu > 1$ , we obtain that

$$\begin{aligned}
& \sum_{l=k_0}^{k-1} \mu^{3N_{\sigma(k)}(l,k)-2} \bar{\zeta}^{k-l-1} \check{y}^T(k) \check{y}(k) \\
& \leq \sum_{l=k_0}^{k-1} \mu^{3N_{\sigma(k)}(l,k)} \bar{\zeta}^{k-l-1} \gamma^2 w^T(k) w(k). \tag{28}
\end{aligned}$$

Multiplying both sides of (28) by  $\mu^{-3N_{\sigma(k)}(k_0,k)}$ , it can be obtained that

$$\begin{aligned}
& \sum_{l=k_0}^{k-1} \mu^{-3N_{\sigma(k)}(k_0,l)-2} \bar{\zeta}^{k-l-1} \check{y}^T(k) \check{y}(k) \\
& \leq \sum_{l=k_0}^{k-1} \mu^{-3N_{\sigma(k)}(k_0,l)} \bar{\zeta}^{k-l-1} \gamma^2 w^T(k) w(k). \tag{29}
\end{aligned}$$

From the above and  $\mu \geq 1$ , we have

$$\begin{aligned}
& \sum_{l=k_0}^{k-1} \mu^{-3N_{\sigma(k)}(k_0,l)-2} \bar{\zeta}^{k-l-1} \check{y}^T(k) \check{y}(k) \\
& \leq \sum_{l=k_0}^{k-1} \mu^{-3N_{\sigma(k)}(k_0,l)} \bar{\zeta}^{k-l-1} \gamma^2 w^T(k) w(k). \tag{30}
\end{aligned}$$

Moreover, it follows from Definition 5 that  $0 \leq N_{\sigma(k)}(k_0, j) \leq N_0 + ((l - k_0)/\tau_a) \leq +N_0((-l - k_0) \ln \bar{\zeta}) / (3 \ln \mu)$ . Note that  $\mu^{(3(l-k_0) \ln \bar{\zeta}) / (3 \ln \mu)} = \bar{\zeta}^{l-k_0}$  and  $0 < \bar{\zeta} < 1$ ; then (30) implies that

$$\sum_{l=k_0}^{k-1} \bar{\zeta}^{l-k_0} \check{y}^T(k) \check{y}(k) \leq \sum_{l=k_0}^{k-1} \mu^2 \gamma^2 w^T(k) w(k). \tag{31}$$

It further implies that

$$\sum_{l=k_0}^{\infty} \bar{\zeta}^{l-k_0} \check{y}^T(k) \check{y}(k) \leq \sum_{l=k_0}^{\infty} (\mu \gamma)^2 d^T(s) d(s). \tag{32}$$

Therefore, we conclude that augmented system (14) is asymptotically stable with the weighted  $L_2$ -gain  $\gamma_s = \mu \gamma$  for satisfying the constraints (17a), (17b), and (17c).  $\square$

### 3.1. Condition for the Fault Detection Objective

**Theorem 8.** Consider system (7), and let  $\alpha, \beta_1, \beta_2, \mu$ , and  $\gamma$  be some constants satisfying  $0 < \alpha < 1, \beta_1 > \beta_2 > 0, \gamma_1 > 0$ , and  $\mu \geq 1$ . If there exist matrix variables  $Y_a, G_a, Z_a, N, Y_{a1}, G_{a1}, Z_{a1}, N_1, Y_{a2}, G_{a2}, Z_{a2}, \widehat{A}, \widehat{B}, \widehat{C}, \widehat{\bar{A}}, \widehat{\bar{B}},$  and  $\widehat{\bar{C}}$ , and symmetric positive-definite matrices

$$\begin{aligned}
\mathcal{P}_{a1} & = \begin{bmatrix} \mathcal{P}_{a11} & \mathcal{P}_{a12} & \mathcal{P}_{a13} \\ * & \mathcal{P}_{a14} & \mathcal{P}_{a15} \\ * & * & \mathcal{P}_{a16} \end{bmatrix} > 0, \\
\mathcal{P}_{a2} & = \begin{bmatrix} \mathcal{P}_{a21} & \mathcal{P}_{a22} & \mathcal{P}_{a23} \\ * & \mathcal{P}_{a24} & \mathcal{P}_{a25} \\ * & * & \mathcal{P}_{a26} \end{bmatrix} > 0, \tag{33} \\
\mathcal{P}_{a3} & = \begin{bmatrix} \mathcal{P}_{a31} & \mathcal{P}_{a32} & \mathcal{P}_{a33} \\ * & \mathcal{P}_{a34} & \mathcal{P}_{a35} \\ * & * & \mathcal{P}_{a36} \end{bmatrix} > 0
\end{aligned}$$

such that

$$\begin{bmatrix} \Theta_{a1} & \Theta_{a2} & \Theta_{a3} & 0 \\ * & \Theta_{a4} & 0 & \Theta_{a5} \\ * & * & -\gamma_1^2 I & \Theta_{a6} \\ * & * & * & -I \end{bmatrix} < 0, \tag{34}$$

$$\begin{bmatrix} \Omega_{a1} & \Omega_{a2} & \Omega_{a3} & 0 \\ * & \Omega_{a4} & 0 & \Omega_{a5} \\ * & * & -\gamma_1^2 I & \Omega_{a6} \\ * & * & * & -I \end{bmatrix} < 0, \tag{35}$$

$$\begin{bmatrix} \Xi_{a1} & \Xi_{a2} & \Xi_{a3} & 0 \\ * & \Xi_{a4} & 0 & \Xi_{a5} \\ * & * & -\gamma_1^2 I & \Xi_{a6} \\ * & * & * & -I \end{bmatrix} < 0, \tag{36}$$

$$\mathcal{P}_{ag} - \mu \mathcal{P}_{ah} \leq 0, \tag{37}$$

where  $g, h \in \{1, 2, 3\}, g \neq h, \bar{\alpha} = 1 - \alpha, \bar{\beta}_1 = 1 + \beta_1,$  and  $\bar{\beta}_2 = 1 + \beta_2,$

$\Theta_{a1}$

$$= \begin{bmatrix} \mathcal{P}_{a11} - He(Y_a) & \mathcal{P}_{a12} + N^T - G_a & \mathcal{P}_{a13} \\ * & \mathcal{P}_{a14} - He(N) & \mathcal{P}_{a15} \\ * & * & \mathcal{P}_{a16} - He(Z_a) \end{bmatrix},$$

$$\Theta_{a5} = \begin{bmatrix} C^T \\ -C^T \\ -C_w^T \end{bmatrix},$$

$$\Theta_{a2} = \begin{bmatrix} Y_a^T A - \widehat{B}C & Y_a^T B_1 \widehat{C} - \widehat{A} & 0 \\ G_a^T A + \widehat{B}C & G_a^T B_1 \widehat{C} + \widehat{A} & 0 \\ 0 & 0 & Z_a^T A_w \end{bmatrix},$$

$$\Theta_{a6} = \begin{bmatrix} D_2^T \\ -D_w^T \end{bmatrix},$$

$$\Theta_{a3} = \begin{bmatrix} Y_a^T B_2 - \widehat{B}D_2 & 0 \\ G_a^T B_2 + \widehat{B}D_2 & 0 \\ 0 & Z_a^T B_w \end{bmatrix},$$

$$\Theta_{a4} = \begin{bmatrix} -\bar{\alpha}\mathcal{P}_{a11} & -\bar{\alpha}\mathcal{P}_{a12} & -\bar{\alpha}\mathcal{P}_{a13} \\ * & -\bar{\alpha}\mathcal{P}_{a14} & -\bar{\alpha}\mathcal{P}_{a15} \\ * & * & -\bar{\alpha}\mathcal{P}_{a16} \end{bmatrix},$$

$\Omega_{a1}$

$$= \begin{bmatrix} \mathcal{P}_{a21} - He(Y_{a1}) & \mathcal{P}_{a22} + N^T - G_{a1} & \mathcal{P}_{a23} \\ * & \mathcal{P}_{a24} - He(N) & \mathcal{P}_{a25} \\ * & * & \mathcal{P}_{a26} - He(Z_{a1}) \end{bmatrix},$$

$$\Omega_{a5} = \begin{bmatrix} C^T \\ -C^T \\ -C_w^T \end{bmatrix},$$

$$\Omega_{a2} = \begin{bmatrix} Y_{a1}^T A - \widehat{B}C & Y_{a1}^T B_1 \rho_1 \widehat{C} - \widehat{A} & 0 \\ G_{a1}^T A + \widehat{B}C & G_{a1}^T B_1 \rho_1 \widehat{C} - \widehat{A} & 0 \\ 0 & 0 & Z_{a1}^T A_w \end{bmatrix},$$

$$\Omega_{a6} = \begin{bmatrix} D_2^T \\ -D_w^T \end{bmatrix},$$

$$\Omega_{a3} = \begin{bmatrix} Y_{a1}^T B_2 - \widehat{B}D_2 & Y_{a1}^T B_1 (I - \rho_1) \\ G_{a1}^T B_2 + \widehat{B}D_2 & G_{a1}^T B_1 (I - \rho_1) \\ 0 & Z_{a1} B_w \end{bmatrix},$$

$$\Omega_{a4} = \begin{bmatrix} -\bar{\beta}_1 \mathcal{P}_{a21} & -\bar{\beta}_1 \mathcal{P}_{a22} & -\bar{\beta}_1 \mathcal{P}_{a23} \\ * & -\bar{\beta}_1 \mathcal{P}_{a24} & -\bar{\beta}_1 \mathcal{P}_{a25} \\ * & * & -\bar{\beta}_1 \mathcal{P}_{a26} \end{bmatrix},$$

$\Xi_{a1}$

$$= \begin{bmatrix} \mathcal{P}_{a31} - He(Y_{a2}) & \mathcal{P}_{a32} + N_1^T - G_{a2} & \mathcal{P}_{a33} \\ * & \mathcal{P}_{a34} - He(N_1) & \mathcal{P}_{a35} \\ * & * & \mathcal{P}_{a36} - He(Z_{a2}) \end{bmatrix},$$

$$\Xi_{a5} = \begin{bmatrix} C^T \\ -C^T \\ -C_w^T \end{bmatrix},$$

$$\Xi_{a2} = \begin{bmatrix} Y_{a2}^T A - \widehat{B}C & Y_{a2}^T B_1 \rho_1 \widehat{C} - \widehat{A} & 0 \\ G_{a2}^T A + \widehat{B}C & G_{a2}^T B_1 \rho_1 \widehat{C} + \widehat{A} & 0 \\ 0 & 0 & Z_{a2}^T A_w \end{bmatrix},$$

$$\Xi_{a6} = \begin{bmatrix} D_2^T \\ -D_w^T \end{bmatrix},$$

$$\Xi_{a3} = \begin{bmatrix} Y_{a2}^T B_2 - \widehat{B}D_2 & Y_{a2}^T B_1 (I - \rho_1) \\ G_{a2}^T B_2 + \widehat{B}D_2 & G_{a2}^T B_1 (I - \rho_1) \\ 0 & Z_{a2} B_w \end{bmatrix},$$

$$\Xi_{a4} = \begin{bmatrix} -\bar{\beta}_2 \mathcal{P}_{a31} & -\bar{\beta}_2 \mathcal{P}_{a32} & -\bar{\beta}_2 \mathcal{P}_{a33} \\ * & -\bar{\beta}_2 \mathcal{P}_{a34} & -\bar{\beta}_2 \mathcal{P}_{a35} \\ * & * & -\bar{\beta}_2 \mathcal{P}_{a36} \end{bmatrix},$$

(38)

then system (7) is asymptotically stable and guarantees the weighted  $L_2$  performance (9) with the weighted  $L_2$  gain  $\gamma_{s1} = \mu\gamma_1$  when system (7) satisfies the constraints (17a), (17b), and (17c).

*Proof.* When  $k \in \mathcal{T}_n(k_i, k_{i+1})$ , according to Lemma 7 and along the trajectory of system (7), one has

$$\Delta V_1(\bar{x}(k)) + \alpha V_1(\bar{x}(k)) - \gamma^2 w(k)^T w(k) + \check{y}(k)^T \check{y}(k)$$

$$= \begin{bmatrix} \bar{x}(k) \\ w(k) \end{bmatrix}^T \times \begin{bmatrix} \bar{A}^T \mathcal{P}_{a1} \bar{A} - (1 - \alpha) \mathcal{P}_{a1} + \bar{C}^T \bar{C} & \bar{A}^T \mathcal{P}_{a1} \bar{B} + \bar{C}^T \bar{D} \\ \bar{B}^T \mathcal{P}_{a1} \bar{A} + \bar{D}^T \bar{C} & \bar{B}^T \mathcal{P}_{a1} \bar{B} - \gamma_1^2 I + \bar{D}^T \bar{D} \end{bmatrix} \times \begin{bmatrix} \bar{x}(k) \\ w(k) \end{bmatrix}.$$

(39)

When  $k \in \mathcal{T}_{nd}(k_i, k_i^1)$ , we obtain

$$\Delta V_2(\bar{x}(k)) - \beta_2 V_2(\bar{x}(k)) - \gamma^2 w(k)^T w(k) + \check{y}(k)^T \check{y}(k)$$

$$= \begin{bmatrix} \bar{x}(k) \\ w(k) \end{bmatrix}^T \times \begin{bmatrix} \bar{A}_1^T \mathcal{P}_{a2} \bar{A}_1 - (1 + \beta_1) \mathcal{P}_{a2} + \bar{C}^T \bar{C} & \bar{A}_1^T \mathcal{P}_{a2} \bar{B}_1 + \bar{C}^T \bar{D} \\ \bar{B}_1^T \mathcal{P}_{a2} \bar{A}_1 + \bar{D}^T \bar{C} & \bar{B}_1^T \mathcal{P}_{a2} \bar{B}_1 - \gamma_1^2 I + \bar{D}^T \bar{D} \end{bmatrix} \times \begin{bmatrix} \bar{x}(k) \\ w(k) \end{bmatrix}.$$

(40)

When  $k \in \mathcal{T}_d(k_i^1, k_i^2)$ , it can be obtained that

$$\Delta V_3(\bar{x}(k)) - \beta_2 V_3(\bar{x}(k)) - \gamma^2 w(k)^T w(k) + \check{y}(k)^T \check{y}(k)$$

$$= \begin{bmatrix} \bar{x}(k) \\ w(k) \end{bmatrix}^T \times \begin{bmatrix} \bar{A}_2^T \mathcal{P}_{a3} \bar{A}_2 - (1 + \beta_2) \mathcal{P}_{a3} + \bar{C}^T \bar{C} & \bar{A}_2^T \mathcal{P}_{a3} \bar{B}_2 + \bar{C}^T \bar{D} \\ \bar{B}_2^T \mathcal{P}_{a3} \bar{A}_2 + \bar{D}^T \bar{C} & \bar{B}_2^T \mathcal{P}_{a3} \bar{B}_2 - \gamma_1^2 I + \bar{D}^T \bar{D} \end{bmatrix} \times \begin{bmatrix} \bar{x}(k) \\ w(k) \end{bmatrix}.$$

(41)

In addition, due to the relation of the Lyapunov-like functions at the moment the fault happened, we have that

$V_g(\tilde{x}(k)) - \mu V_h(\tilde{x}(k)) = \tilde{x}(k)^T (\mathcal{P}_g - \mu \mathcal{P}_h) \tilde{x}(k)$ , where  $g, h \in \{1, 2, 3\}$ ,  $g \neq h$ . Thus, if the inequalities

$$\begin{bmatrix} \tilde{A}_1^T \mathcal{P}_{a1} \tilde{A}_1 - (1 - \alpha) \mathcal{P}_{a1} + \tilde{C}^T \tilde{C} & \tilde{A}_1^T \mathcal{P}_{a1} \tilde{B} + \tilde{C}^T \tilde{D} \\ \tilde{B}^T \mathcal{P}_{a1} \tilde{A}_1 + \tilde{D}^T \tilde{C} & \tilde{B}^T \mathcal{P}_{a1} \tilde{B} - \gamma_1^2 I + \tilde{D}^T \tilde{D} \end{bmatrix} < 0, \quad (42)$$

$$\begin{bmatrix} \tilde{A}_1^T \mathcal{P}_{a2} \tilde{A}_1 - (1 + \beta_1) \mathcal{P}_{a2} + \tilde{C}^T \tilde{C} & \tilde{A}_1^T \mathcal{P}_{a2} \tilde{B}_1 + \tilde{C}^T \tilde{D} \\ \tilde{B}_1^T \mathcal{P}_{a2} \tilde{A}_1 + \tilde{D}^T \tilde{C} & \tilde{B}_1^T \mathcal{P}_{a2} \tilde{B}_1 - \gamma_1^2 I + \tilde{D}^T \tilde{D} \end{bmatrix} < 0, \quad (43)$$

$$\begin{bmatrix} \tilde{A}_2^T \mathcal{P}_{a3} \tilde{A}_2 - (1 + \beta_2) \mathcal{P}_{a3} + \tilde{C}^T \tilde{C} & \tilde{A}_2^T \mathcal{P}_{a3} \tilde{B}_2 + \tilde{C}^T \tilde{D} \\ \tilde{B}_2^T \mathcal{P}_{a3} \tilde{A}_2 + \tilde{D}^T \tilde{C} & \tilde{B}_2^T \mathcal{P}_{a3} \tilde{B}_2 - \gamma_1^2 I + \tilde{D}^T \tilde{D} \end{bmatrix} < 0, \quad (44)$$

$$\mathcal{P}_g - \mu \mathcal{P}_h \leq 0, \quad (45)$$

hold, system (14) is asymptotically stable with the weighted  $L_2$  performance for satisfying constraints (17a), (17b), and (17c) according to Lemma 7.

To reduce the conservatism, (42) can be rewritten as follows:

$$\begin{bmatrix} \tilde{A} & \tilde{B} \\ I & 0 \end{bmatrix}^T \begin{bmatrix} \mathcal{P}_{a1} & 0 \\ 0 & -(1 - \alpha) \mathcal{P}_{a1} \end{bmatrix} \begin{bmatrix} \tilde{A} & \tilde{B} \\ I & 0 \end{bmatrix} + \begin{bmatrix} \tilde{C}^T \tilde{C} & \tilde{C}^T \tilde{D} \\ \tilde{D}^T \tilde{C} & -\gamma_1^2 I + \tilde{D}^T \tilde{D} \end{bmatrix} < 0. \quad (46)$$

Then, we can obtain that (46) is equivalent to

$$\begin{bmatrix} \tilde{A} & \tilde{B} \\ I & 0 \\ 0 & I \end{bmatrix}^T \begin{bmatrix} \mathcal{P}_{a1} & 0 & 0 \\ 0 & -(1 - \alpha) \mathcal{P}_{a1} + \tilde{C}^T \tilde{C} & \tilde{C}^T \tilde{D} \\ 0 & \tilde{D}^T \tilde{C} & -\gamma_1^2 I + \tilde{D}^T \tilde{D} \end{bmatrix} \begin{bmatrix} \tilde{A} & \tilde{B} \\ I & 0 \\ 0 & I \end{bmatrix} < 0. \quad (47)$$

On the other hand,

$$\begin{bmatrix} 0 & 0 \\ I & 0 \\ 0 & I \end{bmatrix}^T \begin{bmatrix} \mathcal{P}_{a1} & 0 & 0 \\ 0 & -(1 - \alpha) \mathcal{P}_{a1} + \tilde{C}^T \tilde{C} & \tilde{C}^T \tilde{D} \\ 0 & \tilde{D}^T \tilde{C} & -\gamma_1^2 I + \tilde{D}^T \tilde{D} \end{bmatrix} \begin{bmatrix} 0 & 0 \\ I & 0 \\ 0 & I \end{bmatrix} = \begin{bmatrix} -(1 - \alpha) \mathcal{P}_{a1} + \tilde{C}^T \tilde{C} & \tilde{C}^T \tilde{D} \\ \tilde{D}^T \tilde{C} & -\gamma_1^2 I + \tilde{D}^T \tilde{D} \end{bmatrix} < 0. \quad (48)$$

Applying Projection Lemma, it follows from (47) and (48) that

$$\begin{bmatrix} \mathcal{P}_{a1} & 0 & 0 \\ 0 & -(1 - \alpha) \mathcal{P}_{a1} + \tilde{C}^T \tilde{C} & \tilde{C}^T \tilde{D} \\ 0 & \tilde{D}^T \tilde{C} & -\gamma_1^2 I + \tilde{D}^T \tilde{D} \end{bmatrix} + He \left( \begin{bmatrix} -I \\ \tilde{A}^T \\ \tilde{B}^T \end{bmatrix} \mathcal{W}_a \begin{bmatrix} I & 0 & 0 \end{bmatrix} \right) < 0. \quad (49)$$

Consider the structure of the matrix  $\tilde{A}$ ; we construct the matrix variable  $\mathcal{W}_a$  as

$$\mathcal{W}_a = \begin{bmatrix} Y_a & G_a & 0 \\ -N_a & N_a & 0 \\ 0 & 0 & Z_a \end{bmatrix}. \quad (50)$$

Define  $\hat{A} = N^T A_k$ ,  $\hat{B} = N^T B_k$ , and  $\hat{C} = C_k$ . By Schur complement, (49) becomes (34). In a similar way, we can obtain the conditions (35) and (36). Hence, if the conditions (34), (35), (36), and (37) hold, system (7) is asymptotically stable and has the weighted  $L_2$  performance gain  $\gamma_{s1}$ , which completes the proof.  $\square$

### 3.2. Condition for the Control Objective

**Theorem 9.** Consider system (7), and let  $\alpha$ ,  $\beta_1$ ,  $\beta_2$ ,  $\mu$ , and  $\gamma$  be some constants satisfying  $0 < \alpha < 1$ ,  $\beta_1 > \beta_2 > 0$ ,  $\gamma_2 > 0$ , and  $\mu \geq 1$ . If there exist matrix variables  $Y_b$ ,  $G_b$ ,  $Z_b$ ,  $N$ ,  $Y_{b1}$ ,  $G_{b1}$ ,  $Z_{b1}$ ,  $Y_{b2}$ ,  $G_{b2}$ ,  $Z_{b2}$ ,  $N_1$ ,  $\hat{A}$ ,  $\hat{B}$ ,  $\hat{C}$ ,  $\hat{\tilde{A}}$ ,  $\hat{\tilde{B}}$ , and  $\hat{\tilde{C}}$  and symmetric positive-definite matrices

$$\begin{aligned} \mathcal{P}_{b1} &= \begin{bmatrix} \mathcal{P}_{b11} & \mathcal{P}_{b12} & \mathcal{P}_{b13} \\ * & \mathcal{P}_{b14} & \mathcal{P}_{b15} \\ * & * & \mathcal{P}_{b16} \end{bmatrix} > 0, \\ \mathcal{P}_{b2} &= \begin{bmatrix} \mathcal{P}_{b21} & \mathcal{P}_{b22} & \mathcal{P}_{b23} \\ * & \mathcal{P}_{b24} & \mathcal{P}_{b25} \\ * & * & \mathcal{P}_{b26} \end{bmatrix} > 0, \\ \mathcal{P}_{b3} &= \begin{bmatrix} \mathcal{P}_{b31} & \mathcal{P}_{b32} & \mathcal{P}_{b33} \\ * & \mathcal{P}_{b34} & \mathcal{P}_{b35} \\ * & * & \mathcal{P}_{b36} \end{bmatrix} > 0, \end{aligned} \quad (51)$$

such that

$$\begin{bmatrix} \Theta_{b1} & \Theta_{b2} & \Theta_{b3} & 0 \\ * & \Theta_{b4} & 0 & \Theta_{b5} \\ * & * & -\gamma_2^2 & \Theta_{b6} \\ * & * & * & -I \end{bmatrix} < 0, \quad (52)$$

$$\begin{bmatrix} \Omega_{b1} & \Omega_{b2} & \Omega_{b3} & 0 \\ * & \Omega_{b4} & 0 & \Omega_{b5} \\ * & * & -\gamma_2^2 I & \Omega_{b6} \\ * & * & * & -I \end{bmatrix} < 0, \quad (53)$$

$$\begin{bmatrix} \Xi_{b1} & \Xi_{b2} & \Xi_{b3} & 0 \\ * & \Xi_{b4} & 0 & \Xi_{b5} \\ * & * & -\gamma_2^2 I & \Xi_{b6} \\ * & * & * & -I \end{bmatrix} < 0, \quad (54)$$

$$\mathcal{P}_{bg} - \mu \mathcal{P}_{bh} \leq 0, \quad (55)$$

where  $g, h \in \{1, 2, 3\}$ ,  $g \neq h$ ,  $\bar{\alpha} = 1 - \alpha$ ,  $\bar{\beta}_1 = 1 + \beta_1$ ,  $\bar{\beta}_2 = 1 + \beta_2$ ,

$\Theta_{b1}$

$$= \begin{bmatrix} \mathcal{P}_{b11} - He(Y_b) & \mathcal{P}_{b12} + N^T - G_b & \mathcal{P}_{b13} \\ * & \mathcal{P}_{b14} - He(N) & \mathcal{P}_{b15} \\ * & * & \mathcal{P}_{b16} - He(Z_b) \end{bmatrix},$$

$$\Theta_{b5} = \begin{bmatrix} E^T \\ -\widehat{C}^T F_1^T \\ 0 \end{bmatrix},$$

$$\Theta_{b2} = \begin{bmatrix} Y_b^T A - \widehat{B}C & Y_b^T B_1 \widehat{C} - \widehat{A} & 0 \\ G_b^T A + \widehat{B}C & G_b^T B_1 \widehat{C} + \widehat{A} & 0 \\ 0 & 0 & Z_b^T A_w \end{bmatrix},$$

$$\Theta_{b6} = \begin{bmatrix} F_2^T \\ 0 \end{bmatrix},$$

$$\Theta_{b3} = \begin{bmatrix} Y_b^T B_2 - p_{b1} \widehat{B}D_2 & 0 \\ G_b^T B_2 + \widehat{B}D_2 & 0 \\ 0 & Z_b^T B_w \end{bmatrix},$$

$$\Theta_{b4} = \begin{bmatrix} -\bar{\alpha} \mathcal{P}_{b11} & -\bar{\alpha} \mathcal{P}_{b12} & -\bar{\alpha} \mathcal{P}_{b13} \\ * & -\bar{\alpha} \mathcal{P}_{b14} & -\bar{\alpha} \mathcal{P}_{b15} \\ * & * & -\bar{\alpha} \mathcal{P}_{b16} \end{bmatrix},$$

$\Omega_{b1}$

$$= \begin{bmatrix} \mathcal{P}_{b21} - He(Y_{b1}) & \mathcal{P}_{b22} + N^T - G_{b1} & \mathcal{P}_{b23} \\ * & \mathcal{P}_{b24} - He(N) & \mathcal{P}_{b25} \\ * & * & \mathcal{P}_{b26} - He(Z_b) \end{bmatrix},$$

$$\Omega_{b5} = \begin{bmatrix} E^T \\ -\widehat{C}^T \rho_i F_1^T \\ 0 \end{bmatrix},$$

$$\Omega_{b2} = \begin{bmatrix} Y_{b1}^T A - \widehat{B}C & Y_{b1}^T B_1 \rho_i \widehat{C} - \widehat{A} & 0 \\ G_{b1}^T A + \widehat{B}C & G_{b1}^T B_1 \rho_i \widehat{C} + \widehat{A} & 0 \\ 0 & 0 & Z_{b1}^T A_w \end{bmatrix},$$

$$\Omega_{b6} = \begin{bmatrix} F_2^T \\ (I - \rho_i)^T F_1^T \end{bmatrix},$$

$$\Omega_{b3} = \begin{bmatrix} Y_{b1}^T B_2 - \widehat{B}D_2 & Y_{b1}^T B_1 (I - \rho_i) \\ G_{b1}^T B_2 + \widehat{B}D_2 & G_{b1}^T B_1 (I - \rho_i) \\ 0 & Z_{b1} B_w \end{bmatrix},$$

$$\Omega_{b4} = \begin{bmatrix} -\bar{\beta}_1 \mathcal{P}_{b21} & -\bar{\beta}_1 \mathcal{P}_{b22} & -\bar{\beta}_1 \mathcal{P}_{b23} \\ * & -\bar{\beta}_1 \mathcal{P}_{b24} & -\bar{\beta}_1 \mathcal{P}_{b25} \\ * & * & -\bar{\beta}_1 \mathcal{P}_{b26} \end{bmatrix},$$

$\Xi_{b1}$

$$= \begin{bmatrix} \mathcal{P}_{b31} - He(Y_{b1}) & \mathcal{P}_{b32} + N_1^T - G_{b1} & \mathcal{P}_{b33} \\ * & \mathcal{P}_{b34} - He(N_1) & \mathcal{P}_{b35} \\ * & * & \mathcal{P}_{b36} - He(Z_{b1}) \end{bmatrix},$$

$$\Xi_{b5} = \begin{bmatrix} E^T \\ -\widehat{C}^T \rho_i F_1^T \\ 0 \end{bmatrix},$$

$$\Xi_{b2} = \begin{bmatrix} Y_{b2}^T A - \widehat{B}C & Y_{b2}^T B_1 \rho_i \widehat{C} - \widehat{A} & 0 \\ G_{b2}^T A + \widehat{B}C & G_{b2}^T B_1 \rho_i \widehat{C} + \widehat{A} & 0 \\ 0 & 0 & Z_{b2}^T A_w \end{bmatrix},$$

$$\Xi_{b6} = \begin{bmatrix} F_2^T \\ (I - \rho_i)^T F_1^T \end{bmatrix},$$

$$\Xi_{b3} = \begin{bmatrix} Y_{b2}^T B_2 - \widehat{B}D_2 & Y_{b2}^T B_1 \rho_i \\ G_{b2}^T B_2 + \widehat{B}D_2 & G_{b2}^T B_1 \rho_i \\ 0 & Z_{b2} B_w \end{bmatrix},$$

$$\Xi_{b4} = \begin{bmatrix} -\bar{\beta}_2 \mathcal{P}_{b31} & -\bar{\beta}_2 \mathcal{P}_{b32} & -\bar{\beta}_2 \mathcal{P}_{b33} \\ * & -\bar{\beta}_2 \mathcal{P}_{b34} & -\bar{\beta}_2 \mathcal{P}_{b35} \\ * & * & -\bar{\beta}_2 \mathcal{P}_{b36} \end{bmatrix},$$

(56)

then system (7) is asymptotically stable and guarantees the weighted  $L_2$  performance with the weighted  $L_2$  gain  $\gamma_{s_2} = \mu\gamma_2$  when system (7) satisfies the constraints (17a), (17b), and (17c).

*Proof.* Similar to the process in Theorem 8, the conditions (52), (53), (54), and (55) can be obtained for system (7) with the weighted  $L_2$  performance (10).  $\square$

**3.3. Algorithm.** The performances (9)-(10) have been formulated as the inequality conditions in Theorems 8 and 9, respectively. But the conditions (34), (35), (52), and (53) are all nonconvex owing to the product terms  $Y_q^T B_1 \widehat{C}$ ,  $G_q^T B_1 \widehat{C}$ ,  $Y_{q_1}^T B_1 \rho_i \widehat{C}$ ,  $G_{q_1}^T B_1 \rho_i \widehat{C}$ ,  $Y_{q_2}^T B_1 \rho_i \widehat{C}$ , and  $G_{q_2}^T B_1 \rho_i \widehat{C}$ ,  $q \in \{a, b\}$ . Then a two-step procedure is presented, which follows from the idea proposed as [26]; it can be summarized as follows.

*Step 1.* Design robust state feedback gain matrices  $C_k, \bar{C}_k$  for the closed-loop system with the state feedback control  $u(k) = C_k x(k)$  for fault free case and  $u(k) = \bar{C}_k x(k)$  for fault detected case; then the performance index (10) is satisfied. This problem is convex and see the appendix for the design of  $C_k, \bar{C}_k$ .

*Step 2.* Put the state feedback gain matrices  $C_k, \bar{C}_k$  into switched system (7) and search for a solution that satisfies the conditions in Theorems 8 and 9. Given  $\gamma_2$ , solving the following problem

$$\begin{aligned} \min \quad & \gamma_1 \\ \text{s.t.} \quad & (34), (35), (36), (37), \\ & (52), (53), (54), (55), \end{aligned} \quad (57)$$

denote  $\widehat{A}, \widehat{B}, \widehat{A}, \widehat{B}$ , and  $N, N_1$  by the optimal solution of (57); the gain matrices  $A_k, B_k, \bar{A}_k, \bar{B}_k$  can be obtained as

$$\begin{aligned} A_k &= N^{-1} \widehat{A}, & B_k &= N^{-1} \widehat{B}, \\ \bar{A}_k &= N_1^{-1} \widehat{A}, & \bar{B}_k &= N_1^{-1} \widehat{B}. \end{aligned} \quad (58)$$

#### 4. Example

Consider a discrete-time system (1) consisting of two subsystems

$$\begin{aligned} x(k+1) &= Ax(k) + B_1 u(k) + B_2 d(k), \\ y(k) &= Cx(k) + D_2 d(k), \\ z(k) &= Ex(k) + F_1 u(k) + F_2 d(k), \end{aligned} \quad (59)$$

where

$$\begin{aligned} & \left[ \begin{array}{c|c|c} A_1 & B_1 & B_2 \\ \hline C & D_1 & D_2 \\ \hline E & F_1 & F_2 \end{array} \right] \\ & = \left[ \begin{array}{ccc|ccc} 0.50 & -0.26 & -0.09 & 0.2 & 0.5 & 0.10 \\ -0.59 & 0.64 & -0.24 & -1.3 & 0.5 & -0.1 \\ 0.54 & -0.25 & 0.11 & 0.5 & -0.5 & 0.4 \\ \hline 0.36 & -0.01 & 0.32 & & & 0.1 \\ -0.01 & 0.1 & 0.3 & 0.1 & 0.2 & 0.2 \end{array} \right]. \end{aligned} \quad (60)$$

Here, we consider the following possible fault modes, and, choosing  $\alpha = 0.2$ ,  $\beta_1 = 60$ ,  $\beta_2 = 5$ , and  $\mu = 1.2$ , we can obtain the gain matrices of the detector/controller as algorithm in Section 3:

$$\begin{aligned} A_{k1} &= \begin{bmatrix} -0.5060 & -0.3372 & -1.0051 \\ 1.5112 & 0.1401 & 2.7485 \\ -0.2425 & 0.1207 & -0.5719 \end{bmatrix}, \\ B_{k1} &= \begin{bmatrix} 2.3951 \\ -5.9280 \\ 2.1928 \end{bmatrix}, \\ \bar{A}_{k1} &= \begin{bmatrix} -0.0523 & -0.1325 & -0.3056 \\ 0.4073 & 0.2041 & 0.3789 \\ -0.3925 & -0.0723 & -0.6093 \end{bmatrix}, \\ \bar{B}_{k1} &= \begin{bmatrix} 1.5261 \\ -3.5448 \\ 2.7507 \end{bmatrix}, \end{aligned} \quad (61)$$

$$\begin{aligned} C_{k1} &= \begin{bmatrix} -0.2413 & -0.0327 & -0.7715 \\ 0.1707 & -0.4837 & -1.1142 \end{bmatrix}, \\ \bar{C}_{k1} &= \begin{bmatrix} 0.0142 & -0.1561 & -0.5887 \\ 0.0429 & -0.4220 & -1.2056 \end{bmatrix}. \end{aligned}$$

Choosing  $\beta = 15$  and  $\zeta = 0.05$ , it is obtained that

$$\tau_a \geq \tau_a^* = \text{ceil} \left[ -\frac{3 \ln \mu}{\ln(1-\zeta)} \right] = 11, \quad (62)$$

$$\frac{\mathcal{T}_{nd}(k_0, k)}{\mathcal{T}_d(k_0, k)} \leq \frac{\ln(1+\beta) - \ln(1+\beta_2)}{\ln(1+\beta_1) - \ln(1+\beta)} = 0.7329, \quad (63)$$

$$\frac{\mathcal{T}_n(k_0, k)}{\mathcal{T}_f(k_0, k)} \geq \frac{\ln(1+\beta) - \ln(1-\zeta)}{\ln(1-\zeta) - \ln(1-\alpha)} = 16.4322. \quad (64)$$

Thus, if the normal operations are larger than the regular intervals 11 steps, meanwhile, it satisfies  $(\mathcal{T}_{nd}/\mathcal{T}_d) \leq 0.7329$  and  $(\mathcal{T}_n/\mathcal{T}_f) > 16.4322$ , then the designed detector/controller makes the closed-loop system asymptotically stable and guarantees the weighted  $L_2$  performance.

Here, for  $k = 0, \dots, 500$ , the disturbances for each subsystem are  $d(k) = 0.5 \sin(0.1k) e^{-0.001k}$ . We consider the two kinds of fault mode to demonstrate the effectiveness of the method proposed by this paper.

*Case 1.* The first actuator is stuck and the second actuator is normal; that is,  $\rho_1 = \begin{bmatrix} 0 & 0 \\ 0 & 1 \end{bmatrix}$ , and the 1st actuator has

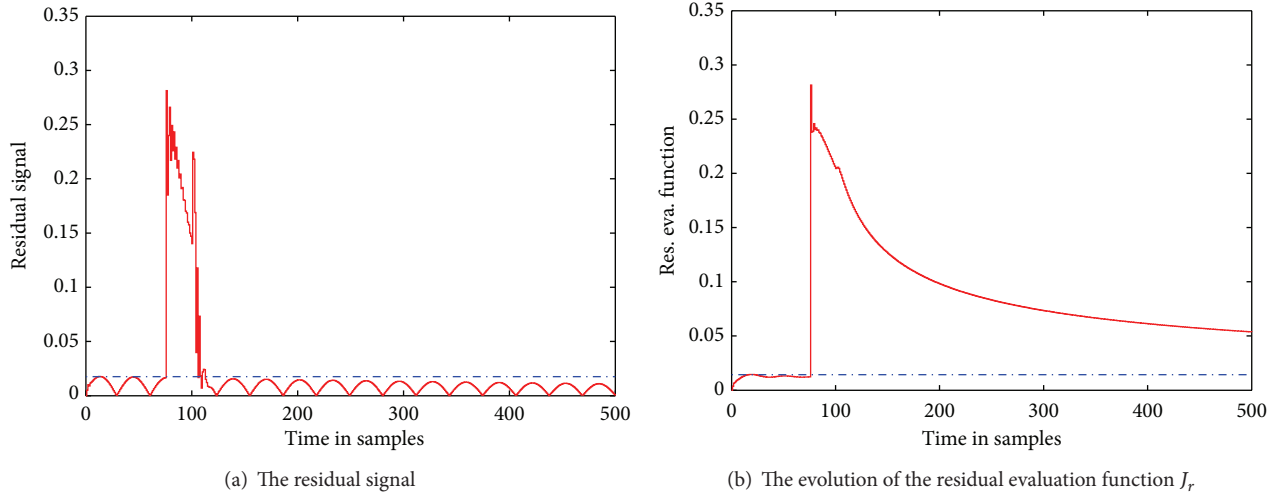
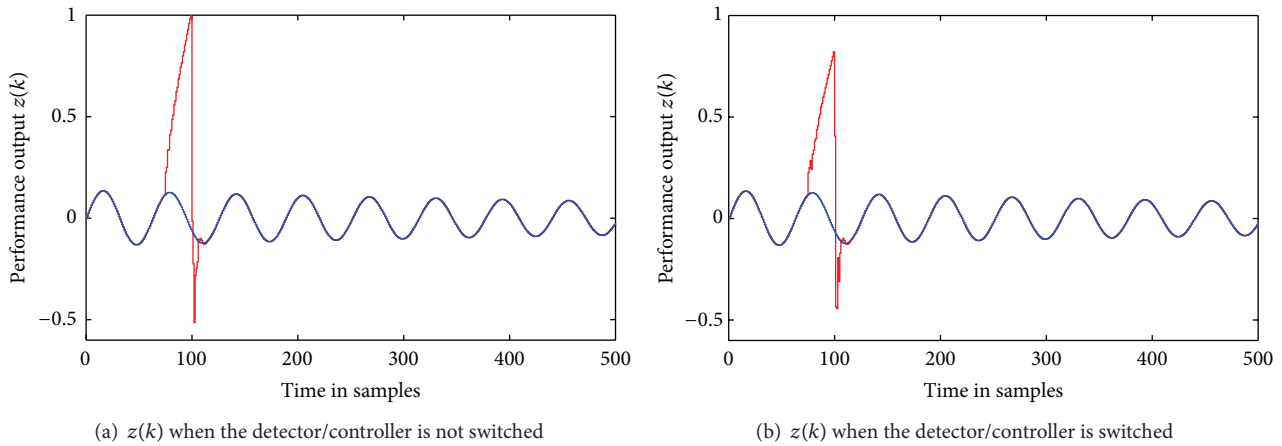


FIGURE 3: The detection objectives for Case 1.


 FIGURE 4: Performance output  $z(k)$  when the fault is detected for Case 1.

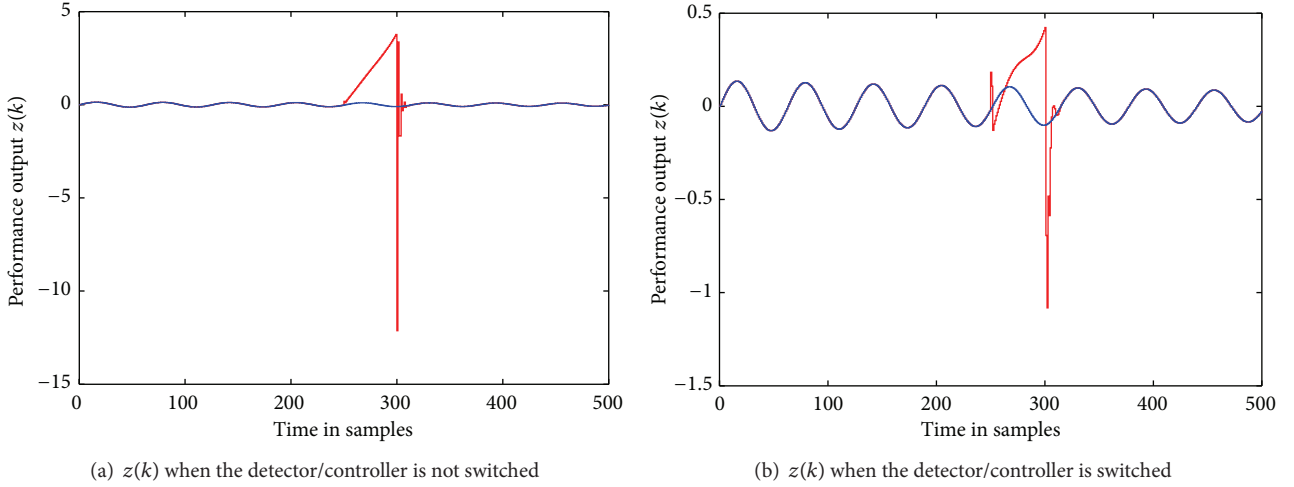
the fault from step 75 to step 100 with the unit amplitude. Suppose the total runtime is 500 steps; the condition (64) has been satisfied; moreover, the closed-loop matrix  $\tilde{A}_1$  is not Hurwitz. We consider the method proposed in this paper which considers the switching strategy. The actuator stuck fault can be detected at step 76; then the controller is switched at step 76. The condition (63) holds; then the closed-loop system with the switching strategy is asymptotically stable and guarantees the weighted  $L_2$  performance. The generated residual  $r(k)$  and the evolution of the residual evaluation function  $J_r(k)$  are shown in Figure 3.

For the detection objectives, it can be seen from Figure 3 that the residual signal  $r(k)$  is larger than the threshold  $r_{th}(k)$  of the residual in step 76 and the residual evaluation function  $J_r(k)$  is larger than the threshold  $J_{th}(k)$  in step 76. It can be deduced that the detector/controller with the parameters  $\tilde{A}_{k1}$ ,  $\tilde{B}_{k1}$ , and  $\tilde{C}_{k1}$  is switched at step 76 to guarantee that the norm of the states increases within acceptable limits. Until the fault is removed in step 100, the residual evaluation function is reset to complete fault detection objective.

For the control objective, we will first demonstrate that the performance output  $z(k)$  is shown in Figure 4(a) if the detector/controller is not switched when the fault is detected, while the performance output  $z(k)$  is shown in Figure 4(b) if the detector/controller is switched when the fault is detected. Comparing these two figures, it can be seen that the effects of disturbances  $d(k)$  and the fault  $f(k)$  on the performance output  $z(k)$  in our method are not disastrous and the performance output  $z(k)$  slowly varies.

*Case 2.* Both of the two actuators are stuck, that is,  $\rho_2 = \begin{bmatrix} 0 & 0 \\ 0 & 0 \end{bmatrix}$ , and the fault from step 250 to step 300. As Case 1, we can also obtain that the conditions (63) and (64) hold, and the closed-loop matrix  $\tilde{A}_1$  is not Hurwitz.

The performance output  $z(k)$  for the detector/controller both no-switched and switched is shown in Figure 5. From Figure 5, we can see that the performance output  $z(k)$  for the no-switched case varies more sharply from  $-12$  to  $4$ , while the performance output  $z(k)$  for the switched case only changes from  $-1.1$  to  $0.4$ .

FIGURE 5: Performance output  $z(k)$  when the fault is detected for Case 2.

The advantage for our method is obvious for the control objective.

From Cases 1 and 2, we see that when the conditions (62), (63), and (64) are satisfied, no matter whether the faults are in the first or in both actuators, all of them can be detected, and the closed-loop system is asymptotically stable and guarantees the given weighted  $L_2$  performance. The fault detection and control for the system with the switching strategy are effective.

## 5. Conclusion

In this paper, the simultaneous fault detection and control problem has been presented for discrete-time systems. The detector/controller is designed as a single unit such that when the fault is detected, the controller is switched to stabilize “destabilizing failure.” The switching strategy which combines event-driven switching with time-driven switching not only

makes the closed-loop system asymptotically stable, but also guarantees the weighted  $L_2$  performance. An example is provided to demonstrate the effectiveness of the proposed design method.

## Appendix

The state feedback case for system (4) is equivalent to consider the constant state feedback controller  $u(k) = C_k x(k)$  for fault free and fault no-detected cases, and  $u(k) = \bar{C}_k x(k)$  for fault detected cases; the following theorem can be used for the state feedback design.

**Theorem A.1.** Let  $\alpha$ ,  $\beta_1$ ,  $\beta_2$ ,  $\mu$ , and  $\gamma_3$  be some constants satisfying  $0 < \alpha < 1$ ,  $\beta_1 > \beta_2 > 0$ ,  $\gamma_3 > 0$ , and  $\mu \geq 1$ . If there exist matrix variables  $\mathcal{E}_k$ ,  $\bar{\mathcal{E}}_k$  and symmetric positive-definite matrices  $\mathcal{Q}_{c1} > 0$  and  $\mathcal{Q}_{c2} > 0$  such that

$$\begin{bmatrix} -\mathcal{Q}_{c1} & A\mathcal{Q}_{c1} + B_1\mathcal{E}_k & B_2 & 0 & 0 \\ * & -(1-\alpha)\mathcal{Q}_{c1} & 0 & 0 & \mathcal{Q}_{c1}E^T + \mathcal{E}_k^T F_1^T \\ * & * & -\gamma_3^2 I & 0 & F_2^T \\ * & * & * & -\gamma_3^2 I & 0 \\ * & * & * & * & -I \end{bmatrix} < 0, \quad (\text{A.1})$$

$$\begin{bmatrix} -\mathcal{Q}_{c1} & A\mathcal{Q}_{c1} + B_1\rho_i\mathcal{E}_k & B_2 & B_1(I-\rho_i) & 0 \\ * & -(1+\beta_1)\mathcal{Q}_{c1} & 0 & 0 & \mathcal{Q}_{c1}E^T + \mathcal{E}_k^T\rho_i^T F_1^T \\ * & * & -\gamma_3^2 I & 0 & F_2^T \\ * & * & * & -\gamma_3^2 I & (I-\rho_i)^T F_1^T \\ * & * & * & * & -I \end{bmatrix} < 0, \quad (\text{A.2})$$

$$\begin{bmatrix} -\mathcal{Q}_{c2} & A\mathcal{Q}_{c2} + B_1\rho_i\bar{\mathcal{E}}_k & B_2 & B_1(I-\rho_i) & 0 \\ * & -(1+\beta_2)\mathcal{Q}_{c2} & 0 & 0 & \mathcal{Q}_{c2}E^T + \bar{\mathcal{E}}_k^T\rho_i^T F_1^T \\ * & * & -\gamma_3^2 I & 0 & F_2^T \\ * & * & * & -\gamma_3^2 I & (I-\rho_i)^T F_1^T \\ * & * & * & * & -I \end{bmatrix} < 0, \quad (\text{A.3})$$

$$\mathcal{Q}_{cg} - \mu\mathcal{Q}_{ch} \leq 0, \quad (\text{A.4})$$

where  $g, h \in \{1, 2\}$ , and  $g \neq h$ , then the closed-loop system for system (4) is asymptotically stable and guarantees the weighted  $L_2$  performance. If the conditions (A.1), (A.2), (A.3), and (A.4) are feasible, the controller parameters can be obtained as  $C_k = \mathcal{E}_k \bar{Q}_{c1}^{-1}$  and  $\bar{C}_k = \bar{\mathcal{E}}_k \bar{Q}_{c2}^{-1}$ .

**Remark A.2.** According to Lemma 7, the closed-loop system for system (4) is asymptotically stable and guarantees the weighted  $L_2$  performance if and only if conditions like (16a), (16b), (16c), and (16d) hold. By some simple calculations like Theorem 8 and Schur complement, (A.1), (A.2), (A.3), and (A.4) can be obtained easily, and the state feedback gains  $C_k$  and  $\bar{C}_k$  can also be obtained.

## Conflict of Interests

The authors declare that there is no conflict of interests regarding the publication of this paper.

## Acknowledgments

This work was supported by the National Natural Science Foundation of China under Grants 61403075, Northeast Dianli University BSJXM-201310 and BSJXM-201311 and Natural Science Foundation of Jilin province, China (no. 20140520060JH).

## References

- [1] R. Wang and J. Zhao, "Reliable guaranteed cost control for uncertain switched non-linear systems," *International Journal of Systems Science*, vol. 40, no. 3, pp. 205–211, 2009.
- [2] G. Yang and D. Ye, "Reliable  $H_\infty$  control of linear systems with adaptive mechanism," *IEEE Transactions on Automatic Control*, vol. 55, no. 1, pp. 242–247, 2010.
- [3] X. G. Guo and G. H. Yang, "Reliable  $H_\infty$  filter design for a class of discrete-time nonlinear systems with time-varying delay," *Optimal Control Applications & Methods*, vol. 31, no. 4, pp. 303–322, 2010.
- [4] J. Li and J. Zhao, "Reliable  $H_\infty$  filtering for switched discrete-time systems with sensor failures: an estimated state-dependent switching method," *Journal of the Franklin Institute*, vol. 350, no. 10, pp. 3082–3099, 2013.
- [5] H. Wang and H. Ju, "Reliable  $H_\infty$  filtering for LPV systems with sensor faults in finite frequency domain," *International Journal of Systems Science*, vol. 44, no. 12, pp. 2310–2320, 2013.
- [6] M. J. Khosrowjerdi, R. Nikoukhah, and N. Safari-Shad, "A mixed  $H_2/H_\infty$  approach to simultaneous fault detection and control," *Automatica*, vol. 40, no. 2, pp. 261–267, 2004.
- [7] H. Wang and G. Yang, "Simultaneous fault detection and control for uncertain linear discrete-time systems," *IET Control Theory & Applications*, vol. 3, no. 5, pp. 583–594, 2009.
- [8] M. R. Davoodi, A. Golabi, H. A. Talebi, and H. R. Momeni, "Simultaneous fault detection and control design for switched linear systems based on dynamic observer," *Optimal Control Applications & Methods*, vol. 34, no. 1, pp. 35–52, 2013.
- [9] X. J. Meng and G. H. Yang, "Simultaneous fault detection and control for stochastic time-delay systems," *International Journal of Systems Science*, vol. 45, no. 5, pp. 1058–1069, 2014.
- [10] D. Liberzon, *Switching in Systems and Control*, Birkhäuser, Boston, Mass, USA, 2003.
- [11] L. Zhang and P. Shi, "Stability,  $L_2$ -gain and asynchronous  $H_\infty$  control of discrete-time switched systems with average dwell time," *IEEE Transactions on Automatic Control*, vol. 54, no. 9, pp. 2192–2199, 2009.
- [12] H. Lin and P. J. Antsaklis, "Stability and stabilizability of switched linear systems: a survey of recent results," *IEEE Transactions on Automatic Control*, vol. 54, no. 2, pp. 308–322, 2009.
- [13] B. Lu, F. Wu, and S. Kim, "Switching LPV control of an F-16 aircraft via controller state reset," *IEEE Transactions on Control Systems Technology*, vol. 14, no. 2, pp. 267–277, 2006.
- [14] S. Lim, "Modeling and  $H_\infty$  control for switched linear parameter-varying missile autopilot," *IEEE Transactions on Control Systems Technology*, vol. 11, no. 6, pp. 830–838, 2003.
- [15] M. S. Branicky, "Multiple Lyapunov functions and other analysis tools for switched and hybrid systems," *IEEE Transactions on Automatic Control*, vol. 43, no. 4, pp. 475–482, 1998.
- [16] D. Du, B. Jiang, P. Shi, and S. Zhou, " $H_\infty$  filtering of discrete-time switched systems with state delays via switched Lyapunov function approach," *IEEE Transactions on Automatic Control*, vol. 52, no. 8, pp. 1520–1525, 2007.
- [17] L. X. Zhang, E. K. Boukas, and P. Shi, "Exponential  $H_\infty$  filtering for uncertain discrete-time switched linear systems with average dwell time: a  $\mu$ -dependent approach," *International Journal of Robust and Nonlinear Control*, vol. 18, no. 11, pp. 1188–1207, 2008.
- [18] Q. Y. Su and J. Zhao, "Stabilization of a class of switched systems with state constraints," *Nonlinear Dynamics*, vol. 70, no. 2, pp. 1499–1510, 2012.
- [19] H. Yang, B. Jiang, and M. Staroswiecki, "Supervisory fault tolerant control for a class of uncertain nonlinear systems," *Automatica*, vol. 45, no. 10, pp. 2319–2324, 2009.
- [20] H. Yang, B. Jiang, V. Cocquempot, and L. Lu, "Supervisory fault tolerant control with integrated fault detection and isolation: a switched system approach," *International Journal of Applied Mathematics and Computer Science*, vol. 22, no. 1, pp. 87–97, 2012.
- [21] R. Wang, J. Zhao, G. M. Dimirovski, and G. Liu, "Output feedback control for uncertain linear systems with faulty actuators based on a switching method," *International Journal of Robust and Nonlinear Control*, vol. 19, no. 12, pp. 1295–1312, 2009.
- [22] X. M. Sun, J. Zhao, and W. Wang, "State feedback control for discrete delay systems with controller failures based on average dwell-time method," *IET Control Theory & Applications*, vol. 2, no. 2, pp. 126–132, 2008.
- [23] G. Yang and H. Wang, "Fault detection for a class of uncertain state-feedback control systems," *IEEE Transactions on Control Systems Technology*, vol. 18, no. 1, pp. 201–212, 2010.
- [24] H. Yang, B. Jiang, and Y. Zhang, "Tolerance of intermittent faults in spacecraft attitude control: switched system approach," *IET Control Theory & Applications*, vol. 6, no. 13, pp. 2049–2056, 2012.
- [25] P. M. Frank and X. Ding, "Survey of robust residual generation and evaluation methods in observer-based fault detection systems," *Journal of Process Control*, vol. 7, no. 6, pp. 403–424, 1997.
- [26] S. Kanev, C. Scherer, M. Verhaegen, and B. de Schutter, "Robust output-feedback controller design via local BMI optimization," *Automatica*, vol. 40, no. 7, pp. 1115–1127, 2004.

## Research Article

# SINS/CNS Nonlinear Integrated Navigation Algorithm for Hypersonic Vehicle

Yong-jun Yu,<sup>1</sup> Jin-fa Xu,<sup>1</sup> and Zhi Xiong<sup>2</sup>

<sup>1</sup> College of Aerospace Engineering, Nanjing University of Aeronautics and Astronautics, Jiangsu, Nanjing 210016, China

<sup>2</sup> Navigation Research Center, Nanjing University of Aeronautics and Astronautics, Jiangsu, Nanjing 210016, China

Correspondence should be addressed to Yong-jun Yu; yongjunbingyu@gmail.com

Received 27 August 2014; Accepted 1 November 2014

Academic Editor: Bin Jiang

Copyright © 2015 Yong-jun Yu et al. This is an open access article distributed under the Creative Commons Attribution License, which permits unrestricted use, distribution, and reproduction in any medium, provided the original work is properly cited.

Celestial Navigation System (CNS) has characteristics of accurate orientation and strong autonomy and has been widely used in Hypersonic Vehicle. Since the CNS location and orientation mainly depend upon the inertial reference that contains errors caused by gyro drifts and other error factors, traditional Strap-down Inertial Navigation System (SINS)/CNS positioning algorithm setting the position error between SINS and CNS as measurement is not effective. The model of altitude azimuth, platform error angles, and horizontal position is designed, and the SINS/CNS tightly integrated algorithm is designed, in which CNS altitude azimuth is set as measurement information. GPF (Gaussian particle filter) is introduced to solve the problem of nonlinear filtering. The results of simulation show that the precision of SINS/CNS algorithm which reaches 130 m using three stars is improved effectively.

## 1. Introduction

Hypersonic Vehicle (HV) which refers to a vehicle flying at Mach 5 or above has already been the research focus in aeronautic and aerospace fields with its great strategic military application values [1, 2].

Although Hypersonic Vehicle has many advantages, such as large flight envelope, high maneuverability, and well penetrability, the dynamic model of an HV is fast time varying and highly nonlinear because of its Mach numbers [3]. Large-scale variations of altitude and velocity lead to uncertainties in the aerodynamic parameters [4, 5]. As a result, HV is a highly nonlinear and uncertain system. Consequently, it is difficult to measure or estimate the dynamic state and characteristics of the vehicle [6]. Autonomous navigation system with high accuracy and reliability has been a major constraint on the improvement in performance of HV.

In recent years, owing to the development of microelectronics and computer technology, as well as the accuracy improvement of Charge Coupled Device (CCD), Charge Inject Device (CID) star trackers, and inertial components, the Strap-down Inertial Navigation System (SINS) and Celestial Navigation System (CNS) are widely used in aircrafts [7].

The celestial navigation method is a kind of autonomous navigation technology which can determine the vehicle's position and attitude [8]. Since Celestial Navigation System (CNS) has characteristics of accurate orientation and strong autonomy, it has become an important component of integrated navigation system of HV [9].

The conventional celestial navigation utilizes the inertial navigation platform technology to realize the vertical vector and compute the vehicle's navigation information by measuring the relative position changes between the vertical vector and the celestial vector. The navigation accuracy of this method depends largely on the accuracy of horizontal reference and celestial sensor measurements [10]. CNS usually gets the inertial horizon reference by inertial navigation platform. Considering that the strap-down type replacing the platform type has been the development trend of INS, it has become extremely difficult to improve the accuracy of the inertial horizon references due to the impact of INS core instruments (gyros and accelerometers) error [11].

In traditional SINS/CNS integrated mode, CNS utilizes the position and attitude information of INS to calculate celestial positions and heading attitude and then realize periodic correction of the INS drifts. This mode can damp

TABLE I: Comparison of SINS/CNS navigation error.

Error	$\delta v/m/s$		$\delta p/m$	
	$\delta v_e$	$\delta v_n$	$\delta \lambda$	$\delta L$
One star	0.21	-0.76	737.7	842.6
Two stars	0.13	-0.38	161.2	89.5
Three stars	-0.10	-0.10	108.9	72.6

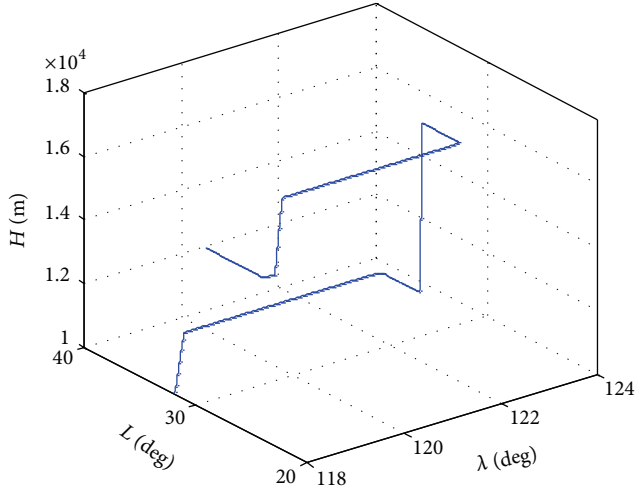


FIGURE 1: Simulation trace.

the divergence of INS position errors; however, since the CNS location and orientation mainly depend upon the inertial reference that contains errors caused by gyro drifts and other error factors, this postcorrection method is not effective.

A number of classical approaches, the Kalman filter (KF), extended Kalman filter (EKF), unscented Kalman filter (UKF), particle filtering (PF), and so forth, have been proposed to the information fusion. Kalman filtering is commonly used algorithms for information integration. A prerequisite for using Kalman filter is that the system dynamics and noise statistics are known [12]. But considering the HV is a highly nonlinear system, the dynamic characteristics of the HV and external environment make these premise conditions often not met.

PF can effectively solve the problem of nonlinear filtering [13, 14]. However, its limitation is obvious.

- (1) PF occasionally has the particle impoverishment (PI) problem that results from resampling process [15].
- (2) The number of particles will increase at a rapid rate along with the increase of the system dimensions.

The Gaussian PF avoids the PI problem that is the disadvantageous feature of PF in the estimation of a static parameter. Furthermore, resampling process is not required in the GPF algorithm. Therefore, its computational complexity (CC) is significantly reduced compared to particle filtering.

This paper will carry out the research on the SINS/CNS integrated navigation algorithm for the HV. In order to improve the accuracy and reliability of SINS/CNS integrated

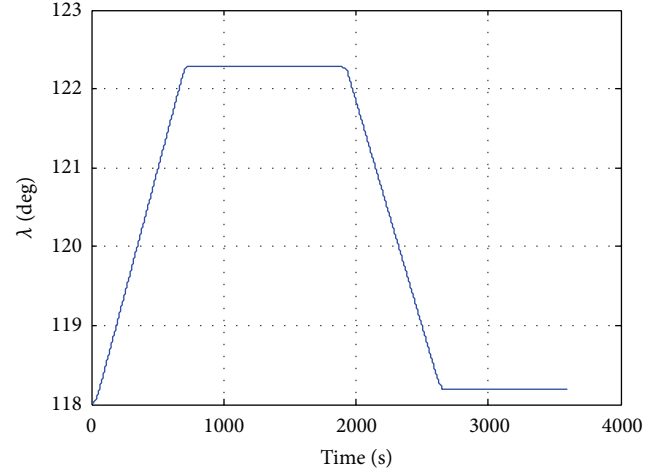


FIGURE 2: Simulation longitude.

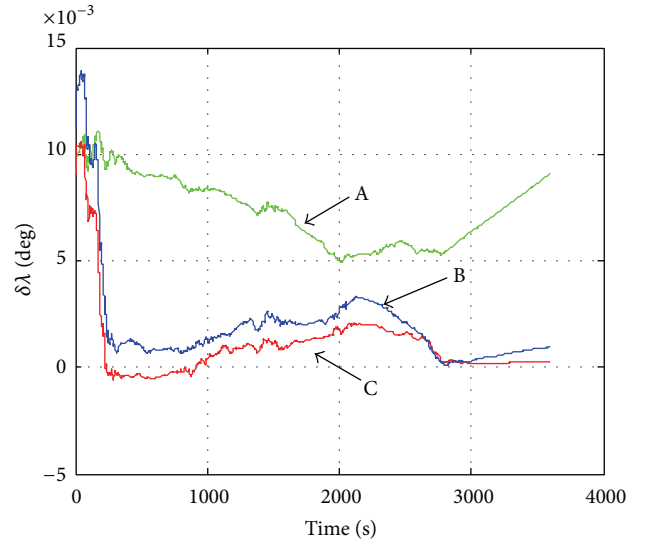


FIGURE 3: Compression of longitude error.

systems, the scheme and algorithm of airborne SINS/CNS integrated navigation based on celestial angle observation have been presented. The theory of SINS/CNS integrated navigation system based on celestial altitude angle observation information has been discussed adequately; a model with celestial altitude angle, platform error angles, and horizontal position is deduced. Meanwhile, a new SINS/CNS tightly integrated localization algorithm using Gaussian particle filter (GPF) is presented, which makes full use of SINS and CNS navigation information to achieve higher accuracy of the SINS/CNS integration.

## 2. SINS/CNS Tightly Integrated Navigation Model

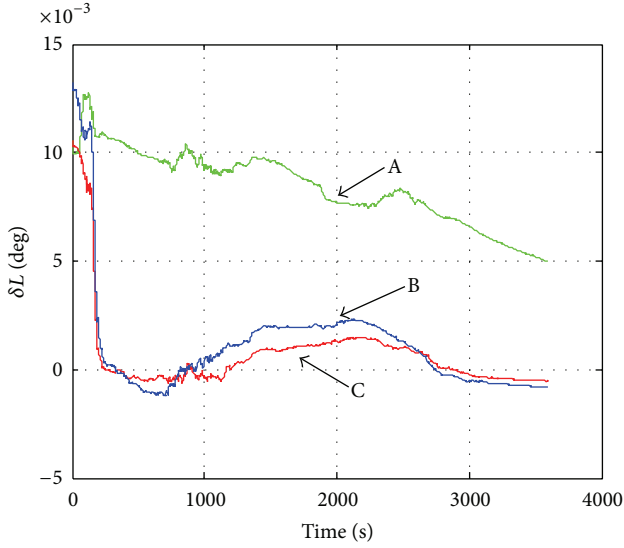


FIGURE 4: Compression of latitude error.

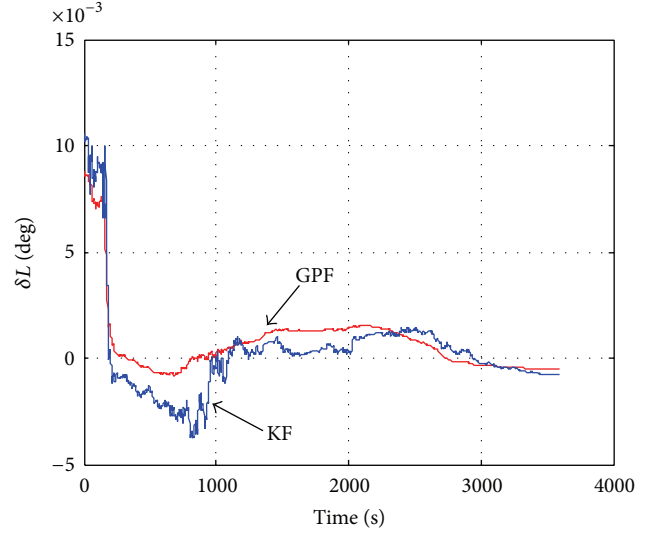


FIGURE 6: Compression of latitude error.

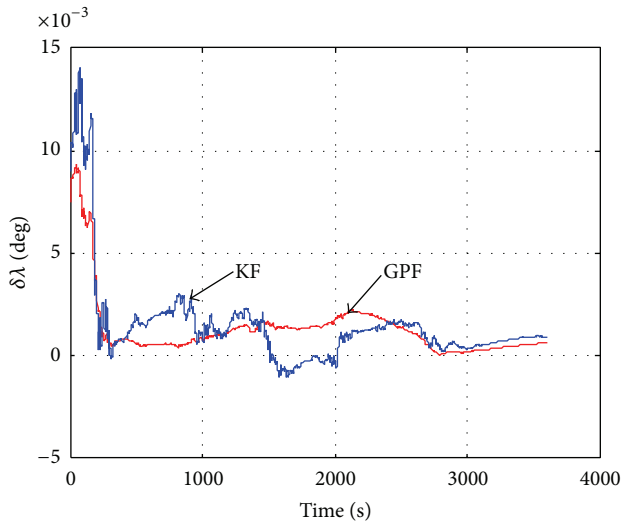


FIGURE 5: Compression of longitude error.

**2.1. The Model of CNS Measurement.** The basic principle of astronomical positioning is given by

$$\sin h_p = \sin \delta_A \sin L + \cos \delta_A \cos L \cos(t_G + \lambda), \quad (1)$$

where  $h_p$  is the observed altitude angle of the navigational stars in Local-Level Frame.  $\lambda$ ,  $L$  are longitude and latitude;  $\delta_A$ ,  $t_G$  are the declination and Greenwich hour angle.

According to (1), using longitude and latitude information from SINS, the computed altitude angle  $h_l$  in Local-Level Frame is received as

$$\sin h_l = \sin L_s \sin \delta_A + \cos L_s \cos \delta_A \cos(\lambda_s + t_G), \quad (2)$$

where  $L_s$ ,  $\lambda_s$  are latitude and longitude from SINS, and

$$h_l = h_p + \delta h, \quad L_s = L + \delta L, \quad \lambda_s = \lambda + \delta \lambda. \quad (3)$$

By using first order approximation of Taylor expansion, (3) can be expressed as

$$\begin{aligned} \sin h_l &= \sin L \sin \delta_A + \cos \delta_A \cos L \cos(t_G + \lambda) \\ &+ (\cos L \sin \delta_A - \cos \delta_A \cos t_G \sin L \cos \lambda \\ &+ \cos \delta_A \sin t_G \sin \lambda \sin L) \cdot \Delta L \\ &- (\cos \delta_A \sin t_G \cos L \cos \lambda \\ &+ \cos \delta_A \cos t_G \cos L \sin \lambda) \cdot \Delta \lambda. \end{aligned} \quad (4)$$

According to (1) and (4), the relation between computed altitude angle  $h_l$  and observed altitude angle  $h_p$  can be expressed as follows:

$$\sin h_l - \sin h_p = \alpha_1 \cdot \Delta \lambda + \beta_1 \cdot \Delta L, \quad (5)$$

where

$$\begin{aligned} \alpha_1 &= -\cos \delta_A \cos t_G \sin \lambda \cos L \\ &- \cos \delta_A \sin t_G \cos \lambda \cos L, \\ \beta_1 &= \sin \delta_A \cos L - \cos \delta_A \cos t_G \cos \lambda \sin L \\ &+ \cos \delta_A \sin t_G \sin \lambda \sin L. \end{aligned} \quad (6)$$

Since CNS gets the inertial horizon reference by SINS, we can not get the observed altitude angle in Local-Level Frame in (1) but the observed altitude angle  $h_c$  in Computational Frame.

The celestial vector in Local-Level Frame can be set as

$$\mathbf{X}_p = [\cosh_p \sin A_p \quad \cosh_p \cos A_p \quad \sin h_p]^T. \quad (7)$$

The celestial vector in Computational-Level Frame can be set as

$$\mathbf{X}_c = [\cosh_c \sin A_c \quad \cosh_c \cos A_c \quad \sin h_c]^T. \quad (8)$$

The relationship between Computational Frame and Local-Level Frame can be expressed as follows:

$$\mathbf{X}_p = \mathbf{C}_c^p \mathbf{X}_c, \quad (9)$$

where  $\mathbf{C}_c^p = \begin{bmatrix} 1 & -\phi_u & \phi_n \\ \phi_u & 1 & -\phi_e \\ -\phi_n & \phi_e & 1 \end{bmatrix}$ , and  $\phi_e, \phi_n, \phi_u$  are east, north, and up platform angle error.

From (7)~(9),

$$\sinh h_p = \sinh h_c - \phi_n \times \cosh h_c \sin A_c + \phi_e \times \cosh h_c \cos A_c. \quad (10)$$

According to (5) and (10), the relationship between computed altitude angle  $h_l$  in Local-Level Frame and the observed altitude angle  $h_c$  in Computational Frame can be expressed as follows:

$$\begin{aligned} \sinh h_l - \sinh h_c &= \alpha_1 \cdot \Delta \lambda + \beta_1 \cdot \Delta L \\ &- \phi_n \times \cosh h_c \sin A_c + \phi_e \times \cosh h_c \cos A_c. \end{aligned} \quad (11)$$

*2.2. Equation of State of SINS/CNS Integrated Algorithm.* The navigation frame is chosen as east-north-upward geographic frame. The  $X$ - $Y$ - $Z$  direction of the body frame is coincident with the Right-Front-Upward direction of the vehicle body.

The state equations are described as

$$\dot{\mathbf{X}}(t) = \mathbf{F}(\mathbf{X}(t), \mathbf{W}(t)), \quad (12)$$

where  $\mathbf{X}(t)$  is the state variables vector, and

$$\mathbf{X}(t) = [\delta q_0, \delta q_1, \delta q_2, \delta q_3, \delta V_E, \delta V_N, \delta V_U, \delta L, \delta \lambda, \delta h, \varepsilon_{bx}, \varepsilon_{by}, \varepsilon_{bz}, \nabla_x, \nabla_y, \nabla_z]^T \quad (13)$$

$\varepsilon_{bx}, \varepsilon_{by}, \varepsilon_{bz}$  are single-order Markov errors of three gyros,  $\nabla_{ax}, \nabla_{ay}, \nabla_{az}$  are single-order Markov errors of three accelerometers, and

$$\begin{aligned} \delta \dot{\boldsymbol{\omega}}_{ib}^b &= [\dot{\varepsilon}_{bx} \ \dot{\varepsilon}_{by} \ \dot{\varepsilon}_{bz}]^T = -\frac{1}{T_\omega} \delta \boldsymbol{\omega}_{ib}^b + \boldsymbol{\sigma}_\omega(t), \\ \dot{\mathbf{V}}^b &= [\dot{\nabla}_x \ \dot{\nabla}_y \ \dot{\nabla}_z]^T = -\frac{1}{T_\nabla} \mathbf{V}^b + \boldsymbol{\sigma}_\nabla(t). \end{aligned} \quad (14)$$

$\mathbf{F}$  is the system matrix,  $\mathbf{W}(t)$  is the system noise matrix, and  $\mathbf{W}(t) = [\boldsymbol{\sigma}_\omega(t) \ \boldsymbol{\sigma}_\nabla(t)]$ .

The attitude equation in the form of a quaternion is written as

$$\dot{\mathbf{Q}}_b^n = \frac{1}{2} [\mathbf{Q}_b^n] \boldsymbol{\omega}_{nb}^b = \frac{1}{2} \langle \boldsymbol{\omega}_{ib}^b \rangle \mathbf{Q}_b^n - \frac{1}{2} [\boldsymbol{\omega}_{in}^n] \mathbf{Q}_b^n, \quad (15)$$

where  $\mathbf{Q}_b^n = [q_0 \ q_1 \ q_2 \ q_3]^T$ ,  $\boldsymbol{\omega}_{ib}^b$  the vehicle body angular rate measured by gyros in the body frame,

$$[\boldsymbol{\omega}_{ib}^b] = \begin{bmatrix} 0 & -\omega_x & -\omega_y & -\omega_z \\ \omega_x & 0 & \omega_z & -\omega_y \\ \omega_y & -\omega_z & 0 & \omega_x \\ \omega_z & \omega_y & -\omega_x & 0 \end{bmatrix}, \quad (16)$$

$\boldsymbol{\omega}_{in}^n = \boldsymbol{\omega}_{ie}^n + \boldsymbol{\omega}_{en}^n$ , and  $\boldsymbol{\omega}_{ie}^n$  is the projection of the earth rotation rate in the navigation frame.  $\boldsymbol{\omega}_{en}^n$  is angular rate of the

navigation frame with respect to the earth frame, expressed in the navigation frame:

$$\langle \boldsymbol{\omega}_{in}^n \rangle = \begin{bmatrix} 0 & -\omega_e & -\omega_n & -\omega_u \\ \omega_e & 0 & -\omega_u & \omega_n \\ \omega_n & \omega_u & 0 & -\omega_e \\ \omega_u & -\omega_n & \omega_e & 0 \end{bmatrix}. \quad (17)$$

The definition of the quaternion error between real quaternion and calculated quaternion is

$$\delta \mathbf{Q} = \widehat{\mathbf{Q}}_b^n - \mathbf{Q}_b^n, \quad (18)$$

where  $\delta \mathbf{Q} = [\delta q_0, \delta q_1, \delta q_2, \delta q_3]^T$ ,  $\widehat{\mathbf{Q}}_b^n$  is calculated quaternion, and  $\mathbf{Q}_b^n$  is real quaternion.

The dynamic vector equation of quaternion error can be presented as

$$\begin{aligned} \delta \dot{\mathbf{Q}} &= \frac{1}{2} \langle \boldsymbol{\omega}_{ib}^b \rangle \delta \mathbf{Q} - \frac{1}{2} [\boldsymbol{\omega}_{in}^n] \delta \mathbf{Q} + \frac{1}{2} \mathbf{U}(\mathbf{Q}) \delta \boldsymbol{\omega}_{ib}^b \\ &- \frac{1}{2} \mathbf{Y}(\mathbf{Q}) \delta \boldsymbol{\omega}_{in}^n, \end{aligned} \quad (19)$$

where  $\delta \boldsymbol{\omega}_{in}^n = \delta \boldsymbol{\omega}_{ie}^n + \delta \boldsymbol{\omega}_{en}^n$ , and

$$\mathbf{Y}(\mathbf{Q}) = \begin{bmatrix} -q_1 & -q_2 & -q_3 \\ q_0 & q_3 & -q_2 \\ -q_3 & q_0 & q_1 \\ q_2 & -q_1 & q_0 \end{bmatrix}, \quad \mathbf{U}(\mathbf{Q}) = \begin{bmatrix} -q_1 & -q_2 & -q_3 \\ q_0 & -q_3 & q_2 \\ q_3 & q_0 & -q_1 \\ -q_2 & q_1 & q_0 \end{bmatrix}. \quad (20)$$

Dynamic vector equation of velocity errors can be expressed as

$$\begin{aligned} \delta\dot{\mathbf{V}} = & \Delta\mathbf{Q}_b^n \widehat{\mathbf{f}}_b + \mathbf{Q}_b^n \nabla^b - (2\boldsymbol{\omega}_{ie}^n + \boldsymbol{\omega}_{en}^n) \times \delta\mathbf{V} \\ & + (\mathbf{V} + \delta\mathbf{V}) \times (2\delta\boldsymbol{\omega}_{ie}^n + \delta\boldsymbol{\omega}_{en}^n), \end{aligned} \quad (21)$$

where  $\delta\mathbf{V} = [\delta V_E, \delta V_N, \delta V_U]$ , and  $\widehat{\mathbf{f}}_b$  represents the specific force measured by the three accelerometers in the body frame.

Dynamic equation of position errors can be expressed as

$$\begin{aligned} \delta\dot{L} = & \frac{\delta V_N}{R_M + h} - \frac{V_N}{(R_M + h)^2} \delta h, \\ \delta\dot{\lambda} = & \frac{\delta V_E}{R_N + h} \sec L + \frac{V_E}{R_N + h} \operatorname{tg} L \sec L \delta L - \frac{V_E \sec L \delta h}{(R_N + h)^2}, \quad (22) \\ \delta\dot{h} = & \delta V_U, \end{aligned}$$

where  $R_M, R_N$  are the earth curvature radius.

From (11), the measurement equation with one navigational star can be set as

$$\mathbf{Z}(t) = \sin h_l - \sin h_c. \quad (23)$$

If there is more than one navigational star, the measurement equation can be set as

$$\mathbf{Z}(t) = \begin{bmatrix} \sin h_{l1} - \sin h_{c1} \\ \vdots \\ \sin h_{lm} - \sin h_{cn} \end{bmatrix} = \mathbf{H}(t) \mathbf{X}(t) + \mathbf{V}(t), \quad (24)$$

where  $\mathbf{H}(t)$  is the matrix that reflects the relations between  $\mathbf{X}(t)$  and  $\mathbf{Z}(t)$ ,  $\mathbf{V}(t)$  is the noise vector of the measurement information, and

$$\mathbf{V}(t) = \begin{bmatrix} \sin \delta h_1 \\ \vdots \\ \sin \delta h_n \end{bmatrix}. \quad (25)$$

According to (12) and (24), the system equations are described as

$$\begin{aligned} \dot{\mathbf{X}}(t) = & \mathbf{F}(\mathbf{X}(t), \mathbf{W}(t)), \\ \mathbf{Z}(t) = & \mathbf{H}(t) \mathbf{X}(t) + \mathbf{V}(t). \end{aligned} \quad (26)$$

### 3. SINS/CNS Gaussian Particle Filter Algorithm

The GPF approximates the filtering and predictive densities by Gaussian distributions in a PF framework. The GPF recursively updates only the posterior mean and the covariance of the parameter of interest. The basic idea of PF is to represent a density by generated samples and their associated weights. The following shows the approximation of a filtering density by particles and their weights.

The equations of nonlinear system model are defined as follows:

$$\begin{aligned} \mathbf{x}_k = & f(\mathbf{x}_{k-1}, \boldsymbol{\omega}_{k-1}), \\ \mathbf{z}_k = & h(\mathbf{x}_k, \mathbf{v}_k). \end{aligned} \quad (27)$$

GPF can be described as the following two steps.

*Measurement Update.* Generate the sample particles following

$$\mathbf{x}_k^i \sim q(\mathbf{x}_k^i | \mathbf{z}_{0:k}), \quad (28)$$

where  $q(\cdot)$  is the importance sampling function,  $i = 1 : M$ , and  $M$  is the particle number.

And the weights can be approximated by the following:

$$\omega_k^i \propto \frac{p(\mathbf{z}_k | \mathbf{x}_k^i) N(\mathbf{x}_k^i; \boldsymbol{\mu}_k; \boldsymbol{\Sigma}_k)}{q(\mathbf{x}_k^i | \mathbf{z}_{0:k})}, \quad (29)$$

where  $p(\cdot)$  is the filtering density, and  $\boldsymbol{\mu}_k, \boldsymbol{\Sigma}_k$  are obtained by sample mean and covariance of the particles generated in the previous time update step.

Then compute the  $\bar{\boldsymbol{\mu}}_k, \bar{\boldsymbol{\Sigma}}_k$  following

$$\bar{\boldsymbol{\mu}}_k = \sum_{i=1}^M \omega_k^i \mathbf{x}_k^i, \quad (30)$$

$$\bar{\boldsymbol{\Sigma}}_k = \sum_{i=1}^M \omega_k^i (\boldsymbol{\mu}_k - \mathbf{x}_k^i) (\boldsymbol{\mu}_k - \mathbf{x}_k^i)^T.$$

*Time Update.* Generate  $\mathbf{x}_{k|k+1}^i$  and compute  $\mathbf{x}_{k+1|k+1}^i$ :

$$\mathbf{x}_{k|k+1}^i \sim N(\mathbf{x}_k^i; \bar{\boldsymbol{\mu}}_k; \bar{\boldsymbol{\Sigma}}_k), \quad (31)$$

$$\mathbf{x}_{k+1|k+1}^i \sim p(\mathbf{x}_{k+1}^i | \mathbf{x}_{k|k+1}^i).$$

Then compute the  $\bar{\boldsymbol{\mu}}_{k+1}, \bar{\boldsymbol{\Sigma}}_{k+1}$  following

$$\bar{\boldsymbol{\mu}}_{k+1} = \frac{1}{M} \sum_{i=1}^M \mathbf{x}_{k+1}^i, \quad (32)$$

$$\bar{\boldsymbol{\Sigma}}_{k+1} = \frac{1}{M} \sum_{i=1}^M (\boldsymbol{\mu}_{k+1} - \mathbf{x}_{k+1}^i) (\boldsymbol{\mu}_{k+1} - \mathbf{x}_{k+1}^i)^T.$$

According to (26), the state equation is nonlinear and the measurement equation is linear; the measurement update of GPF can be estimated by Kalman filter. Thus, (29) and (30) can be simplified as follows:

$$\begin{aligned} \mathbf{K}_k = & \boldsymbol{\Sigma}_k \mathbf{H}_k^T [\mathbf{H}_k \boldsymbol{\Sigma}_k \mathbf{H}_k^T + \mathbf{R}_k]^{-1}, \\ \bar{\boldsymbol{\mu}}_k = & \boldsymbol{\mu}_k + \mathbf{K}_k [\mathbf{z}_k - \mathbf{H}_k \boldsymbol{\mu}_k], \\ \bar{\boldsymbol{\Sigma}}_k = & [\mathbf{I} - \mathbf{K}_k \mathbf{H}_k] \boldsymbol{\Sigma}_k. \end{aligned} \quad (33)$$

The GPF flow chart for (26) is given as follows.

Step 1. Consider

$$\mathbf{x}_k^i \sim q(\mathbf{x}_k^i | \mathbf{z}_{0:k}) = N(\mathbf{x}_k^i; \boldsymbol{\mu}_k; \boldsymbol{\Sigma}_k). \quad (34)$$

Step 2. Consider

$$\begin{aligned} \mathbf{K}_k &= \boldsymbol{\Sigma}_k \mathbf{H}_k^T [\mathbf{H}_k \boldsymbol{\Sigma}_k \mathbf{H}_k^T + \mathbf{R}_k]^{-1}, \\ \bar{\boldsymbol{\mu}}_k &= \boldsymbol{\mu}_k + \mathbf{K}_k [\mathbf{z}_k - \mathbf{H}_k \boldsymbol{\mu}_k], \\ \bar{\boldsymbol{\Sigma}}_k &= [\mathbf{I} - \mathbf{K}_k \mathbf{H}_k] \boldsymbol{\Sigma}_k. \end{aligned} \quad (35)$$

Step 3. Consider

$$\begin{aligned} \mathbf{x}_{k|k+1}^i &\sim N(\mathbf{x}_{k|k+1}^i; \bar{\boldsymbol{\mu}}_k; \bar{\boldsymbol{\Sigma}}_k), \\ \mathbf{x}_{k+1|k+1}^i &\sim p(\mathbf{x}_{k+1}^i | \mathbf{x}_{k|k+1}^i). \end{aligned} \quad (36)$$

Step 4. Consider

$$\begin{aligned} \bar{\boldsymbol{\mu}}_{k+1} &= \frac{1}{M} \sum_{i=1}^M \mathbf{x}_{k+1}^i, \\ \bar{\boldsymbol{\Sigma}}_{k+1} &= \frac{1}{M} \sum_{i=1}^M (\boldsymbol{\mu}_{k+1} - \mathbf{x}_{k+1}^i) (\boldsymbol{\mu}_{k+1} - \mathbf{x}_{k+1}^i)^T. \end{aligned} \quad (37)$$

## 4. Simulation and Analysis

The proposed algorithm is testified by the designed track. The drift of equivalent gyros in inertial navigation system is set to  $0.1^\circ/\text{h}$ , the drift of equivalent accelerometer is  $10^{-4}$  g, and the period of SINS algorithm is 5 ms. The navigation stars are Alioth, Arcturus, and Dubhe. The error of star sensor is 10 arc-second, and the period of CNS is 1.0 s; the period of the GPF is 1.0 s.

The track is set as showed in Figure 1. The longitude is set as showed in Figure 2.

The errors of longitude and latitude are given as in Figures 3 and 4.

In Figures 3 and 4, “A” represents the results of one navigation star and “B” and “C” represent two and three navigation stars.

In Figures 3 and 4, when there are more navigation stars, the position error is smaller. The mean square error average is shown in Table 1.

Test results indicate that the precision of position is about 1100 m with one star. The precision of position using three stars can reach 130 m, which indicate that the method in the paper can improve the precision of navigation system effectively.

The comparison of GPF and KF using three stars is given in Figures 5 and 6.

Through Figures 5 and 6, both KF and GPF can convergence fast, but the accuracy of GPF is higher, and the steady accuracy is less influenced by the carrier mobility.

## 5. Conclusion

The SINS/CNS navigation system is an important autonomous navigation technology of HV for its accurate

orientation and strong autonomy. Traditional SINS/CNS integrated mode, which uses celestial positions correcting the SINS drifts, is not effective because the CNS location mainly depends upon the inertial reference that contains errors caused by gyro drifts. In this paper, the theory of SINS/CNS integrated navigation system based on celestial angle observation information has been proposed for HV. The model with altitude angle, platform error angles, and horizontal position is deduced; the SINS/CNS tightly integrated localization algorithm using GPF is presented. The SINS/CNS algorithm is of important value in engineering application.

## Conflict of Interests

The authors declare that there is no conflict of interests regarding the publication of this paper.

## Acknowledgments

Yong-jun Yu is supported by China Postdoctoral Science Foundation Funded Project (2013M541668); Jiangsu Postdoctoral Science Foundation (1401041B); National Natural Science Foundation of China (Grant No. 61374115); PAPD.

## References

- [1] X. Luo and J. Li, “Fuzzy dynamic characteristic model based attitude control of hypersonic vehicle in gliding phase,” *Science China: Information Sciences*, vol. 54, no. 3, pp. 448–459, 2011.
- [2] P. Wang, G. Tang, L. Liu, and J. Wu, “Nonlinear hierarchy-structured predictive control design for a generic hypersonic vehicle,” *Science China Technological Sciences*, vol. 56, no. 8, pp. 2025–2036, 2013.
- [3] B. Xu, D. Gao, and S. Wang, “Adaptive neural control based on HGO for hypersonic flight vehicles,” *Science China*, vol. 54, no. 3, pp. 511–520, 2011.
- [4] F. R. Chavez and D. K. Schmidt, “Analytical aeropropulsive/aeroelastic hypersonic-vehicle model with dynamic analysis,” *Journal of Guidance, Control, and Dynamics*, vol. 17, no. 6, pp. 1308–1319, 1994.
- [5] M. A. Bolender and D. B. Doman, “A non-linear model for the longitudinal dynamics of a hypersonic air-breathing vehicle,” *AIAA Paper 2005-6255*, 2005.
- [6] H. Xu, M. D. Mirmirani, and P. A. Ioannou, “Adaptive sliding mode control design for a hypersonic flight vehicle,” *AIAA Journal of Guidance, Control, and Dynamics*, vol. 27, no. 5, pp. 829–838, 2004.
- [7] P. M. Janiczek, “STELLA: toward automated celestial navigation,” *Surface Warfare*, vol. 21, no. 2, pp. 34–37, 1996.
- [8] X. Chen, “Investigation on celestial/inertial integrated navigation patterns,” *Optics and Optoelectronic Technology*, vol. 1, no. 3, pp. 21–24, 2003.
- [9] C. C. Liebe, “Accuracy performance of star trackers—a tutorial,” *IEEE Transactions on Aerospace and Electronic Systems*, vol. 38, no. 2, pp. 587–599, 2002.
- [10] A.-G. Wang, “Modern celestial navigation and the key techniques,” *Acta Electronica Sinica*, vol. 35, no. 12, pp. 2347–2353, 2007.

- [11] G. X. Shen and J. F. Sun, *Application of Data Fusion Theory in SINS/CNS/GPS Integrated Navigation Systems*, Defence Industry Press, Beijing, China, 2010.
- [12] T. Gao, H. Ge, J. Rao, Z. Gong, and J. Luo, "Design of double ducted tilting UAV navigation system based on multi-sensor information fusion," in *Proceedings of the IEEE International Conference on Multisensor Fusion and Integration for Intelligent Systems (MFI '12)*, pp. 439–444, Hamburg, Germany, September 2012.
- [13] G. Oppenheim, A. Philippe, and J. de Rigal, "The particle filters and their applications," *Chemometrics and Intelligent Laboratory Systems*, vol. 91, no. 1, pp. 87–93, 2008.
- [14] M. Tanaka, "Reformation of particle filters in simultaneous localization and mapping problems," *International Journal of Innovative Computing, Information and Control*, vol. 5, no. 1, pp. 119–128, 2009.
- [15] M. S. Arulampalam, S. Maskell, N. Gordon, and T. Clapp, "A tutorial on particle filters for online nonlinear/non-Gaussian bayesian tracking," *IEEE Transactions on Signal Processing*, vol. 50, no. 2, pp. 174–188, 2002.

## Research Article

# Sensor Fault Tolerant Control of a Fast Steering Mirror System Using Adaptive PI-Based Sliding Mode Observer and Hardware Redundancy

Hongju Wang,<sup>1,2,3</sup> Qiliang Bao,<sup>1,2</sup> Wenshu Yang,<sup>2</sup> Zidong Liu,<sup>1,2</sup> and Jing Tian<sup>1,2</sup>

<sup>1</sup>Key Laboratory of Optical Engineering, Chinese Academy of Sciences, Mailbox 350, Chengdu 610209, China

<sup>2</sup>Institute of Optics and Electronics, Chinese Academy of Sciences, Mailbox 350, Chengdu 610209, China

<sup>3</sup>University of Chinese Academy of Sciences, Beijing 100191, China

Correspondence should be addressed to Hongju Wang; [ioe-whj@163.com](mailto:ioe-whj@163.com)

Received 24 June 2014; Accepted 1 September 2014

Academic Editor: Ke Zhang

Copyright © 2015 Hongju Wang et al. This is an open access article distributed under the Creative Commons Attribution License, which permits unrestricted use, distribution, and reproduction in any medium, provided the original work is properly cited.

The aim of this paper is to present a sensor fault-tolerant control (FTC) scheme for a two-axis fast steering mirror (FSM) system with minimum power consumption and without changing the controller structure. In this paper, an adaptive PI-based sliding mode observer (APISMO) is adopted firstly to estimate the fault signal, which does not require any prior knowledge of the fault. The estimation is then used by the fault isolation logic to identify the fault. The redundant sensor would be powered up to replace the faulty one when faults occur. During the backup sensor booting up, for maintaining the normal performance of the closed-loop system approximately, a fault-free estimation of the position provided by the APISMO is used as feedback signal. Experimental studies on a prototype system show that the proposed APISMO can effectively reconstruct the fault signals even when the two primary position sensors are faulty simultaneously. Meanwhile, the effectiveness and performance of the proposed scheme have been verified.

## 1. Introduction

The fast steering mirror (FSM) system is popularly applied in situations that require a precision positioning, such as space telescopes, adaptive optics, and free-space optical (FSO) communications [1–3]. In most of the applications, the FSM is adopted to steer the optical beam precisely. Extensive researches have been carried out to improve the closed-loop performance of FSM [4–6]. Most of the control strategies depend on reliable sensor measurements. However, these sensors are usually affected by failures such as offset, drift, and disconnection, which would obviously result in overall performance deterioration. Therefore, it is desirable to develop a sensor FTC scheme for FSM.

To maintain a high level of reliability, the hardware redundancy-based technique has been widely used by the FSM system designed for space application [2, 3, 7]. Because of mass and power constraints, it is still a challenge to design a FTC scheme that provides required reliability with

minimum hardware redundancy. In addition, most sensors and actuators have moving parts and life limited components. Another challenge is determining whether the redundant sensors could be kept unpowered and activated only when necessary [8].

Many approaches have been proposed to overcome the aforementioned problems [9–13]. Among them, the analytical redundancy method is particularly effective. By developing mathematical model of the system, analytical redundancy approach could generate estimations of the measurable or unmeasured variables. The estimations can be used to replace the redundant hardware sensors or design fault diagnosis (FD) scheme. To design an active FTC scheme, the first step is to implement a FD scheme to monitor the system and isolate the fault. Adaptive observer-based FD and sliding mode observer-based FD are two extensively studied methods [14–19]. When the faulty physical sensor has been detected and isolated, its measurement would be replaced by the

estimation, which is the so-called virtual sensor. A fault reconstruction scheme using sliding mode observer is also given in [18, 20, 21]. FTC scheme in terms of correcting the measured output signals using reconstructed fault signals is considered in [17, 21, 22]. However, neither the virtual sensor nor measurement corrected by reconstructed signal is as accurate as the fault-free physical sensor. FTC schemes with only analytical redundancy would have a degraded performance in case of sensor faults. That is one of the reasons why the advanced analytical redundancy-based FTC methods have not been really accepted by the aerospace end-users [23].

This paper develops a FTC scheme for the FSM by combining the sliding mode observer-based method and hardware redundancy. The proposed method could improve the performance of the FSM system with faulty sensors and make it more acceptable to the end-users. A FSM model is firstly developed. Based on the FSM model, an APISMO building on the work [20] is proposed to reconstruct the sensor faults faithfully. Different from the observer used in [20], the discontinuous switching function used in conventional SMO is replaced with an adaptive PI function [24, 25]. The proposed APISMO does not require any prior knowledge of the faults. The reconstructed information is then used by the fault isolation logic to identify the fault and power up the redundant sensors. The redundant sensors are kept unpowered in fault-free case, which reduces the power consumption. However, a period of time is required to activate the backup sensors, during which the measurement of the backup is uncertain. In this proposed scheme, a fault-free estimation of the position provided by the APISMO is used as feedback signal to maintain the desired performance during the cold backup booting-up.

From an industrial perspective, the proposed scheme here is easier to be implemented than the conventional SMO. It does not need to know the bounds of the faults and could maintain the desired fault-free performance in failure case. Compared with the FSM using triple modular redundancy (TMR), the proposed scheme could maintain a higher level of reliability with only dual redundancy. Moreover, the redundant sensors are unpowered in fault-free case. Furthermore, the controller structure does not need to be changed in failure case.

This paper is organized as follows. In Section 2, the considered FSM system and its dynamics model are described. Section 3 presents the fault estimation method based on the proposed APISMO. Section 4 introduces the proposed FTC scheme with the hardware redundancy and the fault isolation logic. Experimental results of the proposed scheme are given in Section 5, followed by some concluding remarks in Section 6.

## 2. FSM Model

**2.1. System Description.** A FSM is generally defined as a mirror mounted to a flexure support system and driven by actuators [6]. The prototype of a two-axis FSM is shown in Figure 1. It consists of six important components: a mirror assembly, a flexure suspension, a mirror base, voice coil

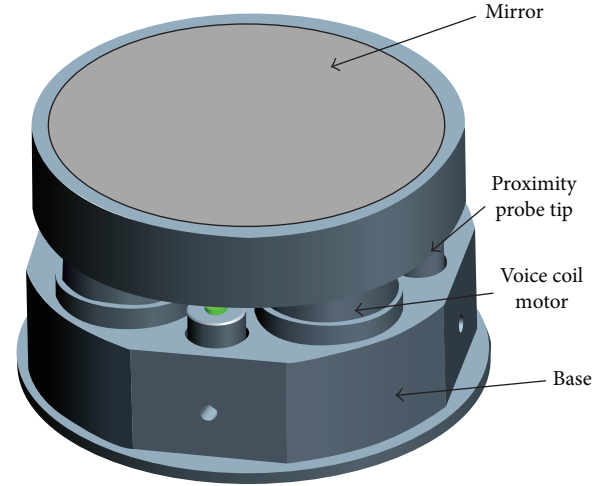


FIGURE 1: Prototype of the fast steering mirror.

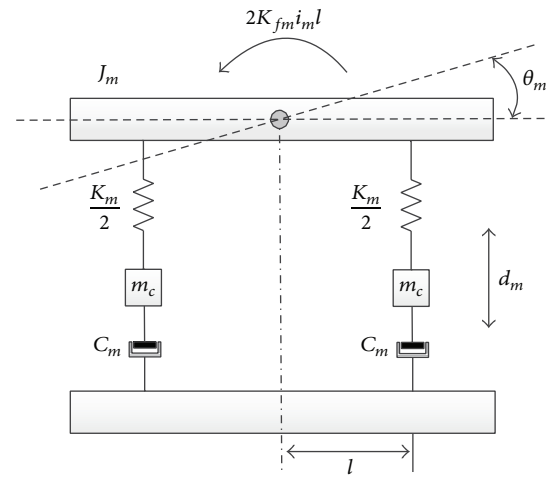


FIGURE 2: Schematic diagram of FSM in single axis.

motors (VCMs), proximity sensors, and drive electronics. Two voice-coils operating in push-pull manner are fixed on the back of the mirror, rotating the mirror about the axis that bisects them. Therefore, two actuator pairs are used to produce two orthogonal rotations  $(\theta_x, \theta_y)$ . A flexure suspension system is used to support the mirror carrier which holds the mirror. This system allows free rotation about orthogonal  $x$ - and  $y$ -axes while constraining piston, side-to-side, and rotation about the normal axis [26].

**2.2. Dynamics Model.** To establish the dynamics model of a two-axis FSM, it is assumed that the motions rotating about the two orthogonal  $x$ - and  $y$ -axes are decoupling with each other. The  $x$ -axis motion and  $y$ -axis motion follow the same working principle. The motions can be equivalently represented by a sketch of spring-mass-dashpot system shown in Figure 2 [27]. The dynamics model of the two-axis FSM can be given as

$$(J_m + 2m_c l^2) \ddot{\theta}_m + 2C_m l^2 \dot{\theta}_m + K_m \theta_m = 2K_{fm} i_m l, \quad (1)$$

where  $m = x$  or  $y$ ; here  $J_m$  is moment of inertia of the mirror rotating about  $x$ - or  $y$ -axis. Parameters  $m_c$ ,  $l$ ,  $\theta_m$ ,  $C_m$ , and  $K_m$  represent mass of the voice-coil, the distance between actuator and the axis, deflection angle, damping coefficient, and spring constant, respectively;  $K_{fm}$  is the force constant and  $i_m$  denotes the driving current.

The actuator driver receives voltage commands from the controller and converts them to driving current. Its dynamical characteristics satisfy Kirchhoff's voltage law

$$U_m = L_m \frac{di_m}{dt} + i_m R_m + k_b \dot{d}_m, \quad (2)$$

where  $U_m$  is the voltage and parameters  $L_m$ ,  $R_m$ ,  $k_b$ , and  $d_m$  represent the coil inductance, coil resistance, back electromotive force constant, and the displacement of the coil.

The deflection angle is generally very small; thus the displacement of the coil  $d_m$  can be approximated as a function of the deflection angle  $\theta_m$ ; that is,  $d_m = l\theta_m$ . Substituting (2) into (1) yields

$$\begin{aligned} & L_m (J_m + 2m_c l^2) \ddot{\theta}_m + [2L_m C_m l^2 + R_m (J_m + 2m_c l^2)] \\ & \times \dot{\theta}_m + (2k_{fm} k_b l^2 + L_m k_m + 2R_m C_m l^2) \\ & \times \theta_m + R_m k_m \theta_m = 2k_{fm} l U_m. \end{aligned} \quad (3)$$

Rewrite (3) in a state-space form as

$$\dot{X}(t) = AX(t) + Bu(t), \quad (4)$$

$$X(t) = [x_1(t), x_2(t), x_3(t), y_1(t), y_2(t), y_3(t)]^T = [\theta_x(t), \dot{\theta}_x(t), \ddot{\theta}_x(t), \theta_y(t), \dot{\theta}_y(t), \ddot{\theta}_y(t)]^T,$$

$$A = \begin{bmatrix} 0 & 1 & 0 & 0 & 0 & 0 \\ 0 & 0 & 1 & 0 & 0 & 0 \\ \frac{-R_x k_x}{L_x (J_x + 2m_c l^2)} & \frac{-2k_{fx} k_b l^2 + L_x k_x + 2R_x C_x l^2}{L_x (J_x + 2m_c l^2)} & \frac{2L_x C_x l^2 + R_x (J_x + 2m_c l^2)}{L_x (J_x + 2m_c l^2)} & 0 & 0 & 0 \\ 0 & 0 & 0 & 0 & 0 & 0 \\ 0 & 0 & 0 & 0 & 0 & 0 \\ 0 & 0 & 0 & 0 & 0 & 0 \end{bmatrix}, \quad B = \begin{bmatrix} 0 & 0 \\ \frac{2k_{fx} l}{L_x (J_x + 2m_c l^2)} & 0 \\ 0 & 0 \\ 0 & 0 \\ 0 & \frac{2k_{fy} l}{L_y (J_y + 2m_c l^2)} \end{bmatrix}, \quad (5)$$

### 3. APISMO Design and Fault Reconstruction

In order to reconstruct the sensor fault signal, an APISMO based on the dynamics model (4) is proposed in this section. For better understanding, the preliminaries and design of the conventional SMO are introduced firstly.

**3.1. Preliminaries.** This section introduces the preliminaries for using a SMO to reconstruct sensor faults. Consider the following linear system affected by sensor faults:

$$\dot{X}(t) = AX(t) + Bu(t), \quad (6)$$

$$Y(t) = CX(t) + Ff_i(t), \quad (7)$$

where  $A \in \mathbb{R}^{n \times n}$ ,  $B \in \mathbb{R}^{n \times m}$ ,  $C \in \mathbb{R}^{p \times n}$ , and  $F \in \mathbb{R}^{p \times r}$ . The matrices  $C$  and  $F$  are full row and column rank, respectively.

The function  $f_i(t)$  is unknown but bounded sensor fault signal.

An effective way to reconstruct the sensor fault  $f_i(t)$  is introducing a filter first [18, 22]. Define a new state  $Z_f$ , satisfying

$$\dot{Z}_f(t) = -A_f Z_f(t) + A_f Y(t), \quad (8)$$

where  $-A_f \in \mathbb{R}^{p \times p}$  is a stable matrix. Substituting (7) into (8) yields

$$\dot{Z}_f(t) = -A_f Z_f(t) + A_f CX(t) + A_f Ff_i(t). \quad (9)$$

By combining (6) and (9) and defining new states  $X_a = \text{col}(X(t), Z_f(t))$ , an augmented system can be given as

$$\begin{aligned} \underbrace{\begin{bmatrix} \dot{X}(t) \\ \dot{Z}_f(t) \end{bmatrix}}_{X_a} &= \underbrace{\begin{bmatrix} A & 0 \\ A_f C & -A_f \end{bmatrix}}_{A_a} \underbrace{\begin{bmatrix} X(t) \\ Z_f(t) \end{bmatrix}}_{X_a} + \underbrace{\begin{bmatrix} B \\ 0 \end{bmatrix}}_{B_a} u(t) \\ &+ \underbrace{\begin{bmatrix} 0 \\ A_f F \end{bmatrix}}_{F_a} f_i(t), \quad (10) \\ Z_f(t) &= \underbrace{\begin{bmatrix} 0 & I_p \\ C_a & \end{bmatrix}}_{C_a} \underbrace{\begin{bmatrix} X(t) \\ Z_f(t) \end{bmatrix}}_{X_a}. \end{aligned}$$

**3.2. Conventional Sliding Mode Observer for Fault Reconstruction.** Considering the new dynamical system in (10), the conventional SMO is constructed as [20]

$$\dot{\hat{X}}_a = A_a \hat{X}_a + B_a u(t) - G_l e_y(t) + G_n v. \quad (11)$$

In (11), the discontinuous term  $v$  is

$$v = \begin{cases} -\rho \|F_2\| \frac{P_0 e_y}{\|P_0 e_y\|} & \text{if } e_y \neq 0, \\ 0 & \text{otherwise,} \end{cases} \quad (12)$$

where  $e_y = C_a \hat{X}_a - Z_f$  is the output estimation error and  $P_0$  is a symmetric positive definite (s.p.d.) matrix. The matrices  $G_l, G_n, F_2$ , and  $P_0$  will be described later. The scalar  $\rho$  must be upper bound on the faults.

It has been proven in [20] that a SMO of the form (11) and (12) which is not affected by the fault  $f_i(t)$  exists if and only if

$$(A1) \text{ rank}(C_a F_a) = r,$$

$$(A2) \text{ invariant zeros of } (A_a, F_a, C_a) \text{ are stable.}$$

Then if the assumptions (A1) and (A2) are satisfied [20], there exists a change of coordinates  $X_a = T_a X_a$ , in which the new triple  $(\bar{A}_a, \bar{F}_a, \bar{C}_a)$  has the following structure:

$$\begin{aligned} \bar{A}_a &= \begin{bmatrix} A_{11} & A_{12} \\ A_{21} & A_{22} \end{bmatrix}, & \bar{F}_a &= \begin{bmatrix} 0 \\ F_2 \end{bmatrix}, \\ \bar{C}_a &= [0 \quad I_p], \end{aligned} \quad (13)$$

where  $A_{11} \in R^{n \times n}$  is a stable matrix,  $A_{12} \in R^{n \times p}$ ,  $A_{21} \in R^{p \times n}$ ,  $A_{22} \in R^{p \times p}$ ,  $F_2 \in R^{p \times r}$ .

Considering the structure (13), the observer gains in (11) can be obtained as

$$G_l = T_a^{-1} \begin{bmatrix} A_{12} \\ A_{22} - A_s \end{bmatrix}, \quad G_n = T_a^{-1} \begin{bmatrix} 0 \\ I_p \end{bmatrix}, \quad (14)$$

where  $A_s$  is a stable matrix which is chosen to make  $(A_a - G_l C_a)$  stable. The matrix  $P_0$  is the unique solution to the Lyapunov equation of  $A_s$  [20].

On condition that the assumptions (A1) and (A2) are satisfied, it could be shown that an ideal sliding motion takes place on the surface (15) in finite time:

$$S_0 = \{e : C_a e = 0\}. \quad (15)$$

During the ideal sliding motion,  $e_y = 0$  and  $\dot{e}_y = 0$ , the discontinuous signal  $v$  will take on average a value to compensate for the fault signal while maintaining a sliding motion [20, 22]. The average quantity can be computed online as

$$v_\delta = -\rho \|F_2\| \frac{P_0 e_y}{\|P_0 e_y\| + \delta}, \quad (16)$$

where  $\delta$  is a small positive scalar.

Consequently, a fault reconstruction signal is

$$\hat{f}_i(t) \approx -\rho \|F_2\| (F_2^T F_2)^{-1} F_2^T \frac{P_0 e_y}{\|P_0 e_y\| + \delta}. \quad (17)$$

For details, see [20, 22].

In fact, design of the conventional SMO needs to know the upper bounds of the faults in advance. However, in practice, these bounds are difficult to obtain. Many literatures take an approximate upper estimation of the faults signal as scalar  $\rho$ . However, some additional dynamics would be introduced by this method. Moreover, if the fault is larger than the scalar  $\rho$ , the conventional method cannot reconstruct the fault properly.

**3.3. APISMO Design and Fault Reconstruction.** To overcome the problems associated with the conventional SMO, an APISMO building on the conventional SMO is proposed by replacing the saturation function in (16) with a continuous term determined by an adaptive PI algorithm. The proposed APISMO has the same structure with the observer in Section 3.2, except that the saturation function is replaced with an adaptive PI function.

The proposed PI function in APISMO takes the sliding surface function  $S_0$  as the input. The PI function is defined as

$$v_{PI} = k_p e_y(t) + k_i \int e_y(t) dt, \quad (18)$$

where the sliding surface function  $C_a e = e_y$  and  $k_p$  and  $k_i$  are the proportional gain and integral gain.

Substitute (18) into (11) and take a change of coordinates  $\hat{X} = [\hat{x}_1 \quad \hat{x}_2]^T = T_a \hat{X}_a$ . In the new coordinate system, the APISMO can be defined as

$$\begin{aligned} \dot{\hat{x}}_1(t) &= A_{11} \hat{x}_1(t) + A_{12} \hat{x}_2(t) + B_1 u(t) - A_{12} e_y(t), \\ \dot{\hat{x}}_2(t) &= A_{21} \hat{x}_1(t) + A_{22} \hat{x}_2(t) + B_2 u(t) \\ &\quad - (A_{22} - A_s) e_y(t) + v_{PI}, \end{aligned} \quad (19)$$

$$\hat{Y}(t) = \hat{x}_2(t).$$

In the new coordinate system, defining new states  $X = [x_1, x_2]^T = T_a X_a$ , then the dynamical system given by (10) has a structure as

$$\begin{aligned} \begin{bmatrix} \dot{x}_1(t) \\ \dot{x}_2(t) \end{bmatrix} &= \begin{bmatrix} A_{11} & A_{12} \\ A_{21} & A_{22} \end{bmatrix} \begin{bmatrix} x_1(t) \\ x_2(t) \end{bmatrix} + \begin{bmatrix} B_1 \\ B_2 \end{bmatrix} u(t) + \begin{bmatrix} 0 \\ F_2 \end{bmatrix} f_i(t), \\ Y(t) &= [0 \quad I_p] \begin{bmatrix} x_1(t) \\ x_2(t) \end{bmatrix}. \end{aligned} \quad (20)$$

Define the state vector of the estimation error as

$$E = [e_1 \ e_2]^T = \widehat{X} - X = [\widehat{x}_1 - x_1 \ \widehat{x}_2 - x_2]^T. \quad (21)$$

By taking the first derivative of (21) and substituting (19) and (20), we have

$$\dot{e}_1(t) = A_{11}e_1(t), \quad (22)$$

$$\begin{aligned} \dot{e}_y(t) = & A_{21}e_1(t) + A_s e_y(t) + k_p e_y(t) \\ & + k_i \int e_y(t) dt - F_2 f_i(t), \end{aligned} \quad (23)$$

where  $e_y(t) = e_2(t)$  in this situation.

For reconstructing sensor faults properly, the sliding surface  $S_0$  in (15) must be reachable. The reachability of the sliding surface  $S_0$  is determined by the proportional gain  $k_p$  and integral gain  $k_i$  according to the following theorem.

**Theorem 1.** *Under the assumptions (A1) and (A2), for the error system given by (22) and (23), the sliding mode surface  $S_0$  in (15) is asymptotically reachable, that is,  $e_y \rightarrow 0$  as  $t \rightarrow \infty$ , if and only if  $k_i \neq 0$  and the roots of*

$$s^2 - A_s s - k_p s - k_i = 0 \quad (24)$$

have negative real parts, where  $s$  is the Laplace transform operator.

*Proof.* Considering that most aerospace systems have self-testing at startup, it is reasonable to assume that there exist no faults at initial time. Therefore,  $f_i(t)$  has zero initial value and  $e_1(t)$  could have a nonzero initial value, then decomposing  $e_1(t)$  as

$$e_1(t) = e_{10}(0) + e_{11}(t), \quad (25)$$

where  $e_{10}(0) \equiv e_1(0)$  is the initial value of  $e_1(t)$  and  $e_{11}(t)$  is the other part of  $e_1(t)$  and has zero initial value.

Substituting (25) into (23) yields

$$\begin{aligned} \dot{e}_y(t) = & A_{21}e_{10}(0) + A_{21}e_{11}(t) + A_s e_y(t) + k_p e_y(t) \\ & + k_i \int e_y(t) dt - F_2 f_i(t). \end{aligned} \quad (26)$$

The system defined by (26) can be regarded as a linear system with three inputs, that is,  $e_{10}(0)$ ,  $e_{11}(t)$ , and  $f_i(t)$ . Then this linear system could be decomposed into three subsystems. Each subsystem takes one of the inputs, that is,  $e_{10}(0)$ ,  $e_{11}(t)$ , and  $f_i(t)$ , as its input while its output being a part of  $e_y(t)$ , that is,  $e_{yn}(t)$ ,  $n = 1, 2, 3$ . For the sliding mode surface  $S_0$  in (15) to be asymptotically reachable, that is,  $e_y \rightarrow 0$  as  $t \rightarrow \infty$ , the error system (26) must be stable. That is, all the three subsystems must be stable. Following that, each subsystem is examined.

The first subsystem has  $e_{11}(t)$  as input and  $e_{y1}(t)$  as output. The transfer function can be obtained as

$$\frac{e_{y1}(s)}{e_{11}(s)} = \frac{sA_{21}}{s^2 - A_s s - k_p s - k_i}. \quad (27)$$

It can be seen that the first subsystem (27) is asymptotically stable if and only if the roots of (24) have negative real parts and  $k_i \neq 0$ .

According to the assumptions (A1) and (A2), the matrix  $A_{11}$  is stable, and then  $e_{11}(\infty) \rightarrow 0$ . Applying the final value theorem to  $e_{y1}(s)$  yields

$$e_{y1}(\infty) = \lim_{s \rightarrow 0} \frac{s * sA_{21}e_{11}(s)}{s^2 - A_s s - k_p s - k_i} = 0. \quad (28)$$

It is easy to find that the remaining two subsystems are asymptotically stable if and only if the roots of (24) have negative real parts and  $k_i \neq 0$  and

$$e_{y2}(\infty) = 0, \quad e_{y3}(\infty) = 0. \quad (29)$$

Therefore, the error system given by (23) or (26) is asymptotically stable if and only if the roots of (24) have negative real parts and  $k_i \neq 0$ . Given the stability condition is satisfied, then

$$e_y(\infty) = e_{y1}(\infty) + e_{y2}(\infty) + e_{y3}(\infty) = 0. \quad (30)$$

That is, the sliding mode surface  $S_0$  in (15) is asymptotically reachable.

According to Theorem 1, for a given proportional gain  $k_p$  of the APISMO, there exists a nonzero integral gain  $k_i^*$  such that the sliding surface (15) is asymptotically reachable; that is, with  $v_{PI} = k_p e_y(t) + k_i^* \int e_y(t) dt$ , the condition  $\dot{S}_0 S_0 < -\eta |S_0|$  is satisfied, where  $\eta$  is a positive scalar [25].  $\square$

Defining the integral gain estimation error as (31) and a Lyapunov function as (32)

$$\tilde{k}_i = k_i^* - k_i, \quad (31)$$

$$V = \frac{1}{2} (s_0^2 + \alpha \tilde{k}_i^2), \quad (32)$$

where  $\alpha$  is a positive constant. Taking the first derivative of  $V$  yields

$$\dot{V} = s_0 \dot{s}_0 + \alpha \tilde{k}_i \dot{\tilde{k}}_i. \quad (33)$$

Substituting (23) and (31) into (33) results in

$$\begin{aligned} \dot{V} = & e_y(t) \left[ A_{21}e_1(t) + A_s e_y(t) + k_p e_y(t) \right. \\ & \left. + k_i^* \int e_y(t) dt - F_2 f_i(t) \right] \\ & - \tilde{k} e_y(t) \int e_y(t) dt + \alpha \tilde{k}_i \dot{\tilde{k}}_i \\ \leq & -\eta |s_0| - \tilde{k} \left[ e_y(t) \int e_y(t) dt - \alpha \dot{\tilde{k}}_i \right]. \end{aligned} \quad (34)$$

Thus the adaptive law for  $k_i$  can be obtained as

$$\dot{\tilde{k}}_i = \frac{1}{\alpha} e_y(t) \int e_y(t) dt. \quad (35)$$

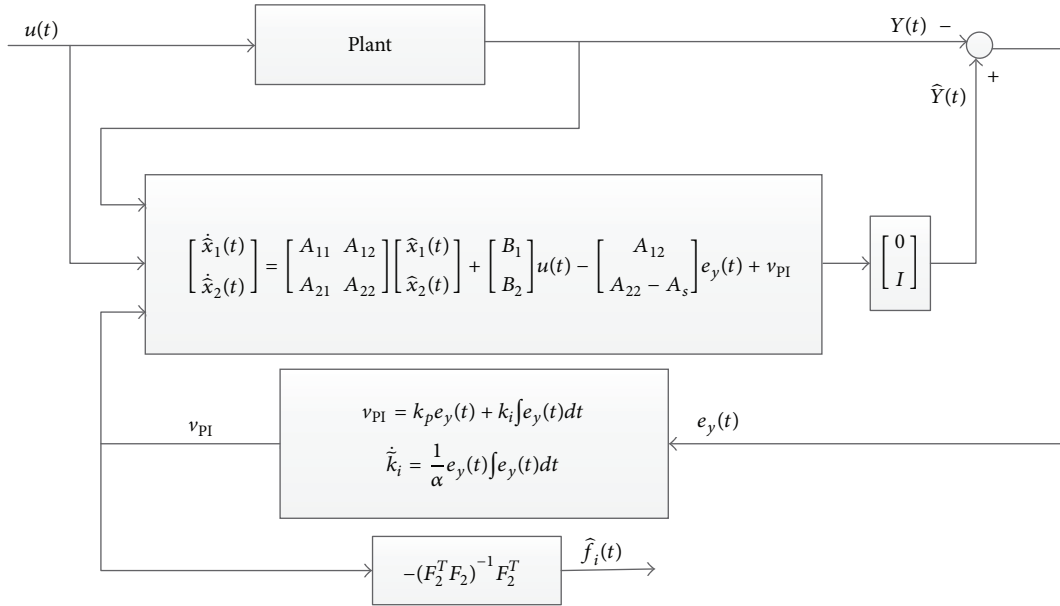


FIGURE 3: Schematic diagram of the proposed APISMO implementation.

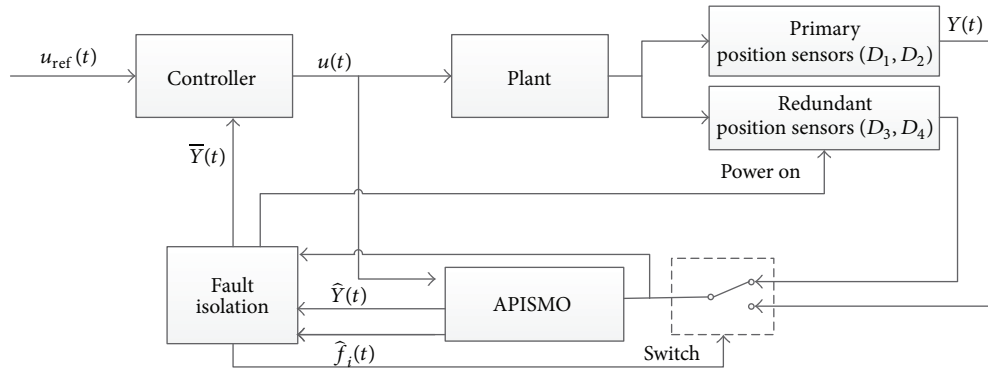


FIGURE 4: Schematic diagram of the proposed FTC scheme.

Finally, the sensor fault can be reconstructed properly by the APISMO as

$$\begin{aligned} \hat{f}_i(t) &\approx -(F_2^T F_2)^{-1} F_2^T v_{PI} \\ &\approx -(F_2^T F_2)^{-1} F_2^T \left[ k_p e_y(t) + k_i \int e_y(t) dt \right], \end{aligned} \quad (36)$$

where the adaptive law for  $k_i$  is

$$\dot{\hat{k}}_i = \frac{1}{\alpha} e_y(t) \int e_y(t) dt = \gamma e_y(t) \int e_y(t) dt, \quad (37)$$

where  $\gamma = 1/\alpha$ .

For better understanding, a schematic representation of the proposed APISMO and fault reconstruction is shown in Figure 3.

#### 4. Fault-Tolerant Control Design

In this section, to improve the performance of the system with only SMO-based FTC scheme, a FTC scheme for FSM is

presented by combining the proposed APISMO and the hardware redundancy. Position sensors installed with dual redundancy are used in the proposed FTC scheme. Figure 4 shows the block diagram of the proposed FTC scheme.

**4.1. Redundancy Design.** At the design stage of the FSM, the sensors were installed with dual redundancy. The redundant sensors are functionally identical to the primary sensors by placing them at symmetrical locations of the primary ones. The placements of the sensors are illustrated in Figure 5.  $D_1$  and  $D_2$  denote the primary sensor probes;  $D_3$  and  $D_4$  are redundant ones. Four proximity probe tips are placed at 90 degrees from each other and 45 degrees from each VCM. The distances between each probe tip and the  $x$ - and  $y$ -axes are equal, which is denoted by  $l$ .

The proximity sensor system provides an output voltage that is directly proportional to the distance between probe tip and the moving mirror. Since deflection angle of the mirror is generally very small, the output voltage of the proximity

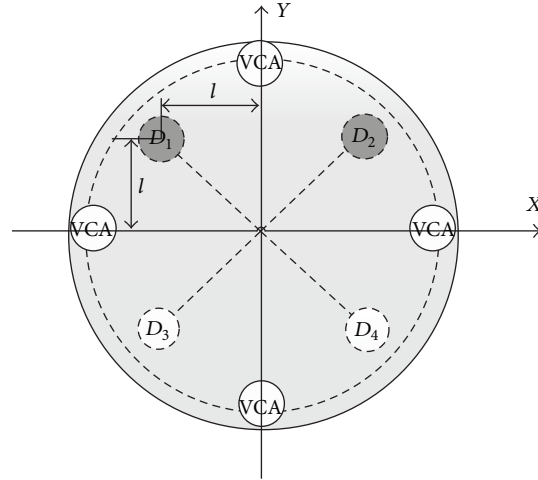


FIGURE 5: The placement of the sensors.

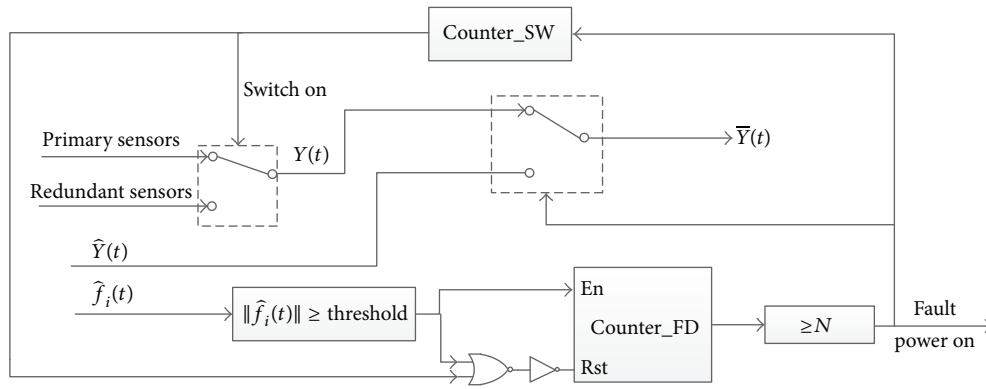


FIGURE 6: Schematic diagram of the fault isolation logic.

sensor system can be used to approximate the deflection angle by the following equation:

$$\begin{aligned} D_1 &= kl(\theta_x + \theta_y), & D_4 &= -kl(\theta_x + \theta_y), \\ D_2 &= kl(\theta_x - \theta_y), & D_3 &= -kl(\theta_x - \theta_y), \end{aligned} \quad (38)$$

where  $D_1, D_2, D_3$ , and  $D_4$  are the output voltages of the four sensors and  $k$  is the proportional scalar of the sensor.

**4.2. Fault Isolation Logic.** In order to keep the feedback signal used by controller free from sensor faults, fault isolation logic shown in Figure 6 is adopted. In fault-free case, the reconstructed fault signal in (36) is approximately zero. The measurements of the primary sensors are used as feedback signals. If the reconstructed signal exceeds a threshold, the counter Counter\_FD begins to work simultaneously, which is used to obtain information on how long a threshold has been crossed. If the value of the counter is greater than or equal to  $N$  counter-steps, the measurement  $D_i$  is identified to be faulty; a signal would be sent out to power on the redundancy.

Since a period of time is required to activate the cold backup sensor, during the cold backup booting up, the measurement of the backup is uncertain. A fault-free estimation

of the position provided by the APISMO is used as feedback signal to maintain the desired performance. The counter Counter\_SW is used to calculate the activation time and send out switch signal. After the backup is activated, the faulty sensor is replaced by the redundant one and the measurement of the redundant sensor is used as feedback signal.

## 5. Experimental Results

In this section, to validate the effectiveness of the proposed scheme, a series of experimental studies were conducted on a prototype of the FSM.

**5.1. Experimental Setup.** The experimental setup of a FSM system is depicted in Figure 7. The tilt of the mirror relative to the fixed base is measured by four proximity sensors placed as in Figure 5. The proximity sensor system provides a measuring range of 2 mm and an output of 20 V/mm. In addition, an embedded computer MICROSPACE PC/104 (from Digital Logic corp.) equipped with a PC/104 expansion board Diamond-MM-16-AT (from Diamond Systems Corp.) offering 12-bit D/A converter and 16-bit A/D converter is adopted to produce excitation voltage signals and acquire

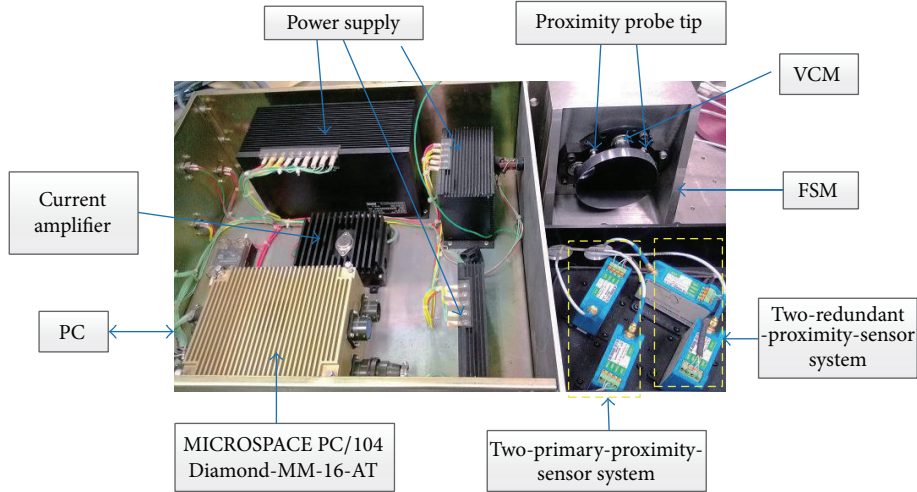


FIGURE 7: Experimental setup of a fast steering mirror system.

the sensor readings. The APISMO, fault isolation logic, and conventional PI control algorithms are developed with MATLAB/Simulink software and downloaded to MICROSPACE PC/104 to realize a real-time fault-tolerant control. The sampling interval used in the experiments is  $200 \mu\text{s}$ .

**5.2. Plant Model Identification.** The mathematical model of the FSM can be identified by using a dynamical signal analyzer. The swept-sine waves applied to the actuators have the amplitude of  $0.3 \text{ V}$  and frequency range of  $1\text{--}2000 \text{ Hz}$ . The position responses of the steering mirror in two orthogonal directions are recorded using a sampling rate of  $5 \text{ kHz}$ . With a push-pull pair of actuators driven, the magnitudes of the output displacement in passive axis are  $20 \text{ dB}$  lower than that in the major axis, which indicates that the two axial motions of the steering mirror are decoupled [28]. Transfer function  $G_{px}$  of the plant rotating about  $x$ -axis can be identified by using the input-output data sets.

The identified third-order transfer function is

$$G_{px}(s) = \frac{275100}{s^3 + 2861s^2 + 155400s + 1.715 \times 10^8}. \quad (39)$$

In the same way, transfer function  $G_{py}$  of the plant rotating about  $y$ -axis can be obtained as

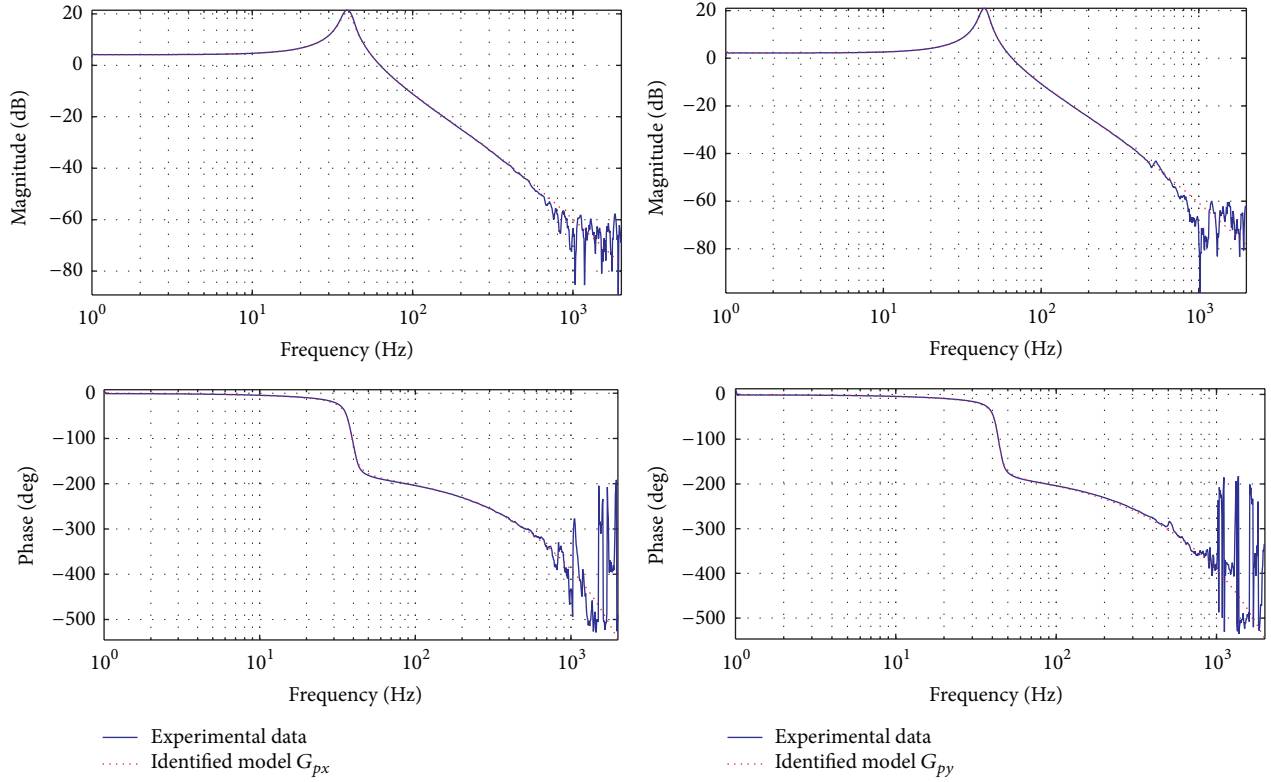
$$G_{py}(s) = \frac{244000}{s^3 + 2543s^2 + 154600s + 1.903 \times 10^8}. \quad (40)$$

The identified models  $G_{px}$  in (39) and  $G_{py}$  in (40) and the frequency responses of the FSM obtained from the experimental data are shown in Figure 8.

Comparing (3) with the inverse Laplace transform of (39) and (40) yields the system matrix  $A$  and input distribution matrix  $B$  of the state-space model (4)

$$A = \begin{bmatrix} 0 & 1 & 0 & 0 & 0 & 0 \\ 0 & 0 & 1 & 0 & 0 & 0 \\ -171500000 & -155400 & -2861 & 0 & 0 & 0 \\ 0 & 0 & 0 & 0 & 1 & 0 \\ 0 & 0 & 0 & 0 & 0 & 1 \\ 0 & 0 & 0 & -190300000 & -154600 & -2543 \end{bmatrix},$$

$$B = \begin{bmatrix} 0 & 0 \\ 0 & 0 \\ 275100 & 0 \\ 0 & 0 \\ 0 & 0 \\ 0 & 244000 \end{bmatrix}.$$


 FIGURE 8: Frequency responses of  $x$ - and  $y$ -axes, respectively.

The fault distribution matrix  $F$  in (7) is defined as  $F = I_2$ . In (38), the scale  $k$  of the proximity sensors is 20 V/mm. The distance between each probe tip and the rotation axis  $l$  is 5.02 cm. Thus, the output matrix  $C$  has the form

$$C = \begin{bmatrix} 1003.94 & 0 & 0 & 1003.94 & 0 & 0 \\ 1003.94 & 0 & 0 & -1003.94 & 0 & 0 \end{bmatrix}. \quad (42)$$

**5.3. Reconstruction of Sensor Faults.** In this section, the fault reconstruction performance of the proposed APISMO is verified by being compared with that of the conventional SMO. A conventional SMO is designed firstly. The influence of filter matrix  $A_f$  on the performance of fault estimation system has been investigated in [29]. Here, the matrix was chosen as  $A_f = 1500I_2$ . It can be seen that system matrix  $A$  given in (41) is stable; therefore, the conditions (A1) and (A2) are satisfied. The design parameters (from (14) and (16)) were chosen as  $A_s = -50I_2$  and  $\delta = 0.1$ . Assuming that the upper bound of the faults is 0.4 mm, the scalar  $\rho$  was set as  $\rho = 8$ . The positive-definite matrix  $P_0$  (from (16)) was selected

by solving the Lyapunov function of  $A_s$ . The associated gains in (14) were obtained as

$$G_l = \begin{bmatrix} 0 & 0 & 0 \\ 0 & 0 & 0 \\ 0 & 0 & 0 \\ 0 & 0 & 0 \\ 0 & 0 & 0 \\ -950 & 0 & 0 \\ 0 & -950 & 0 \\ 0 & 0 & -950 \end{bmatrix}, \quad G_n = \begin{bmatrix} 0 & 0 & 0 \\ 0 & 0 & 0 \\ 0 & 0 & 0 \\ 0 & 0 & 0 \\ 0 & 0 & 0 \\ 1 & 0 & 0 \\ 0 & 1 & 0 \\ 0 & 0 & 1 \end{bmatrix}. \quad (43)$$

The associated gains for the APISMO were the same as that in (43). The parameters for the adaptive PI function were chosen as  $k_p = 1000I_2$ ,  $k_{i\text{-initial}} = I_2$ , and  $\gamma = 0.01$ .

In the experiments, the two primary sensors were corrupted by the faults illustrated in Figure 9 simultaneously. The system is open-loop system. The value of the fault acting on sensor  $D_1$  is smaller than the scalar  $\rho$ , whereas the value of the fault acting on sensor  $D_2$  is larger than the scalar. It is shown in Figure 10 that the proposed APISMO reconstructs the fault faithfully. In comparison, Figure 11 shows the fault signal reconstructed by the conventional SMO. It can be seen from Figures 10(a) and 11(a) that both methods could obtain a very proper reconstruction when the difference between the fault signal and the scalar  $\rho$  is not significant. However, as

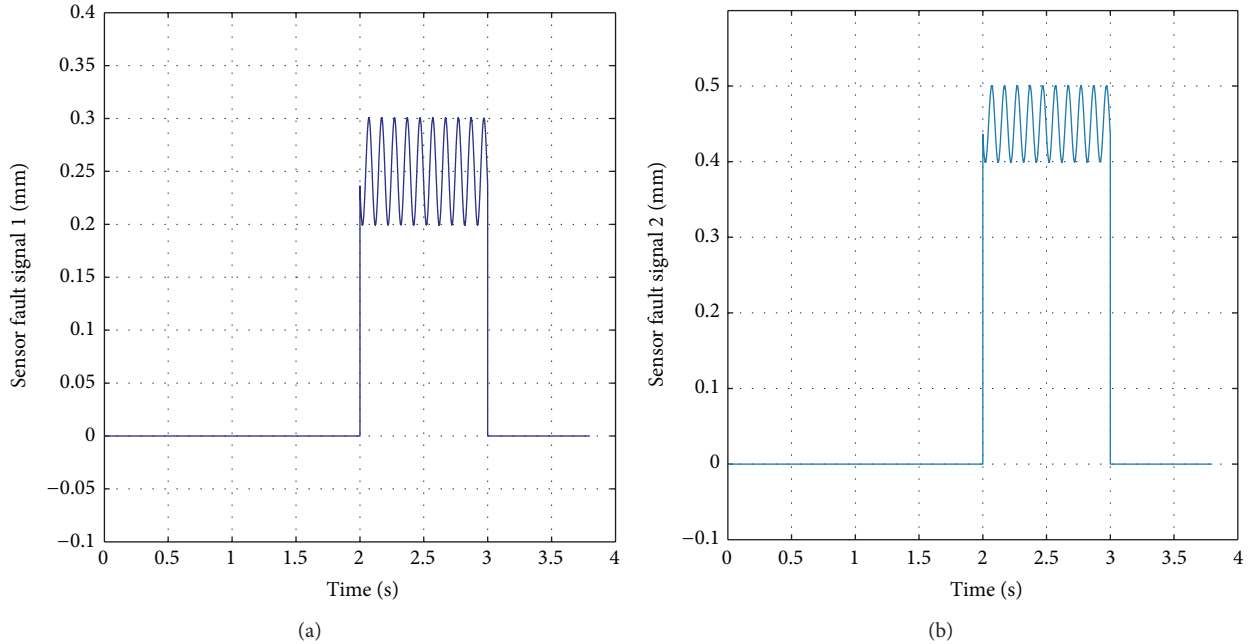


FIGURE 9: (a) Fault acting on sensor  $D_1$ . (b) Fault acting on sensor  $D_2$ .

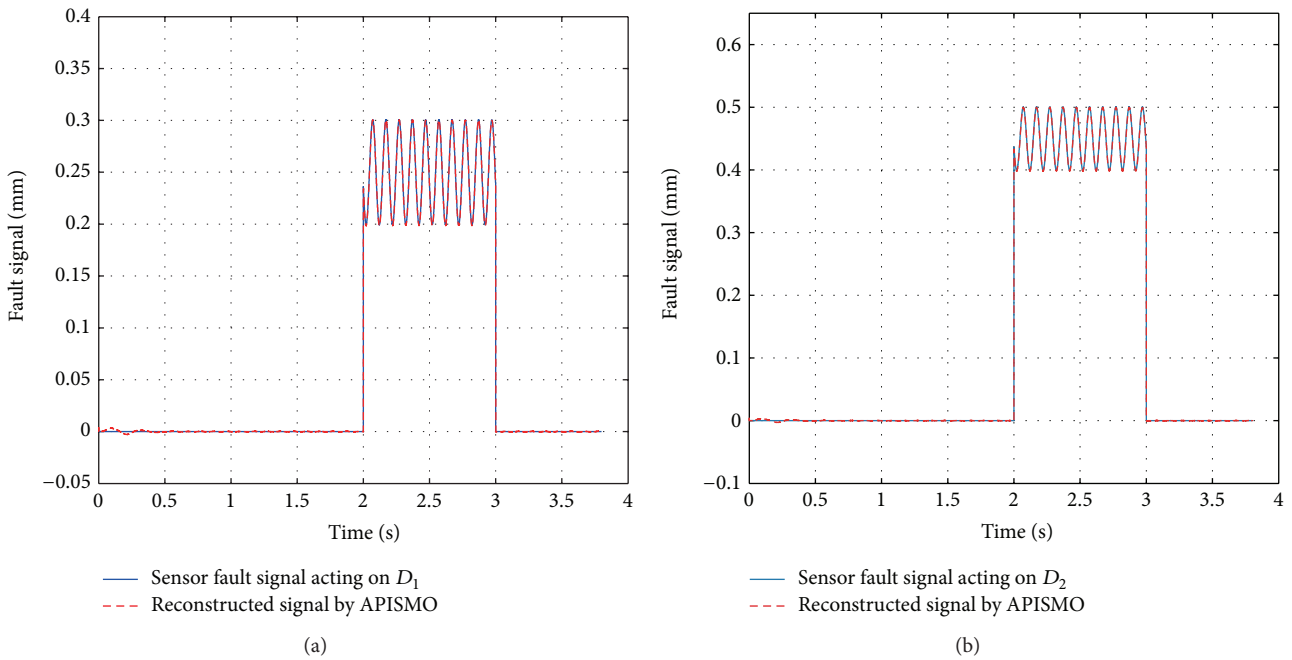


FIGURE 10: (a) Fault acting on sensor  $D_1$  and its reconstruction by APISMO. (b) Fault acting on sensor  $D_2$  and its reconstruction by APISMO.

shown in Figure 11(b), when the fault signal is larger than the scalar  $\rho$ , the conventional SMO cannot reconstruct the fault signal properly.

Figure 12 shows the positions measured by the two primary sensors and the estimated positions provided by APISMO when faults occur. It is observed that, in the presence of faults, the estimated outputs by APISMO are

maintaining the accurate values. Consequently, the performance of the control system could be kept approximately by the estimation during the backup booting up.

5.4. *Fault-Tolerant Control Implementation.* The performance of the proposed FTC scheme is verified by several experimental studies conducted hereinafter.

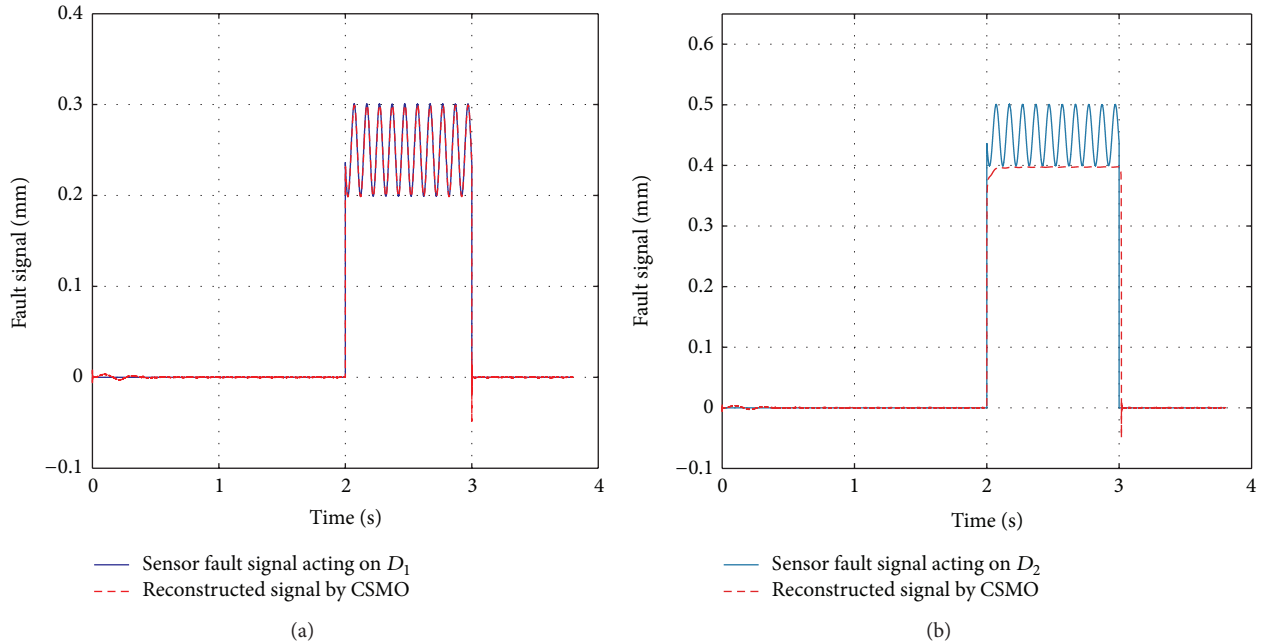


FIGURE 11: (a) Fault acting on sensor  $D_1$  and its reconstruction by conventional SMO (CSMO). (b) Fault acting on sensor  $D_2$  and its reconstruction by conventional SMO (CSMO).

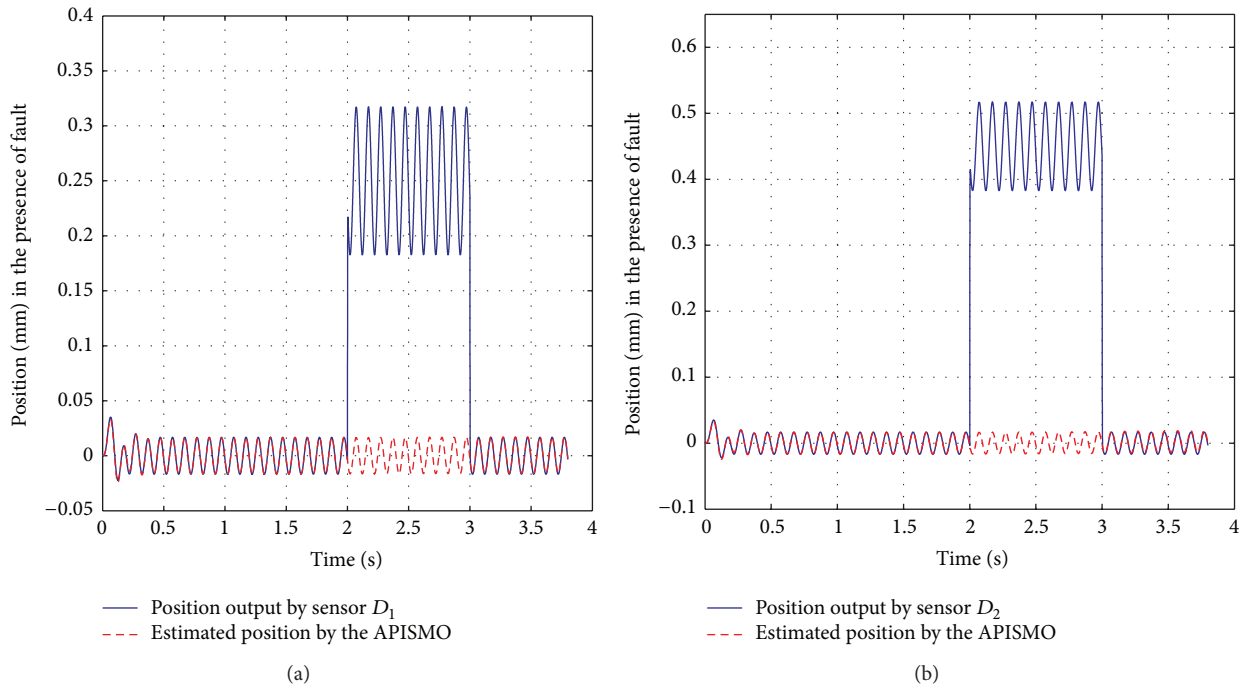


FIGURE 12: (a) Position measured by sensor  $D_1$  and the position estimated by APISMO when fault occurs. (b) Position measured by sensor  $D_2$  and the position estimated by APISMO when fault occurs.

Since the FSM was designed as a decoupled parallel-kinematic structure, for the purpose of validating the proposed FTC scheme, only one traditional PI controller has been designed to handle the mirror rotating about  $x$ -axis. The design parameter for fault isolation was chosen as  $N = 10$  cycles of the counter, equaling 2 ms at 200  $\mu$ s sampling

time. This value represents a reasonable compromise between accuracy and short isolation time. The threshold was chosen as 0.1 V, that is, 5  $\mu$ m. The sensor fault acting on  $D_1$  is shown in Figure 13(a). For the purpose of comparison, Figure 13(b) shows the position tracking error provided by the traditional PI controller in fault-free case. When fault in Figure 13(a) is

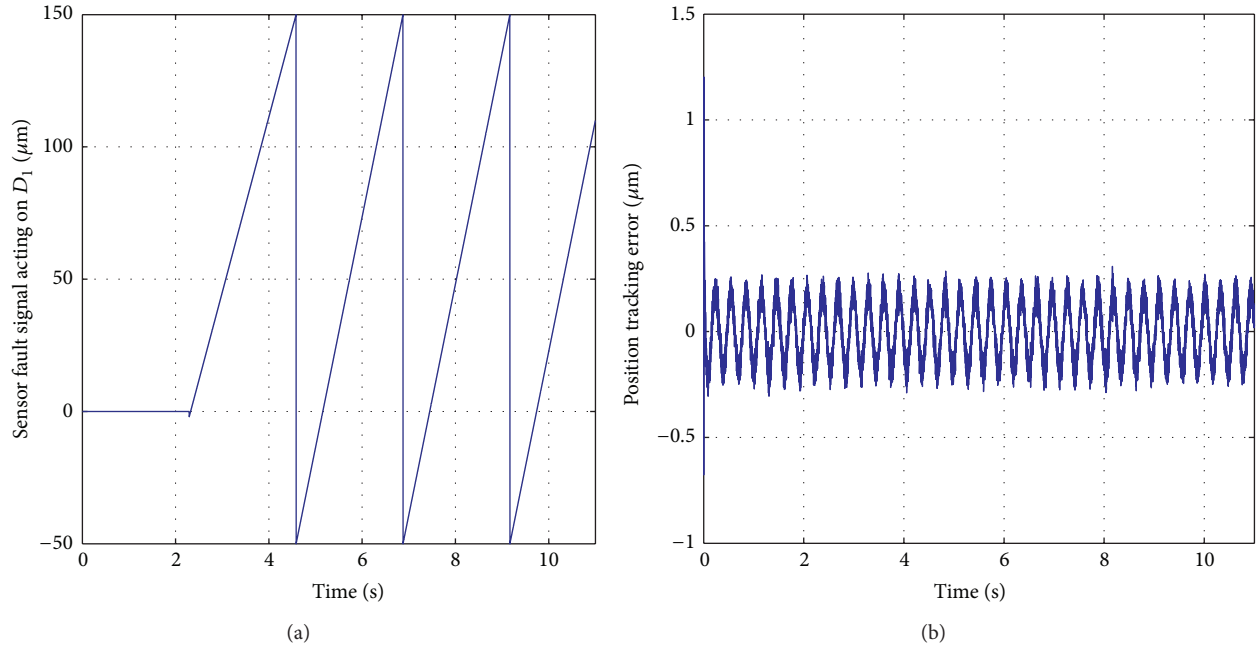


FIGURE 13: (a) Sensor fault signal acting on  $D_1$ . (b) The position tracking error of the PI controller in fault-free case.

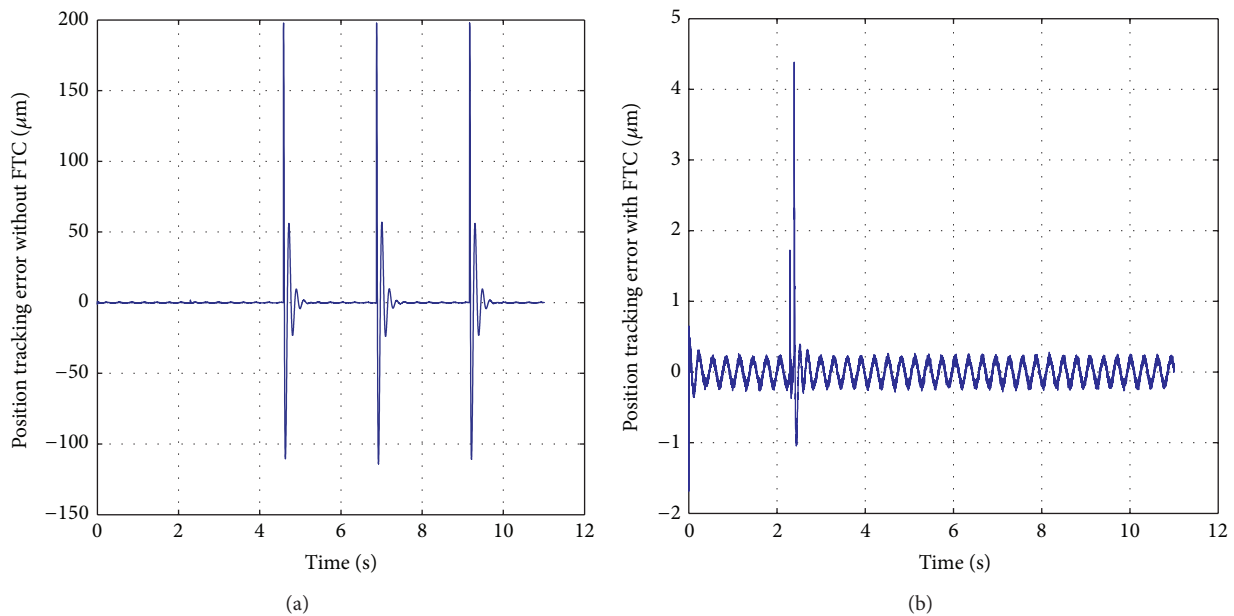


FIGURE 14: The position tracking error in the presence of fault (a) when the FTC scheme is not adopted, (b) when the FTC scheme is implemented.

acting on the primary sensor  $D_1$ , the tracking error provided by the PI controller without the FTC scheme is shown in Figure 14(a). It is obvious that the tracking performance of the control system is degraded.

The proposed FTC scheme illustrated in Figure 4 has been implemented to maintain the desired performance in the presence of sensor fault. The position tracking error of the proposed FTC scheme is shown in Figure 14(b). As

seen in Figure 14(b), when the reconstructed fault signal has exceeded the threshold for about 2 ms, the fault would be detected and isolated by the logic, and the estimation of the position provided by the APISMO would be used by the controller. After the backup is activated, the measurement of the redundant sensor would be used as feedback signal. It can be seen that the proposed FTC scheme could maintain near to desired performance when fault occurs.

## 6. Conclusion

In this paper, a novel FTC scheme for the fast steering mirror system was proposed by integrating an adaptive PI-based sliding mode observer and hardware redundancy. The controller structure did not need to be changed. The proposed scheme adopted an APISMO to reconstruct the fault signal. The advantage of this method is that it does not require any prior knowledge of the faults and has no chattering. The reachability of the sliding surface has been examined. In order to keep the controller free from the sensor faults, fault isolation logic was used to identify the fault and power up the redundant sensor. During the cold backup booting up, the performance of the control system was maintained approximately by estimations of the position provided by the APISMO. Experiments have been conducted to verify the scheme. The experimental results confirmed that FSM system with the proposed FTC scheme could maintain a good tracking despite the presence of the fault.

Since the proposed FTC scheme is easy to be implemented and does not require any prior knowledge of the faults, it can be widely extended to other types of beam control systems. In the experiments, since only the position signal was measured, there was no freedom left to deal with the measurement noises and model uncertainties. Nevertheless, experimental results showed that the effect of the noises and uncertainties on the FTC was not significant. Future works will focus on dealing with measurement noises and model uncertainties.

## Conflict of Interests

The authors declare that there is no conflict of interests regarding the publication of this paper.

## Acknowledgment

This work was supported by Grant no. A09K002 from the Advanced Research Foundation of the Key Laboratory, Chinese Academy of Sciences.

## References

- [1] R. Zhang, J. Wang, G. Zhao, and J. Lv, "Fiber-based free-space optical coherent receiver with vibration compensation mechanism," *Optics Express*, vol. 21, no. 15, pp. 18434–18441, 2013.
- [2] M. Ostaszewski and W. Vermeer, "Fine steering mirror for the James Webb Space Telescope," in *New Developments in Optomechanics*, vol. 6665, p. D6650, 2007.
- [3] A. Bullard and I. Shawki, "Responder fast steering mirror," in *Sensors, Systems, and Next-Generation Satellites XVII*, vol. 8889 of *Proceedings of SPIE*, 2013.
- [4] T. Tang, Y. Huang, C. Fu, and S. Liu, "Acceleration feedback of a CCD-based tracking loop for fast steering mirror," *Optical Engineering*, vol. 48, no. 1, Article ID 013001, 2009.
- [5] T. Tang, R. Ge, J. Ma, and C. Fu, "Compensating for some errors related to time delay in a charge-coupled-device-based fast steering mirror control system using a feedforward loop," *Optical Engineering*, vol. 49, no. 7, Article ID 073005, 2010.
- [6] X. Wu, S. Chen, B. Shi, W. Chen, and X. Xiong, "High-powered voice coil actuator for fast steering mirror," *Optical Engineering*, vol. 50, no. 2, Article ID 023002, 2011.
- [7] I. Pain, B. Stobie, G. S. Wright, T. A. Paul, and C. R. Cunningham, "The SPIRE beam steering mirror: a cryogenic 2 axis mechanism for the Herschel space observatory," in *IRSpace Telescopes and Instruments, Parts 1 and 2*, vol. 4850, pp. 619–627, 2003.
- [8] D. Gorinevsky, G. M. Hoffmann, M. Shmakova, R. W. Mah, S. Cryan, and J. D. Mitchell, "Fault tolerance of relative navigation sensing in Docking approach of spacecraft," in *Proceedings of the IEEE Aerospace Conference (AC '08)*, pp. 1–9, March 2008.
- [9] J. Blesa, D. Rotondo, V. Puig, and F. Nejjari, "FDI and FTC of wind turbines using the interval observer approach and virtual actuators/sensors," *Control Engineering Practice*, vol. 24, no. 1, pp. 138–155, 2014.
- [10] B. Tabbache, M. E. H. Benbouzid, A. Kheloui, and J.-M. Bourgeot, "Virtual-sensor-based maximum-likelihood voting approach for fault-tolerant control of electric vehicle powertrains," *IEEE Transactions on Vehicular Technology*, vol. 62, no. 3, pp. 1075–1083, 2013.
- [11] J.-C. Ponsart, D. Theilliol, and C. Aubrun, "Virtual sensors design for active fault tolerant control system applied to a winding machine," *Control Engineering Practice*, vol. 18, no. 9, pp. 1037–1044, 2010.
- [12] S. Anwar and L. Chen, "An analytical redundancy-based fault detection and isolation algorithm for a road-wheel control subsystem in a steer-by-wire system," *IEEE Transactions on Vehicular Technology*, vol. 56, no. 5, pp. 2859–2869, 2007.
- [13] N. Venkateswaran, M. S. Siva, and P. S. Goel, "Analytical redundancy based fault detection of gyroscopes in spacecraft applications," *Acta Astronautica*, vol. 50, no. 9, pp. 535–545, 2002.
- [14] K. Zhang, B. Jiang, and P. Shi, "Observer-based integrated robust fault estimation and accommodation design for discrete-time systems," *International Journal of Control*, vol. 83, no. 6, pp. 1167–1181, 2010.
- [15] K. Zhang, B. Jiang, and P. Shi, "Fast fault estimation and accommodation for dynamical systems," *IET Control Theory & Applications*, vol. 3, no. 2, pp. 189–199, 2009.
- [16] K. Zhang, B. Jiang, and V. Cocquempot, "Adaptive observer-based fast fault estimation," *International Journal of Control, Automation and Systems*, vol. 6, no. 3, pp. 320–326, 2008.
- [17] H. Alwi and C. Edwards, "Fault detection and fault-tolerant control of a civil aircraft using a sliding-mode-based scheme," *IEEE Transactions on Control Systems Technology*, vol. 16, no. 3, pp. 499–510, 2008.
- [18] C. P. Tan and C. Edwards, "Sliding mode observers for robust detection and reconstruction of actuator and sensor faults," *International Journal of Robust and Nonlinear Control*, vol. 13, no. 5, pp. 443–463, 2003.
- [19] C. P. Tan and C. Edwards, "Sliding mode observers for detection and reconstruction of sensor faults," *Automatica*, vol. 38, no. 10, pp. 1815–1821, 2002.
- [20] C. Edwards, S. K. Spurgeon, and R. J. Patton, "Sliding mode observers for fault detection and isolation," *Automatica*, vol. 36, no. 4, pp. 541–553, 2000.
- [21] H. Alwi, C. Edwards, and C. P. Tan, "Sliding mode estimation schemes for incipient sensor faults," *Automatica*, vol. 45, no. 7, pp. 1679–1685, 2009.

- [22] C. Edwards and C. P. Tan, "Sensor fault tolerant control using sliding mode observers," *Control Engineering Practice*, vol. 14, no. 8, pp. 897–908, 2006.
- [23] A. Zolghadri, "Advanced model-based FDIR techniques for aerospace systems: today challenges and opportunities," *Progress in Aerospace Sciences*, vol. 53, pp. 18–29, 2012.
- [24] M. Z. Li, F. L. Wang, and F. R. Gao, "PID-based sliding mode controller for nonlinear processes," *Industrial and Engineering Chemistry Research*, vol. 40, no. 12, pp. 2660–2667, 2001.
- [25] J. Li and L. Yang, "Adaptive PI-based sliding mode control for nanopositioning of piezoelectric actuators," *Mathematical Problems in Engineering*, vol. 2014, Article ID 357864, 10 pages, 2014.
- [26] P. V. Mitchell, P. B. Griffith, and D. K. Henderson, "Fast-steering mirrors improve active beam stabilization," *Laser Focus World*, vol. 37, no. 10, pp. S13–S17, 2001.
- [27] Q. Zhou, P. Ben-Tzvi, D. Fan, and A. A. Goldenberg, "Design of fast steering mirror systems for precision laser beams steering," in *Proceedings of the International Workshop on Robotic and Sensors Environments*, pp. 144–149, Ottawa, Canada, April 1995.
- [28] Q. S. Xu and Y. M. Li, "Micro-/nanopositioning using model predictive output integral discrete sliding mode control," *IEEE Transactions on Industrial Electronics*, vol. 59, pp. 1161–1170, 2012.
- [29] C. Edwards and C. P. Tan, "A comparison of sliding mode and unknown input observers for fault reconstruction," *European Journal of Control*, vol. 12, no. 3, pp. 245–260, 2006.

## Research Article

# Robust Fault Diagnosis Design for Linear Multiagent Systems with Incipient Faults

Jingping Xia,<sup>1</sup> Bin Jiang,<sup>1</sup> Ke Zhang,<sup>1</sup> and Jinfa Xu<sup>2</sup>

<sup>1</sup> College of Automation Engineering, Nanjing University of Aeronautics and Astronautics, Nanjing 210016, China

<sup>2</sup> College of Aerospace Engineering, Nanjing University of Aeronautics and Astronautics, Nanjing 210016, China

Correspondence should be addressed to Jingping Xia; [xiajingping@nuaa.edu.cn](mailto:xiajingping@nuaa.edu.cn)

Received 30 July 2014; Accepted 24 September 2014

Academic Editor: Peng Shi

Copyright © 2015 Jingping Xia et al. This is an open access article distributed under the Creative Commons Attribution License, which permits unrestricted use, distribution, and reproduction in any medium, provided the original work is properly cited.

The design of a robust fault estimation observer is studied for linear multiagent systems subject to incipient faults. By considering the fact that incipient faults are in low-frequency domain, the fault estimation of such faults is proposed for discrete-time multiagent systems based on finite-frequency technique. Moreover, using the decomposition design, an equivalent conclusion is given. Simulation results of a numerical example are presented to demonstrate the effectiveness of the proposed techniques.

## 1. Introduction

In the past two decades, the study of multiagent systems has been a very hot topic and attracted considerable attention [1–7]. Multiagent systems appear in various fields, such as cooperative control of unmanned air vehicles and satellite formation flying. However, fault diagnosis is an important problem in automatic control systems and has been an active research area during the past three decades. Fruitful results related to this topic can be found in several excellent works [8–10] and references therein. However, there are very few results about fault diagnosis of multiagents.

In general, according to the varying rate of faults, the faults can be classified into abrupt and incipient in practical systems. Abrupt faults denote system parameter changes faster than the fault-free cases, whose property is able to detect this type of fault quickly to avoid serious consequences, while incipient faults are represented by drift-type changes and are more important in slowly developing problems. Compared with abrupt faults, early fault detection is the key objective for the class of incipient faults. Therefore, the development of effective fault diagnosis schemes for incipient faults is very important. In [11, 12], an adaptive online approximation method was proposed to detect incipient faults. And a system decomposition based method was proposed in [13, 14]

to achieve incipient fault diagnosis, while, in this paper, we consider the problem of fault diagnosis from the perspective of frequency property of incipient faults.

As we know the  $H_\infty$  performance is the maximum singular value of the transfer function of the studied system. However, if the possible occurring faults are classified into a finite-frequency range, the nominal  $H_\infty$  design for the entire range will bring much conservatism. For example, incipient faults belong to low-frequency range. Reference [15] not only considered  $H_\infty$  properties in different frequency domains, but also provided exact linear matrix inequalities (LMIs) characterization in finite-frequency ranges, which can be viewed a useful tool to handle incipient fault diagnosis. Therefore, the issue of incipient fault estimation of discrete-time multiagent systems is a meaningful research and motivates our study.

In this paper, on the basis of existing results [16–18], main contributions of this paper are as follows. According to the frequency range of incipient faults, a fault estimation observer is proposed to achieve incipient fault estimation for multiagent systems using the finite-frequency design. Moreover, an equivalent conclusion of the obtained results is derived by the decomposition technique.

The rest of this paper is organized as follows. Preliminaries and the system description of multiagents have been presented in Section 2. In Section 3, the fault estimation

observer of multiagents with incipient faults is presented. Simulation results are presented in Section 4 to show the effectiveness of the proposed approach, followed by some conclusions in Section 5.

## 2. Preliminaries and Problem Statement

**2.1. Graph Theory.** Consider a directed graph  $\mathcal{G} = (\mathcal{V}, \mathcal{E}, \mathcal{A})$  with a nonempty finite set of  $N$  nodes  $\mathcal{V} = (v_1, v_2, \dots, v_N)$ , a set of edges or arcs  $\mathcal{E} \subset \mathcal{V} \times \mathcal{V}$ , and the associated adjacency matrix  $\mathcal{A} = [a_{ij}] \in \mathbb{R}^{N \times N}$ . In this note, the graph is assumed to be time-invariant; that is,  $\mathcal{A}$  is constant. An edge rooted at node  $j$  and ended at node  $i$  is denoted by  $(v_j, v_i)$ , which means information can flow from node  $j$  to node  $i$ .  $a_{ij}$  is the weight of edge  $(v_j, v_i)$  and  $a_{ij} = 1$  if  $(v_j, v_i) \in \mathcal{E}$ ; otherwise  $a_{ij} = 0$ . We assume there are no repeated edges and no self-loops, that is,  $a_{ii} = 0$ ,  $i \in \mathcal{N}$  with  $\mathcal{N} = \{1, 2, \dots, N\}$ . Node  $j$  is called a neighbor of node  $i$  if  $(v_j, v_i) \in \mathcal{E}$ . The set of neighbors of node  $i$  is denoted by  $N_i = \{j \mid (v_j, v_i) \in \mathcal{E}\}$ . Define the in-degree matrix as  $D = \text{diag}\{d_i\} \in \mathbb{R}^{N \times N}$  with  $d_i = \sum_{j \in N_i} a_{ij}$  and the Laplacian matrix as  $L = D - \mathcal{A}$ . In this paper, we consider the case of undirected graph.

**2.2. Problem Statement.** Consider the following multiagent systems with  $N$  nodes and a communication graph  $\mathcal{G}$ :

$$\begin{aligned} x_i(k+1) &= Ax_i(k) + Bu_i(k) + Hf_i(k) + D_1\omega_i(k), \\ y_i(k) &= Cx_i(k) + D_2\omega_i(k), \end{aligned} \quad (1)$$

where  $x_i(k) \in \mathbb{R}^n$  is the state vector,  $u_i(k) \in \mathbb{R}^m$  is the input vector,  $y_i(k) \in \mathbb{R}^p$  is the output vector,  $\omega(k) \in \mathbb{R}^d$  is the disturbance and noise which belong to  $l_2[0, +\infty)$ , and  $f_i(k) \in \mathbb{R}^r$  represents the actuator fault.  $A, B, H, C, D_1$ , and  $D_2$  are constant real matrices of appropriate dimensions. It is supposed that matrices  $H$  and  $C$  are of full rank. It is supposed that the pair  $(A, C)$  is observable.

The dynamics of the leader or control node, labeled 0, is given by

$$\begin{aligned} x_0(k+1) &= A_0x_0(k), \\ y_0(k) &= C_0x_0(k), \end{aligned} \quad (2)$$

where  $x_0(k) \in \mathbb{R}^n$  is the state vector and  $y_0(k) \in \mathbb{R}^p$  is the output vector. It can be considered as a command generator, which generates the desired target trajectory. The leader node can be observed from a small subset of nodes in graph  $\mathcal{G}$ . If node  $i$  observes the leader, an edge  $(v_0, v_i)$  is said to exist with weighting gain  $g_i = 1$ . We refer to node  $i$  with  $g_i = 1$  as a pinned or controlled node. Denote the pinning matrix as  $G = \text{diag}\{g_i\} \in \mathbb{R}^{N \times N}$ .

**Lemma 1** (see [15]). *For the following linear discrete-time system*

$$\begin{aligned} \mathcal{X}(k+1) &= \mathcal{A}\mathcal{X}(k) + \mathcal{B}\mathcal{U}(k) \\ \mathcal{Y}(k) &= \mathcal{C}\mathcal{X}(k) + \mathcal{D}\mathcal{U}(k), \end{aligned} \quad (3)$$

its transfer function can be written as  $\mathcal{G}(e^{j\theta}) = \mathcal{C}(e^{j\theta}I - \mathcal{A})^{-1}\mathcal{B} + \mathcal{D}$ . Given a symmetric matrix  $\Pi$ , the following two statements are equivalent.

(i) *The finite-frequency inequality*

$$\begin{bmatrix} \mathcal{G}(e^{j\theta}) \\ \mathcal{F} \end{bmatrix}^T \Pi \begin{bmatrix} \mathcal{G}(e^{j\theta}) \\ \mathcal{F} \end{bmatrix} < 0. \quad (4)$$

(ii) *There exist Hermitian matrices  $\mathcal{P}$  and  $\mathcal{Q}$  (where  $\mathcal{Q} > 0$ ), and*

$$\begin{bmatrix} \mathcal{A} & \mathcal{B} \\ \mathcal{F} & 0 \end{bmatrix}^T \Xi \begin{bmatrix} \mathcal{A} & \mathcal{B} \\ \mathcal{F} & 0 \end{bmatrix} + \begin{bmatrix} \mathcal{C} & \mathcal{D} \\ 0 & \mathcal{F} \end{bmatrix}^T \Pi \begin{bmatrix} \mathcal{C} & \mathcal{D} \\ 0 & \mathcal{F} \end{bmatrix} < 0, \quad (5)$$

where

$$\Xi = \begin{bmatrix} \mathcal{P} & \mathcal{Q} \\ \mathcal{Q} & -\mathcal{P} - 2 \cos(\vartheta_l) \mathcal{Q} \end{bmatrix} \quad (6)$$

for low-frequency range  $|\vartheta| \leq \vartheta_l$ , and

$$\Xi = \begin{bmatrix} \mathcal{P} & -\mathcal{Q} \\ -\mathcal{Q} & -\mathcal{P} + 2 \cos(\vartheta_h) \mathcal{Q} \end{bmatrix} \quad (7)$$

for high-frequency range  $|\vartheta| \geq \vartheta_h$ .

## 3. Main Results

For the dynamics (1), the fault estimation observer of the  $i$ th node is constructed:

$$\begin{aligned} \hat{x}_i(k+1) &= A\hat{x}_i(k) + Bu_i(k) + H\hat{f}_i(k) - R\zeta_i(k), \\ \hat{y}_i(k) &= C\hat{x}_i(k), \\ \hat{f}_i(k+1) &= \hat{f}_i(k) - F\zeta_i(k), \end{aligned} \quad (8)$$

where  $\hat{x}_i(k) \in \mathbb{R}^n$  is the observer state,  $\hat{y}_i(k) \in \mathbb{R}^p$  is the observer output,  $\hat{f}_i(k) \in \mathbb{R}^r$  is an estimate of  $f_i(k)$ , and  $R \in \mathbb{R}^{n \times p}$ ,  $F \in \mathbb{R}^{r \times p}$  are observer gain matrices of node  $i$ .  $\zeta_i(k)$  is the neighborhood output estimation error of the  $i$ th node, that is,

$$\begin{aligned} \zeta_i(k) &= \sum_{j \in N_i} a_{ij} \left( (\hat{y}_i(k) - y_i(k)) - (\hat{y}_j(k) - y_j(k)) \right) \\ &\quad + g_i \left( (\hat{y}_i(k) - y_i(k)) - (\hat{y}_0(k) - y_0(k)) \right). \end{aligned} \quad (9)$$

**Remark 2.** Here, it is assumed that the state of leader mode is measured or available, so the observed output obtained from the observer is equal to the measured output, that is,  $\hat{y}_0(k) - y_0(k) = 0$ .

For the  $i$ th node, let

$$\begin{aligned} e_{xi}(k) &= \hat{x}_i(k) - x_i(k), & e_{yi}(k) &= \hat{y}_i(k) - y_i(k), \\ e_{fi}(k) &= \hat{f}_i(k) - f_i(k); \end{aligned} \quad (10)$$

one gets

$$\begin{aligned}
e_{xi}(k+1) &= Ae_{xi}(k) + He_{fi}(k) \\
&\quad - R \left[ \sum_{j \in N_i} a_{ij} (Ce_{xi}(k) - D_2\omega_i(k) - Ce_{xj}(k) + D_2\omega_j(k)) \right. \\
&\quad \left. + g_j (Ce_{xi}(k) - D_2\omega_i(k)) \right] - D_1\omega_i(k), \\
e_{fi}(k+1) &= e_{fi}(k) \\
&\quad - F \left[ \sum_{j \in N_i} a_{ij} (Ce_{xi}(k) - D_2\omega_i(k) - Ce_{xj}(k) + D_2\omega_j(k)) \right. \\
&\quad \left. + g_j (Ce_{xi}(k) - D_2\omega_i(k)) \right] - \Delta f_i(k),
\end{aligned} \tag{11}$$

where  $\Delta f_i(k) = f_i(k+1) - f_i(k)$ .

Based on (11), the following augmented system can be obtained:

$$\begin{aligned}
&\begin{bmatrix} e_{xi}(k+1) \\ e_{fi}(k+1) \end{bmatrix} \\
&= \begin{bmatrix} A & H \\ 0 & I \end{bmatrix} \begin{bmatrix} e_{xi}(k) \\ e_{fi}(k) \end{bmatrix} - \begin{bmatrix} R \\ F \end{bmatrix} \\
&\quad \times \left[ \sum_{j \in N_i} a_{ij} (Ce_{xi}(k) - D_2\omega_i(k) - Ce_{xj}(k) \right. \\
&\quad \left. + D_2\omega_j(k)) + g_j (Ce_{xi}(k) - D_2\omega_i(k)) \right] \\
&\quad - \begin{bmatrix} D_1 \\ 0 \end{bmatrix} \omega_i(k) - \begin{bmatrix} 0 \\ I \end{bmatrix} \Delta f_i(k).
\end{aligned} \tag{12}$$

Furthermore, denote new vectors and matrices:

$$\begin{aligned}
\bar{e}_i(k) &= \begin{bmatrix} e_{xi}(k) \\ e_{fi}(k) \end{bmatrix}, \quad \nu_i(k) = \begin{bmatrix} \omega_i(k) \\ \Delta f_i(k) \end{bmatrix}, \\
\bar{A} &= \begin{bmatrix} A & H \\ 0 & I \end{bmatrix}, \quad \bar{R} = \begin{bmatrix} R \\ F \end{bmatrix}, \quad \bar{C} = [C \ 0], \\
\bar{D}_1 &= \begin{bmatrix} D_1 \\ 0 \end{bmatrix}, \quad \bar{I}_r = \begin{bmatrix} 0 \\ I \end{bmatrix};
\end{aligned} \tag{13}$$

then for the  $i$ th node, it follows that

$$\begin{aligned}
\bar{e}_i(k+1) &= \bar{A}\bar{e}_i(k) \\
&\quad - \bar{R} \left[ \sum_{j \in N_i} a_{ij} (\bar{C}\bar{e}_i(k) - D_2\omega_i(k) - \bar{C}e_j(k) + D_2\omega_j(k)) \right. \\
&\quad \left. + g_j (\bar{C}\bar{e}_i(k) - D_2\omega_i(k)) \right] - \bar{D}_1\omega_i(k) - \bar{I}_r\Delta f_i(k) \\
e_{fi}(k) &= \bar{I}_r^T \bar{e}_i(k).
\end{aligned} \tag{14}$$

Denote the global variable

$$\begin{aligned}
\bar{e}(k) &= [\bar{e}_1^T(k), \bar{e}_2^T(k), \dots, \bar{e}_N^T(k)]^T, \\
e_f(k) &= [e_{f1}^T(k), e_{f2}^T(k), \dots, e_{fN}^T(k)]^T, \\
\omega(k) &= [\omega_1^T(k), \omega_2^T(k), \dots, \omega_N^T(k)]^T, \\
\Delta f(k) &= [\Delta f_1^T(k), \Delta f_2^T(k), \dots, \Delta f_N^T(k)]^T;
\end{aligned} \tag{15}$$

then the global error dynamics can be expressed as

$$\begin{aligned}
\bar{e}(k+1) &= (I_N \otimes \bar{A}) \bar{e}(k) - (I_N \otimes \bar{R}) \\
&\quad \times [(L+G) \otimes \bar{C}\bar{e}(k) - (L+G) \otimes D_2\omega(k)] \\
&\quad - (I_N \otimes \bar{D}_1) \omega(k) - (I_N \otimes \bar{I}_r) \Delta f(k) \\
&= [(I_N \otimes \bar{A}) - (L+G) \otimes (\bar{R}\bar{C})] \bar{e}(k) \\
&\quad + [(L+G) \otimes (\bar{R}D_2) - (I_N \otimes \bar{D}_1)] \omega(k) \\
&\quad - (I_N \otimes \bar{I}_r) \Delta f(k), \\
e_f(k) &= (I_N \otimes \bar{I}_r^T) \bar{e}(k),
\end{aligned} \tag{16}$$

where  $\otimes$  denotes Kronecker product [19].

**Theorem 3.** Given scalars  $\gamma_1, \gamma_2 > 0$ . The global error dynamics (16) satisfy the  $H_\infty$  performances  $\|T_{\omega(k)e_f(k)}\|_\infty < \gamma_1$  and  $\|T_{\Delta f(k)e_f(k)}\|_\infty < \gamma_2$  if there exist symmetric positive definite matrices  $\bar{Q}_1, \bar{Q}_2$ , symmetric matrices  $\bar{P}_1, \bar{P}_2$ , and matrices  $\bar{S}, \bar{Y}$  such that the following conditions hold:

$$\begin{bmatrix} I_N \otimes (-\bar{S} - \bar{S}^T + \bar{P}_1) & I_N \otimes (\bar{Q}_1 + \bar{S}A) - (L + G) \otimes (\bar{Y}C) & \phi & 0 \\ * & I_N \otimes (-2 \cos(\theta_f) \bar{Q}_1 - \bar{P}_1) & 0 & I_N \otimes \bar{I}_r \\ * & * & -\gamma_1 I & 0 \\ * & * & * & -\gamma_1 I \end{bmatrix} < 0, \quad (17)$$

$$\begin{bmatrix} I_N \otimes (-\bar{S} - \bar{S}^T + \bar{P}_2) & I_N \otimes (-\bar{Q}_2 + \bar{S}A) - (L + G) \otimes (\bar{Y}C) & \varphi & 0 \\ * & I_N \otimes (2 \cos(\theta_d) \bar{Q}_2 - \bar{P}_2) & 0 & I_N \otimes \bar{I}_r \\ * & * & -\gamma_2 I & 0 \\ * & * & * & -\gamma_2 I \end{bmatrix} < 0,$$

where  $\phi = (L + G) \otimes (\bar{Y}D_2) - I_N \otimes (\bar{S}D_1)$  and  $\varphi = -I_N \otimes (\bar{S}I_r)$ ; then the fault estimation observer gain matrix is given by  $\bar{R} = \bar{S}^{-1} \bar{Y}$ .

**Remark 4.** In general, the noises are in high-frequency domain and incipient faults are in low-frequency one. So according to [17] and Lemma 1, the proof of Theorem 3 can be deduced by choosing symmetric positive definite matrices  $I_N \otimes \bar{Q}_1, I_N \otimes \bar{Q}_2$ , symmetric matrices  $I_N \otimes \bar{P}_1, I_N \otimes \bar{P}_2$ , and a matrix  $I_N \otimes \bar{S}, I_N \otimes \bar{Y}$ . For brevity, this proof is not provided here.

**Remark 5.** From the process of fault estimation observer design, we can see that there is no parameter value of leader node 0 because of the assumption that the state of leader node is measurable, as shown in Remark 2. Since undirected

graph is considered in this paper, matrix  $L$  is symmetric such that one of the eigenvalues of  $L$  is zero, and the others are positive. Therefore, the presented leader node can be viewed as a virtual node, whose function is to make matrix  $(L + G)$  nonsingular.

**Remark 6.** From [20], we can get the matrix  $(L + G)$  is nonsingular. Furthermore, based on the decomposition design in [21], an equivalent conclusion of Theorem 3 is obtained, that is, Theorem 7.

**Theorem 7.** Given scalars  $\gamma_1, \gamma_2 > 0$ . The global error dynamics (16) satisfy the  $H_\infty$  performances  $\|T_{\omega(k)e_f(k)}\|_\infty < \gamma_1$  and  $\|T_{\Delta f(k)e_f(k)}\|_\infty < \gamma_2$  if there exist symmetric positive definite matrices  $\bar{Q}_1, \bar{Q}_2$ , symmetric matrices  $\bar{P}_1, \bar{P}_2$ , and matrices  $\bar{S}, \bar{Y}$  such that the following conditions hold:

$$\begin{bmatrix} -\bar{S} - \bar{S} + \bar{P}_1 & \bar{Q}_1 + \bar{S}A - \lambda_i (\bar{Y}C) & \lambda_i (\bar{Y}D_2) - \bar{S}D_1 & 0 \\ * & -2 \cos(\theta_f) \bar{Q}_1 - \bar{P}_1 & 0 & \bar{I}_r \\ * & * & -\gamma_1 I & 0 \\ * & * & * & -\gamma_1 I \end{bmatrix} < 0, \quad i = 1, \dots, N, \quad (18)$$

$$\begin{bmatrix} -\bar{S} - \bar{S} + \bar{P}_2 & -\bar{Q}_2 + \bar{S}A - \lambda_i (\bar{Y}C) & -\bar{S}I_r & 0 \\ * & 2 \cos(\theta_d) \bar{Q}_2 - \bar{P}_2 & 0 & \bar{I}_r \\ * & * & -\gamma_2 I & 0 \\ * & * & * & -\gamma_2 I \end{bmatrix} < 0, \quad i = 1, \dots, N,$$

where  $\lambda_i$  ( $i = 1, \dots, N$ ) are the eigenvalues of  $(L + G)$  and the fault estimation observer gain matrix is given by  $\bar{R} = \bar{S}^{-1} \bar{Y}$ .

*Proof.* Since matrix  $(L + G)$  is symmetric positive definite, there always exists a nonsingular matrix  $V \in \mathbb{R}^{N \times N}$  such that  $V^T(L + G)V = \Lambda$  and  $V^T V = I$ , where  $\Lambda = \text{diag}(\lambda_1, \lambda_2, \dots, \lambda_N) \in \mathbb{R}^{N \times N}$  and  $\lambda_1, \lambda_2, \dots, \lambda_N$  are positive. Under the coordinate transformation

$$\begin{aligned} \bar{e}(k) &= (V \otimes I_{n+r}) \check{e}(k), & \omega(k) &= (V \otimes I_d) \check{\omega}(k), \\ \Delta f(k) &= (V \otimes I_r) \check{\Delta} f(k), & \bar{e}_f(k) &= (V \otimes I_r) \check{e}_f(k). \end{aligned} \quad (19)$$

And let

$$\begin{aligned} \check{e}(k) &= [\check{e}_1^T(k), \check{e}_2^T(k), \dots, \check{e}_N^T(k)]^T, \\ \check{\omega}(k) &= [\check{\omega}_1^T(k), \check{\omega}_2^T(k), \dots, \check{\omega}_N^T(k)]^T, \\ \check{\Delta} f(k) &= [\check{\Delta} f_1^T(k), \check{\Delta} f_2^T(k), \dots, \check{\Delta} f_N^T(k)]^T, \\ \check{e}_f(k) &= [\check{e}_{f1}^T(k), \check{e}_{f2}^T(k), \dots, \check{e}_{fN}^T(k)]^T; \end{aligned} \quad (20)$$

then it gets

$$\begin{aligned}
 & \check{e}(k+1) \\
 &= \left[ (I_N \otimes \bar{A}) - \Lambda \otimes (\overline{RC}) \right] \check{e}(k) \\
 & \quad + \left[ \Lambda \otimes (\overline{RD}_2) - (I_N \otimes \overline{D}_1) \right] \check{\omega}(k) - (I_N \otimes \overline{I}_r) \check{\Delta}f(k), \\
 & \check{e}_f(k) = (I_N \otimes \overline{I}_r^T) \check{e}(k).
 \end{aligned} \tag{21}$$

Since  $\Lambda$  is a diagonal matrix, the transfer function

$$\begin{aligned}
 T_{\check{\omega}(k)\check{e}_f(k)} &= \text{diag} \left( T_{\check{\omega}_1(k)\check{e}_{f1}(k)}, \dots, T_{\check{\omega}_N(k)\check{e}_{fN}(k)} \right) \\
 &= (V^{-1} \otimes I_d) T_{\omega(k)e_f(k)} (V \otimes I_r), \\
 T_{\check{\Delta}f(k)\check{e}_f(k)} &= \text{diag} \left( T_{\check{\Delta}f_1(k)\check{e}_{f1}(k)}, \dots, T_{\check{\Delta}f_N(k)\check{e}_{fN}(k)} \right) \\
 &= (V^{-1} \otimes I_r) T_{\Delta f(k)e_f(k)} (V \otimes I_r),
 \end{aligned} \tag{22}$$

where  $V$  is orthogonal. It follows that

$$\begin{aligned}
 \|T_{\check{\omega}(k)\check{e}_f(k)}\|_{\infty} &= \max_{i=1, \dots, N} \|T_{\check{\omega}_i(k)\check{e}_{fi}(k)}\|_{\infty} = \|T_{\omega(k)e_f(k)}\|_{\infty}, \\
 \|T_{\check{\Delta}f(k)\check{e}_f(k)}\|_{\infty} &= \max_{i=1, \dots, N} \|T_{\check{\Delta}f_i(k)\check{e}_{fi}(k)}\|_{\infty} = \|T_{\Delta f(k)e_f(k)}\|_{\infty}.
 \end{aligned} \tag{23}$$

Moreover, by choosing the same matrix variables  $\overline{Q}_1, \overline{Q}_2, \overline{P}_1, \overline{P}_2, \overline{S}, \overline{Y}$  shown in Theorem 3, one gets the two conditions of Theorems 3 and 7 are equivalent.  $\square$

*Remark 8.* Theorem 7 is an equivalent conclusion of Theorem 3 by using decomposition technique. And note that the eigenvalues of matrix  $(L + G)$  are positive; that is,  $\lambda_i > 0$ ,  $i = 1, \dots, N$ .

#### 4. Simulation Results

In this section, the following example is presented to illustrate the effectiveness of the proposed method. It is assumed that there are four agents of multiagent systems, that is,  $N = 4$ , and each node is

$$\begin{aligned}
 x_i(k+1) &= \begin{bmatrix} 0.1 & -0.1 \\ 0.2 & 0.5 \end{bmatrix} x_i(k) + \begin{bmatrix} 1.2 \\ 1 \end{bmatrix} u_i(k), \\
 y_i(k) &= [1 \ 1] x_i(k).
 \end{aligned} \tag{24}$$

The disturbance matrices are  $D_1 = [0.1 \ 0.1]^T$  and  $D_2 = 0.1$ . Here, actuator faults are considered, that is, the fault distribution matrix  $H = B$ .

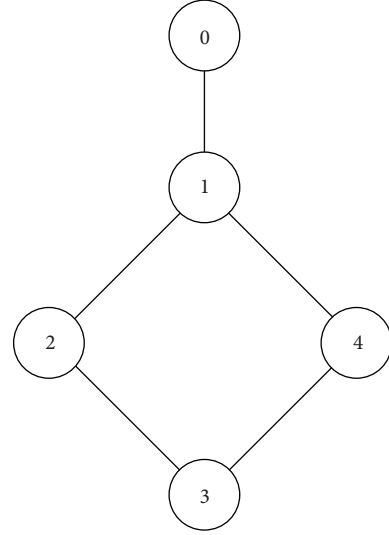


FIGURE 1: The communication topology of multiagent systems.

For these multiagent systems subject to four nodes, we assume that each node only contacts with its nearest neighbors, as shown in Figure 1. From Figure 1, one gets Laplacian matrix

$$L = \begin{bmatrix} 2 & -1 & 0 & -1 \\ -1 & 2 & -1 & 0 \\ 0 & -1 & 2 & -1 \\ -1 & 0 & -1 & 2 \end{bmatrix}. \tag{25}$$

And only the first node links the leader node, so we have

$$G = \begin{bmatrix} 1 & 0 & 0 & 0 \\ 0 & 0 & 0 & 0 \\ 0 & 0 & 0 & 0 \\ 0 & 0 & 0 & 0 \end{bmatrix}. \tag{26}$$

It is readily verified that  $(L + G)$  is nonsingular and its eigenvalues are positive, that is, 0.1864, 2.0000, 2.4707, and 4.3429.

It is assumed that the noise is in high-frequency domain  $\vartheta_d = \pi$  rad, and the derivative of actuator faults is in low-frequency domain  $\vartheta_f = \pi/10$  rad.

By solving the conditions of Theorem 3, one gets  $\gamma_1 + \gamma_2 = 4.9257$  and the observer matrix

$$\overline{R} = \begin{bmatrix} 0.0873 \\ 0.2476 \\ 0.0728 \end{bmatrix}. \tag{27}$$

And we are able to verify that the minimum value is also  $\gamma_1 + \gamma_2 = 4.9257$  by calculating the conditions of Theorem 7.

For simulation, we firstly consider an incipient fault occurring in the first node as follows:

$$f_1(k) = \begin{cases} 0, & 0 \leq t < 50 \text{ s}, \\ 1 - e^{-0.05(t-50)}, & 50 \leq t. \end{cases} \tag{28}$$

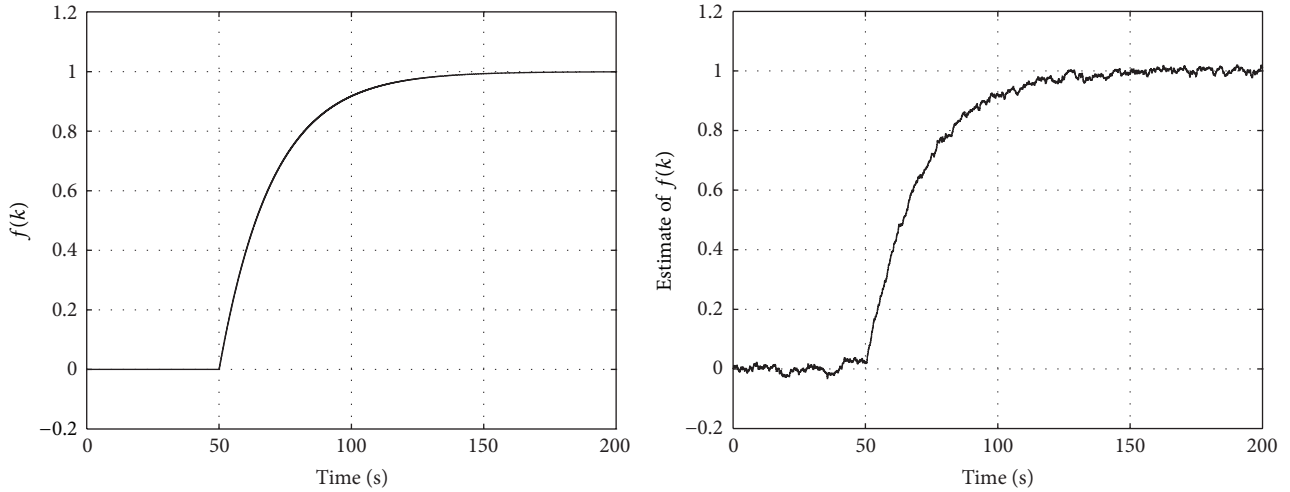


FIGURE 2: Simulation of the incipient fault in the first node.

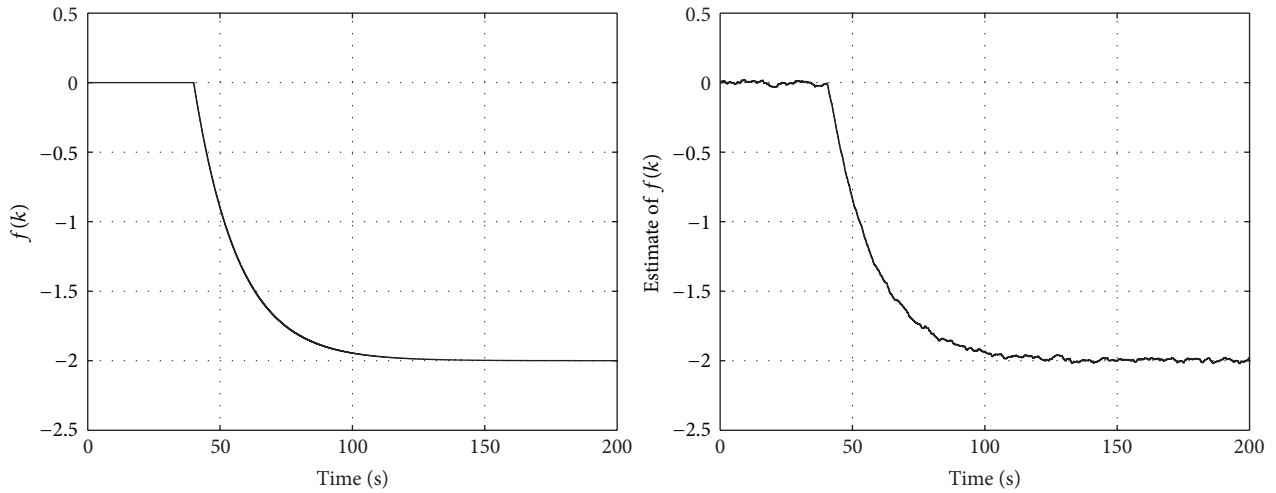


FIGURE 3: Simulation of the incipient fault in the third node.

Simulation result of this fault in the first node is shown in Figure 2.

Secondly, we assume that there is an incipient fault in the third node:

$$f_3(k) = \begin{cases} 0, & 0 \leq t < 40 \text{ s}, \\ -2(1 - e^{-0.06(t-40)}), & 40 \leq t. \end{cases} \quad (29)$$

For such fault, Figure 3 illustrates the online fault estimation.

From simulation results, it is concluded that the presented fault estimation observer can achieve incipient fault estimation of multiagent systems.

## 5. Conclusions

In this paper, a fault estimation design has been proposed for a class of multiagent systems with incipient faults. According to the frequency properties of incipient faults and noises, a robust  $H_\infty$  design with finite-frequency domain is obtained

in terms of linear matrix inequalities. An equivalent result of the proposed fault estimation is further presented. Finally, simulation results of incipient faults in the two different nodes have been given to illustrate the effectiveness of the proposed design. Fault diagnosis of nonlinear multiagent systems will be studied in our future work.

## Conflict of Interests

The authors declare that there is no conflict of interests regarding the publication of this paper.

## Acknowledgments

This work is partially supported by the National Natural Science Foundation of China (61304112, 61428303), Natural Science Foundation of Jiangsu Province (BK20131364), China Postdoctoral Science Foundation Funded Project (2012M521079, 2013T60535), and Jiangsu Postdoctoral Science Foundation (1201013B).

## References

- [1] Y. Hong, G. Chen, and L. Bushnell, "Distributed observers design for leader-following control of multi-agent networks," *Automatica*, vol. 44, no. 3, pp. 846–850, 2008.
- [2] C.-Q. Ma and J.-F. Zhang, "Necessary and sufficient conditions for consensusability of linear multi-agent systems," *IEEE Transactions on Automatic Control*, vol. 55, no. 5, pp. 1263–1268, 2010.
- [3] Z. Li, Z. Duan, and G. Chen, "Dynamic consensus of linear multi-agent systems," *IET Control Theory and Applications*, vol. 5, no. 1, pp. 19–28, 2011.
- [4] H. Du, S. Li, and P. Shi, "Robust consensus algorithm for second-order multi-agent systems with external disturbances," *International Journal of Control*, vol. 85, no. 12, pp. 1913–1928, 2012.
- [5] Y. Liu and Y. Jia, " $H_\infty$  consensus control for multi-agent systems with linear coupling dynamics and communication delays," *International Journal of Systems Science*, vol. 43, no. 1, pp. 50–62, 2012.
- [6] M. H. Nguyen and D. Q. Tran, "A combination trust model for multi-agent systems," *International Journal of Innovative Computing, Information and Control*, vol. 9, no. 6, pp. 2405–2420, 2013.
- [7] A. Sedziwy, "Effective graph representation supporting multi-agent distributed computing," *International Journal of Innovative Computing, Information and Control*, vol. 10, no. 1, pp. 101–113, 2014.
- [8] M. Blanke, M. Kinnaert, J. Lunze, and M. Staroswiecki, *Diagnosis and Fault-Tolerant Control*, Springer, New York, NY, USA, 2006.
- [9] S. X. Ding, *Model-Based Fault Diagnosis Techniques: Design Schemes, Algorithms, and Tools*, Springer, Berlin, Germany, 2008.
- [10] K. Zhang, B. Jiang, and P. Shi, *Observer-Based Fault Estimation and Accommodation for Dynamic Systems*, Springer, Berlin, Germany, 2013.
- [11] M. A. Demetriou and M. M. Polycarpou, "Incipient fault diagnosis of dynamical systems using online approximators," *IEEE Transactions on Automatic Control*, vol. 43, no. 11, pp. 1612–1617, 1998.
- [12] X. Zhang, M. M. Polycarpou, and T. Parisini, "A robust detection and isolation scheme for abrupt and incipient faults in nonlinear systems," *IEEE Transactions on Automatic Control*, vol. 47, no. 4, pp. 576–593, 2002.
- [13] W. Chen and F. N. Chowdhury, "Analysis and detection of incipient faults in post-fault systems subject to adaptive fault-tolerant control," *International Journal of Adaptive Control and Signal Processing*, vol. 22, no. 9, pp. 815–832, 2008.
- [14] W. Chen and F. N. Chowdhury, "A synthesized design of sliding-mode and Luenberger observers for early detection of incipient faults," *International Journal of Adaptive Control and Signal Processing*, vol. 24, no. 12, pp. 1021–1035, 2010.
- [15] T. Iwasaki and S. Hara, "Generalized KYP lemma: unified frequency domain inequalities with design applications," *IEEE Transactions on Automatic Control*, vol. 50, no. 1, pp. 41–59, 2005.
- [16] K. Zhang, B. Jiang, and P. Shi, "Observer-based integrated robust fault estimation and accommodation design for discrete-time systems," *International Journal of Control*, vol. 83, no. 6, pp. 1167–1181, 2010.
- [17] K. Zhang, B. Jiang, P. Shi, and J. Xu, "Fault estimation observer design for discrete-time systems in finite-frequency domain," *International Journal of Robust and Nonlinear Control*, 2014.
- [18] Q. Shen, B. Jiang, P. Shi, and J. Zhao, "Cooperative adaptive fuzzy tracking control for networked unknown nonlinear multi-agent systems with time-varying actuator faults," *IEEE Transactions on Fuzzy Systems*, vol. 22, no. 3, pp. 494–504, 2014.
- [19] H. Zhang, F. L. Lewis, and A. Das, "Optimal design for synchronization of cooperative systems: state feedback, observer and output feedback," *IEEE Transactions on Automatic Control*, vol. 56, no. 8, pp. 1948–1952, 2011.
- [20] Z. Li, Z. Duan, and G. Chen, " $H_\infty$  and  $H_2$  performance regions of multi-agent systems," *Automatica*, vol. 47, no. 4, pp. 797–803, 2011.
- [21] R. Ghadami and B. Shafai, "Decomposition-based distributed control for continuous-time multi-agent systems," *IEEE Transactions on Automatic Control*, vol. 58, no. 1, pp. 258–264, 2013.

## Research Article

# Bayesian Network Based Fault Prognosis via Bond Graph Modeling of High-Speed Railway Traction Device

Yunkai Wu,<sup>1,2</sup> Bin Jiang,<sup>1,2</sup> Ningyun Lu,<sup>1,2</sup> and Yang Zhou<sup>3</sup>

<sup>1</sup>College of Automation Engineering, Nanjing University of Aeronautics and Astronautics, Nanjing 210016, China

<sup>2</sup>Jiangsu Key Laboratory of Internet of Things and Control Technologies, Nanjing University of Aeronautics and Astronautics, Nanjing 210016, China

<sup>3</sup>School of Computer Science and Engineering, Jiangsu University of Science and Technology, Zhenjiang 212003, China

Correspondence should be addressed to Bin Jiang; [binjiang@nuaa.edu.cn](mailto:binjiang@nuaa.edu.cn)

Received 5 September 2014; Accepted 25 December 2014

Academic Editor: Peng Shi

Copyright © 2015 Yunkai Wu et al. This is an open access article distributed under the Creative Commons Attribution License, which permits unrestricted use, distribution, and reproduction in any medium, provided the original work is properly cited.

Reliability of the traction system is of critical importance to the safety of CRH (China Railway High-speed) high-speed train. To investigate fault propagation mechanism and predict the probabilities of component-level faults accurately for a high-speed railway traction system, a fault prognosis approach via Bayesian network and bond graph modeling techniques is proposed. The inherent structure of a railway traction system is represented by bond graph model, based on which a multilayer Bayesian network is developed for fault propagation analysis and fault prediction. For complete and incomplete data sets, two different parameter learning algorithms such as Bayesian estimation and expectation maximization (EM) algorithm are adopted to determine the conditional probability table of the Bayesian network. The proposed prognosis approach using Pearl's polytree propagation algorithm for joint probability reasoning can predict the failure probabilities of leaf nodes based on the current status of root nodes. Verification results in a high-speed railway traction simulation system can demonstrate the effectiveness of the proposed approach.

## 1. Introduction

CRH (China Railway High-speed) high-speed train traction system is a complex electromechanical coupling system, which consists of a lot of electrical and mechanical devices, such as pantograph, traction transformers, traction converters, and traction motors. Along with the growth of running time, some components in a traction system like IGBTs (insulated gate bipolar transistors) and diodes will degrade with age. These fatigued components are likely to have various abrupt faults such as short-circuit or open-circuit faults, which definitely increase the risk of serious accidents in the entire railway. Thus, fault prognosis is urgently demanded in high-speed railway traction systems.

Due to the complex structures and behaviors of electromechanical coupling traction systems, it is difficult to describe the causalities accurately through analytical models, which limits the application of the existing analytical model based fault prognosis methods [1]. Instead, the data-driven

statistical model based prognosis methods, especially the Bayesian networks, have become the mainstream [2–7]. However, constructing an accurate Bayesian network structure is a big challenge in practice. Some scholars have proposed approaches to learn the Bayesian network structure from data [4, 5]. Due to the reason that the accuracy of the learned Bayesian network is largely affected by the richness of the data and the prior knowledge of the network ordering, few attractive results have been obtained, according to which an idea of constructing Bayesian network via bond graph model is proposed in this paper.

Bond graph modeling has been widely applied to lots of engineering fields for modeling various dynamic systems. It is particularly popular for modeling electromechanical coupling systems. In bond graphs, different elements that belong to different energy domains (such as mechanical, electrical, and electromagnetic domains) can be described by the same model structure with uniform modeling language. Bond graph theory and its recent applications have been

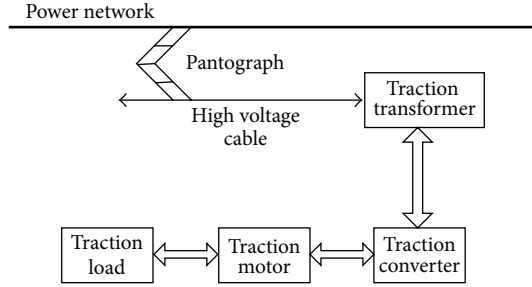


FIGURE 1: Schematic diagram of CRH<sub>5</sub> traction system.

summarized in [8–10]. Due to its capability in describing the causality of a complex system, bond graph has been investigated in modeling of high-speed railway vehicles in recent years [11–13]. The bond graph model of a squirrel cage induction motor is introduced in [14], which contributes to the bond graph modeling of high-speed train traction device. Model based [15–17] and data-driven based [18, 19] FDD (fault detection and diagnosis) approaches, especially the bond graph based methods [20–25], are becoming hot research topics. However, the causal relationships in a bond graph that consist of important information for reasoning are seldom used in fault prognosis domain directly.

This paper proposes a general procedure for constructing a Bayesian network structure on the basis of bond graph modeling for fault prognosis of high-speed train traction device. The causal relationships revealed by the bond graph model are combined with the reasoning capacity of the Bayesian network. For complete and incomplete data sets, Bayesian estimation and expectation maximization (EM) algorithm are adopted, respectively, to determine the conditional probability table of the Bayesian network. Pearl's polytree propagation algorithm is used for joint probability reasoning. The failure probabilities of the other leaf nodes are determined by the current status of root nodes. The simulation results on CRH<sub>5</sub> traction system can verify the effectiveness of the proposed approach.

## 2. Modeling of CRH<sub>5</sub> Traction Device

**2.1. Railway Traction System.** CRH<sub>5</sub> high-speed trains are providing convenient public transportation among major cities in China. According to [26], the CRH<sub>5</sub> traction system is made up of pantograph (model: DSA250), vacuum circuit breaker (model: 22CBNG), traction transformer (electrical standard: IEC 60310), traction converter (model: YGN2Q213), traction motor (model: YJ87A, three-phase squirrel cage induction motor), and other components. An AC-DC-AC driving method is adopted, as shown in Figure 1, where 25 kV HVAC (high voltage alternating current) is transformed into 1700 V AC (alternating current) by the traction transformer through pantograph; then, the converter (AC-DC-AC) outputs three-phase AC with controllable voltage and frequency for the traction motors.

For simplicity, the traction system consisting of two sets of inverters and induction motors is studied in this paper.

The three-phase inverter bridge circuits can realize VVVF (variable velocity variable frequency) drive of the three-phase ACIMs (alternating current induction motors). The inverter circuit, as shown in Figure 2, uses IGBTs as switch elements in its main circuit and control system design, where the voltage-space vector control scheme is adopted in the inverter control circuit.

Open-circuit fault and short-circuit fault are two kinds of common faults in traction inverters. Switch-on failure of the transistors and breakdown of the motor phase can cause open-circuit faults, which will increase torque pulsations, copper losses or reduce mean torque and efficiency. Switch-off failure of the transistors and ground of the phase terminals can cause short-circuit faults, which will bring overload burning of the stator and rotor circuits.

### 2.2. Bond Graph Modeling

**2.2.1. Bond Graph: Basis.** Electromechanical systems are governed by many effects issued from different physical phenomena and various technological components. Bond graph, a unified and multidomain modeling and simulation approach, is well suited for such systems. Bond graph provides possibilities for both structural and behavioral system analysis [27]. According to [28], power variable is the product of effort (represented by  $e$ ) and flow (represented by  $f$ ), where effort variable represents force, voltage, or pressure and flow variable represents current, flow, or velocity. Capacitance ( $C$ ), inertias ( $I$ ), resistances ( $R$ ), sources  $\{S_e, S_f\}$ , gyrator ( $GY$ ), transformer ( $TF$ ), and junctions  $0, 1$  are generic bond graph components, which can be classified as 1-port components  $\{S_e, S_f, I, R, C\}$ , 2-port components  $\{TF, GY\}$ , and multiple-ports components  $\{1, 0\}$ . These bond graph components are connected by a set of bonds represented by half arrows indicating positive energy flow from one variable to another. For each bond, an effort and a flow variable were remarked to describe the signals of the bond graph components connected to the bonds. The generic components and bond connections form the structure of bond graph model, where a set of relations called constitutive relations is used to describe the behavior of each component [29].

Besides the modeling capability for electromechanical systems, bond graph approach can derive equations or information from the graph itself by using a concept called the causality. In bond graphs, a stroke is marked at one end of each bond, which indicates the direction of an effort or flow signal. Users can derive the relations or analytical expressions between system variables to understand how fault signals propagate in the system.

**2.2.2. Equivalent Circuits for CRH<sub>5</sub> Traction Devices.** The converter in CRH<sub>5</sub> unit consists of two sets of rectifiers, two sets of inverters, one set of traction control device, and cooling system. Each traction motor is controlled by one set of inverters, whose equivalent circuit is shown in Figure 3. The three-phase AC motors can be equivalent to a series circuit of resistances, inductances, and counter electromotive force, where the effect of the counter electromotive force

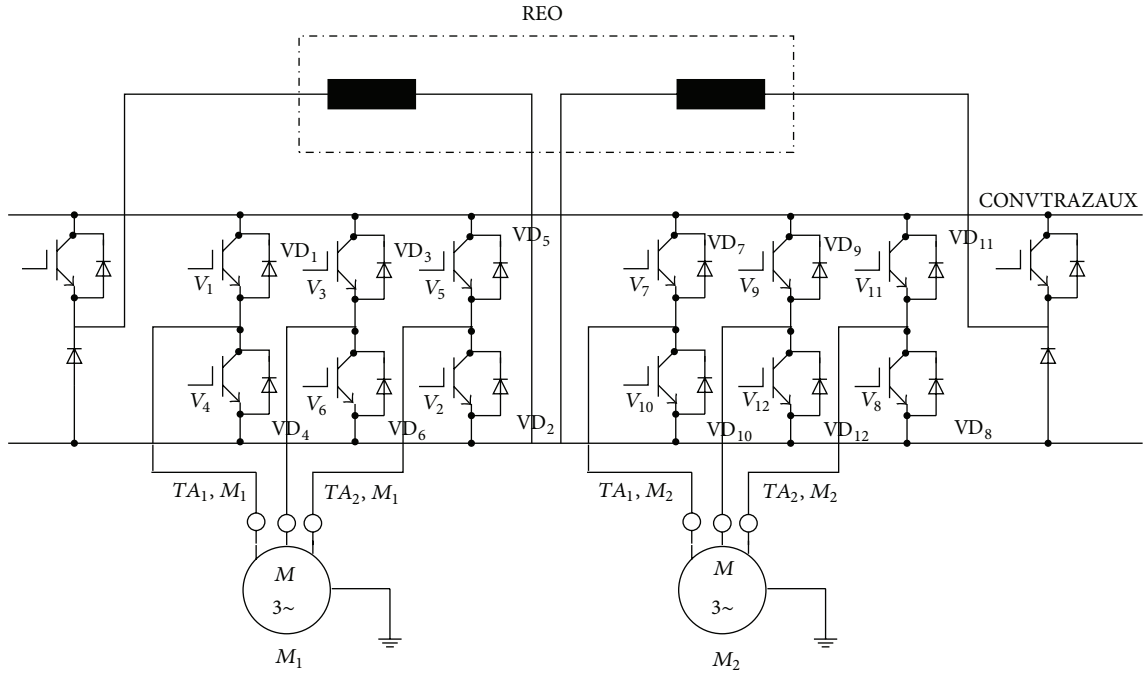


FIGURE 2: Schematic diagram of CRH<sub>5</sub> inverter.

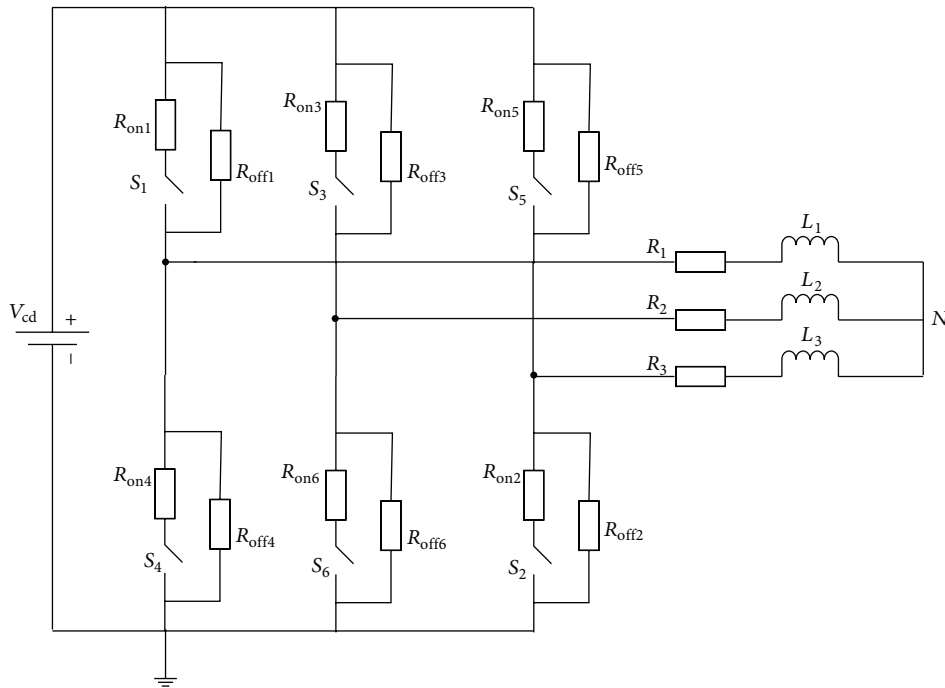


FIGURE 3: Equivalent circuit of the inverter and three-phase AC motor.

can be neglected when the load side is unloaded. For bond graph modeling of the inverter part, IGBT and diode circuit can be simplified by a switch model consisting of a turn-on resistance  $R_{on}$  with low resistor value, a turn-off resistance  $R_{off}$  with high resistor value, and an ideal switch  $S$ . In Figure 3, the series connecting  $R_{on1}$  and  $S_1$  is the equivalent circuit of IGBT  $V_1$ ,  $R_{off1}$  is the equivalent circuit of diode  $VD_1$ , and so

on. Different equivalent resistances ( $R_{eq}$ ) corresponding to different status can be calculated as follows:

$$R_{eq} = \begin{cases} R_{off} & \text{for } S \text{ turned off} \\ \frac{R_{on}R_{off}}{R_{on} + R_{off}} \approx R_{on} & \text{for } S \text{ turned on.} \end{cases} \quad (1)$$

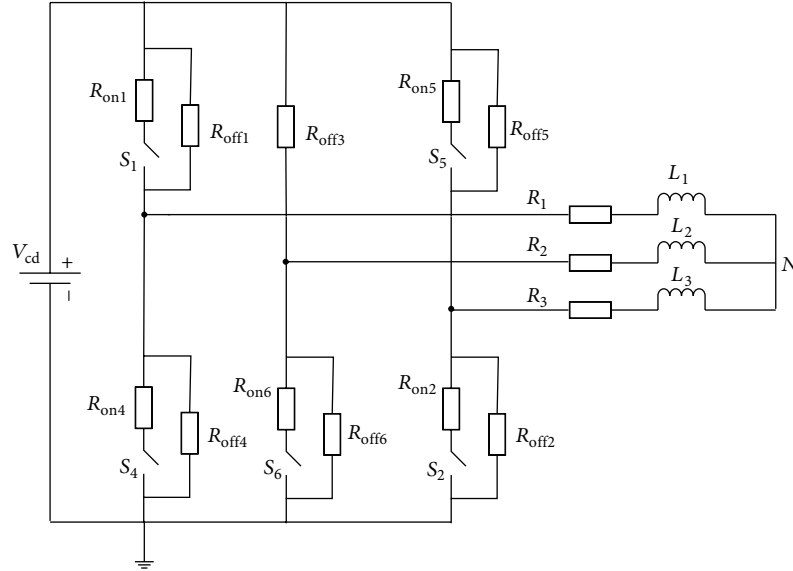


FIGURE 4: Equivalent circuit for open-circuit fault.

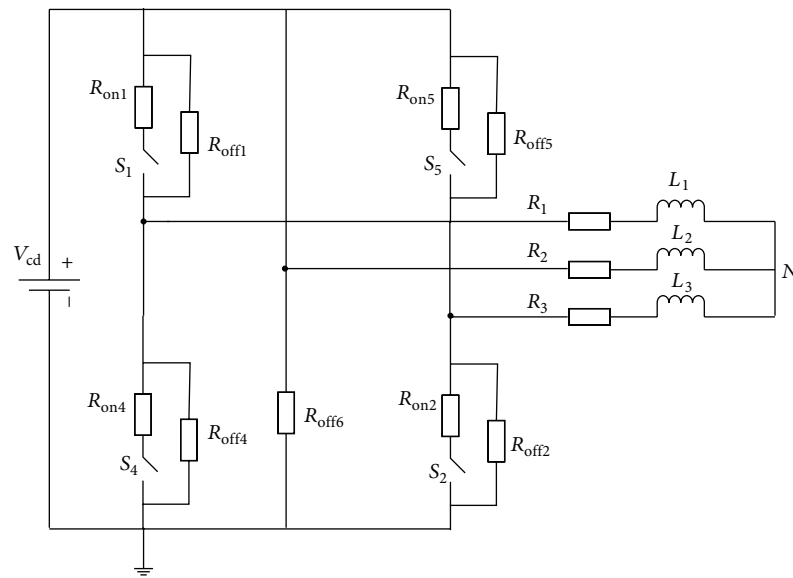


FIGURE 5: Equivalent circuit for short-circuit fault.

The final equivalent circuit of the inverter and three-phase AC motors for open-circuit fault and short-circuit fault status are shown in Figures 4 and 5, respectively.

**2.2.3. Bond Graph Modeling of Traction System.** According to [28], the main difficulty in bond graph modeling of power switching device is how to describe the discrete system dynamics. So far, many bond graph based modeling approaches for power switching device have been proposed, such as enumeration method, Petri Net method, and MTF (multitransformer) method. MTF method is the most popular method, where modulus  $m = 0$  or  $m = 1$  represents the status (ON or OFF) of power switching devices. As

shown in Figure 6,  $S_1-S_{12}$  and  $R_{off1}-R_{off12}$  represent switching tubes  $V_1-V_{12}$  and diodes  $VD_1-VD_{12}$ , respectively, in the inverter circuit. In bond graph modeling of the three-phase AC motors, the resistance  $R_e$  and the winding  $L_e$  determine the behavior of the stator circuit; the resistance  $R_p$  and the winding  $L_p$  indicate the losses of hysteresis and the magnetic flux losses in the stator and rotor circuit; the resistance  $R_r$  and the winding  $L_r$  determine the rotor circuit behavior. The mechanical power generated by each phase is modeled by the “MGY” ports. The rotational mechanical power is added to the “1” junction, which can be applied to the motor shaft modeling by the inertia port “I” with parameter “J.” The friction losses are modeled by the resistance port “R” with parameter “ $\mu$ .”

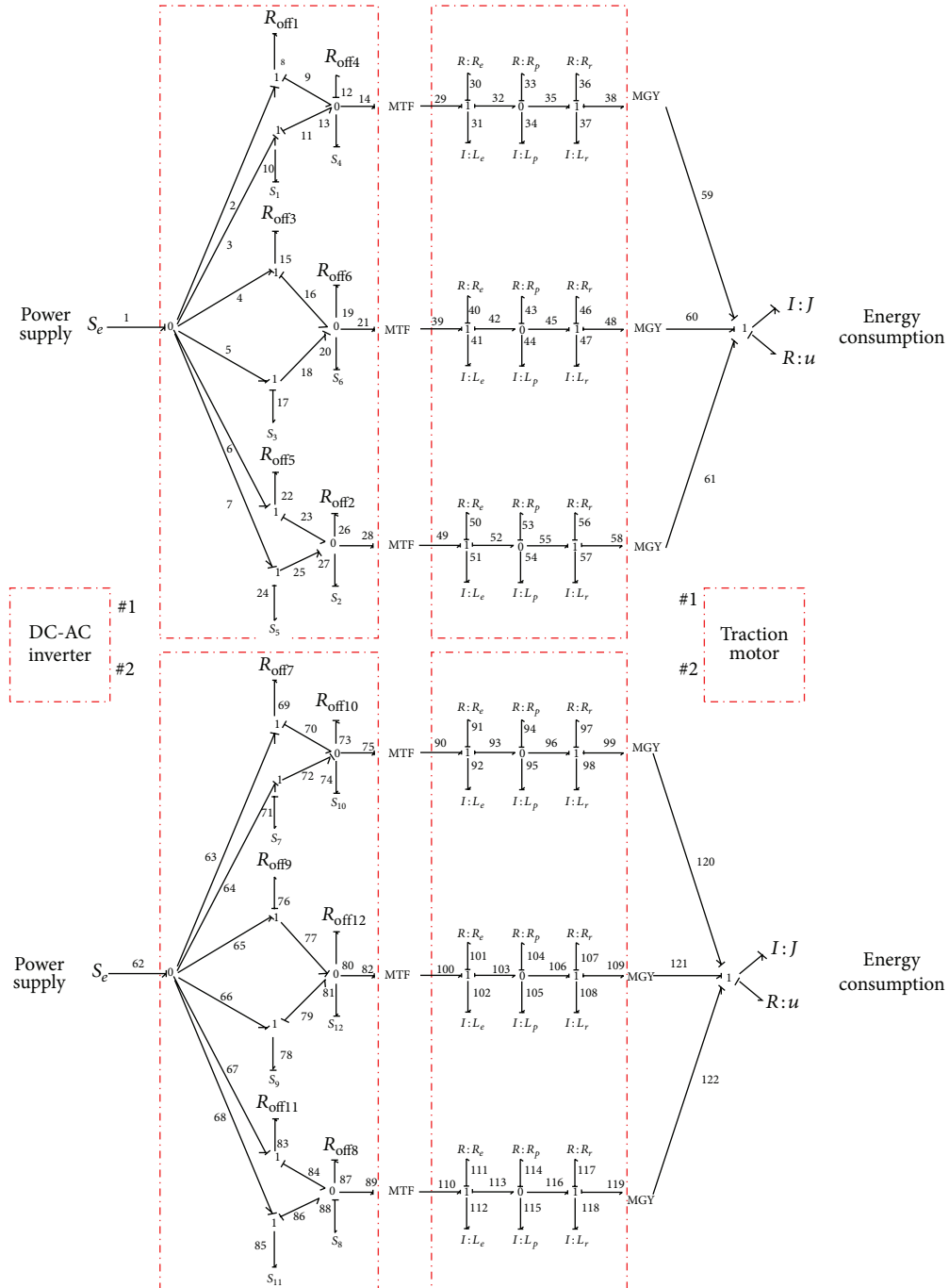


FIGURE 6: Bond graph modeling of CRH<sub>5</sub> inverter and three-phase AC motor.

Open-circuit fault and short-circuit fault are two kinds of common faults in inverter circuits. According to circuit analysis, the features of the collector-emitter average voltage of the switching tube are the same when an open-circuit fault happens on  $V_1, V_3,$  or  $V_5$  or a short-circuit fault happens on  $V_2, V_4,$  or  $V_6$ . Aiming at accurate fault location, define the behaviors of  $R_{on}$  and  $R_{off}$  as follows: the value of  $R_{on}$  increases rapidly when an open-circuit fault happens; the value of  $R_{off}$  decreases rapidly when a short-circuit fault happens. In Table 1,  $e_{10}, e_{13}, e_{17}, e_{20}, e_{24},$  and  $e_{27}$  represent the

collector-emitter average voltages of the bonds numbers 10, 13, 17, 20, 24, and 27, respectively. “0” represents the nominal value of the collector-emitter average voltage; “+” represents the increase of collector-emitter voltage; “-” represents the decrease of collector-emitter voltage.

According to the equivalent circuit shown in Figures 4 and 5, Figure 7(a) shows the bond graph of B-phase circuit in number 1 inverter, where IGBT  $V_3$  has an open-circuit fault. Figure 7(b) shows the bond graph of B-phase circuit in number 1 inverter, where IGBT  $V_3$  has a short-circuit fault.

TABLE 1: Common faults in the bond graph model of CRH<sub>5</sub> traction system.

Fault	Description	$e_{10}$	$e_{13}$	$e_{17}$	$e_{20}$	$e_{24}$	$e_{27}$
$F_1$	Open-circuit fault ( $S_1$ ) or short-circuit fault ( $S_4$ )	+	-	0	0	0	0
$F_2$	Short-circuit fault ( $S_1$ ) or open-circuit fault ( $S_4$ )	-	+	0	0	0	0
$F_3$	Open-circuit fault ( $S_3$ ) or short-circuit fault ( $S_6$ )	0	0	+	-	0	0
$F_4$	Short-circuit fault ( $S_3$ ) or open-circuit fault ( $S_6$ )	0	0	-	+	0	0
$F_5$	Open-circuit fault ( $S_5$ ) or short-circuit fault ( $S_2$ )	0	0	0	0	+	-
$F_6$	Short-circuit fault ( $S_5$ ) or open-circuit fault ( $S_2$ )	0	0	0	0	-	+

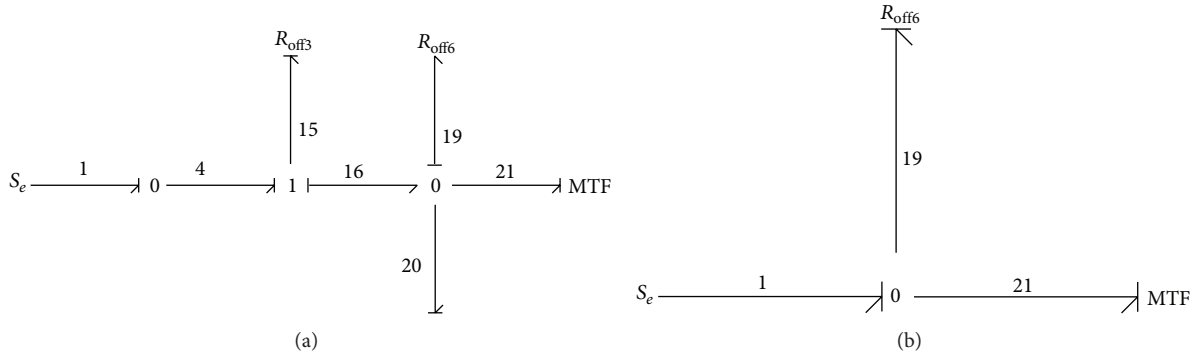


FIGURE 7: Bond graph modeling of B-phase inverter circuit in fault.

### 3. Fault Prognosis Based on Bayesian Network

**3.1. Key Idea.** Since the three-phase circuits in the inverter are exactly the same, B-phase circuit is shown as an example to study the fault prognosis in this paper. Figure 8 illustrates the fault prognosis mechanism using the Bayesian network of B-phase circuit to predict the fault probability of the stator or rotor circuit. For offline implementation, the bond graph model of CRH<sub>5</sub> inverter and three-phase AC motor are used to construct a Bayesian network for fault prognosis. The Bayesian network based fault prognosis module is activated when the structure of predictive Bayesian network is obtained and the conditional probability distributions are acquired. For online implementation, evidence extracted from the system measurements can propagate through the network when the probability distributions for each variable are inferred.

#### 3.2. From Bond Graph to Bayesian Network

**3.2.1. Bayesian Network.** Bayesian network is a directed acyclic graph (DAG), where nodes represent the random variables. The directed edges leading from cause variables to effect variables represent the causal relations. The measurements are donated by conditional probabilities between nodes and father-nodes. According to [30], prior probabilities need to be specified for root nodes, while conditional probability distributions (CPDs) are specified for nonroot nodes. The edges in the Bayesian network represent the joint probability distributions which can be defined as

$$P(x) = \prod_{i=1}^n P(x_i | \text{parents}(x_i)), \quad (2)$$

where  $\text{parents}(x_i)$  is the parent set of node  $x_i$ . The equation above, known as a chain rule indicating the joint probability distribution of all variables in the Bayesian network, is the product of each variable's probabilities when its parents' values are given. The probability distribution of each variable or partial variable can be obtained by Bayesian network inference when other variables are known.

A Bayesian network comprises two parts  $B = \langle G, \Theta \rangle$ , where  $G$  is a DAG conveying the direct dependence relationships within the data set, while  $\Theta$  is the CPD of each variable. Assume that  $\prod_{x_i}$  represents the set of direct parents of  $x_i$  in  $G$ .  $\Theta$  contains a parameter  $\theta_{x_i | \prod_{x_i}} = P_B(x_i | \prod_{x_i})$  for each  $x_i$ , such that the network  $B$  can represent the following joint probability distribution [31]:

$$P_B(x_1, x_2, \dots, x_n) = \prod_{i=1}^n P_B(x_i | \prod_{x_i}) = \prod_{i=1}^n \theta_{x_i | \prod_{x_i}}. \quad (3)$$

**3.2.2. Bond Graph Based Causality Analysis.** The consistent causality description facilitates FDI or fault prognosis design because it is helpful for analyzing the fault propagation in the whole system. Causal path, a graphic representation based on the concept of causality, shows the causal relationships among the system variables. "0" and "1" controlled junctions are the multiple-ports components in bond graph based modeling. According to the definition of flow variable and effort variable, "1" junction indicates that every flow variable of the bonds connected to the junction equals the other, where the input variable is defined as the flow variable of the connected bond that has no causal stroke assigned at the junction. Similarly, a "0" junction indicates that each effort variable of the adjacently connected bonds equals the other,

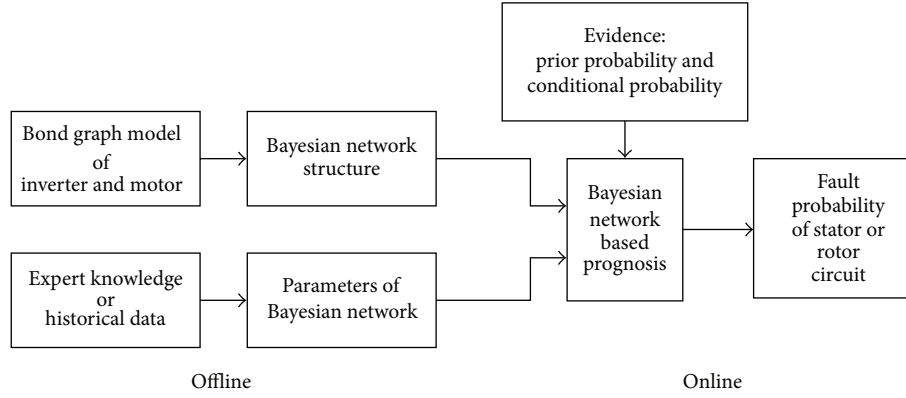


FIGURE 8: Overview of the fault prognosis based on Bayesian network.

where the input variable is defined as the effort variable of the connected bond that has a causal stroke assigned at the “0” junction. The storage elements are usually assigned preferred derivative causality [29].

The bond graph modeling implies the state equations describing the system dynamics. The causal relationships and power transfer between each component can be obtained clearly through the state equations coming from the bond graph. List the causal relationships of B-phase circuit in number 1 inverter as follows:

$$e_{15} = e_1 - e_{16},$$

$$e_{19} = e_{16} = e_{18} = e_{20} = e_{21},$$

$$f_{15} = \frac{e_{15}}{R_{\text{off}3}},$$

$$e_{40} = R_e f_{40},$$

$$e_{17} = e_1 - e_{18},$$

$$f_{41} = \frac{1}{L_e} \int e_{41} dt,$$

$$f_{17} = \frac{m_3^2}{R_{\text{on}3}} e_{17},$$

$$e_{43} = R_p f_{43},$$

$$e_{19} = R_{\text{off}6} f_{19},$$

$$f_{44} = \frac{1}{L_p} \int e_{44} dt,$$

$$f_{20} = \frac{m_6^2}{R_{\text{on}6}} e_{20},$$

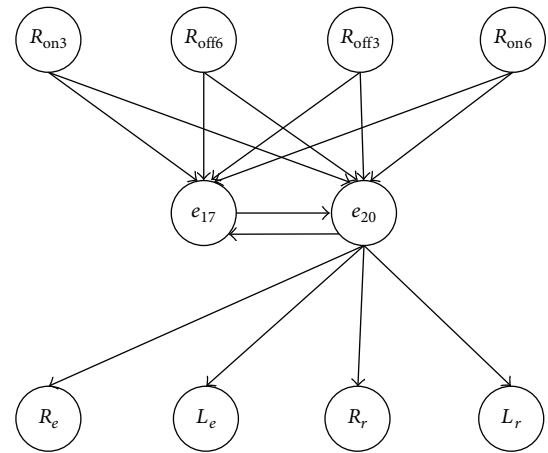


FIGURE 9: Directed graph of B-phase circuit.

$$e_{46} = R_r f_{46},$$

$$f_{19} = f_{16} + f_{18} - f_{20} - f_{21},$$

$$f_{47} = \frac{1}{L_r} \int e_{47} dt,$$

(4)

where  $e_{ij}$  represents the effort variable of bond number  $ij$  and  $f_{ij}$  represents the flow variable of bond number  $ij$ . According to (4), the sum of  $e_{17}$  and  $e_{20}$  equals a constant value  $e_1$ , the DC input, such that the effort variables  $e_{17}$  and  $e_{20}$  are the interrelationship of cause and effect. The directed graph (DG) of B-phase circuit in number 1 inverter is shown as in Figure 9.

**3.2.3. Building Bayesian Network.** The first step is to establish the directed links between variables for a causal network by using the causality derived from the bond graph model of CRH<sub>5</sub> traction system. Secondly, use intermediate variables

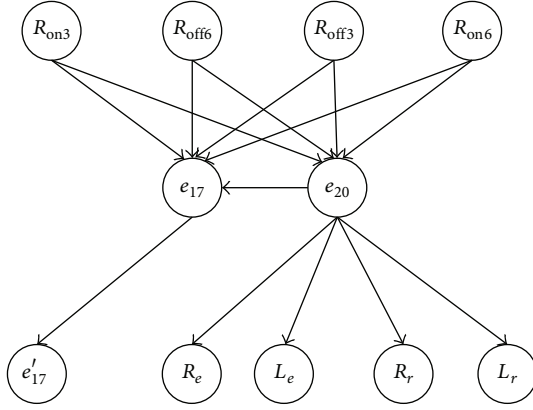


FIGURE 10: Bayesian network of B-phase circuit.

to obtain the conditional probability distributions (CPDs). Thirdly, specify the CPDs for each variable.

The directed graph model of B-phase circuit transforming from bond graph model is shown in Figure 9. Due to the reason that Bayesian network is a directed acyclic graph, some necessary simplifications are proposed for directed graph model having loops in [2]. The Bayesian network of B-phase circuit is shown in Figure 10,  $R_{on3}$ ,  $R_{off6}$ ,  $R_{off3}$ , and  $R_{on6}$  are the root nodes corresponding to the components of B-phase circuit in equivalent diagram.  $R_e$ ,  $L_e$ ,  $R_r$ , and  $L_r$  can indicate the behavior of the stator and rotor circuits which are the leaf nodes in the Bayesian network of the B-phase circuit.  $e'_{17}$  is the copied node of node  $e_{17}$  according to the procedure in [2].

**3.3. The Parameters of Bayesian Network.** Different parameter learning algorithms are used to obtain the conditional probability table of the Bayesian network for complete and incomplete data sets. For complete data sets, Bayesian estimation algorithm is used for parameter estimation. It searches the parameter value with maximum posterior probability according to the a priori knowledge when the topological structure  $S$  and training data set  $D$  are known:

$$P(\theta | D, S) = \frac{P(D | \theta, S) P(\theta | S)}{P(D | S)}, \quad (5)$$

where  $\theta$  is a fixed unknown parameter and  $P(\theta | S)$  is the prior probability of  $\theta$  under the topological structure  $S$ . Let polynomial parameters  $\theta_1, \theta_2, \dots, \theta_k$  satisfy  $\sum_{i=1}^k \theta_i = 1$ ; then the posterior probability of the parameter can be represented by (6) when  $P(\theta | S)$  is subject to Dirichlet distribution:

$$\begin{aligned} P(\theta | D, S) &= \text{Dir}(\theta | \alpha_1, \alpha_2, \dots, \alpha_k) \\ &= \frac{T(\alpha)}{\prod_{i=1}^k T(\alpha_i)} \prod_{i=1}^k \theta_i^{\alpha_i - 1}. \end{aligned} \quad (6)$$

The formula of parameter estimation is as follow:

$$\hat{\theta}_{v|u} = \text{Dir}(\alpha_l + N(x_1, u), \dots, \alpha_{v_k} + N(v_k, u)). \quad (7)$$

For incomplete data sets, the expectation maximization (EM) based iterative algorithm is used to compute the maximum likelihood probability of the network. Let initial value of the parameter be equal  $\theta^{(0)}$ . Modify the parameter constantly to achieve its maximum value of the maximum likelihood probability  $E[\ln p(Y | \theta)]$ , where  $Y$  is the whole of the training sample.

The probability distribution expectation of data set  $Y$  is represented as follows when the observable training sample  $D$  and current  $\theta$  are given:

$$\begin{aligned} Q(\theta^{(t)} | \theta) &= E[\ln p(Y | \theta^{(t)}) | \theta, D] \\ &= \sum_l \sum_{Z_l} \ln p(D_l, Z_l | \theta) p(Z_l | D_l, \theta^{(t)}). \end{aligned} \quad (8)$$

Maximize the function  $Q(\theta^{(t)} | \theta)$  by means of maximum likelihood estimation algorithm:

$$\theta^{(t)} = \arg \max_{\theta^{(t)}} Q(\theta^{(t)} | \theta), \quad (9)$$

where  $D$  represents observable data set;  $Z$  represents the data set which has not been observed; the whole training data  $Y = D \cup Z$ .

**3.4. Fault Prognosis Scheme.** In this paper, fault prognosis scheme based on Bayesian network of B-phase circuit is designed to predict fault probability of stator or rotor circuit that may cause abnormal behaviors of overall system. The Bayesian network based fault prognosis is a kind of prediction mechanism using joint probability distribution to obtain the fault probability of child nodes, when network structure, fault probabilities of the root nodes, and conditional probability table of the other nodes are given. The causal variable analysis is main application of Bayesian network when the observed statuses on any of the random variables are given. Conditional probability of unobserved nodes is updated through belief propagation and inference can be made about the most probable status [32]. In the example of Figure 10, if variable  $R_e$  is observed as true, the statuses of  $R_{off6}$  can be inferred from this evidence such that the probability  $P_{R_{off6}|R_e}(a, \text{ture})$  is needed for this inference, and it can be quantified by marginalizing the joint distribution under the condition that the status of  $R_e$  is known:

$$\begin{aligned} &P_{R_{off6}|R_e}(a, \text{true}) \\ &= \sum_b \sum_c \sum_e \sum_f \sum_g P(R_{off6}, R_{on3}, R_{off3}, R_e, R_{on6}, e_{20}, e_{17}) \\ &= \sum_b \sum_c \sum_e \sum_f \sum_g P_{R_{off6}}(a) P_{R_{on3}}(b) P_{R_{off3}|R_{off6}R_{on3}}(a, b, c) \dots, \end{aligned} \quad (10)$$

where  $a, b, c, d, e, f$ , and  $g$  are the values of the nodes  $R_{off6}$ ,  $R_{on3}$ ,  $R_{off3}$ ,  $R_e$ ,  $R_{on6}$ ,  $e_{20}$ , and  $e_{17}$ . The difficulty of this approach is that, as the number of nodes grows big, precise calculation of new condition probability becomes an NP-hard problem. Due to the reason above, the polytree propagation algorithm,

a Monte Carlo based approximate reasoning algorithm, is adopted in this paper. According to the Bayesian network in Figure 10, the fault probabilities of each node are as follows:

$$\begin{aligned}
P(e_{20} = f) &= \sum_{R_{on3,6}, R_{off3,6}} P(e_{20} = f | R_{on3}, R_{off6}, R_{off3}, R_{on6}) \\
&\quad \cdot P(R_{on3}, R_{off6}, R_{off3}, R_{on6}), \\
P(e_{17} = f) &= \sum_{R_{on3,6}, R_{off3,6}, e_{20}} P(e_{17} = f | R_{on3}, R_{off6}, R_{off3}, R_{on6}, e_{20}) \\
&\quad \cdot P(R_{on3}, R_{off6}, R_{off3}, R_{on6}, e_{20}), \\
P(R_e = f) &= \sum_{R_{on3,6}, R_{off3,6}, e_{20}} P(R_e = f | R_{on3}, R_{off6}, R_{off3}, R_{on6}, e_{20}) \\
&\quad \cdot P(R_{on3}, R_{off6}, R_{off3}, R_{on6}, e_{20}). \tag{11}
\end{aligned}$$

#### 4. Results and Discussions

Firstly, a bond graph model of CRH<sub>5</sub> traction system is formed in the environment of 20-SIM. When open-circuit fault happens on IGBT  $v_3$ , load current  $i_b$  loses its positive half wave, which may cause the motor stalling. When short-circuit fault happens on IGBT  $v_3$ ,  $i_b$  increases rapidly, such that short circuit on IGBT which may cause catastrophic failure on stator or rotor circuit is the fault we studied in simulation section.

In this section, 10000 sets of data produced by experiments are divided into 10 groups, where 600 sets of data are for training and 400 sets of data are for test in each group. According to [33], the fault distribution in electric drive system is as follows: power devices (37%), capacitors (20%), inductors (5%), resistors (2%), connectors (15%), gate drives (16%), and others (5%). What is more, in [33], the fault probabilities of IGBT open-circuit fault (37%) and short-circuit fault (43%) are also given. Regarding the complete data from experiments as the training sample of parameter learning, compute the conditional probability of intermediate nodes and leaf nodes by maximum likelihood estimation. The conditional probability table is shown in Table 2, where  $n$ ,  $f$  represent normal nodes and faulty nodes, respectively.

Predict the fault probability of stator or rotor circuit when short-circuit fault of IGBT components in B-phase inverter circuit happens. According to Pearl's polytree propagation algorithm used for joint probability reasoning, the prediction results on fault probability of stator and rotor circuit through 10000 sets of complete data are shown in Figures 11 and 12.

In modern engineering systems, some values in the measurement data set are missing such that EM (expectation maximization) method, a well-known parameter estimation algorithm, is used for probabilistic reasoning, combining with

TABLE 2: Conditional probability table of parameter learning.

Conditional probability	Value
$P(R_{on3} = f)$	0.137
$P(R_{off6} = f)$	0.159
$P(R_{off3} = f)$	0.159
$P(R_{on6} = f)$	0.137
$P(e_{20} = f   R_{on3} = n, R_{off6} = n, R_{off3} = n, R_{on6} = n)$	0
$P(e_{20} = f   R_{on3} = f, R_{off6} = n, R_{off3} = n, R_{on6} = n)$	0.95
$P(e_{20} = f   R_{on3} = n, R_{off6} = f, R_{off3} = n, R_{on6} = n)$	0.95
$P(e_{20} = f   R_{on3} = n, R_{off6} = n, R_{off3} = f, R_{on6} = n)$	0.95
$P(e_{20} = f   R_{on3} = n, R_{off6} = n, R_{off3} = n, R_{on6} = f)$	0.95
$P(e_{20} = f   R_{on3} = f, R_{off6} = f, R_{off3} = n, R_{on6} = n)$	0.98
$P(e_{20} = f   R_{on3} = f, R_{off6} = n, R_{off3} = n, R_{on6} = f)$	0.92
$P(e_{20} = f   R_{on3} = n, R_{off6} = f, R_{off3} = f, R_{on6} = n)$	0.92
$P(e_{20} = f   R_{on3} = n, R_{off6} = n, R_{off3} = f, R_{on6} = f)$	0.98
$P(R_e   e_{20})$	0.511
$P(L_e   e_{20})$	0.511
$P(R_r   e_{20})$	0.370
$P(L_r   e_{20})$	0.370

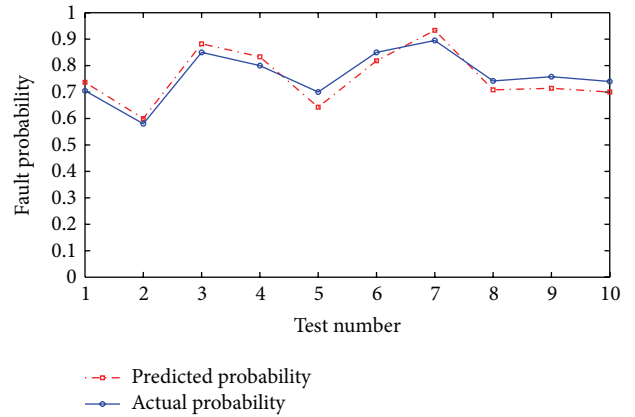


FIGURE 11: Fault prognosis of stator circuit.

Pearl's polytree propagation algorithm. Each iteration step of EM algorithm contains two steps: the E-step (expectation) and the M-step (maximization). The procedure alternates between the two steps until convergence is achieved. It should be pointed out that the search speed will slow down when EM algorithm comes close to its convergence point.

In this simulation, 10000 sets of data are hidden randomly by 20% to imitate the data missing. The remaining sets are divided into 10 groups, where 600 sets of data are for training and 200 sets of data are for test in each group. The conditional probability table of each node can be obtained by EM algorithm. Predict the fault probability of leaf nodes by Pearl's polytree propagation algorithm when prior probabilities of the root nodes are given. In Figures 13 and 14, the prediction results of stator or rotor circuit under incomplete data can also verify effectiveness of the proposed approach.

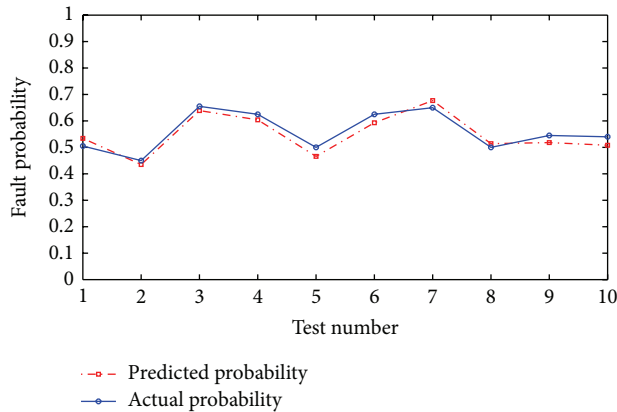


FIGURE 12: Fault prognosis of rotor circuit.

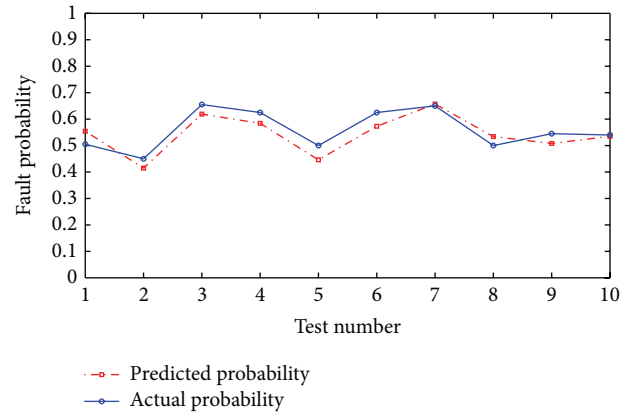


FIGURE 14: Fault prognosis of rotor circuit.

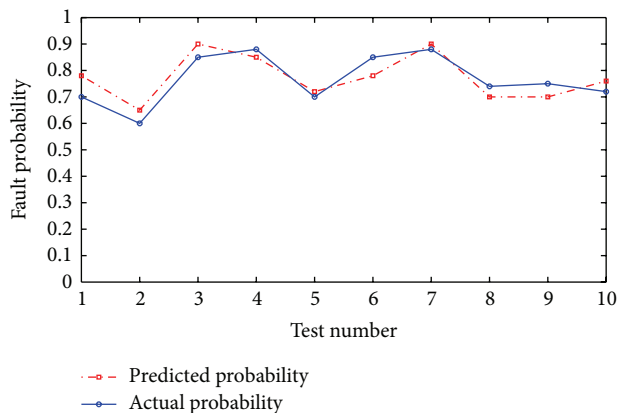


FIGURE 13: Fault prognosis of stator circuit.

## 5. Conclusion

According to the schematic diagram of CRH<sub>5</sub> traction system, a bond graph based model of inverter circuit and three-phase AC motor is built. Then, a bond graph and Bayesian network based fault prognosis approach is proposed to predict the fault probability of stator and rotor circuit, when the prior fault probabilities of IGBT components are given. The bond graph based model of CRH<sub>5</sub> traction system is used for building the Bayesian network, which can solve the problem of constructing an accurate Bayesian network structure in practice. Different parameter learning algorithms, such as Bayesian estimation and EM algorithm, are adopted to determine the conditional probability table of the Bayesian network for complete and incomplete data sets. The fault probabilities of leaf nodes (stator and rotor circuit) can be predicted by joint probability reasoning through Pearl's polytree propagation algorithm. The simulation results can verify its effectiveness in fault prognosis for both complete and incomplete data sets. Our future works lie in the following: (1) the bond graph modeling of junction parts should be considered; (2) some new bond graph modeling approaches of power switching device (IGBT) can be adopted in our future work to achieve a more accurate modeling.

## Conflict of Interests

The authors declare that there is no conflict of interests regarding the publication of this paper.

## Acknowledgments

This work was supported by National Natural Science Foundation of China (61490703, 61374141 and 61304112), Funding of Jiangsu Innovation Program for Graduate Education KYLX.0280, and the Fundamental Research Funds for the Central Universities (NE2014202).

## References

- [1] G. Vachtsevanos, F. L. Lewis, M. Roemer, A. Hess, and B. Wu, *Intelligent Fault Diagnosis and Prognosis for Engineering Systems*, John Wiley & Sons, New York, NY, USA, 2007.
- [2] N. Lu, K. He, and B. Jiang, "A fault prognosis method using Bayesian network," *Journal of Southeast University*, vol. 42, no. A01, pp. 87–91, 2012.
- [3] L.-J. Xu, H.-J. Wang, and B. Long, "Fault prediction of complex systems based on Bayesian network," *Systems Engineering and Electronics*, vol. 30, no. 4, pp. 780–784, 2008.
- [4] F. V. Jensen, *Bayesian Networks and Decision Graphs*, Springer, New York, NY, USA, 2001.
- [5] M. Singh and M. Valtorta, "Construction of Bayesian network structures from data: a brief survey and an efficient algorithm," *International Journal of Approximate Reasoning*, vol. 12, no. 2, pp. 111–131, 1995.
- [6] A. Okutan and O. T. Yıldız, "Software defect prediction using Bayesian networks," *Empirical Software Engineering*, vol. 19, no. 1, pp. 154–181, 2014.
- [7] J. Lin, M. Asplund, and A. Parida, "Reliability analysis for degradation of locomotive wheels using parametric Bayesian approach," *Quality and Reliability Engineering International*, vol. 1, no. 1, pp. 1–11, 2013.
- [8] H. Paynter, *Analysis and Design of Engineering Systems*, MIT Press, Cambridge, Mass, USA, 1961.
- [9] G. Dauphin-Tanguy, *Les Bond Graphs*, HERMES Science, Paris, France, 2007.

- [10] J. U. Thoma, *Introduction to Bond Graphs and Their Applications*, Pergamon Press, New York, NY, USA, 1975.
- [11] N. Banerjee and R. Karmakar, "Bond graph modeling of rail wheelset on curved track," *Simulation*, vol. 83, no. 10, pp. 695–706, 2007.
- [12] G. Gandanegara, X. Roboam, B. Sareni, and G. Dauphin-Tanguy, "Bond-graph-based model simplification for system analysis: application to a railway traction device," *Proceedings of the Institution of Mechanical Engineers, Part I: Journal of Systems and Control Engineering*, vol. 220, no. 7, pp. 553–571, 2006.
- [13] J. Lozano, J. Felez, and J. D. Sanz, "Comparative study of railway drive systems using bond-graph," in *Proceedings of the Spring Simulation Multiconference*, April 2010.
- [14] J. Kim and M. D. Bryant, "Bond graph model of a squirrel cage induction motor with direct physical correspondence," *Journal of Dynamic Systems, Measurement, and Control*, vol. 122, no. 3, pp. 461–469, 2000.
- [15] D. Du, B. Jiang, P. Shi, and H. Karimi, "Fault detection for continuous-time switched systems under asynchronous switching," *International Journal of Robust and Nonlinear Control*, vol. 24, no. 11, pp. 1694–1706, 2014.
- [16] D. Du, B. Jiang, and P. Shi, "Fault detection for discrete-time switched systems with intermittent measurements," *International Journal of Control*, vol. 85, no. 1, pp. 78–87, 2012.
- [17] Z. Mao, B. Jiang, and P. Shi, "Fault detection for a class of nonlinear networked control systems," *International Journal of Adaptive Control and Signal Processing*, vol. 24, no. 7, pp. 610–622, 2010.
- [18] X.-Z. Gao, H. Xu, X. Wang, and K. Zenger, "A study of negative selection algorithm-based motor fault detection and diagnosis," *International Journal of Innovative Computing, Information and Control*, vol. 9, no. 2, pp. 875–901, 2013.
- [19] Y. Kourad, D. Lefebvre, and N. Guersi, "Fault diagnosis based on neural networks and decision trees: application to DAMADICS," *International Journal of Innovative Computing, Information and Control*, vol. 9, no. 8, pp. 3185–3196, 2013.
- [20] P. J. Mosterman and G. Biswas, "Diagnosis of continuous valued systems in transient operating regions," *IEEE Transactions on Systems, Man, and Cybernetics Part A: Systems and Humans*, vol. 29, no. 6, pp. 554–565, 1999.
- [21] K. Medjaher, A. K. Samantaray, B. O. Bouamama, and M. Staroswiecki, "Supervision of an industrial steam generator. Part II: online implementation," *Control Engineering Practice*, vol. 14, no. 1, pp. 85–96, 2006.
- [22] A. K. Samantaray, K. Medjaher, B. O. Bouamama, M. Staroswiecki, and G. Dauphin-Tanguy, "Diagnostic bond graphs for online fault detection and isolation," *Simulation Modelling Practice and Theory*, vol. 14, no. 3, pp. 237–262, 2006.
- [23] A. K. Samantaray and S. K. Ghoshal, "Bicausal bond graphs for supervision: from fault detection and isolation to fault accommodation," *Journal of the Franklin Institute*, vol. 345, no. 1, pp. 1–28, 2008.
- [24] X. Zhang and K. A. Hoo, "Effective fault detection and isolation using bond graph-based domain decomposition," *Computers and Chemical Engineering*, vol. 35, no. 1, pp. 132–148, 2011.
- [25] M. Yu and D. Wang, "Model-based health monitoring for a vehicle steering system with multiple faults of unknown types," *IEEE Transactions on Industrial Electronics*, vol. 61, no. 7, pp. 3574–3586, 2014.
- [26] S. Zhang, *CRH5 Series High-Speed Railway Vehicle*, China Railway Publishing, Beijing, China, 2008.
- [27] M. A. Djeziri, R. Merzouki, B. Ould Bouamama, and G. Dauphin-Tanguy, "Bond graph model based for robust fault diagnosis," in *Proceedings of the American Control Conference (ACC '07)*, pp. 3017–3022, July 2007.
- [28] A. K. Samantaray and B. O. Bouamama, *Model-Based Process Supervision: A Bond Graph Approach*, Springer, Berlin, Germany, 2008.
- [29] C. B. Low, D. Wang, S. Arogeti, and J. B. Zhang, "Causality assignment and model approximation for hybrid bond graph: fault diagnosis perspectives," *IEEE Transactions on Automation Science and Engineering*, vol. 7, no. 3, pp. 570–580, 2010.
- [30] C. H. Lo, Y. K. Wong, and A. B. Rad, "Bond graph based Bayesian network for fault diagnosis," *Applied Soft Computing Journal*, vol. 11, no. 1, pp. 1208–1212, 2011.
- [31] K. Dejaeger, T. Verbraken, and B. Baesens, "Toward comprehensible software fault prediction models using bayesian network classifiers," *IEEE Transactions on Software Engineering*, vol. 39, no. 2, pp. 237–257, 2013.
- [32] L. Yang and J. Lee, "Bayesian Belief Network-based approach for diagnostics and prognostics of semiconductor manufacturing systems," *Robotics and Computer-Integrated Manufacturing*, vol. 28, no. 1, pp. 66–74, 2012.
- [33] S. Yang, A. Bryant, P. Mawby, D. Xiang, L. Ran, and P. Tavner, "An industry-based survey of reliability in power electronic converters," *IEEE Transactions on Industry Applications*, vol. 47, no. 3, pp. 1441–1451, 2011.

## Research Article

# Fault Tolerant Control for Uncertain Time-Delay Systems with a Trajectory Tracking Approach

ShiLei Zhao, Hong Guo, and YuPeng Liu

*School of SoftWare, Harbin University of Science and Technology, Harbin 150036, China*

Correspondence should be addressed to ShiLei Zhao; zhaosli210@126.com

Received 13 September 2014; Revised 31 December 2014; Accepted 2 January 2015

Academic Editor: Vincent Cocquempot

Copyright © 2015 ShiLei Zhao et al. This is an open access article distributed under the Creative Commons Attribution License, which permits unrestricted use, distribution, and reproduction in any medium, provided the original work is properly cited.

This paper studies the problem of fault tolerant control by trajectory tracking for a class of linear constant time-delay systems. The aim is to design a control law by considering the fault detected by the observer to make the faulty system track the reference model even if faults occur. By considering two kinds of actuator faults, one constant and another time-varying, the corresponding proportional integral observers and active FTC control laws are designed, respectively. State tracking error, state estimation error, output estimation error, and fault estimation error are combined into a descriptor system. Based on Lyapunov-Krasovskii functional approach stability problems of the descriptor system are easily solved in terms of the Linear Matrix Inequalities (LMI). Finally, a numerical example is considered to prove the effectiveness in both cases.

## 1. Introduction

Over the past few decades, problems of fault tolerant control, well known as FTC, in dynamic systems have attracted lots of attention [1, 2]. FTC has been developed to preserve the system stability and maintain acceptable performances in case of faults occurring. The existing FTC strategies can be divided into two categories. The first one, named as the passive FTC, treats the fault as uncertainty; therefore, it involves no fault detection and estimation (see [3–5]). The second one, the active FTC, differs from the passive FTC in that it requires a fault detection and isolation (FDI) block to detect, isolate, and estimate faults which are used to compensate the fault and ensure an acceptable system performance (e.g., [6–8]). As the obtained fault information is used, the active FTC is more reliable.

On the other hand, time-delay is another factor that can degrade system performance; it is a built-in feature in many engineering systems. The presence of time-delay, together with faults, could cause system to be instable easily. Therefore, researching on FTC design of time-delay system has great practical and theoretical significance [9]; this challenging topic has ignited the interest of some authors. For example, [10, 11] provide a kind of fault detection method based on an

iterative learning observer for nonlinear constant state delay systems. Reference [12] designs  $H_\infty$  fault detection filters for multiple time-delay discrete-time systems. Based on a switched descriptor observer approach, [13] deals with sensor fault estimation and compensation problems of time-delay switched systems. In [14], for both additive and multiplicative faults, a robust fault detection and isolation scheme is proposed for uncertain continuous linear systems with discrete state delays. In [15], a fault detection filter is investigated for a class of discrete-time switched linear systems with time-varying delays so that the different estimation errors are minimized. In [16], some adaptive fault diagnosis observers (AFDO) are designed to deal with fast fault estimation and accommodation problems for time-varying delay systems.

Recently, there is also an active FTC approach based on trajectory tracking, developed to solve the FTC problem. This scheme is composed of faulty system, reference model, observer, and controller and its aim is to design a control law by considering actuator faults detected by observers and to make the faulty system states track the reference model states which are not effected by faults [17–19].

This paper is about to develop a strategy for linear constant time-delay systems based on trajectory tracking. The motivation of this paper mainly stems from two facts:

(1) some FTC schemes of time-delay systems are obtained [20, 21], but less work which studies on FTC problems employs the descriptor redundancy property and solves the fault isolation, estimation, and FTC problems together; (2) there is some work addressing FTC designs based on trajectory tracking which focused on linear time invariant (LTI) system without time-delay, but few work is focused on FTC of time-delay systems. Our work will extend earlier results of fault estimation using trajectory tracking to the time-delay systems.

In this paper, our purpose is to study the FTC design problem for linear state time-delay systems subjected to constant or time-varying faults. The main idea is to design an active FTC controller and PI observer and to use the virtual dynamic [22–24] in both active FTC law and output estimation error expression to turn the problem under study into a descriptor system. By using the Lyapunov-Krasovskii functional approach, the stability of the descriptor system has been proved. The advantages of the proposed method is also based on the above two facts: (1) the introduction of trajectory tracking can ensure the tracking of faulty systems to reference models, which could guarantee an acceptable system performance even if faults occur; (2) the descriptor redundancy property can avoid crossed terms in the LMI and then decrease the number of LMI conditions and consequently relax the conservatism [17].

This paper is organized as follows. In the next section, the system under study and the active FTC scheme based on trajectory tracking are presented. In Section 3, FTC design for linear state time-delay systems affected by constant fault without uncertainties is established. Then, some FTC design for linear state time-delay systems affected by time-varying faults with uncertainties is given. In the last section, a numerical example for constant faults without uncertainties and time-varying faults with uncertainties is considered to illustrate the applicability and effectiveness of the proposed approaches.

*Notations.* In a block matrix, the notation  $*$  stands for the terms induced by symmetry. The superscript  $T$  denotes matrix transpose,  $\text{sym}(A)$  denotes  $A + A^T$ , and  $\text{diag}\{\dots\}$  stands for a block-diagonal matrix.

The following lemma is needed to provide LMI conditions.

**Lemma 1.** *For any matrices  $X$ ,  $Y$ , and  $\Sigma(t)$  with appropriate dimensions and  $\Sigma^T(t)\Sigma(t) < I$  and for any positive real number  $t$ , it follows that*

$$X^T \Sigma^T(t) Y + Y^T \Sigma(t) X \leq t X^T X + t^{-1} Y^T Y. \quad (1)$$

## 2. Problem Formulation

Consider the following system without faults corresponding to a reference model:

$$\begin{aligned} \dot{x}(t) &= Ax(t) + Bu(t) + A_d x(t-h), \\ y &= Cx(t) + C_d x(t-h), \end{aligned} \quad (2)$$

where  $x(t) \in R^n$  is the state vector,  $u(t) \in R^m$  is the input vector, and  $y(t) \in R^p$  is the output vector.  $A$ ,  $B$ ,  $A_d$ ,  $C$ , and  $C_d$  are known constant real matrices of appropriate dimensions.  $h$  is the state delay and  $h \in R^+$  is a constant real number.

Consider the faulty system given by

$$\begin{aligned} \dot{x}_f(t) &= \bar{A}x_f(t) + \bar{A}_d x_f(t-h) + \bar{B}u_f(t) + \bar{B}f(t), \\ y_f(t) &= \bar{C}x_f(t) + \bar{C}_d x_f(t-h), \end{aligned} \quad (3)$$

where  $x_f(t) \in R^n$ ,  $u_f(t) \in R^m$ ,  $y_f(t) \in R^p$ , and  $f(t) \in R^m$  are the faulty state vector, the fault tolerant control vector, the faulty output vector, and the fault vector affecting the system behavior. And the uncertainties of system (3) are defined by

$$\bar{X}(t) = X + \Delta X(t), \quad X \in \{A, A_d, B, C, C_d\}, \quad (4)$$

where  $\Delta A$ ,  $\Delta A_d$ ,  $\Delta B$ ,  $\Delta C$ , and  $\Delta C_d$  are time-varying unknown matrices describing the bounded model uncertainties, defined by

$$\begin{aligned} \Delta X(t) &= M_x F(t) N_x, \\ (X, x) &= \{(A, a), (A_d, ad), (B, b), (C, c), (C_d, cd)\}, \end{aligned} \quad (5)$$

where  $M_a$ ,  $M_{ad}$ ,  $M_b$ ,  $M_c$ ,  $M_{cd}$ ,  $N_a$ ,  $N_{ad}$ ,  $N_b$ ,  $N_c$ , and  $N_{cd}$  are known constant real matrices with appropriate dimensions and the matrix function  $F(t)$  is bounded by

$$F(t) F(t)^T \leq I. \quad (6)$$

In order to estimate the fault vector  $f(t)$  which is required by the FTC scheme and the faulty system states  $x_f(t)$ , we consider the PI observer as follows:

$$\begin{aligned} \hat{\dot{x}}_f(t) &= A\hat{x}_f(t) + A_d \hat{x}_f(t-h) + Bu_f(t) \\ &\quad + B\hat{f}(t) + H_1(y_f(t) - \hat{y}_f(t)), \\ \hat{f}(t) &= H_2(y_f(t) - \hat{y}_f(t)), \\ \hat{y}_f(t) &= C\hat{x}_f(t) + C_d \hat{x}_f(t-h), \end{aligned} \quad (7)$$

where  $H_1 \in R^{n \times p}$  and  $H_2 \in R^{r \times p}$  are the observer's gain matrices to be determined.

## 3. Fault Tolerant Controller Design

In this section, two cases are considered according to the characteristics of faults. First, we assume that the fault is a constant one and there are no uncertainties in faulty system (6). Second, assume that the fault is a time-varying one and there are uncertainties in the faulty system.

The FTC design scheme is illustrated in Figure 1. The objective of this work is to ensure the tracking of the faulty system to the nominal one. In other words, the scheme is to design FTC law and observer gain matrices to minimize the differences between the faulty states of (3) and the reference states given by model (2), the faulty system states and the observer states, the faulty system estimation output and

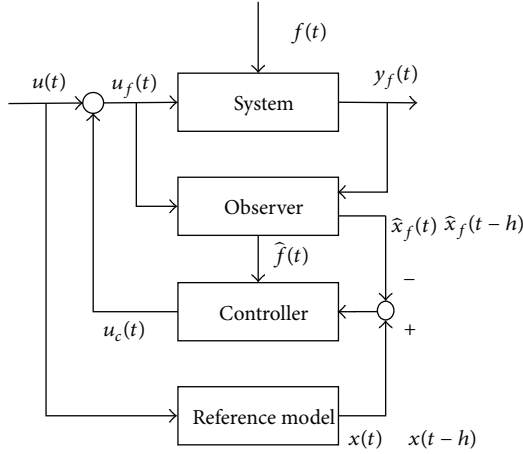


FIGURE 1: The controller scheme.

the reference model output, and the nominal input and the FTC input plus the fault.

From the FTC scheme of Figure 1, the following FTC law structure is proposed [17]:

$$u_f(t) = u(t) + K_1(x(t) - \hat{x}_f(t)) - \hat{f}(t) + K_2(x(t-h) - \hat{x}_f(t-h)), \quad (8)$$

where  $K_1, K_2 \in R^{m \times n}$  are the state feedback gain matrices to guarantee the stability of the faulty system even if the fault occurs and minimize the difference between the faulty system and the reference one.

**3.1. First Case: Constant Fault without Uncertainties.** It is here considered that the fault which affects the system actuator is a constant bias. Obviously, it is a special case that the fault satisfies

$$\dot{f}(t) = 0. \quad (9)$$

In the following part, to ensure the tracking, we first give state error, fault estimation error, output error and tracking error, and the difference between nominal input and FTC input plus the fault, respectively, by

$$\begin{aligned} e_p(t) &= x(t) - x_f(t), \\ e_s(t) &= x_f(t) - \hat{x}_f(t), \\ e_f(t) &= f(t) - \hat{f}(t), \\ e_y(t) &= y_f(t) - \hat{y}_f(t), \\ e_u(t) &= u(t) - (u_f(t) + f(t)). \end{aligned} \quad (10)$$

By using formulae (2), (3), (7), and (10), the dynamics of  $e_p(t)$  and  $e_s(t)$  are given by

$$\begin{aligned} \dot{e}_p(t) &= Ae_p(t) + Be_u(t) + A_d e_p(t-h), \\ \dot{e}_s(t) &= Ae_s(t) + Be_f(t) - H_1 e_y(t) + A_d e_s(t-h). \end{aligned} \quad (11)$$

The fault estimation error dynamics  $e_f(t)$  is expressed as follows:

$$\dot{e}_f(t) = \dot{f}(t) - \dot{\hat{f}}(t) = -H_2 e_y(t). \quad (12)$$

The output estimation error  $e_y(t)$  can be written in the form of

$$e_y(t) = Ce_s(t) + C_d e_s(t-h). \quad (13)$$

In order to organize the above equations into the form of descriptor systems, we can introduce a ‘‘virtual dynamics’’ in the output estimation error; this latter can be rewritten as

$$0\dot{e}_y(t) = Ce_s(t) + C_d e_s(t-h) - e_y(t). \quad (14)$$

By adding and subtracting  $K_1 x_f(t)$ ,  $K_2 x_f(t-h)$ , and  $f(t)$  in (8) and using (10), one can obtain

$$\begin{aligned} 0\dot{e}_u(t) &= K_1 e_p(t) + K_1 e_s(t) + K_2 e_p(t-h) \\ &\quad + K_2 e_s(t-h) + e_f(t) + e_u(t). \end{aligned} \quad (15)$$

The combinations of (11), (12), (14), and (15) yield a descriptor system expressed as follows:

$$E\dot{e}(t) = \tilde{A}e(t) + \tilde{A}_d e(t-h), \quad (16)$$

where  $E = \text{diag}\{I_{2n+m}, 0_{m+p}\}$ ,

$$\begin{aligned} e(t) &= (e_p^T(t), e_s^T(t), e_f^T(t), e_u^T(t), e_y^T(t))^T, \\ \tilde{A} &= \begin{bmatrix} A & 0 & 0 & B & 0 \\ 0 & A & B & 0 & -H_1 \\ 0 & 0 & 0 & 0 & -H_2 \\ K_1 & K_1 & I & I & 0 \\ 0 & C & 0 & 0 & -I \end{bmatrix}, \\ \tilde{A}_d &= \begin{bmatrix} A_d & 0 & 0 & 0 & 0 \\ 0 & A_d & 0 & 0 & 0 \\ 0 & 0 & 0 & 0 & 0 \\ K_2 & K_2 & 0 & 0 & 0 \\ 0 & C_d & 0 & 0 & 0 \end{bmatrix}. \end{aligned} \quad (17)$$

The main proposed result can now be established [25].

**Theorem 2.** *The tracking error  $e_p(t)$ , the state error  $e_s(t)$ , and fault estimation error  $e_f(t)$  asymptotically converge to zero if there exist some matrices  $P_1 > 0$ ,  $P_2 > 0$ ,  $P_3 > 0$ , and matrices  $Y_2$  and  $Y$  with appropriate dimensions, such that the following inequalities hold:*

$$\begin{bmatrix} \Omega & Y \\ Y^T & -\frac{P_3}{h} \end{bmatrix} < 0, \quad (18)$$

where the expression of  $\Omega$  is shown as follows:

$$\begin{aligned} \Omega &= W_p P_2 W_p^T + h W_{p1} E^T P_3 E W_{p1}^T - W_{ph} P_2 W_{ph}^T \\ &+ \text{sym} \left[ W_p P_1 W_{p1}^T + Y E W_p^T + Y E W_{ph}^T \right. \\ &\quad \left. + (Y_2 A_0 - H C_1 - X C_2) W_p^T \right. \\ &\quad \left. + (Y_2 A_{d0} - K C_3) W_{ph}^T \right], \\ W_p &= [I_{2n+2m+p} \ 0 \ 0], \quad W_{ph} = [0 \ I_{2n+2m+p} \ 0], \\ W_{p1} &= [0 \ 0 \ I_{2n+2m+p}], \\ Y_2 &= [\tilde{Y}_2^T \ \tilde{Y}_2^T \ \tilde{Y}_2^T]^T, \quad X = [\tilde{X}^T \ \tilde{X}^T \ \tilde{X}^T]^T, \\ \tilde{X} &= [0 \ 0 \ 0 \ X_{41}^T \ 0]^T, \quad K = [\tilde{K}^T \ \tilde{K}^T \ \tilde{K}^T]^T, \\ \tilde{K} &= [0 \ 0 \ 0 \ K_{42}^T \ 0]^T, \quad H = [\tilde{H}^T \ \tilde{H}^T \ \tilde{H}^T]^T, \\ \tilde{H} &= [0 \ H_{21}^T \ H_{32}^T \ 0 \ 0]^T, \quad C_1 = [0 \ 0 \ 0 \ 0 \ I], \\ C_2 &= [I \ I \ 0 \ 0 \ 0], \quad C_3 = C_2, \\ A_0 &= \begin{bmatrix} A & 0 & 0 & B & 0 \\ 0 & A & B & 0 & 0 \\ 0 & 0 & 0 & 0 & 0 \\ 0 & 0 & I & I & 0 \\ 0 & C & 0 & 0 & -I \end{bmatrix}, \quad A_{d0} = \begin{bmatrix} A_d & 0 & 0 & 0 & 0 \\ 0 & A_d & 0 & 0 & 0 \\ 0 & 0 & 0 & 0 & 0 \\ 0 & 0 & 0 & 0 & 0 \\ 0 & C_d & 0 & 0 & 0 \end{bmatrix}, \\ \tilde{Y}_2 &= \begin{bmatrix} Y_{11} & 0 & 0 & 0 & 0 \\ 0 & Y_{12} & 0 & 0 & 0 \\ 0 & 0 & Y_{13} & 0 & 0 \\ Y_{16} & 0 & 0 & Y_{14} & Y_{18} \\ Y_{17} & 0 & 0 & 0 & Y_{15} \end{bmatrix}, \end{aligned} \quad (19)$$

where  $Y_{12}$ ,  $Y_{13}$ , and  $Y_{14}$  are invertible matrices and  $Y_{11}$ ,  $Y_{15}$ ,  $Y_{16}$ ,  $Y_{17}$ , and  $Y_{18}$  are slack matrices.

The observer and controller gains are then computed by

$$\begin{aligned} K_1 &= (Y_{14})^{-1} X_{41}, \quad K_2 = (Y_{14})^{-1} K_{42}, \\ H_1 &= (Y_{12})^{-1} H_{21}, \quad H_2 = (Y_{13})^{-1} H_{32}. \end{aligned} \quad (20)$$

**Remark 3.** It should be mentioned that the free weighting matrix  $Y_2$  has the structure of  $Y_2 = [\tilde{Y}_2^T \ \tilde{Y}_2^T \ \tilde{Y}_2^T]^T$ . But the conservatism would increase; in order to obtain a tractable matrix condition, we can adopt the method by defining

$$Y_2 = \begin{bmatrix} \alpha_1 I & 0 & 0 \\ 0 & \alpha_2 I & 0 \\ 0 & 0 & \alpha_3 I \end{bmatrix} \begin{bmatrix} \tilde{Y}_2 \\ \tilde{Y}_2 \\ \tilde{Y}_2 \end{bmatrix}, \quad (21)$$

where  $\alpha_1$ ,  $\alpha_2$ , and  $\alpha_3$  are the real number.

By choosing these scalars appropriately, the conservatism cannot increase much. This method has been used by [23].

*Proof.* Choose a Lyapunov-Krasovskii functional candidate as

$$V(t) = V_1(t) + V_2(t) + V_3(t), \quad (22)$$

$$V_1(t) = e^T(t) E^T P_1 e(t),$$

$$V_2(t) = \int_{-h}^0 \int_{t+\nu}^t e^T(\omega) E^T P_3 E \dot{e}(\omega) d\omega d\nu, \quad (23)$$

$$V_3(t) = \int_{t-h}^t e^T(\omega) P_2 e(\omega) d\omega,$$

where  $P_1$  satisfies  $E^T P_1 = P_1 E$ .

The time derivatives of  $V(t)$  are given by

$$\begin{aligned} \dot{V} &= 2e^T(t) P_1 E \dot{e}(t) + h \dot{e}^T(t) E^T P_3 E \dot{e}(t) \\ &\quad - \int_{t-h}^t \dot{e}^T(\omega) E^T P_3 E \dot{e}(\omega) d\omega + e^T(t) P_2 e(t) \\ &\quad - e^T(t-h) P_2 e(t-h). \end{aligned} \quad (24)$$

According to the Newton-Lebniz formula and closed-loop system equation, the following equations are true:

$$\Pi_1 = \xi^T(t) Y E \left[ e(t) - e(t-h) - \int_{t-h}^t \dot{e}(\omega) d\omega \right] = 0, \quad (25)$$

$$\Pi_2 = \xi^T(t) Y_2 [\tilde{A}e(t) - \tilde{A}_d e(t-h) - E\dot{e}(t)] = 0,$$

where  $Y, Y_2$  are appropriate dimensioned matrices and  $\xi(t) = [e^T(t), e^T(t-h), (E\dot{e}(t))^T]^T$ .

Adding  $2\Pi_1$ ,  $2\Pi_2$ , and  $h\xi^T(t) Y P_3^{-1} Y^T \xi(t)$  and subtracting  $\int_{t-h}^t \xi^T(t) Y P_3^{-1} Y^T \xi(t) d\omega$ , respectively, in (24) yield (26) which is shown as follows:

$$\begin{aligned} \dot{V}(t) &= 2e^T(t) E^T P_1 \dot{e}(t) + h \dot{e}^T(t) E^T P_3 E \dot{e}(t) \\ &\quad - \int_{t-h}^t \dot{e}^T(\omega) E^T P_3 E \dot{e}(\omega) d\omega + e^T(t) P_2 e(t) \\ &\quad - e^T(t-h) P_2 e(t-h) \\ &\quad + 2\xi^T(t) Y E \left[ e(t) - e(t-h) - \int_{t-h}^t \dot{e}(\omega) d\omega \right] \\ &\quad + 2\xi^T(t) Y_2 [\tilde{A}e(t) + \tilde{A}_d e(t-h) - E\dot{e}(t)] \\ &= 2e^T(t) P_1 E \dot{e}^T(t) + h \dot{e}^T(t) E^T P_3 E \dot{e}(t) \\ &\quad - \int_{t-h}^t \dot{e}^T(\omega) E^T P_3 E \dot{e}(\omega) d\omega + e^T(t) P_2 e(t) \\ &\quad - e^T(t-h) P_2 e(t-h) \\ &\quad + 2\xi^T(t) Y E \left[ e(t) - e(t-h) - \int_{t-h}^t \dot{e}(\omega) d\omega \right] \\ &\quad + 2\xi^T(t) Y_2 [\tilde{A}e(t) + \tilde{A}_d e(t-h) - E\dot{e}(t)] \\ &\quad + h \xi^T(t) Y P_3^{-1} Y^T \xi(t) - \int_{t-h}^t \xi^T(t) Y P_3^{-1} Y^T \xi(t) d\omega \end{aligned}$$

$$\begin{aligned}
 &= \xi^T(t) \Omega \xi(t) + h \xi^T(t) Y P_3^{-1} Y^T \xi(t) \\
 &\quad - \int_{t-h}^t \left[ \xi^T(t) Y + \dot{e}^T(\omega) E^T P_3 \right] \\
 &\quad \times P_3^{-1} \left[ Y^T \xi(t) + P_3 E \dot{e}(\omega) \right] d\omega.
 \end{aligned} \tag{26}$$

Then, we know from (26) that  $\Omega + h Y P_3^{-1} Y^T < 0$  which guarantees  $\dot{V}(t)$  is nonpositiveness for nonzero  $\xi(t)$ . One can always find a sufficiently small  $\epsilon > 0$  such that  $\dot{V}(t) \leq -\epsilon \|e(t)\|^2$  and the asymptotic stability of the system is proved.  $\square$

**3.2. Second Case: Time-Varying Fault with Uncertainties.** In this part, we consider system (3) with the uncertainties and the fault being time-varying one. Here, we modify PI observer slightly as follows:

$$\begin{aligned}
 \dot{\hat{x}}_f(t) &= A \hat{x}_f(t) + A_d \hat{x}_f(t-h) + B u_f(t) \\
 &\quad + B \hat{f}(t) + H_1 (y_f(t) - \hat{y}_f(t)), \\
 \dot{\hat{f}}(t) &= H_2 (y_f(t) - \hat{y}_f(t)) - \hat{f}(t), \\
 \hat{y}_f(t) &= C \hat{x}_f(t) + C_d \hat{x}_f(t-h).
 \end{aligned} \tag{27}$$

The dynamics of  $e_p(t)$ ,  $e_s(t)$ , and  $e_f(t)$  are given by

$$\begin{aligned}
 \dot{e}_p(t) &= A e_p(t) + \Delta A e_p(t) + B e_u(t) + \Delta B e_u(t) \\
 &\quad + A_d e_p(t-h) - \Delta A x(t) \\
 &\quad + \Delta A_d e_p(t-h) - \Delta A_d x(t-h) - \Delta B u(t), \\
 \dot{e}_s(t) &= -\Delta A e_p(t) + A e_s(t) + B e_f(t) - \Delta B e_u(t) \\
 &\quad - \Delta A_d e_p(t-h) + A_d e_s(t-h) \\
 &\quad + \Delta A x(t) - H_1 e_y(t) + \Delta B u(t) + \Delta A_d x(t-h), \\
 \dot{e}_f(t) &= \dot{f}(t) - \hat{f}(t) = -e_f(t) - H_2 e_y + f(t) + \dot{f}(t).
 \end{aligned} \tag{28}$$

The output estimation error  $e_y(t)$  is given by

$$\begin{aligned}
 e_y(t) &= -\Delta C e_p(t) + C e_s(t) - \Delta C_d e_p(t-h) \\
 &\quad + C_d e_s(t-h) + \Delta C x(t) + \Delta C_d x(t-h).
 \end{aligned} \tag{29}$$

The substitution of  $e_u(t)$  in (8) implies

$$\begin{aligned}
 e_u(t) &= -K_1 e_p(t) - K_1 e_s(t) - K_2 e_p(t-h) \\
 &\quad - K_2 e_s(t-h) - e_f(t).
 \end{aligned} \tag{30}$$

Equation (29) and (30) can be rewritten as

$$\begin{aligned}
 0 \dot{e}_u(t) &= K_1 e_p(t) + K_1 e_s(t) + K_2 e_p(t-h) \\
 &\quad + K_2 e_s(t-h) + e_u(t) + e_f(t), \\
 0 \dot{e}_y(t) &= -\Delta C e_p(t) + C e_s(t) - e_y(t) - \Delta C_d e_p(t-h) \\
 &\quad + C_d e_s(t-h) + \Delta C_d x(t-h) + \Delta C x(t).
 \end{aligned} \tag{31}$$

The combination of (28) and (31) leads to the following descriptor system:

$$\begin{aligned}
 E \dot{e}(t) &= (\bar{A} + \Delta \bar{A}) e(t) + (\bar{A}_d + \Delta \bar{A}_d) e(t-h) \\
 &\quad + (\bar{B} + \Delta \bar{B}) v(t),
 \end{aligned} \tag{32}$$

where  $E$ ,  $\bar{A}_d$ , and  $e(t)$  have been given above and the expressions of  $\bar{A}$ ,  $\Delta \bar{A}$ ,  $\bar{B}$ ,  $\Delta \bar{B}$ ,  $\bar{A}_d$ , and  $v(t)$  are shown as follows:

$$\begin{aligned}
 \bar{A} &= \begin{bmatrix} A & 0 & 0 & B & 0 \\ 0 & A & B & 0 & -H_1 \\ 0 & 0 & -I & 0 & -H_2 \\ K_1 & K_1 & I & I & 0 \\ 0 & C & 0 & 0 & -I \end{bmatrix}, \\
 \Delta \bar{A} &= \begin{bmatrix} \Delta A & 0 & 0 & \Delta B & 0 \\ -\Delta A & 0 & 0 & -\Delta B & 0 \\ 0 & 0 & 0 & 0 & 0 \\ 0 & 0 & 0 & 0 & 0 \\ -\Delta C & 0 & 0 & 0 & 0 \end{bmatrix}, \\
 \bar{B} &= \begin{bmatrix} 0 & 0 & 0 & 0 & 0 \\ 0 & 0 & 0 & 0 & 0 \\ 0 & 0 & 0 & I & I \\ 0 & 0 & 0 & 0 & 0 \\ 0 & 0 & 0 & 0 & 0 \end{bmatrix}, \\
 \Delta \bar{B} &= \begin{bmatrix} -\Delta A & -\Delta A_d & -\Delta B & 0 & 0 \\ \Delta A & \Delta A_d & \Delta B & 0 & 0 \\ 0 & 0 & 0 & 0 & 0 \\ 0 & 0 & 0 & 0 & 0 \\ \Delta C & \Delta C_d & 0 & 0 & 0 \end{bmatrix}, \\
 \Delta \bar{A}_d &= \begin{bmatrix} \Delta A_d & 0 & 0 & 0 & 0 \\ -\Delta A_d & 0 & 0 & 0 & 0 \\ 0 & 0 & 0 & 0 & 0 \\ 0 & 0 & 0 & 0 & 0 \\ -\Delta C_d & 0 & 0 & 0 & 0 \end{bmatrix},
 \end{aligned} \tag{33}$$

$$v(t) = [x^T(t), x^T(t-h), u^T(t), f^T(t), \dot{f}^T(t)]^T.$$

The condition ensuring the stability of the descriptor system (32) and the attenuation level  $\gamma > 0$  from the perturbation-like term  $v(t)$  to the error dynamic  $e(t)$  are provided in the following theorem.

**Theorem 4.** *System (32) describing the different errors is stable and the gain from  $v(t)$  to  $e(t)$  is bounded by  $\gamma > 0$  if there exist some matrices  $P_1 > 0$ ,  $P_2 > 0$ , and  $P_3 > 0$  and matrices  $Y_2, Y$*

with appropriate dimensions and positive scalars  $t_1, t_2, t_3$  such that the matrix inequality (34) holds.

$$\begin{bmatrix} \bar{\Omega} & Y_2 B & Y & Y_2 M_{ea} & Y_2 M_{eb} & Y_2 M_{ead} \\ * & -\gamma^2 I + t_2 N_{eb}^T N_{eb} & 0 & 0 & 0 & 0 \\ * & * & -\frac{P_3}{h} & 0 & 0 & 0 \\ * & * & * & -t_1 I & 0 & 0 \\ * & * & * & * & -t_2 I & 0 \\ * & * & * & * & * & -t_3 I \end{bmatrix} < 0, \quad (34)$$

and the observer and controller gains are then computed by

$$\begin{aligned} K_1 &= (Y_{14})^{-1} X_{41}, & K_2 &= (Y_{14})^{-1} X_{42}, \\ H_1 &= (Y_{11})^{-1} H_{21}, & H_2 &= (Y_{12})^{-1} H_{32}. \end{aligned} \quad (35)$$

*Proof.* Let us consider the weighted  $L_2$  constraint given by

$$\int_0^t e^T(\sigma) Q e(\sigma) d\sigma < \gamma^2 \int_0^t v^T(\sigma) v(\sigma) d\sigma, \quad (36)$$

where  $\gamma$  is the attenuation level from the perturbation-like term  $v(t)$  to the error  $e(t)$  in (32) and  $Q$  is a symmetric semipositive-definite weighted matrix. It is well known that the constraint is satisfied if there exists a Lyapunov-Krasovskii function such that

$$\dot{V}(t) + e^T(t) Q e(t) - \gamma^2 v^T(t) v(t) < 0. \quad (37)$$

Choose Lyapunov-Krasovskii functional candidate as  $V(t) = V_1(t) + V_2(t) + V_3(t)$  and  $V_1(t), V_2(t), V_3(t)$  are defined in (22).

Adding  $2\Pi_1, 2\Pi_2$ , and  $h\xi^T(t) Y P_3^{-1} Y^T \xi(t)$  and subtracting  $\int_{t-h}^t \xi^T(t) Y P_3^{-1} Y^T \xi(t) d\omega$ , respectively, in (37) yield (38) which is shown as follows:

$$\begin{aligned} \dot{V}(t) &\leq 2e^T(t) E^T P_1 \dot{e}(t) + h\dot{e}^T(t) E^T P_3 E \dot{e}(t) \\ &\quad - \int_{t-h}^t \dot{e}^T(\omega) E^T P_3 E \dot{e}(\omega) d\omega + e^T(t) P_2 e(t) \\ &\quad - e^T(t-h) P_2 e(t-h) \\ &\quad + 2\xi^T(t) Y E \left[ e(t) - e(t-h) - \int_{t-h}^t \dot{e}(\omega) d\omega \right] \\ &\quad + 2\xi^T(t) Y_2 \left[ (\bar{A} + \Delta\bar{A}) e(t) + (\bar{A}_d + \Delta\bar{A}_d) e(t-h) \right. \\ &\quad \quad \left. + (\bar{B} + \Delta\bar{B}) v(t) - E \dot{e}(t) \right] \\ &= 2e^T(t) P_1 E \dot{e}(t) + h\dot{e}^T(t) E^T P_3 E \dot{e}(t) \\ &\quad - \int_{t-h}^t \dot{e}^T(\omega) E^T P_3 E \dot{e}(\omega) d\omega + e^T(t) P_2 e(t) \\ &\quad - e^T(t-h) P_2 e(t-h) \end{aligned}$$

$$\begin{aligned} &+ 2\xi^T(t) Y E \left[ e(t) - e(t-h) - \int_{t-h}^t \dot{e}(\omega) d\omega \right] \\ &+ 2\xi^T(t) Y_2 \left[ \bar{A} e(t) + \bar{A}_d e(t-h) + \bar{B} v(t) - E \dot{e}(t) \right] \\ &+ \text{sym} \left( \xi^T(t) Y_2 M_{ea} F_5(t) N_{ea} e(t) \right. \\ &\quad \left. + \xi^T(t) Y_2 M_{ead} F_5(t) N_{ead} e(t-h) \right. \\ &\quad \left. + \xi^T(t) Y_2 M_{eb} F_5(t) N_{eb} v(t) \right). \end{aligned} \quad (38)$$

By applying Lemma 1, (38) yields

$$\begin{aligned} \dot{V}(t) &\leq \xi^T(t) \bar{\Omega} \xi(t) + t_1^{-1} \xi^T(t) Y_2 M_{ea} M_{ea}^T Y_2^T \xi(t) \\ &\quad + t_2^{-1} \xi^T(t) Y_2 M_{ead} M_{ead}^T Y_2^T \xi(t) \\ &\quad + t_3^{-1} \xi^T(t) Y_2 M_{eb} M_{eb}^T Y_2^T \xi(t) \\ &\quad + 2\xi^T(t) Y_2 \bar{B} v(t) + t_2 v^T(t) N_{eb}^T N_{eb} v(t), \end{aligned} \quad (39)$$

where the  $\bar{\Omega}$  is expressed as follows:

$$\begin{aligned} \bar{\Omega} &= W_p Q W_p^T + t_1 W_p N_{ea}^T N_{ea} W_p^T \\ &\quad + t_3 W_{ph} N_{ead}^T N_{ead} W_{ph}^T + W_p P_2 W_p^T \\ &\quad + h W_{p1} E^T P_3 E W_{p1}^T - W_{ph} P_2 W_{ph}^T \\ &\quad + \text{sym} \left( W_p P_1 W_{p1}^T + Y E W_p^T + Y E W_{ph}^T \right. \\ &\quad \left. + (Y_2 A_0 - H C_1 - X C_2) W_p^T \right. \\ &\quad \left. + (Y_2 A_{d0} - K C_3) W_{ph}^T \right). \end{aligned} \quad (40)$$

$W_p, W_{p1}, W_{ph}, A_0, A_{d0}, \bar{Y}_2, X, K, H, C_1, C_2$ , and  $C_3$  are defined by Theorem 2 and  $M_{ea}, M_{eb}, M_{ead}, N_{ea}, N_{eb}$ , and  $N_{ead}$  are shown as follows:

$$\begin{aligned} M_{ea} &= \begin{bmatrix} M_a & 0 & M_b & 0 & 0 \\ 0 & M_a & 0 & M_b & 0 \\ 0 & 0 & 0 & 0 & 0 \\ 0 & 0 & 0 & 0 & 0 \\ 0 & 0 & 0 & 0 & 0 \end{bmatrix}, \\ N_{ea} &= \begin{bmatrix} N_a & 0 & 0 & 0 & 0 \\ -N_a & 0 & 0 & 0 & 0 \\ 0 & 0 & 0 & N_b & 0 \\ 0 & 0 & 0 & -N_b & 0 \\ -N_c & 0 & 0 & 0 & M_c \end{bmatrix}, \\ M_{ead} &= \begin{bmatrix} M_{ad} & 0 & 0 & 0 & 0 \\ -M_{ad} & 0 & 0 & 0 & 0 \\ 0 & 0 & 0 & 0 & 0 \\ 0 & 0 & 0 & 0 & 0 \\ 0 & M_{cd} & 0 & 0 & 0 \end{bmatrix}, \end{aligned}$$

$$\begin{aligned}
 N_{ead} &= \begin{bmatrix} N_{ad} & 0 & 0 & 0 & 0 \\ -N_{ad} & 0 & 0 & 0 & 0 \\ 0 & 0 & 0 & 0 & 0 \\ 0 & 0 & 0 & 0 & 0 \\ 0 & 0 & 0 & 0 & 0 \end{bmatrix}, \\
 M_{eb} &= \begin{bmatrix} -M_a & M_b & -M_{ad} & 0 & 0 \\ M_a & -M_b & M_{ad} & 0 & 0 \\ 0 & 0 & 0 & 0 & 0 \\ 0 & 0 & 0 & 0 & 0 \\ 0 & 0 & 0 & M_c & M_{cd} \end{bmatrix}, \\
 N_{eb} &= \begin{bmatrix} N_a & 0 & 0 & 0 & 0 \\ 0 & 0 & -N_b & 0 & 0 \\ 0 & N_{ad} & 0 & 0 & 0 \\ N_c & 0 & 0 & 0 & 0 \\ 0 & N_{cd} & 0 & 0 & 0 \end{bmatrix}.
 \end{aligned} \tag{41}$$

Following the similar steps of previous proofs and applying Schur complement on (39), the sufficient LMI conditions proposed in Theorem 4 follow.  $\square$

*Remark 5.* It should be mentioned that our study to this paper is mainly motivated by the work of [17]. There are three differences between the work given in [17] and ours. First, the system in [17] are Takagi-sugeno fuzzy models and in our study, the linear system is investigated; however, the results of the linear system theories can be applied for the design of Takagi-sugeno fuzzy models. Second, the Takagi-sugeno models of the work [17] taken are combinations of linear time invariant systems. Our study is the extend of linear systems to linear time-delay systems, but it is not taken into account in [17]. Third, problems of the stability and the  $H_\infty$  control for delayed systems use the Lyapunov-Krasovskii approach other than the Lyapunov-Razumikhin approach and the results of using Lyapunov-Krasovskii approach are usually less conservative than those using Lyapunov-Razumikhin approach [25].

#### 4. Numerical Example

In this section, we will provide a numerical example to demonstrate the effectiveness of the design methods proposed in the previous section. This example is taken from [23] and the faulty system is defined by

$$\begin{aligned}
 A &= \begin{bmatrix} -1.4274 & 0.0757 \\ -1.4189 & -0.9442 \end{bmatrix}, & B &= \begin{bmatrix} 0 \\ 0.3 \end{bmatrix}, \\
 A_d &= \begin{bmatrix} 0.25 & 0 \\ 0 & 0.25 \end{bmatrix}, & C &= \begin{bmatrix} 0.1 & 0 \\ 0 & 0.1 \end{bmatrix}, \\
 C_d &= \begin{bmatrix} 0.1 & 0 \\ 0 & 0.1 \end{bmatrix}.
 \end{aligned} \tag{42}$$

We assume that the time delay is given by  $h = 0.1$ . Letting the nominal input signal  $u(t) = \sin(t)$  and the constant fault  $f = 1$  affecting the system behavior at  $30 \text{ s} \leq t \leq 100 \text{ s}$ , one

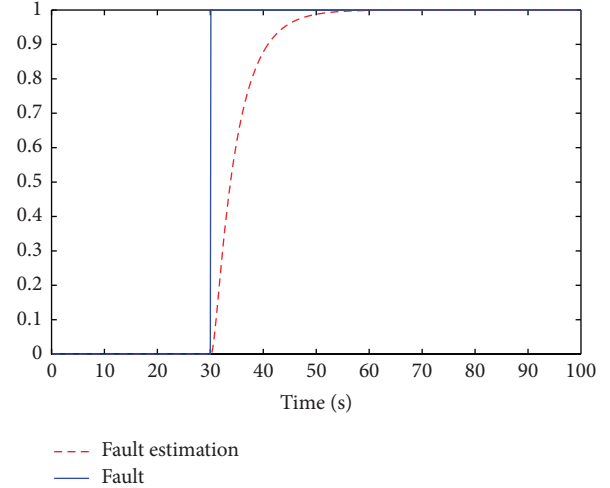


FIGURE 2: Fault and its estimation.

can obtain the following solution by solving the conditions in the Theorem 2:

$$\begin{aligned}
 H_1 &= \begin{bmatrix} 0.7233 & 2.3038 \\ -9.2496 & 5.2505 \end{bmatrix}, \\
 H_2 &= [-1.8912 \quad 5.6556], \\
 K_1 &= [-0.1582 \quad 0.0076], \\
 K_2 &= [0.2101 \quad 0.7059].
 \end{aligned} \tag{43}$$

The simulation results are shown in Figures 2, 3, 4, and 5. In Figure 2, the real fault and its estimate are depicted. Figures 3 and 4 compare the state variables of the reference model, the observer, and the faulty system with FTC. Figure 5 shows the comparison of the nominal control input and FTC signal.

In the next, we will consider the time-varying fault with system uncertainties; the uncertainties are defined by

$$\begin{aligned}
 M_{ad} &= M_b = M_a = \text{diag}\{0.1, 0.1\}, \\
 M_c &= M_{cd} = \text{diag}\{0.1, 0.1\}, \\
 N_a &= N_{ad} = N_c = N_{cd} = \text{diag}\{0.01, 0.01\}, \\
 N_b &= [0.01, 0.01]^T.
 \end{aligned} \tag{44}$$

The system uncertainties are given by  $F(t) = 0.5 \sin(t)$ . The definition of the time delay  $h$  and the nominal input signal  $u(t)$  is given by  $h = 0.1$  and  $u(t) = \sin(t)$ . The time-varying fault  $f = \sin(0.5 * t - 8) * \cos(t)$  affects the system behavior at  $30 \text{ s} \leq t \leq 100 \text{ s}$ .

When choosing the free weighting matrix  $Y_2 = [\tilde{Y}_2^T \quad 0 \quad \tilde{Y}_2^T]^T$  and solving the conditions in Theorem 4 with

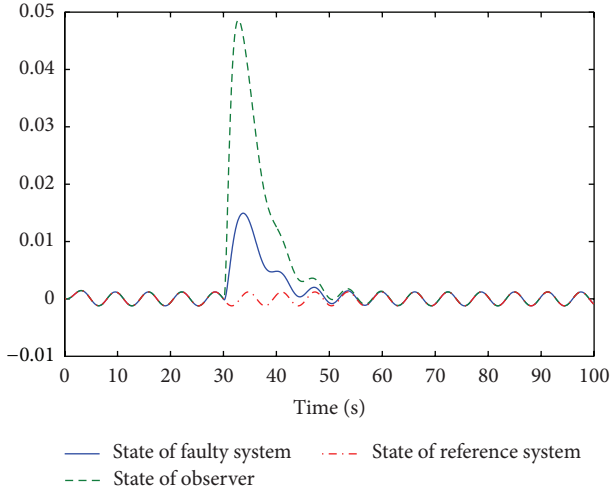


FIGURE 3: Comparison of reference mode state  $x_1$ , faulty system state  $x_{f1}$ , and the observer state  $\hat{x}_{f1}$ .

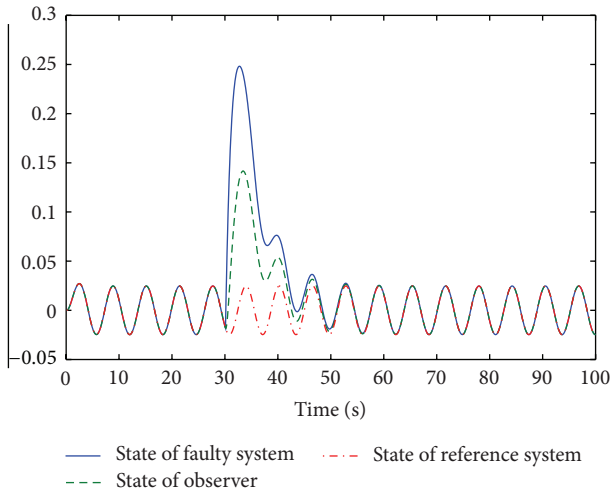


FIGURE 4: Comparison of reference mode state  $x_2$ , faulty system state  $x_{f2}$ , and the observer state  $\hat{x}_{f2}$ .

$Q = \text{diag}\{I_2, I_2, I_1, I_1, I_2\}$ , one can obtain the attenuation value  $\gamma = 0.346928$  with

$$\begin{aligned} H_1 &= \begin{bmatrix} 0.9485 & 2.1521 \\ 3.8575 & 109.0013 \end{bmatrix}, \\ H_2 &= [0.0278 \quad 2.5129] \times 10^3, \\ K_1 &= [28.9781 \quad -2.7970], \\ K_2 &= [4.1592 \quad 3.4426]. \end{aligned} \quad (45)$$

In order to show the effective influence of the FTC on the system trajectory, we make the comparison between the systems with and without FTC when faults occur. The simulation results are shown in Figures 6, 7, 8, 9, 10, and 11. Figure 6 illustrates the simulation result of fault estimation. Figures 7 and 8 show the state variables of the reference

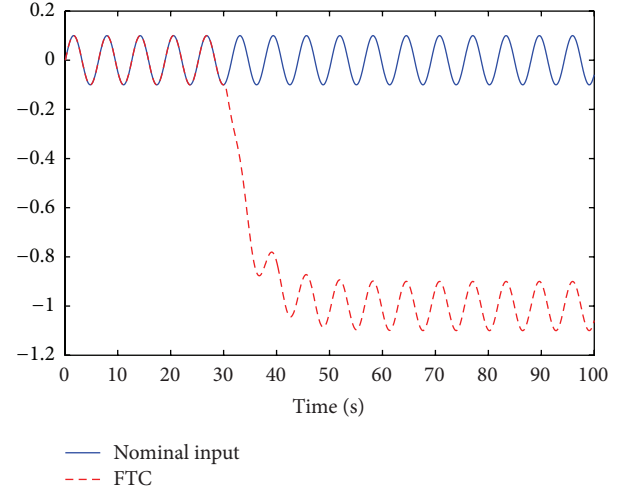


FIGURE 5: Nominal input  $u(t)$  and FTC  $u_f(t)$ .

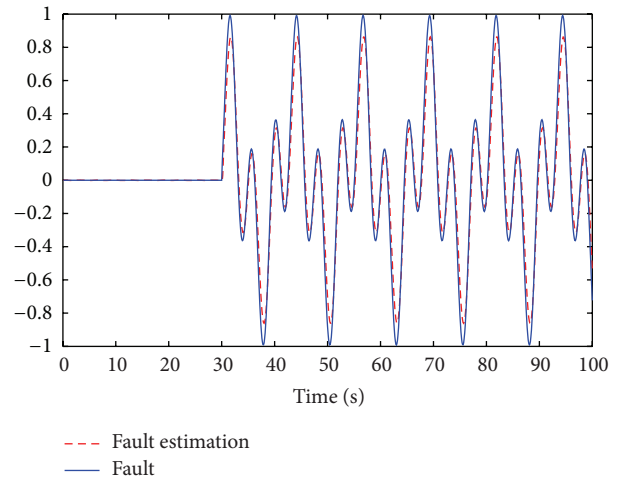


FIGURE 6: Fault and its estimation.

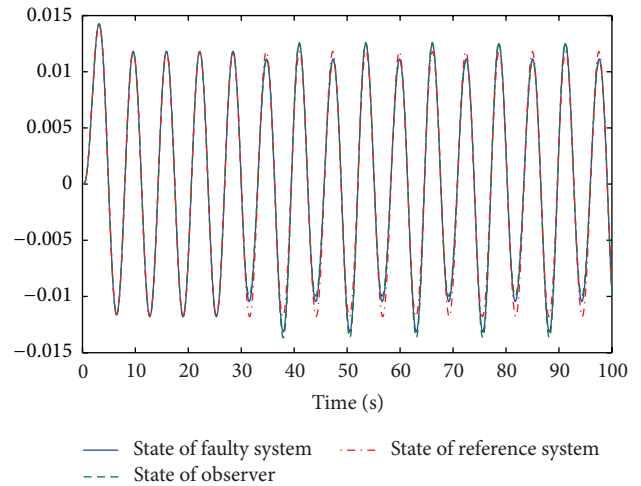


FIGURE 7: Comparison of reference mode state  $x_1$ , faulty system state  $x_{f1}$ , and the observer state  $\hat{x}_{f1}$  with FTC.

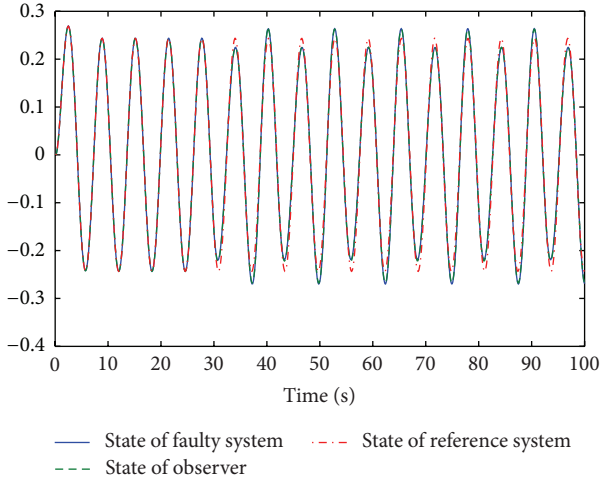


FIGURE 8: Comparison of reference mode state  $x_2$ , faulty system state  $x_{f2}$ , and the observer state  $\hat{x}_{f2}$  with FTC.

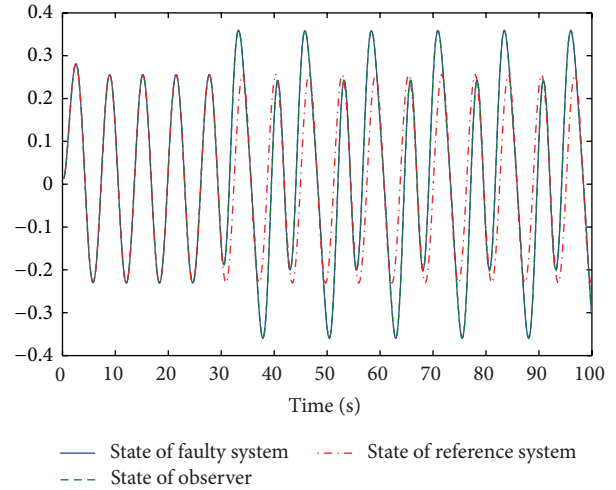


FIGURE 11: Comparison of reference mode state  $x_2$ , faulty system state  $x_{f2}$ , and the observer state  $\hat{x}_{f2}$  without FTC.

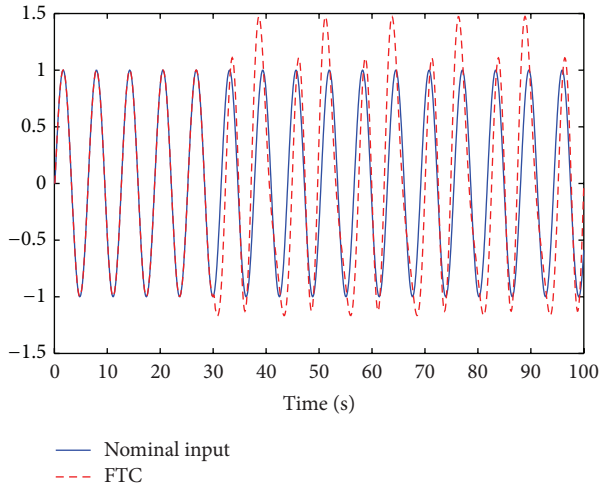


FIGURE 9: Nominal input  $u(t)$  and FTC  $u_f(t)$ .

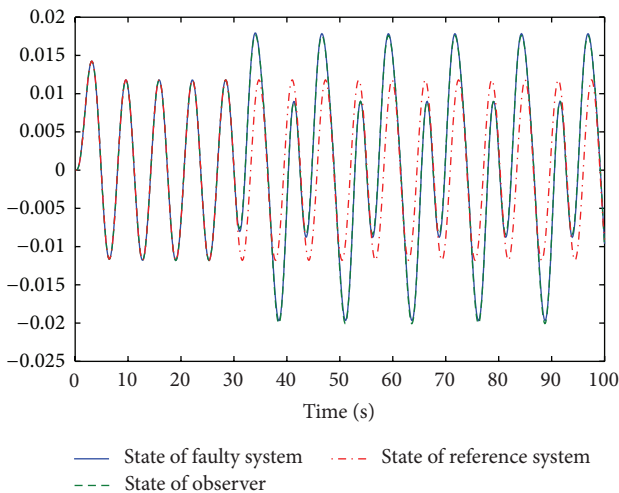


FIGURE 10: Comparison of reference mode state  $x_1$ , faulty system state  $x_{f1}$ , and the observer state  $\hat{x}_{f1}$  without FTC.

model, the observer, and the faulty system with FTC. The comparison of the nominal control and FTC signal is shown in Figure 9. Figures 10 and 11 show the state variables of the reference model, the observer, and the faulty system without FTC.

Two different cases are considered including constant fault without uncertainties and time-varying fault with uncertainties. From the above simulation results, one can see that the synthesized observers and FTC controllers showed their effectiveness, since the fault is estimated (Figures 2 and 6) and the state variables of the faulty system with FTC are closed to reference model (Figures 3, 4, 7, and 8), and the tracking between the faulty system and the reference model is ensured. On the other hand, if FTC is not employed in the faulty system (Figures 10 and 11), the state trajectories of faulty system deviate from the state trajectories of reference model and the tracking is not achieved.

### 5. Conclusion

In this paper, the problem of active FTC design for linear time-delay systems with and without uncertainties is treated. The aim of the FTC law and observer design is to ensure the trajectory tracking of faulty system. By considering the descriptor redundancy of closed-loop systems and using Lyapunov-Krasovskii functional approach, the proposed FTC scheme has been easily formulated in LMI terms. Two kinds of faults have been considered. The first one deals with the constant faults without uncertainties as a special case, and the other deals with the time-varying faults with system uncertainties. Finally, one example has been considered to illustrate the efficiency of the proposed scheme in both cases. In addition, it is interesting to develop the FTC control law by taking into account modeling multiplicative faults and some external perturbations and considering how to deal with sensor faults and how to apply this scheme to T-S models.

## Conflict of Interests

The authors declare that there is no conflict of interests regarding the publication of this paper.

## Acknowledgments

The authors would like to thank the reviewers for their constructive comments and suggestions which have helped to improve the presentation of the paper. This work was supported by the National Natural Science Foundation of China (no. 61300115).

## References

- [1] J. Chen and R. J. Patton, *Robust Model-Based Fault Diagnosis for Dynamic Systems*, Kluwer Academic Publishers, Boston, Mass, USA, 1999.
- [2] M. Blanke, M. Kinnaert, and J. Lunze, *Diagnosis and Fault-Tolerant Control*, Springer, Berlin, Germany, 2006.
- [3] H. Niemann and J. Stoustrup, "Passive fault tolerant control of a double inverted pendulum—a case study," *Control Engineering Practice*, vol. 13, no. 8, pp. 1047–1059, 2005.
- [4] H. Wang and S. Daley, "Actuator fault diagnosis: an adaptive observer-based technique," *IEEE Transactions on Automatic Control*, vol. 41, no. 7, pp. 1073–1078, 1996.
- [5] B. Jiang, M. Staroswiecki, and V. Cocquempot, "Fault identification for a class of time-delay systems," in *Proceedings of the American Control Conference*, pp. 2239–2244, Anchorage, Alaska, USA, May 2002.
- [6] C. Edwards, S. K. Spurgeon, and R. J. Patton, "Sliding mode observers for fault detection and isolation," *Automatica*, vol. 36, no. 4, pp. 541–553, 2000.
- [7] N. E. Wu, Y. Zhang, and K. Zhou, "Detection, estimation, and accommodation of loss of control effectiveness," *International Journal of Adaptive Control and Signal Processing*, vol. 14, no. 7, pp. 775–795, 2000.
- [8] B. Marx, D. Koenig, and D. Georges, "Robust fault-tolerant control for descriptor systems," *IEEE Transactions on Automatic Control*, vol. 49, no. 10, pp. 1869–1875, 2004.
- [9] M. Wang, B. Chen, and S. Tong, "Adaptive fuzzy tracking control for strict-feedback nonlinear systems with unknown time delays," *International Journal of Innovative Computing, Information and Control*, vol. 4, no. 4, pp. 829–837, 2008.
- [10] W. Chen and M. Saif, "An iterative learning observer for fault detection and accommodation in nonlinear time-delay systems," *International Journal of Robust and Nonlinear Control*, vol. 16, no. 1, pp. 1–19, 2006.
- [11] W. Chen and M. Saif, "Fault detection and accommodation in nonlinear time-dealy systems," in *Proceedings of the American Control Conference*, pp. 4255–4260, June 2003.
- [12] B. Jiang, M. Staroswiecki, and V. Cocquempot, " $H_\infty$  fault detection filter design for linear discretetime systems with multiple time delays," *International Journal of Systems Science*, vol. 34, no. 5, pp. 365–373, 2003.
- [13] D. Du, B. Jiang, and P. Shi, "Sensor fault estimation and compensation for time-delay switched systems," *International Journal of Systems Science*, vol. 43, no. 4, pp. 629–640, 2012.
- [14] C. Jiang, D. H. Zhou, and F. Gao, "Robust fault detection and isolation for uncertain linear retarded systems," *Asian Journal of Control*, vol. 8, no. 2, pp. 141–152, 2006.
- [15] D. Zhang, L. Yu, and W.-A. Zhang, "Delay-dependent fault detection for switched linear systems with time-varying delays—the average dwell time approach," *Signal Processing*, vol. 91, no. 4, pp. 832–840, 2011.
- [16] B. Jiang, K. Zhang, and P. Shi, "Less conservative criteria for fault accommodation of time-varying delay systems using adaptive fault diagnosis observer," *International Journal of Adaptive Control and Signal Processing*, vol. 24, no. 4, pp. 322–334, 2010.
- [17] T. Bouarar, B. Marx, D. Maquin, and J. Ragot, "Fault-tolerant control design for uncertain Takagi-Sugeno systems by trajectory tracking: a descriptor approach," *IET Control Theory & Applications*, vol. 7, no. 14, pp. 1793–1805, 2013.
- [18] D. Ichalal, B. Marx, J. Ragot, and D. Maquin, "Observer based actuator fault tolerant control for nonlinear Takagi-Sugeno systems: an LMI approach," in *Proceedings of the 18th Mediterranean Conference on Control and Automation (MED '10)*, pp. 1278–1283, Marrakech, Morocco, June 2010.
- [19] T. Bouarar, B. Marx, D. Maquin, and J. Ragot, "Trajectory tracking fault tolerant controller design for Takagi-Sugeno systems subject to actuator faults," in *Proceedings of the International Conference on Communications, Computing and Control Applications (CCCA '11)*, pp. 1–6, Hammamet, Tunisia, March 2011.
- [20] K. Guelton, T. Bouarar, and N. Manamanni, "Robust dynamic output feedback fuzzy Lyapunov stabilization of Takagi-Sugeno systems—a descriptor redundancy approach," *Fuzzy Sets and Systems*, vol. 160, no. 19, pp. 2796–2811, 2009.
- [21] T. Bouarar, K. Guelton, and N. Manamanni, "Static output feedback controller design for Takagi-Sugeno systems—a fuzzy Lyapunov LMI approach," in *Proceedings of the 48th IEEE Conference on Decision and Control Held Jointly with 28th Chinese Control Conference (CDC/CCC '09)*, pp. 4150–4155, IEEE, Shanghai, China, December 2009.
- [22] T. Bouarar, K. Guelton, and N. Manamanni, "Robust fuzzy Lyapunov stabilization for uncertain and disturbed Takagi-Sugeno descriptors," *ISA Transactions*, vol. 49, no. 4, pp. 447–461, 2010.
- [23] Y. Zhao, J. Wu, and P. Shi, " $H_\infty$  control of non-linear dynamic systems: a new fuzzy delay partitioning approach," *IET Control Theory & Applications*, vol. 3, no. 7, pp. 917–928, 2009.
- [24] X. F. Jiang and Q.-L. Han, "Robust  $H_\infty$  control for uncertain Takagi-Sugeno fuzzy systems with interval time-varying delay," *IEEE Transactions on Fuzzy Systems*, vol. 15, no. 2, pp. 321–331, 2007.
- [25] G. J. Zhang, C. S. Han, and L. G. Wu, "Admissibility and  $H_\infty$  performance analysis of T-S fuzzy descriptor systems with time-delay," in *Proceedings of the 2nd International Conference on Intelligent Control and Information Processing (ICICIP '11)*, pp. 77–81, July 2011.

## Research Article

# Actuator Fault Diagnosis with Application to a Diesel Engine Testbed

**Boulaïd Boulkroune,<sup>1</sup> Abdel Aitouche,<sup>1</sup> Vincent Cocquempot,<sup>2</sup> Li Cheng,<sup>3</sup> and Zhijun Peng<sup>3</sup>**

<sup>1</sup>*Hautes Etudes d'Ingénieur, Centre de Recherche en Informatique, Signal et Automatique de Lille (CRISTAL), 13 rue de Toul, 59046 Lille, France*

<sup>2</sup>*Lille 1 University, Centre de Recherche en Informatique, Signal et Automatique de Lille (CRISTAL), rue Paul Langevin, 59655 Villeneuve d'Ascq, France*

<sup>3</sup>*Department of Engineering & Design, University of Sussex, Room 2D3, Richmond Building, Brighton BN1 9QT, UK*

Correspondence should be addressed to Boulaïd Boulkroune; [boulkrb@gmail.com](mailto:boulkrb@gmail.com)

Received 3 September 2014; Revised 20 February 2015; Accepted 26 February 2015

Academic Editor: Kui Fu Chen

Copyright © 2015 Boulaïd Boulkroune et al. This is an open access article distributed under the Creative Commons Attribution License, which permits unrestricted use, distribution, and reproduction in any medium, provided the original work is properly cited.

This work addresses the issues of actuator fault detection and isolation for diesel engines. We are particularly interested in faults affecting the exhaust gas recirculation (EGR) and the variable geometry turbocharger (VGT) actuator valves. A bank of observer-based residuals is designed using a nonlinear mean value model of diesel engines. Each residual on the proposed scheme is based on a nonlinear unknown input observer and designed to be insensitive to only one fault. By using this scheme, each actuator fault can be easily isolated since only one residual goes to zero while the others do not. A decision algorithm based on multi-CUSUM is used. The performances of the proposed approach are shown through a real application to a Caterpillar 3126b engine.

## 1. Introduction

On-board diagnosis of automotive engines has become increasingly important because of environmentally based legislative regulations such as OBDII (On-Board Diagnostics-II) [1]. On-board diagnosis is also needed to guarantee high-performance engine behavior. Today, due to the legislation, the majority of the code in modern engine management systems is dedicated to diagnosis.

Model-based diagnosis of automotive engines has been considered in earlier papers (see, e.g., [2, 3]), to name only a few. However, the engines investigated in these previous works were all gasoline-fuelled and did not include exhaust gas recirculation (EGR) and variable geometry turbocharger (VGT). Both of these components make the diagnosis problem significantly more difficult since the air flows through the EGR valve, and also the exhaust side of the engine has to be taken into account. An interesting approach to model-based air-path faults detection for an engine which includes EGR and VGT can be found in [4, 5]. By using several

models in parallel, where each one is sensitive to one kind of fault, predicted outputs are compared and a diagnosis is provided. The hypothesis test methodology proposed in [4] deals with the multifault detection in air-path system. In [5] the authors propose an extended adaptive Kalman filter to find which faulty model best matches with measured data; then a structured hypothesis allows going back to the faults. A structural analysis for air path of an automotive diesel engine was developed in order to study the monitorability of the system [6–8]. Other approaches to detect intake leakages in diesel engines based on adaptive observers are proposed in [9, 10] and recently in [11]. Note that, in all these approaches, the leakage size is assumed to be constant. To overcome this limitation, an approach based on a nonlinear unknown input observer (NIUO), for intake leakage detection, is proposed in [12]. No *a priori* assumption about the leakage size is made. In [13, 14], an interesting method for bias compensation in model-based estimation using model augmentation is proposed. The extended Kalman filter (EKF) is used for estimating the states of the augmented model. Also,

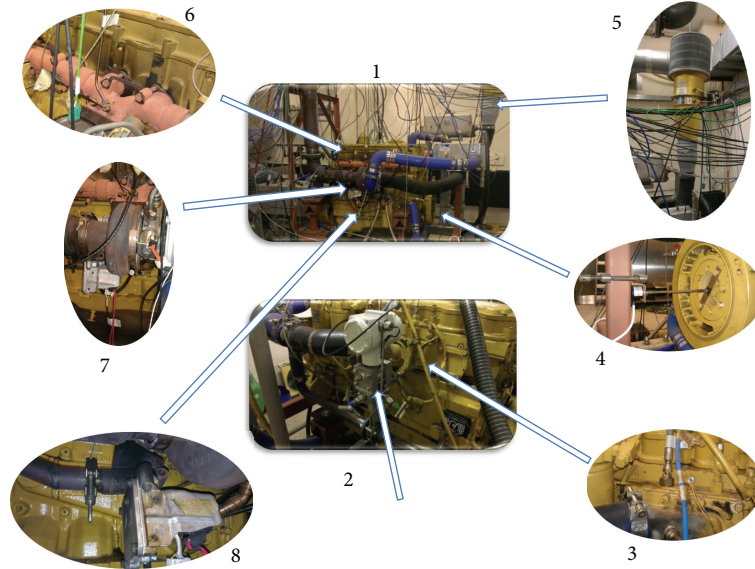


FIGURE 1: Caterpillar testbed 3126, Sussex University.

the observability of the augmented model is well discussed. Recently, an automated model-based and data-driven design methodology for automotive engine fault detection and isolation (FDI) is proposed in [15]. This methodology, which combines model-based sequential residual generation and data-driven statistical residual evaluation, is used to create a complete FDI system for an automotive diesel engine.

The problem of designing unknown input observers (UIO) has received great attention in literature. This problem is motivated by certain applications such as fault diagnosis and control system design. If this issue in linear case is well solved, it remains an open problem in the nonlinear case. The first unknown input observers dedicated to linear systems were proposed in [16, 17]. Necessary and sufficient conditions of the existence of the UIO have been well established. New sufficient conditions formulated in terms of linear matrix inequality (LMI) were given by [18]. This result is extended in [12] to cover a wide class of nonlinear systems that cannot be treated by the previous approach as well as nonlinear systems with a large Lipschitz constant.

Our aim is to address the issue of actuator fault detection and isolation for diesel engines. Indeed, actuators (EGR and VGT) fault diagnosis is necessary and crucial to guarantee its healthy operation. In this work, a fault detection and isolation (FDI) system is developed. The proposed FDI system is composed of two parts: residual generation and decision system. A multiobserver strategy is used for residual generation. A mean model of diesel engine is exploited for the design of a set of nonlinear unknown input observers. These observers are designed in order to estimate the states behavior without any knowledge of the unknown inputs. The sufficient conditions of the existence of the NUIO are given in terms of linear matrix inequalities (LMIs). The advantage of this method is that no a priori assumption on the unknown input is required and also can be employed for a wider class of nonlinear systems. To achieve fault detection and isolation,

a decision system based on a statistical approach, multi-CUSUM (cumulative sum), is used to process the resulting set of residuals.

This paper is organized as follows. The experimental setup is described in Section 2. The diesel engine model and its validation are described in Section 3. A nonlinear unknown input observer is presented in Section 4. Section 5 describes the residual generation system while the decision system is presented in Section 6. The experimental results and discussion are presented in Section 7. Finally, conclusion and future works are given in the last section.

The notations used in this paper are quite standard. Let  $\mathfrak{R}$  denote the set of real numbers. The set of  $p$  by  $q$  real matrices is denoted as  $\mathfrak{R}^{p \times q}$ .  $A^T$  and  $A^{-1}$  represent the transpose of  $A$  and its left inverse (assuming  $A$  has full column rank), respectively.  $I_r$  represents the identity matrix of dimension  $r$ .  $(*)$  is used for the blocks induced by symmetry.  $\|\cdot\|$  represents the usual Euclidean norm.  $\mathfrak{L}_2^2$  denotes the Lebesgue space.  $f_{a,i}$  denotes the  $i$ th component of the vector  $f_a$ .

## 2. Experimental Installation

The testbed is built with a Caterpillar 3126b truck engine coupled to a SCHORCH dynamometer controlled by CP Cadet Software. The Caterpillar engine is presented in Figure 1. The front and back view of the testbed are shown by the pictures numbered (1) and (2), respectively. Engine's components are inlet manifold (3), encoder for measuring of the engine speed (4), intake air flow meter (5), exhaust manifold (6), GT3782VA variable geometry turbocharger, (7) and exhaust gas valve (8). In order to enable a transient control of the EGR and VGT, a dSPACE MicroAutoBox 1401/1501 real-time controller is connected (see Figure 2). Apart from the standard OEM electronic sensors built in for ECU and dynamometer control, additional sensors and actuators have

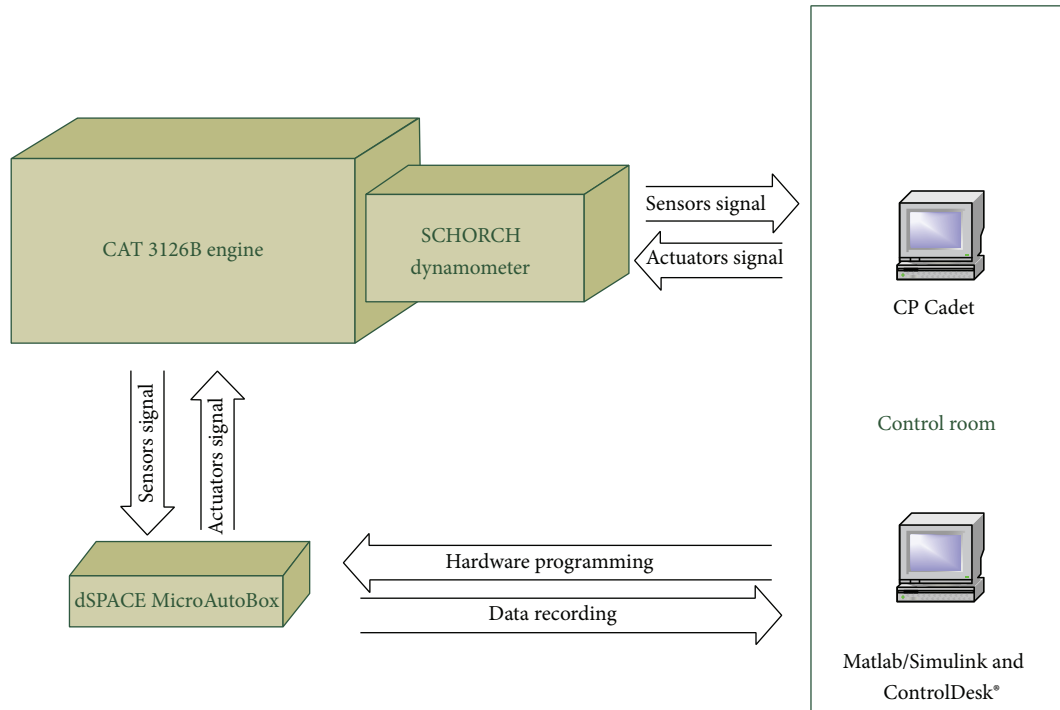


FIGURE 2: Experimental installation schematic, Sussex University.

TABLE 1: Sensors and actuators list.

Sensors	Actuators
Inlet temperature sensor	EGR valve drive actuator
Inlet air flow meter	VGT vanes drive actuator
Inlet pressure sensor	
Pre-turbo exhaust pressure sensor	
Acceleration pedal position sensor	
Engine speed sensor	
Inlet manifold oxygen sensor	
Exhaust manifold oxygen sensor	
Exhaust opacity sensor (AVL Opacimeter 439)	
Exhaust emission sensor (Testo 350 Engine test kit)	
EGR position feedback sensor	
VGT position feedback sensor	

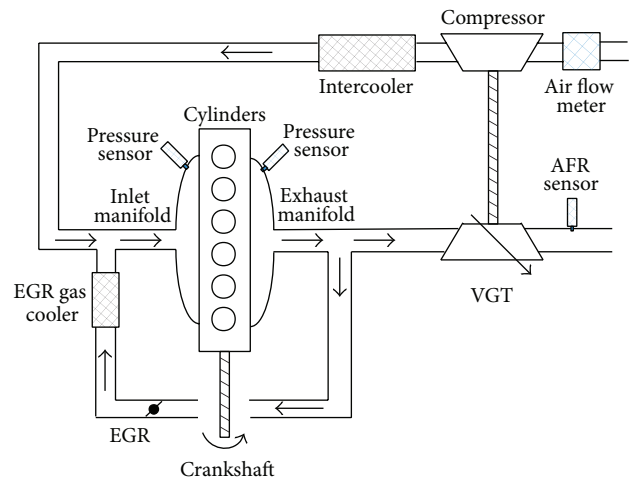


FIGURE 3: Turbocharged air-intake system schematic.

been wired in specifically for the MicroAutoBox. These sensors and actuators are listed in Table 1.

The data and control signal flow are illustrated in Figure 2. The engine is connected with two control platforms, which are CP Cadet and dSPACE Control Desk. The engine tests are conducted and monitored by CP Cadet Platform while the EGR and VGT valve positions can be adjusted through dSPACE Control Desk in real time. Testing data can be collected from both platforms and used for data analysis purpose.

The specification of the Caterpillar 3126b midrange truck engine is given in Table 3.

### 3. Engine Model and Validation

The considered diesel engine is a six-cylinder engine with a high-pressure EGR and VGT. A principle illustration scheme of the air-path system is shown in Figure 3. It consists of two parts: the turbocharger and exhaust gas recirculation. The turbocharger is a turbine driven by the exhaust gas and connected via a common shaft to the compressor, which

compresses the air in the intake. The exhaust gas recirculation (EGR) allows for recirculating gas from the exhaust manifold to the intake manifold. First, the mixture of air coming from the compressor and exhaust gas coming through the EGR valve enters the intake manifold before injecting it into the cylinders. Then, the fuel is injected directly in the cylinders and burned, producing the torque on the crank shaft. Exhaust gases are expelled into the exhaust manifold. As shown in Figure 3, part of exhaust gas comes out from the exhaust manifold through the turbine and the other part is recirculated through EGR valve. We noted that the temperature of gases (compressed air and EGR gas) entering the intake manifold is reduced using the intercooler and the EGR cooler.

The mean value engine modeling approach is one of the most considered approaches in the literature [19]. It uses temporal and spatial averages of relevant temperatures, pressures, and mass flow rates. The engine model is derived based on the laws of conservation of mass and energy and also on the ideal gas law (see, for instance, [5, 20]). As an example, the pressure dynamics in the inlet manifold is obtained by differentiating the ideal gas law equation  $PV = mRT$ . The complete considered mean value model is expressed as follows [5]:

$$\begin{aligned} \dot{P}_{\text{Inlet}} &= \frac{1}{V_{\text{Inlet}}} \left( \frac{R_{\text{Air}} c_{p,\text{Air}}}{c_{v,\text{Air}}} W_{\text{HFM}} T_{\text{CAC}} + \frac{R_{\text{Exh}} c_{p,\text{Exh}}}{c_{v,\text{Exh}}} W_{\text{EGR}} T_{\text{EGR}} \right. \\ &\quad \left. - \frac{R_{\text{Inlet}} c_{p,\text{Inlet}}}{c_{v,\text{Inlet}}} W_{\text{Inlet}} T_{\text{Inlet}} \right), \\ \dot{m}_{\text{Air}} &= W_{\text{HFM}} - \frac{m_{\text{Air}}}{m_{\text{Air}} + m_{\text{EGR}}} W_{\text{Inlet}}, \\ \dot{m}_{\text{EGR}} &= W_{\text{EGR}} - \frac{m_{\text{EGR}}}{m_{\text{Air}} + m_{\text{EGR}}} W_{\text{Inlet}}, \\ \dot{m}_{\text{Exh}} &= W_{\text{Exh}} - W_{\text{Turb}} - W_{\text{EGR}} \end{aligned} \quad (1)$$

with

$$\Psi\left(\frac{p_1}{p_0}\right) = \begin{cases} \sqrt{\frac{2\kappa}{\kappa-1} \left\{ \left(\frac{p_1}{p_0}\right)^{2/\kappa} - \left(\frac{p_1}{p_0}\right)^{(\kappa+1)/\kappa} \right\}} & \text{if } \left(\frac{p_1}{p_0}\right) \geq \left(\frac{2}{\kappa+1}\right)^{\kappa/(\kappa-1)} \\ \sqrt{\kappa \left(\frac{2}{\kappa+1}\right)^{(\kappa+1)/(\kappa-1)}} & \text{otherwise,} \end{cases}$$

$$W_{\text{EGR}} = \frac{A_{\text{EGR}} P_{\text{Exh}}}{\sqrt{R_{\text{Exh}} T_{\text{Exh}}}} \Psi_{\kappa_{\text{Exh}}}\left(\frac{P_{\text{Inlet}}}{P_{\text{Exh}}}\right),$$

$$W_{\text{Inlet}} = f_{\text{vol}}\left(N_{\text{Eng}}, \frac{P_{\text{Inlet}}}{T_{\text{Inlet}} R_{\text{Inlet}}}\right) \frac{N_{\text{Eng}} P_{\text{Inlet}}}{T_{\text{Inlet}} R_{\text{Inlet}}} \frac{V_{\text{Eng}}}{120},$$

$$T_{\text{Inlet}} = \frac{P_{\text{Inlet}} V_{\text{Inlet}}}{(m_{\text{Air}} + m_{\text{EGR}}) R_{\text{Inlet}}},$$

$$\begin{aligned} T_{\text{EGR}} &= \left(\frac{P_{\text{Inlet}}}{P_{\text{Exh}}}\right)^{(\kappa_{\text{Exh}}-1)/\kappa_{\text{Exh}}} T_{\text{Exh}}, \\ W_{\text{Exh}} &= W_{\text{Inlet}} + W_{\text{Fuel}}, \\ T_{\text{Exh}} &= T_{\text{Inlet}} + \frac{Q_{\text{LHV}} h(W_{\text{Fuel}}, N_{\text{Eng}})}{c_{p,\text{Exh}} (W_{\text{Inlet}} + W_{\text{Fuel}})}, \\ P_{\text{Exh}} &= \frac{m_{\text{Exh}} R_{\text{Exh}} T_{\text{Exh}}}{V_{\text{Exh}}}, \\ W_{\text{Turb}} &= \frac{P_{\text{Exh}}}{\sqrt{T_{\text{Exh}}}} \tau\left(\frac{P_{\text{Exh}}}{P_{\text{Atm}}}, u_{\text{XVNT}}\right), \\ R_{\text{Inlet}} &= \frac{R_{\text{Air}} m_{\text{Air}} + R_{\text{Exh}} m_{\text{EGR}}}{m_{\text{Air}} + m_{\text{EGR}}}, \\ c_{v,\text{Inlet}} &= \frac{c_{v,\text{Air}} m_{\text{Air}} + c_{v,\text{Exh}} m_{\text{EGR}}}{m_{\text{Air}} + m_{\text{EGR}}}, \\ c_{p,\text{Inlet}} &= c_{v,\text{Inlet}} + R_{\text{Inlet}}, \\ A_{\text{EGR}} &= A_{\text{EGRmax}} f_{\text{EGR}}(u_{\text{EGR}}), \end{aligned} \quad (2)$$

where  $P_{\text{Inlet}}$  is the pressure in intake manifold.  $m_{\text{Air}}$  and  $m_{\text{EGR}}$  are, respectively, the mass of air and EGR-gas in intake manifold.  $m_{\text{Exh}}$  represents the mass of exhaust gas in exhaust manifold. The other model variables and constant parameters with their value are listed in Table 4. The temperatures  $T_{\text{EGR}}$  and  $T_{\text{Exh}}$  are assumed to be constant and equal to 329.436 K and 837 K, respectively.  $A_{\text{EGRmax}}$  is the maximum opening area for the EGR. The EGR valve (VGT) is closed when  $u_{\text{EGR}} = 0\%$  ( $u_{\text{XVGT}} = 0\%$ ) and open when  $u_{\text{EGR}} = 100\%$  ( $u_{\text{XVGT}} = 100\%$ ). The static functions,  $f_{\text{vol}}$ ,  $f_{\text{EGR}}$ ,  $h$ , and  $\tau$ , are represented as interpolation in lookup tables. All these parameters are estimated using weighted least squares optimization approach. It is worth noting that the compressor and the CAC are not considered in the model as in [3] since the mass flow and the temperature after the charge-air cooler (CAC) are known variables because they are measured by the production sensors. The considered control inputs are the VGT vane position  $u_{\text{XVGT}}$  and the EGR valve position  $u_{\text{EGR}}$ . Notice that the following variables:  $T_{\text{CAC}}$ ,  $W_{\text{HFM}}$ ,  $N_{\text{Eng}}$ ,  $W_{\text{Fuel}}$ , and  $T_{\text{Exh}}$  are considered as measurable signals. The measured outputs are the inlet and exhaust pressures.

We draw the reader's attention that another more general mean value model composed of eight states is developed, parameterized, and validated in [21]. The obtained model describes the gas flow dynamics including the dynamics in the manifold pressures, EGR, turbocharger, and actuators.

The mean value model described in the previous section was simulated and compared with real measurements obtained from the Caterpillar testbed. The results are depicted in Figures 4–7. The input variables used for the validation purpose are illustrated in Figure 4. The measured and modeled outputs ( $P_{\text{Inlet}}$  and  $P_{\text{Exh}}$ ) are presented in Figure 5. The absolute value of the difference between the real and estimated variables is shown in Figure 6. One can conclude that the used model can reproduce engine dynamic behavior

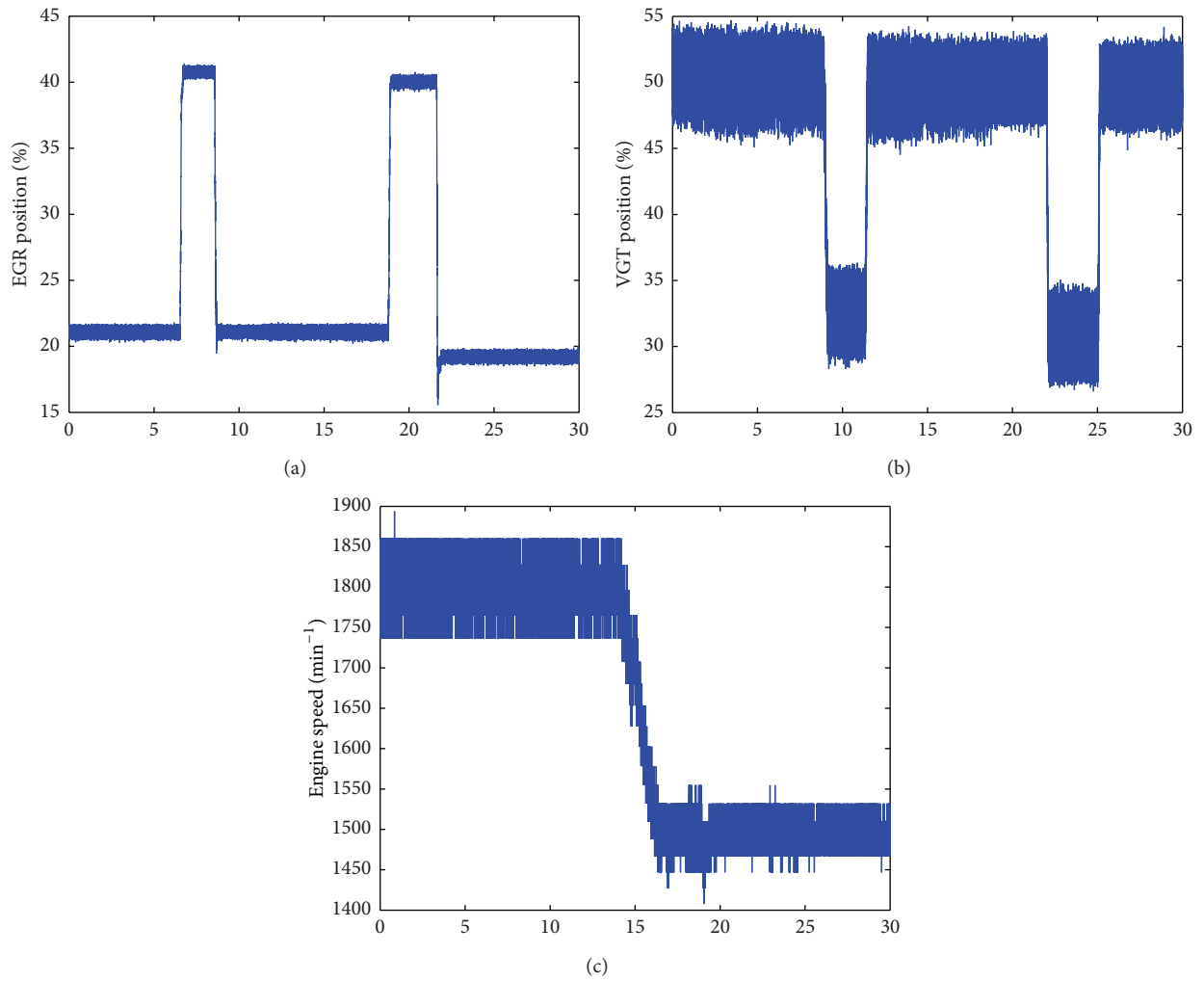


FIGURE 4: Input variables: (a) EGR position [%], (b) VGT position [%], and (c) engine speed [ $\text{min}^{-1}$ ].

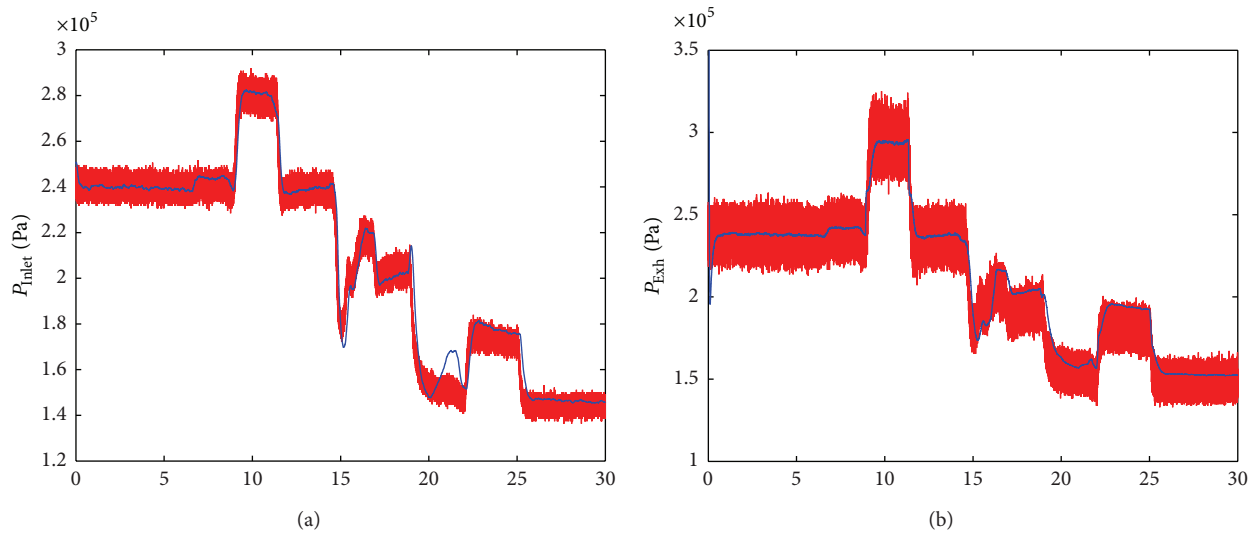


FIGURE 5: Modeled (blue color) and measured (red color) inlet and exhaust pressures.

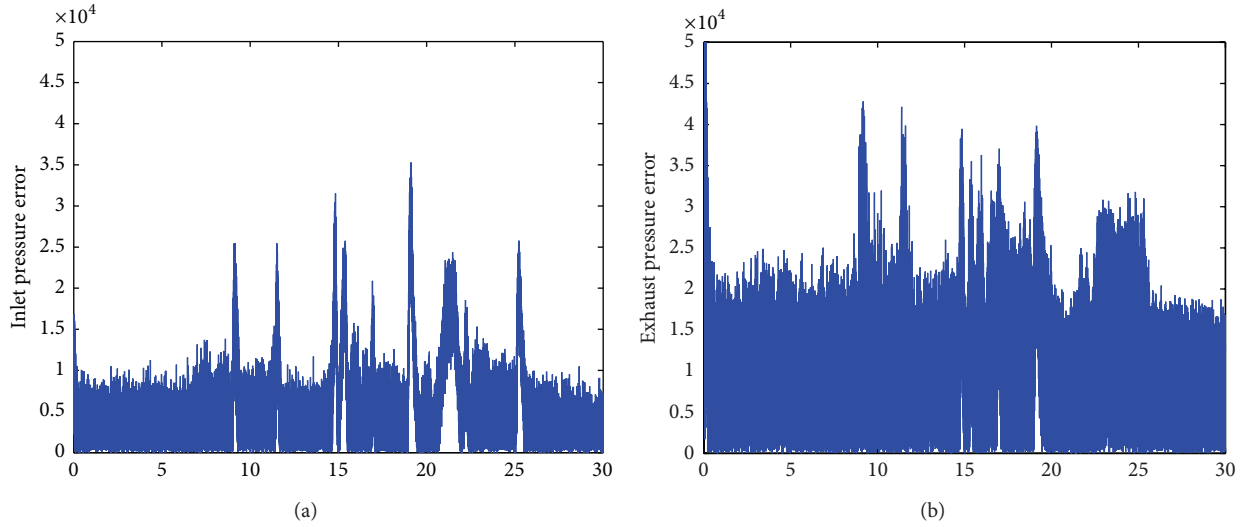


FIGURE 6: Absolute value of the difference between the measured and modeled pressures: (a) inlet pressure error and (b) exhaust pressure error.

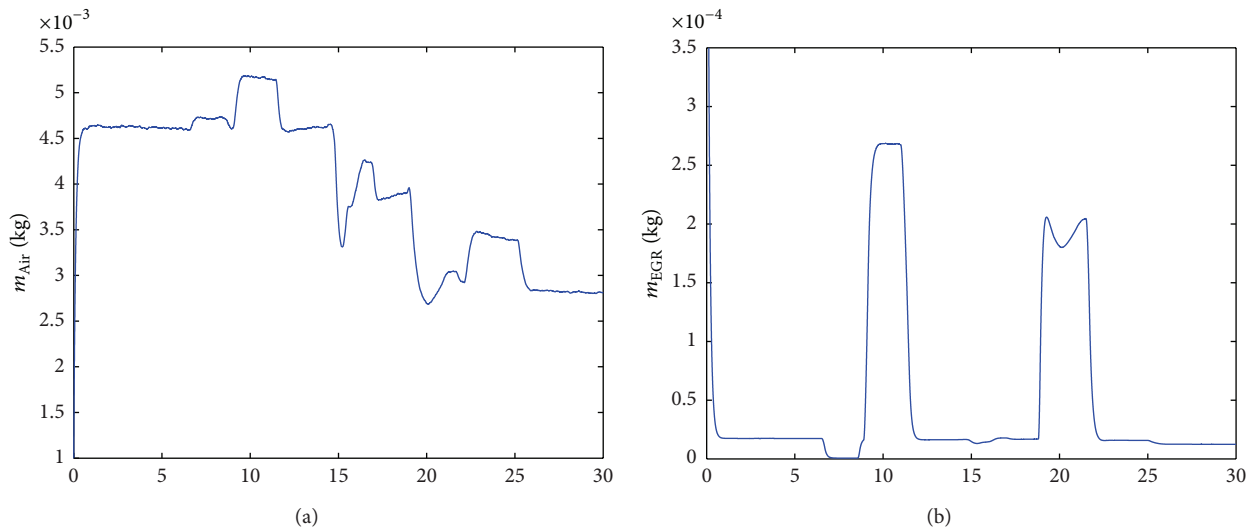


FIGURE 7: Air and EGR mass flows ( $m_{\text{Air}}$  and  $m_{\text{EGR}}$ ).

with good accuracy since the obtained average error is below 3%. Besides, the output measurements are very noisy as shown in Figure 5. Furthermore, the air and exhaust gas mass flows ( $m_{\text{Air}}$  and  $m_{\text{Exh}}$ ) are also presented in Figure 7.

#### 4. Nonlinear Unknown Input Observer Design

In this section, we will present briefly a nonlinear unknown input observer developed in [12]. It was proposed for a class of Lipschitz nonlinear systems with large Lipschitz constant. The sufficient existence conditions for this observer are formulated in terms of LMIs.

Obviously, engine model (1) can be put into the form (3a) and (3b). One can see that this form contains three parts: one linear parameter varying part, a nonlinear term with known variables, and a nonlinear state-dependent part. By

considering the form (3a) and (3b), this will allow us to tackle our synthesis problem based on Lyapunov theory for LPV systems. Thus, let us consider the general class of nonlinear systems described by the following equations:

$$\dot{x} = \sum_{j=1}^{n_p} \rho_j A_j x + B_g g(v, y, u) + f(x, u) + B_f f_a + B_{\bar{w}} \bar{w}, \quad (3a)$$

$$y = Cx + D_{\bar{w}} \bar{w}, \quad (3b)$$

where  $x \in \mathfrak{R}^{n_x}$  is the state vector,  $u \in \mathfrak{R}^{n_u}$  is the control input vector,  $f_a \in \mathfrak{R}^{n_{f_a}}$  represents the actuator faults assimilated as unknown inputs,  $y \in \mathfrak{R}^{n_y}$  is the output vector,  $\bar{w} \in \mathfrak{R}^{n_{\bar{w}}}$  is the vector of disturbances/noises, and  $v \in \mathfrak{R}^{n_v}$  is the vector of measurable signals. Notice that  $v$  contains any other

measured signals which have no link with the system output ( $y$ ) (e.g., temperature measurement, air mass flow ( $W_{\text{HFM}}$ ), etc.).  $A_j$ , for  $j = 1, \dots, n_p$ ,  $B_g$ ,  $B_f$ ,  $B_{\bar{w}}$ ,  $C$ , and  $D_{\bar{w}}$  are constant matrices with appropriate dimensions. Without loss of generality, the matrix  $B_f$  is assumed to be of full column rank. The functions  $g(v, y, u)$  and  $f(x, u)$  are nonlinear. No assumption is made about the function  $g(v, y, u)$ . However, the function  $f(x, u)$  is assumed to be once differentiable with large Lipschitz constant. The weighting functions  $\rho_j$  are assumed to be known and depend on measurable variables. They verify the convex sum property:

$$\sum_{j=1}^{n_p} \rho_j = 1, \quad \rho_j \geq 0, \quad \forall j \in \{1, \dots, n_p\}. \quad (4)$$

Let us first rewrite  $B_f f_a$  as follows:

$$B_f f_a = \sum_{i=1}^{n_{f_a}} B_{f,i} f_{a,i}, \quad (5)$$

where  $B_{f,i}$  is the distribution matrix of the fault  $f_{a,i}$ .

The aim is to construct an NUIO-based residual generator which is insensitive to only one actuator fault (e.g.,  $B_{f,i} f_{a,i}$ ). By choosing the unknown input (scalar)  $d = f_{a,i}$ , the system (3a) and (3b) can be rewritten as

$$\dot{x} = \sum_{j=1}^{n_p} \rho_j A_j x + B_g g(v, y, u) + f(x, u) + B_d d + B_w w, \quad (6a)$$

$$y = Cx + D_w w, \quad (6b)$$

where  $B_d = B_{f,i}$ ,  $B_w = [B_{\bar{w}} \quad \bar{B}_f]$ ,  $D_w = [D_{\bar{w}} \quad 0]$ , and  $w = \begin{bmatrix} \bar{w} \\ \bar{f}_a \end{bmatrix}$  with  $\bar{f}_a$  the actuator fault vector  $f_a$  without the  $i$ th component.  $\bar{B}_f$  is the matrix  $B_f$  without the  $i$ th column.

It is worth noting that the necessary condition for the existence of a solution to the unknown input observer design is the following ([18, 22] for a more explanation):  $\text{Rank}(CB_d) = \text{Rank}(B_d)$ , where  $B_d$  is a matrix of full column rank as is a column of the matrix  $B_f$  which is assumed before to be full column rank.

The considered residual generator for the system (6a) and (6b) is given by

$$\dot{z} = N(\rho)z + Gg(v, y, u) + Mf(\hat{x}, u) + L(\rho)y, \quad (7a)$$

$$\hat{x} = z - Ey, \quad (7b)$$

$$r = \Pi_r (y - C\hat{x}) \quad (7c)$$

with  $N(\rho) = \sum_{j=1}^{n_p} \rho_j N_j$  and  $L(\rho) = \sum_{j=1}^{n_p} \rho_j L_j$ .  $\Pi_r$  is a known matrix.  $\hat{x}$  represents the state estimation vector. Matrices  $N$ ,  $G$ ,  $M$ ,  $L$ , and  $E$  are the observer gains and matrices which must be determined such that  $\hat{x}$  converges asymptotically to  $x$ . Notice that the index  $\rho$  is omitted where it is not necessary to simplify the notations.

By defining the state estimation error as  $e(t) = \hat{x}(t) - x(t)$ , the error dynamics can be expressed as

$$\begin{aligned} \dot{e} = & Ne + (G - MB_g)g(v, y, u) + (NM + LC - MA)x \\ & - MB_d d + M\tilde{f} + (KD_w - MB_w)w - ED_w \dot{w} \end{aligned} \quad (8)$$

with  $\tilde{f} = f(\hat{x}, u) - f(x, u)$  and  $K = L + NE$ . Now, if the following matrix equations are satisfied:

$$N(\rho) = MA(\rho) - K(\rho)C, \quad \text{with each } N_j \text{ stable}, \quad (9a)$$

$$L(\rho) = K(\rho) \times (I + CE) - MA(\rho)E, \quad (9b)$$

$$G = MB_g, \quad (9c)$$

$$M = I + EC, \quad (9d)$$

$$MB_d = 0, \quad (9e)$$

$e(t)$  goes to zero asymptotically if  $w = 0$  and is invariant with respect to the unknown input  $d(t)$ . The notation  $I$  stands for the identity matrix.

Conditions (9d) and (9e) are equivalent to  $ECB_d = -B_d$ . One necessary condition to have for  $ECB_d = -B_d$  is that  $CB_d$  is of full column rank since  $B_d$  is of full column rank. If  $CB_d$  is of full column rank, then all possible solutions of  $ECB_d = -B_d$  can be expressed as follows [18]:

$$E = U + YV \quad (10)$$

with  $U = -B_d(CB_d)^\dagger$  and  $V = (I - CB_d(CB_d)^\dagger)$  where  $Y$  can be any compatible matrix and  $X^\dagger = (X^T X)^{-1} X^T$ .

Then, the error dynamics becomes

$$\dot{e} = (MA - KC)e + M\tilde{f} + (KD_w - MB_w)w - ED_w \dot{w}. \quad (11)$$

In order to minimize the effect of disturbances on the observer error, the  $H_\infty$  performance criterion can be used. However, the presence of the term  $\dot{w}$  makes the task difficult because it should be discarded from the derivative of the Lyapunov function as we will see later. Another solution is to add a negative term depending on  $\dot{w}^T \dot{w}$  as proposed in [23]. This solution needs to modify the classical  $H_\infty$  criterion. In this work, the modified  $H_\infty$  criterion presented in [23] is used.

The modified  $H_\infty$  estimation problem consists in computing the matrices  $N$  and  $L$  such that

$$\lim_{t \rightarrow \infty} e(t) = 0 \quad \text{for } w(t) = 0, \quad (12a)$$

$$\|e\|_{\mathcal{L}_2^{n_x}} \leq \gamma \|w\|_{1,2}^r \quad \text{for } w(t) \neq 0; e(0) = 0, \quad (12b)$$

where  $\|\cdot\|_{k,p}^r$  represents the Sobolev norm (see [23]).

Then to satisfy (12a)-(12b), it is sufficient to find a Lyapunov function  $Y$  such that

$$\Gamma = \dot{Y} + e^T e - \gamma^2 w^T w - \gamma^2 \dot{w}^T \dot{w} < 0, \quad (13)$$

where  $Y = e^T P e$  with  $P$  a positive definite symmetric matrix. From (11),  $\Gamma$  is given by

$$\begin{aligned} \Gamma = & e^T \left( (MA - KC)^T P + P(MA - KC) \right) e \\ & + e^T P M \tilde{f} + (M \tilde{f})^T P e \\ & + e^T P (KD_w - MB_w) w + w^T (KD_w - MB_w)^T P e \quad (14) \\ & - e^T P E D_w \dot{w} \\ & - \dot{w}^T (E D_w)^T P e + e^T e - \gamma^2 w^T w - \gamma^2 \dot{w}^T \dot{w}. \end{aligned}$$

Before introducing our main result, let us present the modified mean value theorem [24] for a vector function.

**Theorem 1** (see [24]). *Let the canonical basis of the vectorial space  $\mathfrak{R}^s$  for all  $s \geq 1$  be defined by*

$$\begin{aligned} E_s \\ = \left\{ e_s(i) \mid e_s(i) = \left( \underbrace{0, \dots, 0, \overbrace{1}^{ith}, 0, \dots, 0}_{s \text{ components}} \right)^T, i = 1 \dots s \right\}. \end{aligned} \quad (15)$$

Let  $f(x) : \mathfrak{R}^n \rightarrow \mathfrak{R}^n$  be a vector function continuous on  $[a, b] \in \mathfrak{R}^n$  and differentiable on convex hull of the set  $(a, b)$ . For  $s_1, s_2 \in [a, b]$ , there exist  $\delta_{ij}^{\max}$  and  $\delta_{ij}^{\min}$  for  $i = 1 \dots n$  and  $j = 1 \dots n$  such that

$$\begin{aligned} f(s_2) - f(s_1) \\ = \left[ \left( \sum_{i,j=1}^{n,n} H_{ij}^{\max} \delta_{ij}^{\max} \right) + \left( \sum_{i,j=1}^{n,n} H_{ij}^{\min} \delta_{ij}^{\min} \right) \right] (s_2 - s_1) \\ \delta_{ij}^{\max}, \delta_{ij}^{\min} \geq 0, \quad \delta_{ij}^{\max} + \delta_{ij}^{\min} = 1, \end{aligned} \quad (16)$$

where

- (i)  $h_{ij}^{\max} \geq \max(\partial f_i / \partial x_j)$  and  $h_{ij}^{\min} \leq \min(\partial f_i / \partial x_j)$ ,
- (ii)  $H_{ij}^{\max} = e_n(i) e_n^T(j) h_{ij}^{\max}$  and  $H_{ij}^{\min} = e_n(i) e_n^T(j) h_{ij}^{\min}$ .

The proof of this theorem is given in [24].

In our case, the nonlinear function  $f$  depends on the state vector  $x$  and also on the known input  $u$ . Although the previous theorem is applicable in our case,  $u$  is bounded.

Now, we can give a sufficient condition under which the observer given by (7a), (7b), and (7c) is a NUIO. Thus, the negativity of  $\Gamma$  is ensured by the following theorem.

**Theorem 2** (see [25]). *The observer error  $e(t)$  converges asymptotically towards zero if there exist matrices  $\bar{K}_k$ ,  $\bar{Y}$ ,*

*a positive definite symmetric matrix  $P$ , and a positive scalar  $\mu$  such that the following LMIs are satisfied:*

$$P > 0, \quad (17a)$$

$$\begin{bmatrix} \Xi_{ijk}^{\max} & \Phi_k & -PYD_w - \bar{Y}VD_w \\ (*) & -\mu I & 0 \\ (*) & (*) & -\mu I \end{bmatrix} < 0, \quad (17b)$$

$$\begin{bmatrix} \Xi_{ijk}^{\min} & \Phi_k & -PYD_w - \bar{Y}VD_w \\ (*) & -\mu I & 0 \\ (*) & (*) & -\mu I \end{bmatrix} < 0 \quad (17c)$$

$\forall i = 1, \dots, n, j = 1, \dots, n$  and  $k = 1, \dots, n_p$ , where

$$\Phi_k = -\bar{K}_k D_w + P(I + UC)B_w + \bar{Y}VCB_w, \quad \mu = \gamma^2,$$

$$\begin{aligned} \Xi_{ijk}^{\max} = & \left[ (I + UC) \left( A + \bar{H}_{ij}^{\max} \right) \right]^T P \\ & + P(I + UC) \left( A + \bar{H}_{ij}^{\max} \right) - C^T \bar{K}_k^T \\ & - \bar{K}_k C + \left( A + \bar{H}_{ij}^{\max} \right)^T C^T V^T \bar{Y}^T \\ & + \bar{Y}VC \left( A + \bar{H}_{ij}^{\max} \right) + I, \\ \Xi_{ijk}^{\min} = & \left[ (I + UC) \left( A + \bar{H}_{ij}^{\min} \right) \right]^T P \\ & + P(I + UC) \left( A + \bar{H}_{ij}^{\min} \right) - C^T \bar{K}_k^T \\ & - \bar{K}_k C + \left( A + \bar{H}_{ij}^{\min} \right)^T C^T V^T \bar{Y}^T \\ & + \bar{Y}VC \left( A + \bar{H}_{ij}^{\min} \right) + I, \\ \bar{H}_{ij}^{\max} = & Z_H H_{ij}^{\max}, \quad \bar{H}_{ij}^{\min} = Z_H H_{ij}^{\min} \end{aligned} \quad (18)$$

with  $Z_H = n \times n$ . Solving LMIs (17a)–(17c) leads to determine matrices  $P$ ,  $\bar{Y}$ , and  $\bar{K}_k$ . The matrices  $K_k$  and  $Y$  can be obtained from  $K_k = P^{-1} \bar{K}_k$  and  $Y = P^{-1} \bar{Y}$ . The other matrices  $N$  and  $L$  can then be deduced easily from (9a) and (9b), respectively.

*Proof.* The proof is omitted. A sketch of this proof is presented in [25].  $\square$

Notice that if there exist terms such that  $\partial f_i / \partial x_j = 0$ , then the scaling factor  $\sum_{i,j=1}^{n,n} (\delta_{ij}^{\max} + \delta_{ij}^{\min})$  is less than 1. Consequently, the scaling factor  $\bar{Z}_H$  must be redefined as follows:

$$\begin{aligned} \bar{Z}_H = & \sum_{i,j=1}^{n,n} (\delta_{ij}^{\max} + \delta_{ij}^{\min}) = n \times n - n_0, \\ \frac{\sum_{i,j=1}^{n,n} (\delta_{ij}^{\max} + \delta_{ij}^{\min})}{\bar{Z}_H} = & 1, \end{aligned} \quad (19)$$

where  $n_0$  is the number of terms in  $\partial f_i / \partial x_j$  that equal zero.

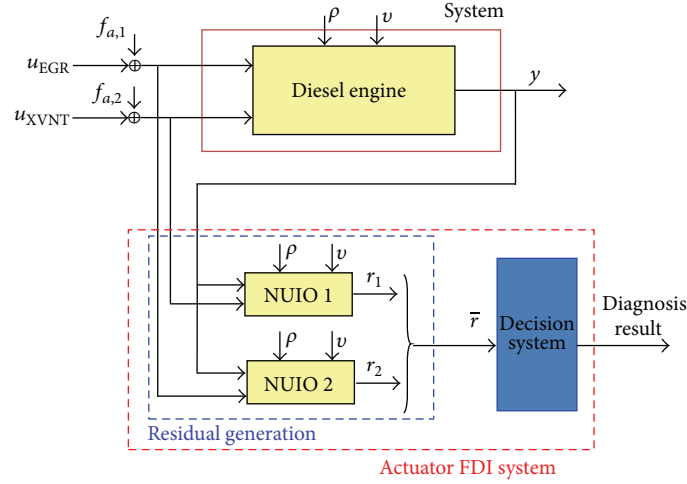


FIGURE 8: FDI system.

The procedure to design the NUIO parameters is summarized by the following algorithm.

*Algorithm 3.* NUIO design is as follows:

- (1) compute  $U$  and  $V$  from (10),
- (2) determine matrices  $Y$  and  $K_k$ , with  $k = 1, \dots, n_p$  from the LMI sets (17a)–(17c),
- (3) compute the observer matrices  $E$ ,  $M$ ,  $G$ ,  $N$ , and  $L$  from (10), (9d), (9c), (9b), and (9a), respectively.

## 5. Residual Generation

This section addresses the problem of actuator faults isolation based on a bank of residual generators (see Figure 8). Each residual on the proposed scheme is an NUIO based on model (6a) and (6b). Notice that the system (1) can be easily rewritten in a state space form as (3a) and (3b) (see Appendix C). Furthermore, each residual is designed to be insensitive to only one fault. Thus, the actuator faults can be easily isolated since only one residual goes to zero while the others do not. Therefore, for our application, the combination of two observers is sufficient to detect and isolate any faulty actuator. It is also assumed that only a single actuator fault can occur at one time.

To construct the bank of residual generators we have to

- (i) design an NUIO which generates the residual  $r_1$  insensitive to  $f_{a,1}$  by taking

$$B_d = \begin{bmatrix} \frac{R_{\text{Exh}} T_{\text{EGR}} A_{\text{EGRmax}} c_{p,\text{Exh}}}{V_{\text{Inlet}} c_{v,\text{Exh}}} & 0 & A_{\text{EGRmax}} & -A_{\text{EGRmax}} \end{bmatrix}^T, \quad (20)$$

- (ii) design an NUIO which generates the residual  $r_2$  insensitive to  $f_{a,2}$  by taking

$$B_d = [0 \ 0 \ 0 \ 1]^T. \quad (21)$$

TABLE 2: Effect of the faults on the residuals.

$\bar{r}$	$f_1$	$f_2$
$r_1$	0	×
$r_2$	×	0

To obtain  $B_d$  as in (20), it suffices to replace in the original system the input vector  $u$  by  $u + f_a$ , where  $f_a$  represents the actuator fault vector. Thus,  $B_d$  can be obtained easily by gathering the terms multiplying the vector  $f_a$  in one matrix.

Each residual,  $r_i(t)$  ( $i = 1, 2$ ), computed from (7a), (7b), and (7c), is a 1-dimensional vector associated with one of the actuators  $u_{\text{EGR}}$  and  $u_{\text{XVGT}}$ . By stacking the two vectors, one defines  $\bar{r}(t) = [r_1'(t), r_2'(t)]'$ . In the absence of faults, this vector of residuals has zero mean, while, upon occurrence of a single step-like fault, the effect on each of its components is indicated in Table 2. A “×” is placed when the fault located in the corresponding column affects the mean of the residual component on the corresponding row, and a “0” when the residual component presents very low sensitivity to the fault. The sampled vector  $\bar{r}(k)$  can be rewritten as

$$\bar{r}(k) = \bar{r}_0(k) + \sum_{\ell=1}^2 \nu_{\ell} \Gamma_{\ell}(k) 1_{\{k \geq k_0\}} \delta_{\ell}, \quad (22)$$

where the sample number  $k$  corresponds to the time instant  $t = kT_s$  with  $T_s$  denoting the sampling period,  $\bar{r}_0(k)$  is the fault-free residual,  $\Gamma_{\ell}(k)$  is the dynamic profile of the change on  $\bar{r}(k)$  due to a unit step-like fault  $f_{\ell}$ , and  $\nu_{\ell}$  is the magnitude of fault  $\ell$ . Model (22) will be used as the basis for the decision system design in the next section.

One can see that residuals are designed in a deterministic framework. However, due to measurement noise and system disturbances, parameters uncertainties, and variations, the computed residuals are stochastic signals. As a consequence, a multi-CUSUM method will be used for the decision step. Another way would have been to consider the noise and stochastic disturbances characteristics to design robust residuals, analyze the stochastic characteristics of the residuals,

TABLE 3: Caterpillar 3126B engine characteristics.

Description	
Model	Caterpillar 3126B
Type of engine	Inline, 4-stroke
Number of cylinders	6
Number of inlet valves	2
Number of exhaust valves	1
Firing order	1-5-3-6-2-4
Type of combustion	Direct injection
Maximum torque	1166 Nm @ 1440 rpm
Maximum power	224 kw @ 2200 rpm
Idle speed	700 rpm
Maximum speed	2640 rpm
Geometrical characteristics	
Bore	110 mm
Stroke	127 mm
Compression ratio	16
Total displacement	7.25 liter
Connecting rod length	199.9 mm
Crank throw radius	63.5 mm
Injection system	
Type	HEUI
Injection pressure	200–145 bar
Injection orifices number	6
Type of combustion	Direct injection
Geometrical characteristics of manifolds and pipes	
Intake manifold	5 L
Exhaust manifold	0.945 L

and design the decision algorithm with respect to these characteristics. However, this would be too complex to do for our application and would lie anyway on given assumptions on the stochastic disturbances.

## 6. Decision System

In this section, we will present a decision system based on a statistical approach proposed in [26]. This approach, named multi-CUSUM, was developed in [27] and refined in [28]. Indeed, in model (22), it is seen that an actuator fault induces a change in the mean of the residual vector  $\bar{r}(k)$ . Thus, the problem amounts to detecting and isolating a step-like signal within a white Gaussian noise sequence. Therefore, the change detection/isolation problem can be stated as the following hypothesis testing:

$$\begin{aligned}
\mathcal{H}_0 : \mathcal{L}(\bar{r}(i)) &= \mathcal{N}(\boldsymbol{\mu}_0, \Sigma), \quad i = 1, \dots, k, \\
\mathcal{H}_\ell : \mathcal{L}(\bar{r}(i)) &= \mathcal{N}(\boldsymbol{\mu}_\ell, \Sigma), \quad i = 1, \dots, k_0 - 1, \\
\mathcal{L}(\bar{r}(i)) &= \mathcal{N}(\boldsymbol{\mu}_\ell, \Sigma), \quad i = k_0, \dots, k,
\end{aligned} \quad (23)$$

where  $k_0 \in [1, k]$ , and  $\boldsymbol{\mu}_\ell = \boldsymbol{\mu}_0 + \nu_\ell \Gamma_\ell$  is the mean value of the residual sequence when the  $\ell$ th fault has occurred, for  $\ell \in \{1, 2\}$ . The decision system is based on a combination of CUSUM decision functions [27], each of them involving the log-likelihood ratio between hypotheses  $\mathcal{H}_\ell$  and  $\mathcal{H}_0$ , namely,

$$s_k(\ell, 0) = \ln \frac{p_\ell(\bar{r}(k))}{p_0(\bar{r}(k))}, \quad (24)$$

where  $p_\ell$  is the probability density function of  $\bar{r}(k)$  under the hypothesis  $\mathcal{H}_\ell$ . Under the Gaussian hypothesis, the log-likelihood ratio can be rewritten as

$$s_k(\ell, 0) = (\boldsymbol{\mu}_\ell - \boldsymbol{\mu}_0)^T \Sigma^{-1} \left( \bar{r}(k) - \frac{1}{2}(\boldsymbol{\mu}_\ell + \boldsymbol{\mu}_0) \right). \quad (25)$$

The CUSUM decision function is defined recursively as

$$g_k(\ell, 0) = \max(0, g_{k-1}(\ell, 0) + s_k(\ell, 0)). \quad (26)$$

In order to estimate the fault occurrence time, the number of successive observations for which the decision function remains strictly positive is computed as  $N_\ell(k) = N_\ell(k-1) \mathbb{1}_{\{g_{k-1}(\ell, 0) > 0\}} + 1$ . To decide whether fault  $\ell$  has occurred, one has to check that, on average, all the likelihood ratios  $s_k(\ell, j)$ , for  $1 \leq j \neq \ell \leq 2$ , are significantly larger than zero. Noticing that  $s_k(\ell, j) = s_k(\ell, 0) - s_k(j, 0)$ , one can build a CUSUM algorithm to decide between hypotheses  $\mathcal{H}_\ell$  and  $\mathcal{H}_j$  by taking into account the difference between  $g_k(\ell, 0)$  and  $g_k(j, 0)$ . Hence a decision that  $\mathcal{H}_\ell$  holds can be issued when the following decision function becomes positive:

$$\bar{g}_\ell = \min_{0 \leq j \neq \ell \leq 2} (g_k(\ell, 0) - g_k(j, 0) - h_{\ell, j}) \quad (27)$$

for  $\ell = 1, 2$  and  $g_k(0, 0) = 0$ .

Like in [26, 27], it is advisable to consider only two values for the thresholds  $h_{\ell, j}$ , for each  $\ell = 1, \dots, n_f$ , namely,

$$h_{\ell, j} = \begin{cases} h_{ed}, & \text{for } j = 0, \\ h_{ei}, & \text{for } 1 \leq j \neq \ell \leq n_f, \end{cases} \quad (28)$$

where  $h_{ed}$  is the detection threshold and  $h_{ei}$  is the isolation threshold. Notice that the mean detection delay, the mean time before false alarm, and the probability of a false isolation depend on the choice of these thresholds. Indeed, the thresholds  $h_{ed}$  and  $h_{ei}$  can be linked to the mean detection delay ( $\bar{\tau}$ ) for the fault  $\ell$  thanks to the following expression [27] assuming that  $h_{ed} = \bar{\gamma} h_{ei}$  where  $\bar{\gamma} \geq 1$  is a constant:

$$\bar{\tau} = \max \left( \frac{h_{ed}}{\bar{\kappa}_{\ell, 0}}, \frac{h_{ei}}{\min_{j \neq 0, \ell} (\bar{\kappa}_{\ell, j})} \right) \quad \text{as } h_{ei} \rightarrow \infty, \quad (29)$$

where  $\bar{\kappa}_{\ell, j}$  is the Kullback-Leibler information defined as

$$\bar{\kappa}_{\ell, j} = \frac{1}{2} (\boldsymbol{\mu}_\ell - \boldsymbol{\mu}_j)^T \Sigma^{-1} (\boldsymbol{\mu}_\ell - \boldsymbol{\mu}_j). \quad (30)$$

TABLE 4: The variables used in the engine model.

Symb.	Quantity	Value/unit
$P_{\text{Inlet}}$	Pressure in intake manifold	Pa
$P_{\text{Atm}}$	Atmospheric pressure	Pa
$W_{\text{Turb}}$	Exhaust mass flow past the turbine	kg·s <sup>-1</sup>
$u_{\text{XVNT}}$	Position of VNT vanes	%
$N_{\text{Eng}}$	Engine speed	min <sup>-1</sup>
$W_{\text{Fuel}}$	Mass flow of injected fuel	kg·s <sup>-1</sup>
$Q_{\text{LHV}}$	Lower heating value	J·kg <sup>-1</sup>
$A_{\text{EGR}}$	Effective area of EGR valve	m <sup>2</sup>
$R_{\text{Inlet}}$	Gas constant in intake manifold	J·(kg·K)
$W_{\text{Inlet}}$	Mass flow into engine inlet ports	kg·s <sup>-1</sup>
$T_{\text{Inlet}}$	Temperature in the intake manifold	K
$m_{\text{Air}}$	Mass of air in intake manifold	kg
$m_{\text{EGR}}$	Mass of EGR gas in intake manifold	kg
$W_{\text{Exh}}$	Exhaust mass flow into the exhaust manifold	kg·s <sup>-1</sup>
$m_{\text{Exh}}$	Mass of exhaust gas in exhaust manifold	kg
$P_{\text{Exh}}$	Pressure in exhaust manifold	Pa
$c_{p,\text{Inlet}}$	Specific heat at const. pres. in intake manifold	J·(kg·K)
$c_{v,\text{Inlet}}$	Specific heat at const. vol. in intake manifold	J·(kg·K)
$\kappa$	Ratio of specific heats	$c_p/c_v$
$W_{\text{HFM}}$	Air mass flow past the air mass flow sensor	kg·s <sup>-1</sup>
$W_{\text{EGR}}$	EGR mass flow into intake manifold	kg·s <sup>-1</sup>
$V_{\text{Inlet}}$	Volume of intake manifold	$1.8 \times 10^{-3} \text{ m}^3$
$R_{\text{Air}}$	Gas constant of air	288.2979 J·(kg·K)
$c_{p,\text{Air}}$	Specific heat at const. pres. of air	1067.4 J·(kg·K)
$c_{v,\text{Air}}$	Specific heat at const. vol. of air	779.1021 J·(kg·K)
$R_{\text{Exh}}$	Gas constant of exhaust gas of exhaust gas	290.155 J·(kg·K)
$c_{p,\text{Exh}}$	Specific heat at const. pres. of exhaust gas	1288.08 J·(kg·K)
$c_{v,\text{Exh}}$	Specific heat at const. vol. of exhaust gas	997.9250 J·(kg·K)
$T_{\text{CAC}}$	Temperature of the air after the charge-air cooler	322.5 K
$T_{\text{EGR}}$	Temperature of EGR gas flow into the i.m.	322 K
$T_{\text{Exh}}$	Temperature in exhaust manifold	837 K
$V_{\text{Eng}}$	Engine displacement	$7.239 \times 10^{-3} \text{ m}^3$
$V_{\text{Exh}}$	Volume of exhaust manifold	$9.4552 \times 10^{-3} \text{ m}^3$

When considering  $h_{\ell,d} = h_{\ell,i} = h_{\ell}$ , (31) is used instead of (27):

$$g_{\ell}^* = \min_{0 \leq j \neq \ell \leq 2} (g_k(\ell, 0) - g_k(j, 0)) \quad (31)$$

and an alarm is generated when a  $g_{\ell}^* \geq h_{\ell}$ .

The reader can refer to [26, 27] for more detailed information.

## 7. Experimental Results and Discussion

The proposed fault detection and isolation approach has been tested on the caterpillar 3126 engine located at Sussex University, UK. The aim is to detect and isolate any additive actuator fault. The detection delay  $\bar{\tau}$  should be lower than 0.01 s in average. This delay is defined as the difference between the alarm time and the actual fault occurrence time.

*7.1. Design Parameters.* For the design of the residual generators, the gain matrices given by (9a)–(9e) should be determined. Unfortunately, we cannot present their values due to pages limitation. Notice that the LMIs (17a)–(17c) are solved by using the software YALMIP toolbox, which is a toolbox for modeling and optimization in Matlab. Matrix  $\Pi_r$  for the two residual generators is chosen as  $\Pi_r = [0, 1]$ . The sampling period  $T_s$  is set as  $10^{-3}$  s.

*Remark 4.* It is worth noting that no feasible solution is obtained with the approach presented in [18] due to the Lipschitz constant value of the nonlinear function  $f$  (see (C.7)). In fact, the Lipschitz constant value is bigger than  $10^{10}$  in our case. Other methods can be used, or extended to our case, as that proposed in [23] for estimating the state and unknown input vectors. Unfortunately, these methods are computationally demanding since the number of LMIs,

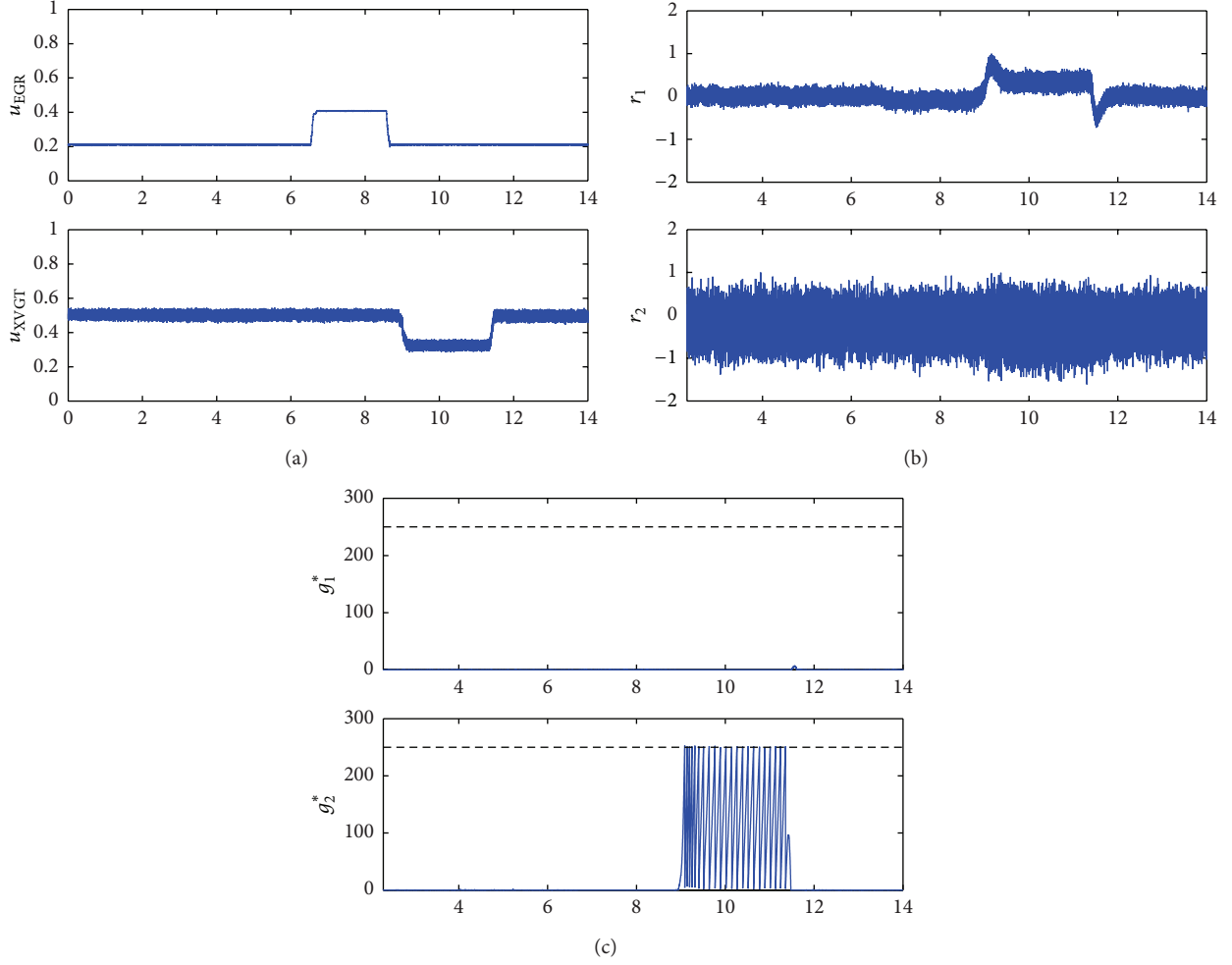


FIGURE 9: Experimental results: (a) EGR and VGT actuators, (b) residuals ( $r_i$ ), and (c) multi-CUSUM decision functions.

in each residual generator, that should be solved is equal to  $N_{\text{LMI}} = 2^{n \times n_f}$ , where  $n_f$  is the number of nonlinearities in the system. So, in our case  $N_{\text{LMI}} = 2^{4 \times 4} = 65536$ . In addition, it is only proposed for the standard systems with a linear time-invariant part ( $Ax$ ). We know that the number of LMIs will be strongly increased if this method is extended to our LPV case.

The covariance matrix  $\Sigma$  and the mean  $\mu_0$  used for designing the multi-CUSUM algorithm are estimates of the variance and the mean of  $\bar{r}$  obtained from a set of simulation data generated in healthy operating conditions. Assuming that all considered faults should be detected and isolated with a mean detection delay  $\bar{\tau} \leq 0.1$  s, the threshold is selected as  $h_\ell = 1000$ .

**7.2. Validation Step.** For illustrating the performance of this approach, the following scenario is considered. First, a positive step-like change in the EGR actuator appears when  $t \in [6.5, 8]$  s. Next, a single negative step-like fault in the VGT actuator is introduced in the time interval  $[8.9, 11.5]$  s.

The experiment is performed with engine average speed  $N_{\text{Eng}} = 1800$  rpm, where the minimum and maximum

value of  $N_{\text{Eng}}$  ( $N_{\text{Eng}}$  and  $\bar{N}_{\text{Eng}}$ ) are 1700 rpm and 1900 rpm, respectively. The initial conditions for the two observers are randomly chosen as follows:

$$\begin{aligned} z1_0 &= [12 \ 0 \ 2 \times 10^{-7} \ 10^{-10}]^T, \\ z2_0 &= [12 \ 0 \ 2 \times 10^{-7} \ 10^{-10}]^T. \end{aligned} \quad (32)$$

The experimental results are shown in Figure 9. First, the actuators ( $u_{\text{EGR}}$  and  $u_{\text{XVGT}}$ ) behavior is illustrated in Figure 9(a). Then, the normalized residuals  $r_1$  and  $r_2$  are shown in Figure 9(b). Finally, the decision functions resulting from the multi-CUSUM algorithm are presented in Figure 9(c). It is clear from the last figures (Figure 9(c)) that only the exact decision function  $g_2^*$ , corresponding to an occurred fault in  $u_{\text{XVGT}}$ , crosses the threshold. It means that this fault is correctly detected and isolated. The obtained mean detection delay  $\bar{\tau}$ , given by (29), is equal to 0.0890 s. As expected, this fault is detected and isolated with a mean detection delay  $\bar{\tau} \leq 0.1$  s.

## 8. Conclusion

The problem of actuator fault detection and isolation for diesel engines is treated in this paper. The faults affecting the EGR system and VGT actuator valves are considered. A bank of NUIO has been used. Each residual is designed to be insensitive to only one fault. By using this kind of scheme and by assuming that only a single fault can occur at one time, each actuator fault can be easily isolated since only one residual goes to zero while the others do not. A multi-CUSUM algorithm for statistical change detection and isolation is used as a decision system. Fault detection/isolation is achieved within the imposed timeslot. Experimental results are presented to demonstrate the effectiveness of the proposed approach.

## Appendices

### A. Engine Characteristics

See Table 3.

### B. Nomenclature

See Table 4.

### C. Diesel Engine Model

The system (1) can be easily rewritten in state space form as (3a) and (3b). Indeed, it suffices to extract the linear part by doing product development and to separate the nonlinear part with known or measurable variables ( $v, y, u$ ). The rest is gathered in the general nonlinear part ( $f(x, u)$ ). The state, known input and output vectors, and the variables  $\rho$  and  $v$  are defined as

$$\begin{aligned} x &= [P_{\text{Inlet}} \ m_{\text{Air}} \ m_{\text{EGR}} \ m_{\text{Exh}}]^T, \\ u &= [u_{\text{EGR}} \ u_{\text{XVNT}}]^T, \\ y &= [P_{\text{Inlet}} \ P_{\text{Exh}}]^T, \\ \rho &= N_{\text{Eng}}, \\ v &= [T_{\text{CAC}} \ W_{\text{HFM}} \ W_{\text{Fuel}}]^T. \end{aligned} \quad (\text{C.1})$$

The matrices  $A_1$  and  $A_2$  are given by

$$A_1 = \begin{bmatrix} -\frac{f_{\text{vol}} N_{\text{Eng}} V_{\text{Eng}}}{120V_{\text{Inlet}}} & 0 & 0 & 0 \\ 0 & -\frac{f_{\text{vol}} N_{\text{Eng}} V_{\text{Eng}}}{120V_{\text{Inlet}}} & 0 & 0 \\ 0 & 0 & -\frac{f_{\text{vol}} N_{\text{Eng}} V_{\text{Eng}}}{120V_{\text{Inlet}}} & 0 \\ 0 & \frac{f_{\text{vol}} N_{\text{Eng}} V_{\text{Eng}}}{120V_{\text{Inlet}}} & \frac{f_{\text{vol}} N_{\text{Eng}} V_{\text{Eng}}}{120V_{\text{Inlet}}} & 0 \end{bmatrix},$$

$$A_2 = \begin{bmatrix} -\frac{f_{\text{vol}} \bar{N}_{\text{Eng}} V_{\text{Eng}}}{120V_{\text{Inlet}}} & 0 & 0 & 0 \\ 0 & -\frac{f_{\text{vol}} \bar{N}_{\text{Eng}} V_{\text{Eng}}}{120V_{\text{Inlet}}} & 0 & 0 \\ 0 & 0 & -\frac{f_{\text{vol}} \bar{N}_{\text{Eng}} V_{\text{Eng}}}{120V_{\text{Inlet}}} & 0 \\ 0 & \frac{f_{\text{vol}} \bar{N}_{\text{Eng}} V_{\text{Eng}}}{120V_{\text{Inlet}}} & \frac{f_{\text{vol}} \bar{N}_{\text{Eng}} V_{\text{Eng}}}{120V_{\text{Inlet}}} & 0 \end{bmatrix}, \quad (\text{C.2})$$

where  $\underline{N}_{\text{Eng}}$  and  $\bar{N}_{\text{Eng}}$  are, respectively, the minimum and maximum value of the measurable variable  $N_{\text{Eng}}$ .  $\rho_1$  and  $\rho_2$  are defined as

$$\rho_1 = \frac{\bar{N}_{\text{Eng}} - N_{\text{Eng}}}{\bar{N}_{\text{Eng}} - \underline{N}_{\text{Eng}}}, \quad \rho_2 = \frac{N_{\text{Eng}} - \underline{N}_{\text{Eng}}}{\bar{N}_{\text{Eng}} - \underline{N}_{\text{Eng}}}. \quad (\text{C.3})$$

The matrices  $B_g$ ,  $C$ , and  $B_w$  are expressed as

$$B_g = \begin{bmatrix} \frac{R_{\text{Air}} c_{p,\text{Air}}}{c_{v,\text{Air}} V_{\text{Inlet}}} & 0 & 0 \\ 0 & 1 & 0 \\ 0 & 0 & 0 \\ 0 & 0 & 1 \end{bmatrix}, \quad C = \begin{bmatrix} 1 & 0 & 0 & 0 \\ 0 & 0 & 0 & \frac{R_{\text{Exh}} T_{\text{Exh}}^{\text{moy}}}{V_{\text{Exh}}} \end{bmatrix},$$

$$B_w = [0 \ 0 \ 0 \ 0]^T, \quad (\text{C.4})$$

where  $T_{\text{Exh}}^{\text{moy}}$  is the mean value of measurable variable  $T_{\text{Exh}}$ . The matrix  $B_f$  and the vector  $f_a$  are chosen as follows:

$$B_f = \begin{bmatrix} \frac{R_{\text{Exh}} T_{\text{EGR}} A_{\text{EGRmax}} c_{p,\text{Exh}}}{V_{\text{Inlet}} c_{v,\text{Exh}}} & 0 \\ 0 & 0 \\ A_{\text{EGRmax}} & 0 \\ -A_{\text{EGRmax}} & 1 \end{bmatrix}, \quad (\text{C.5})$$

$$f_a = \begin{bmatrix} \frac{P_{\text{Exh}}}{\sqrt{R_{\text{Exh}} T_{\text{Exh}}}} \Psi_{\kappa_{\text{Exh}}} \left( \frac{P_{\text{Inlet}}}{P_{\text{Exh}}} \right) f_{\text{EGR}}(u_{\text{EGR}}) \\ \frac{P_{\text{Exh}}}{\sqrt{T_{\text{Exh}}}} \tau \left( \frac{P_{\text{Exh}}}{P_{\text{Atm}}}, u_{\text{XVNT}} \right) \end{bmatrix}.$$

Finally, the functions  $g$  and  $f$  are given by

$$g = [W_{\text{HFM}} T_{\text{CAC}} \ W_{\text{HFM}} \ W_{\text{Fuel}}]^T, \quad (\text{C.6})$$

$$f = \begin{bmatrix} \frac{R_{\text{Inlet}} P_{\text{Inlet}}}{c_{v,\text{Inlet}}} \\ 0 \\ \frac{A_{\text{EGR}} m_{\text{Exh}} \Psi_{\kappa_{\text{Exh}}} T_{\text{Exh}}}{\sqrt{R_{\text{Exh}} T_{\text{Exh}}}} \\ -\frac{R_{\text{Exh}} T_{\text{Exh}} m_{\text{Exh}} \tau (P_{\text{Exh}}/P_{\text{Atm}}, u_{\text{XVNT}})}{V_{\text{Exh}} \sqrt{T_{\text{Exh}}}} \end{bmatrix}. \quad (\text{C.7})$$

As mentioned in Section 3, the parameters  $f_{\text{vol}}$ ,  $f_{\text{EGR}}$ ,  $\tau$ , and  $h$  are computed by interpolation in lookup tables. However, in this work, we are interested in the diagnosis in the steady state. So, we choose these parameters constant at each operating point to validate our approach. Furthermore, the proposed approach can take easily the parameter variation into account. For example, if we choose  $f_{\text{vol}}$  as variable parameter, the variable  $\rho$  can be chosen as  $\rho = f_{\text{vol}} N_{\text{Eng}}$  instead of  $\rho = N_{\text{Eng}}$ . By doing this, there is no need to change the design approach since the engine model has always the form (3a) and (3b).

## Conflict of Interests

The authors declare that there is no conflict of interests regarding the publication of this paper.

## Acknowledgments

This work was produced in the framework of SCODECE (Smart Control and Diagnosis for Economic and Clean Engine), a European territorial cooperation project part-funded by the European Regional Development Fund (ERDF) through the INTERREG IV A 2 Seas Programme, and the Research Department of the Region Nord Pas de Calais, France.

## References

- [1] CARB, "California's obd-ii regulation (section 1968.1 title 13, california code of regulations)," in *Resolution 93-40*, pp. 220.7(h)–220.12(h), 1993.
- [2] J. Gertler, M. Costin, X. Fang, Z. Kowalczyk, M. Kunwer, and R. Monajemy, "Model based diagnosis for automotive engines—algorithm development and testing on a production vehicle," *IEEE Transactions on Control Systems Technology*, vol. 3, no. 1, pp. 61–68, 1995.
- [3] M. Nyberg and A. Perkovic, "Model based diagnosis of leaks in the air-intake system of an engine," SAE 980514, SAE International, 1998.
- [4] M. Nyberg, "Model-based diagnosis of an automotive engine using several types of fault models," *IEEE Transactions on Control Systems Technology*, vol. 10, no. 5, pp. 679–689, 2002.
- [5] M. Nyberg and T. Stutte, "Model based diagnosis of the air path of an automotive diesel engine," *Control Engineering Practice*, vol. 12, no. 5, pp. 513–525, 2004.
- [6] I. Djemili, A. Aitouche, and V. Cocquempot, "Structural analysis for air path of an automotive diesel engine," in *Proceedings of the International Conference on Communications, Computing and Control Applications (CCCA '11)*, pp. 1–6, Hammamet, Tunisia, March 2011.
- [7] V. De Flaugergues, V. Cocquempot, M. Bayart, and N. Lefebvre, "Exhaustive search of residuals computation schemes using macro-graphs and invertibility constraints," in *Proceedings of the 7th IFAC Symposium on Fault Detection, Supervision and Safety of Technical Processes*, Barcelona, Spain, 2009.
- [8] V. de Flaugergues, V. Cocquempot, M. Bayart, and M. Pengov, "On non-invertibilities for structural analysis," in *Proceedings of the 21st International Workshop on Principles of Diagnosis (DX '10)*, Portland, Ore, USA, 2010.
- [9] R. Ceccarelli, C. Canudas-de Wit, P. Moulin, and A. Sciarretta, "Model-based adaptive observers for intake leakage detection in diesel engines," in *Proceedings of the IEEE American Control Conference (ACC '09)*, pp. 1128–1133, St. Louis, Mo, USA, June 2009.
- [10] R. Ceccarelli, P. Moulin, and C. Canudas-de-Wit, "Robust strategy for intake leakage detection in Diesel engines," in *Proceedings of the IEEE International Conference on Control Applications (CCA '09)*, pp. 340–345, IEEE, Saint Petersburg, Russia, July 2009.
- [11] I. Djemili, A. Aitouche, and V. Cocquempot, "Adaptive observer for Intake leakage detection in diesel engines described by Takagi-Sugeno model," in *Proceedings of the 19th Mediterranean Conference on Control & Automation (MED '11)*, pp. 754–759, Corfu, Greece, June 2011.
- [12] B. Boulkroune, I. Djemili, A. Aitouche, and V. Cocquempot, "Nonlinear unknown input observer design for diesel engines," in *Proceedings of the IEEE American Control Conference (ACC '13)*, pp. 1076–1081, Washington, DC, USA, June 2013.
- [13] E. Höckerdal, E. Frisk, and L. Eriksson, "EKF-based adaptation of look-up tables with an air mass-flow sensor application," *Control Engineering Practice*, vol. 19, no. 5, pp. 442–453, 2011.
- [14] E. Höckerdal, E. Frisk, and L. Eriksson, "Observer design and model augmentation for bias compensation with a truck engine application," *Control Engineering Practice*, vol. 17, no. 3, pp. 408–417, 2009.
- [15] C. Svärd, M. Nyberg, E. Frisk, and M. Krysander, "Automotive engine FDI by application of an automated model-based and data-driven design methodology," *Control Engineering Practice*, vol. 21, no. 4, pp. 455–472, 2013.
- [16] P. Kudva, N. Viswanadham, and A. Ramakrishna, "Observers for linear systems with unknown inputs," *IEEE Transactions on Automatic Control*, vol. AC-25, no. 1, pp. 113–115, 1980.
- [17] M. Hou and P. C. Muller, "Design of observers for linear systems with unknown inputs," *IEEE Transactions on Automatic Control*, vol. 37, no. 6, pp. 871–875, 1992.
- [18] W. Chen and M. Saif, "Unknown input observer design for a class of nonlinear systems: an lmi approach," in *Proceedings of the IEEE American Control Conference*, Minneapolis, Minn, USA, June 2006.
- [19] M. Kao and J. J. Moskwa, "Turbocharged diesel engine modeling for nonlinear engine control and state estimation," *Journal of Dynamic Systems, Measurement and Control, Transactions of the ASME*, vol. 117, no. 1, pp. 20–30, 1995.
- [20] J. Heywood, *Internal Combustion Engine Fundamentals*, McGraw-Hill Series in Mechanical Engineering, McGraw-Hill, New York, NY, USA, 1992.
- [21] J. Wahlström and L. Eriksson, "Modelling diesel engines with a variable-geometry turbocharger and exhaust gas recirculation by optimization of model parameters for capturing non-linear system dynamics," *Proceedings of the Institution of Mechanical Engineers, Part D: Journal of Automobile Engineering*, vol. 225, no. 7, pp. 960–986, 2011.
- [22] M. Witczak, *Modelling and Estimation Strategies for Fault Diagnosis of Nonlinear Systems*, Springer, Berlin, Germany, 2007.
- [23] A. Zemouche and M. Boutayeb, "Sobolev norms-based state estimation and input recovery for a class of nonlinear systems design and experimental results," *IEEE Transactions on Signal Processing*, vol. 57, no. 3, pp. 1021–1029, 2009.
- [24] G. Phanomchoeng, R. Rajamani, and D. Piyabongkarn, "Non-linear observer for bounded Jacobian systems, with applications

- to automotive slip angle estimation,” *IEEE Transactions on Automatic Control*, vol. 56, no. 5, pp. 1163–1170, 2011.
- [25] B. Boulkroune, I. Djemili, A. Aitouche, and V. Cocquempot, “Robust nonlinear observer design for actuator fault detection in diesel engines,” *International Journal of Applied Mathematics and Computer Science*, vol. 23, no. 3, pp. 557–569, 2013.
- [26] M. Gálvez-Carrillo and M. Kinnaert, “Fault detection and isolation in current and voltage sensors of doubly-fed induction generators,” in *Proceedings of the 7th IFAC Symposium on Fault Detection, Supervision and Safety of Technical Processes (SafeProcess '09)*, Barcelona, Spain, 2009.
- [27] I. Nikiforov, “A simple recursive algorithm for diagnosis of abrupt changes in signals and systems,” in *Proceedings of the IEEE American Control Conference*, vol. 3, pp. 1938–1942, Philadelphia, Pa, USA, 1998.
- [28] M. Kinnaert, D. Vrančić, E. Denolin, D. Juričić, and J. Petrovčić, “Model-based fault detection and isolation for a gas-liquid separation unit,” *Control Engineering Practice*, vol. 8, no. 11, pp. 1273–1283, 2000.

## Research Article

# Joint Feature and Model Selection for SVM Fault Diagnosis in Solid Oxide Fuel Cell Systems

**Gabriele Moser,<sup>1</sup> Paola Costamagna,<sup>2</sup> Andrea De Giorgi,<sup>1</sup> Andrea Greco,<sup>3</sup>  
Loredana Magistri,<sup>3</sup> Lissy Pellaco,<sup>1</sup> and Andrea Trucco<sup>1,4</sup>**

<sup>1</sup>DITEN, University of Genoa, 16145 Genoa, Italy

<sup>2</sup>DICCA, University of Genoa, 16145 Genoa, Italy

<sup>3</sup>DIME, University of Genoa, 16145 Genoa, Italy

<sup>4</sup>PAVIS, Istituto Italiano di Tecnologia, 16163 Genoa, Italy

Correspondence should be addressed to Andrea Trucco; [trucco@dibe.unige.it](mailto:trucco@dibe.unige.it)

Received 5 September 2014; Accepted 27 January 2015

Academic Editor: Vincent Cocquempot

Copyright © 2015 Gabriele Moser et al. This is an open access article distributed under the Creative Commons Attribution License, which permits unrestricted use, distribution, and reproduction in any medium, provided the original work is properly cited.

This paper describes an original technique for the joint feature and model selection in the context of support vector machine (SVM) classification applied as a diagnosis strategy in model-based fault detection and isolation (FDI). We demonstrate that the proposed technique contributes to the solution of an open research problem: to design a robust FDI procedure, correctly functioning with different operating conditions and fault sizes, specifically settled for an electric generation system based on solid oxide fuel cells (SOFCs). By using a quantitative model of the generation system coupled to an optimized SVM classifier, a satisfactory FDI procedure is achieved, which is robust against modeling and measurement errors and is compliant with practical deployment.

## 1. Introduction

The interest in electric generation plants based on the fuel cell (FC) technology [1, 2] is constantly growing owing to their high energy conversion efficiency and environmental compatibility. However, plants based on FC stacks still suffer from a low reliability and a limited lifetime, and thus the development of specific methods for the automatic online fault diagnosis is of paramount importance for their commercial diffusion. According to [3, 4], among the possible FDI approaches, the model-based scheme [5, 6] is currently the preferred one in the context of the FC technology.

Although systems based on SOFC stacks are universally reputed to be one of the best options for distributed electric generation plants, the literature regarding the FDI procedure in these systems is still scarce [7–10]. Moreover, in many of these papers [7, 8], the proposed diagnosis strategy [6] is limited to inference approaches that use a binary fault signature matrix arranged according to a fault tree analysis (i.e., a deductive top-down tool, typically used in safety and reliability engineering) or an improved version of such

a matrix [10]. To overcome the weaknesses of the binary signature matrix [11], we recently proposed [9] a supervised classification approach, implemented through a SVM, as a possible diagnosis strategy. We demonstrated that the detection and isolation of faults of random size, occurring in an SOFC generation system that works under many different steady-state operating conditions, is possible by using a supervised SVM classifier.

However, only preliminary results (obtained under the assumption that the model provides exact predictions) are reported in [9], leaving many issues unresolved. One of them is the choice of the best physicochemical variables to be measured during the system operation and used for the FDI procedure. Although virtually all the physicochemical variables that characterize the functioning of an SOFC plant can be predicted by the related mathematical model [6], the practical measurement of these variables offers different levels of difficulty, from variables that are easy to measure to variables that are extremely difficult to measure. Therefore, the evaluation of the contribution that each of these variables provides to the FDI procedure is of crucial importance.

An additional open issue regards the model selection for the SVM classifier. Model selection generally consists in tuning the parameters of the SVM classifier, affecting the FDI performance and possibly choosing the kernel function. When the kernel is predefined, the values of the parameters of the SVM need to be optimized prior to the training phase of the classifier. In turn, this optimization depends on the features that are chosen for the classification procedure. Because in model-based FDI the residuals (i.e., the differences between the values of the physicochemical variables measured during SOFC system operation and the values of the same variables predicted by the system model) are used as features [6], it is evident that the selection of the variables to be used and the parameter optimization are strictly interconnected and need a combined investigation.

In this paper, we propose an original technique to carry out feature selection and parameter optimization jointly, in the context of a model-based FDI procedure applied to SOFC systems and performed through SVM classification. Dimensionality reduction has received great attention in the fault diagnosis field [12–15]. It can be performed with projections that create a set of a few synthetic features (i.e., feature transformation methods [12, 13, 15]) or by selecting the most relevant features (i.e., a subset of residuals) for diagnosis [14, 16, 17].

To determine, among the variables that can be measured in the SOFC system, those which play the most critical role in view of the discrimination among the considered fault classes, we focus on feature selection. This approach preserves the physical meaning and interpretability of the features used for classification purposes. Here, a technique based on the minimization of an analytical error bound [18, 19] is proposed. Many previous feature selection methods apply discrete optimization algorithms either to interclass distance measures (e.g., Bhattacharyya or Jeffries-Matusita distances), computed through parametric (usually multivariate Gaussian) models for the feature statistics conditioned to class membership, or to the classification accuracy on a validation set [17]. However, the former method does not fit the FDI procedure addressed here well because no well-defined parametric model is available for the joint statistics of highly heterogeneous physicochemical variables of an SOFC system. The latter method would be pursuable in the present application, but it would require setting aside part of the samples available for the training phase and using them only for validation purposes. Instead, the proposed technique extends the algorithm in [20] by combining it with a nonparametric error bound that can be derived as a by-product of the SVM training. In this way, the feature selection is performed without reserving a portion of the training samples for the validation.

Moreover, while a given kernel function (e.g., a Gaussian radial basis function, RBF) is predefined, the feature selection technique is also integrated with the optimization of the parameters of the SVM classifier (i.e., the model selection) in a single, innovative method. Working in this way, feature selection indicates which variables need to be measured in the SOFC system to attain a given (optimized) level of performance. In addition, by combining this outcome with

the measurement difficulty, it is possible to derive subsets of variables that provide a satisfactory performance with an acceptable measurement difficulty.

The present paper is organized as follows. Section 2 introduces the background concepts, describes the joint feature and model selection, and presents the SOFC system, its quantitative model, and the faults considered. The generation of the dataset and the achieved results with different feature subsets are described in Section 3. Finally, the conclusions are drawn in Section 4.

## 2. Materials and Methods

*2.1. Model-Based FDI.* In model-based fault diagnosis [5, 6], a model of the monitored system (encompassing all the system components) is used to predict the values of several physicochemical variables that characterize the behavior of the nonfaulty system under different operating conditions. The predicted values of these variables are then compared to the real values and measured during plant operation, and the residuals (i.e., indicators of deviations between the measurements and model-based predictions) are used in the FDI procedure through an appropriate diagnosis strategy. When the model is run in parallel with the real system (with the same inputs), the residuals can be computed for each variable through parity equations [6], whereby the values predicted by the model are subtracted from the those measured in the real system.

Because the model and the real system receive the same inputs and because the model simulates a nonfaulty system, when the real system is nonfaulty as well, the residuals are zero or less than the model uncertainty and measurement tolerance. Instead, when a fault occurs, the magnitudes of one or more residuals increase, allowing for fault detection and possible isolation. As mentioned above, the diagnosis strategy can be implemented through an inference or classification approach [6]. In the present study, we propose a classification approach; specifically, we use the classify-before-detect paradigm [21, 22]. According to this paradigm, the detection and classification are not a sequence of distinct tasks but are instead performed jointly, defining the nonfaulty state as a class of the classification scheme. The advantage of this approach is that setting (fixed or adaptive) thresholds for the detection task is no longer necessary.

To train and test an FDI procedure, samples (i.e., sets of residuals) obtained from the monitored system working under several different faulty operating conditions are necessary. To circumvent the problems arising from implanting real faults in real systems (i.e., irreparable damage with related economic loss), we follow the approach described in [23]. Indeed, fictitious faults can be implanted into the same model used to predict the physicochemical variables of the healthy system. In this way, as illustrated in Figure 1, two models are run in parallel: the first in place of the real system, operating under healthy or faulty conditions; the second to predict the variables characterizing a healthy system. The replacement of the real system with a model able to simulate also the faulty conditions is effective only if the model is reliable and accurate. This requirement is typically satisfied when

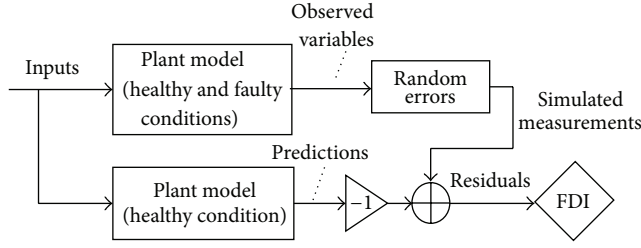


FIGURE 1: Schematic of the simulated deployment of the model-based FDI procedure in industrial plants, according to the approach of parity equations [6].

a quantitative mathematical model (i.e., a model that is based on the physical equations ruling all the processes governing the real system, also called the “first-principle” or “white-box” model [4]) is available and has been validated with experimental trials encompassing several operating conditions. Section 2.5 reports further details about the model of the electric generation SOFC system under consideration in the present paper.

The scheme in Figure 1 can be used to both train and test the FDI procedure [23]. However, the samples used for the SVM classifier training (i.e., the training set, exploited also for the joint feature and model selection) should be different from the samples used to evaluate the FDI performance (i.e., the test set).

Training the classifier requires a substantial amount of data, representative of the possible combinations among operating conditions, fault classes, and fault sizes. Large data collections joined with pattern recognition techniques are typical of data-driven FDI approaches [23–25]. Although model-based and data-driven approaches are traditionally considered distinct, alternative approaches to the FDI problem such as our model-based approach include some aspects of data-driven approaches. Some authors identified this case as the *hybrid* or *integrated approach* [24, 25]. More precisely, in the FDI system we propose, data produced by quantitative experimental validated physically based simulations are used to assemble a statistical knowledge of the relationships between residuals and faults, that is, to train the SVM classifier [23].

**2.2. SVM Classification.** SVMs are a family of learning machines that are based on methodological contributions from statistical learning, kernel-based processing, functional analysis, and optimization theory [26]. SVM approaches have been proposed for classification [19, 26–28], regression [26, 29], and probability density modeling [30].

Focusing first on binary classification, let  $\ell$  samples, associated with faulty or nonfaulty situations, be generated through the quantitative model. Let  $d$  be the number of features (here, the residuals), let  $\mathbf{x}_i$  ( $i = 1, 2, \dots, \ell$ ) be the  $d$ -dimensional vector collecting the  $d$  residuals, and let  $y_i$  be a binary variable (named label) that takes on the value  $+1$  or value  $-1$  depending on the membership of the  $i$ th sample to either one of the two classes. The set  $\{(\mathbf{x}_i, y_i)\}_{i=1}^{\ell}$  is the training

set. An SVM classifier assigns an unknown sample  $\mathbf{x} \in \mathbb{R}^d$  the class label  $\hat{y}(\mathbf{x}) = \text{sgn } f(\mathbf{x})$ , where the discriminant function  $f(\cdot)$  is the following kernel expansion:

$$f(\mathbf{x}) = \sum_{i=1}^{\ell} \alpha_i y_i K(\mathbf{x}_i, \mathbf{x}) + b, \quad (1)$$

and  $K(\cdot, \cdot)$  is a kernel function. The coefficients  $\alpha_i$  ( $i = 1, 2, \dots, \ell$ ) are determined by solving the following quadratic programming (QP) problem (multidimensional vectors are considered column vectors, the  $i$ th component of  $\mathbf{u} \in \mathbb{R}^n$  is denoted as  $u_i$  ( $i = 1, 2, \dots, n$ ), and the superscript “ $T$ ” denotes matrix transpose):

$$\begin{aligned} \min_{\alpha} \left( \frac{1}{2} \alpha^T Q \alpha - \mathbf{1}^T \alpha \right), \\ \mathbf{y}^T \alpha = 0, \quad 0 \leq \alpha_i \leq C, \quad i = 1, 2, \dots, \ell, \end{aligned} \quad (2)$$

and the bias  $b$  is derived as a by-product of this solution. The matrix  $Q$  is the  $\ell \times \ell$  matrix whose  $(i, j)$ th entry is  $Q_{ij} = y_i y_j K(\mathbf{x}_i, \mathbf{x}_j)$ ,  $\mathbf{1}$  is an  $\ell$ -dimensional vector with unitary components,  $\mathbf{y}$  is the vector of the labels of the  $\ell$  training samples, and  $C$  is a parameter [26]. The expansion (1) is typically sparse; that is,  $\alpha_i = 0$  for the majority of training samples; those for which  $\alpha_i > 0$  are named support vectors.

A function  $K$  of two vectors is a kernel if it is equivalent to the evaluation of an inner-product in some nonlinearly transformed space. Specifically, there are a separable Hilbert space  $\mathcal{H}$  and a mapping  $\Phi : \mathcal{X} \rightarrow \mathcal{H}$  from a compact subset  $\mathcal{X}$  of  $\mathbb{R}^d$  to  $\mathcal{H}$ , such that  $K(\mathbf{x}, \mathbf{x}') = \langle \Phi(\mathbf{x}), \Phi(\mathbf{x}') \rangle$  for all  $\mathbf{x}, \mathbf{x}' \in \mathcal{X}$  (where  $\langle \cdot, \cdot \rangle$  denotes the inner product on  $\mathcal{H}$ ) [26, 31]. The compactness of  $\mathcal{X}$  yields no loss of generality because a compact subset (e.g., a box or a closed ball) that includes all training samples always exists. The so-called Mercer’s conditions are known for a function  $K$  to be a kernel. Details can be found in [26]. Here, we only recall that a well-known example is the Gaussian RBF kernel:

$$K(\mathbf{x}, \mathbf{x}') = \exp\left(-\frac{\|\mathbf{x} - \mathbf{x}'\|^2}{2\sigma^2}\right) \quad (\mathbf{x}, \mathbf{x}' \in \mathcal{X}), \quad (3)$$

where  $\sigma$  is a positive parameter.

It is also possible to prove that (1) is equivalent to a linear discriminant function in the transformed space  $\mathcal{H}$ :

$$f(\mathbf{x}) = \langle w, \Phi(\mathbf{x}) \rangle + b, \quad (4)$$

where  $w \in \mathcal{H}$  and the bias  $b \in \mathbb{R}$  solve the following minimization problem [26]:

$$\min_{w, \xi, b} \left( \frac{1}{2} \langle w, w \rangle + C \cdot \mathbf{1}^T \xi \right), \quad (5)$$

$$y_i (\langle w, \Phi(\mathbf{x}_i) \rangle + b) \geq 1 - \xi_i, \quad \xi_i \geq 0, \quad i = 1, 2, \dots, \ell.$$

$\{\xi_i\}_{i=1}^{\ell}$  is a set of slack variables that determine if and how much the discriminant function erroneously classifies the training samples. On one hand, the term  $\mathbf{1}^T \xi$  to the objective

function in (5) favors fitting the discriminant function with the available training set. On the other hand, it can be proven that the term  $\langle w, w \rangle$  in (5) favors minimizing the expectation (over the probability distribution of the training samples) of the error on an unknown test sample and minimizing overfitting [26].  $C$  tunes the tradeoff between the two terms.

Mapping to the usually higher (possibly infinite) dimensional space  $\mathcal{H}$  optimizes the chances that a linear decision boundary can effectively discriminate the classes, while equivalently providing a flexible nonlinear decision boundary in the original space  $\mathbb{R}^d$ . At the same time,  $\mathcal{H}$  is never computationally involved because all calculations only use the kernel  $K$  (see (1) and (2)).

Unlike other popular approaches to nonparametric learning, such as neural networks, the training problem (2) is quadratic and is not plagued with many local minima. Case-specific numerical algorithms have also been proposed to efficiently address it [32].

Generalization to  $M$  classes ( $M > 2$ ) is usually achieved by decomposing the multiclass problem into a collection of binary subproblems [19, 26, 28]. Here, the one-against-one (OAO) approach is used, which is usually a good tradeoff between accuracy and computational burden. First, a binary discriminant function  $f_{hk}(\cdot)$  is separately determined to discriminate between the  $h$ th and  $k$ th classes ( $h, k = 1, 2, \dots, M; k > h$ ). Then, to label an unknown sample  $\mathbf{x}$ , each function  $f_{hk}(\cdot)$  is applied to  $\mathbf{x}$  and a vote is cast in favor of either the  $h$ th or the  $k$ th class depending on the sign of  $f_{hk}(\mathbf{x})$ . Finally,  $\mathbf{x}$  is assigned to the class that received the most votes.

**2.3. Feature and Model Selection.** A relevant issue in the present FDI scheme is to determine which of the residuals are most informative with respect to the discrimination of the considered classes to minimize both the number of measurements to be taken on the SOFC system and the memory and computational requirements of the FDI procedure. At the same time, the SVM classifier involves parameters (i.e.,  $C$  in the QP problem (2)) and possible additional parameters in the kernel (e.g.,  $\sigma$  in (3)). Their values generally affect the classification performance and need to be set prior to training.

Here, a novel method is developed and embedded into the proposed FDI procedure to select jointly the most informative residuals (i.e., to perform feature selection) and optimize the parameters (i.e., to perform model selection, after fixing the kernel type). The goal is to achieve full automation of the FDI procedure. The key idea is to identify the feature subset and the parameter configuration that minimize an analytical error bound, that is, the so-called span bound. Under mild assumptions, the span bound can be proven to be a tight upper bound on the leave-one-out error rate [18]. It also exhibits a usually high correlation with the error rate on test samples disjointed from the training samples, provided that they are drawn from the same distribution [19, 29]. However, its computation remarkably involves only training samples and no additional validation data. To minimize the span bound, the proposed method combines the approaches introduced in [19, 20] for SVM parameter optimization and feature selection, respectively.

Let  $\mathcal{R}$ ,  $\mathcal{S}$ , and  $\boldsymbol{\theta}$  be the set of all  $d$  features (i.e., the residuals), a subset of  $m$  features ( $\mathcal{S} \subset \mathcal{R}$ ), and a vector collecting the input SVM parameters (e.g.,  $C$  and  $\sigma$ , if the Gaussian RBF kernel is used), respectively. Considering again the binary case first, let us explicitly stress the dependence on  $\mathcal{S}$  and  $\boldsymbol{\theta}$  by denoting as  $\alpha_i(\mathcal{S}, \boldsymbol{\theta})$  ( $i = 1, 2, \dots, \ell$ ) and  $f(\cdot | \mathcal{S}, \boldsymbol{\theta})$  the solution of the QP problem in (2) and the discriminant function in (1), respectively, when the SVM is trained using the  $m$  features in  $\mathcal{S}$  and the input parameter vector  $\boldsymbol{\theta}$ . The span bound is defined as the fraction  $\mathcal{F}(\mathcal{S}, \boldsymbol{\theta})$  of the training samples such that  $\alpha_i(\mathcal{S}, \boldsymbol{\theta}) > 0$  and ( $i = 1, 2, \dots, \ell$ ):

$$\alpha_i(\mathcal{S}, \boldsymbol{\theta}) S_i^2(\mathcal{S}, \boldsymbol{\theta}) \geq y_i f(\mathbf{x}_i | \mathcal{S}, \boldsymbol{\theta}), \quad (6)$$

where the coefficient  $S_i^2(\mathcal{S}, \boldsymbol{\theta})$  (named span) can be obtained as a by-product of the training phase by solving a further QP problem [18] or through a fast linear algebra argument [33]. In the multiclass case,  $\mathcal{F}(\mathcal{S}, \boldsymbol{\theta})$  is computed through OAO as a weighted average of the span bound values obtained separately for each pair of distinct classes, the weights being proportional to the relative frequencies of the classes in the training set [19]. Further details on this point can be found in [19, 33].

Indeed,  $\mathcal{F}(\mathcal{S}, \boldsymbol{\theta})$  is a nondifferentiable function of  $\boldsymbol{\theta}$  [18]. According to the definition recalled above for the binary case,  $\ell \cdot \mathcal{F}(\mathcal{S}, \boldsymbol{\theta})$  is integer-valued and  $\mathcal{F}(\mathcal{S}, \boldsymbol{\theta})$  proves to be piecewise constant on the space of the admissible parameter vectors  $\boldsymbol{\theta}$ . Similar comments hold in the multiclass case as well. This prevents applying numerical minimization algorithms that make use of derivatives (e.g., the gradient or the Newton-Raphson's methods) [34]. In general, suitable numerical gradients and difference quotients might be used to replace gradients and derivatives, but *ad hoc* convergence theorems would be necessary for their specific application to the span bound. In [34], a regularized differentiable version of the span bound is introduced to allow gradient descent to be applied, but an additional regularization parameter, which has to be manually tuned, is necessary. Here, similar to [19], the Powell's algorithm is used to minimize  $\mathcal{F}(\mathcal{S}, \boldsymbol{\theta})$  with respect to  $\boldsymbol{\theta}$ . Powell's method is an unconstrained minimization technique that emulates the behavior of the conjugate gradient method without using derivatives and converges, under mild assumptions, to a local minimum [35].

To minimize the resulting functional,

$$\mathcal{F}_*(\mathcal{S}) = \min_{\boldsymbol{\theta}} \mathcal{F}(\mathcal{S}, \boldsymbol{\theta}), \quad (7)$$

with respect to  $\mathcal{S}$ , the steepest ascent algorithm in [20] is adapted and extended. It is an iterative algorithm, initialized with a preliminary subset of  $m$  features, which has been demonstrated to be effective when applied to the maximization of Bayesian interclass distance measures in problems of remote sensing image classification [20, 36]. Here, it is extended to the minimization (steepest descent) of the span bound functional, combined with the Powell's algorithm, and integrated in the proposed FDI procedure.

Specifically, given a subset  $\mathcal{S}$  of  $m$  features, the proposed feature selection and parameter optimization method evaluates each possible replacement of one of the  $m$  features in

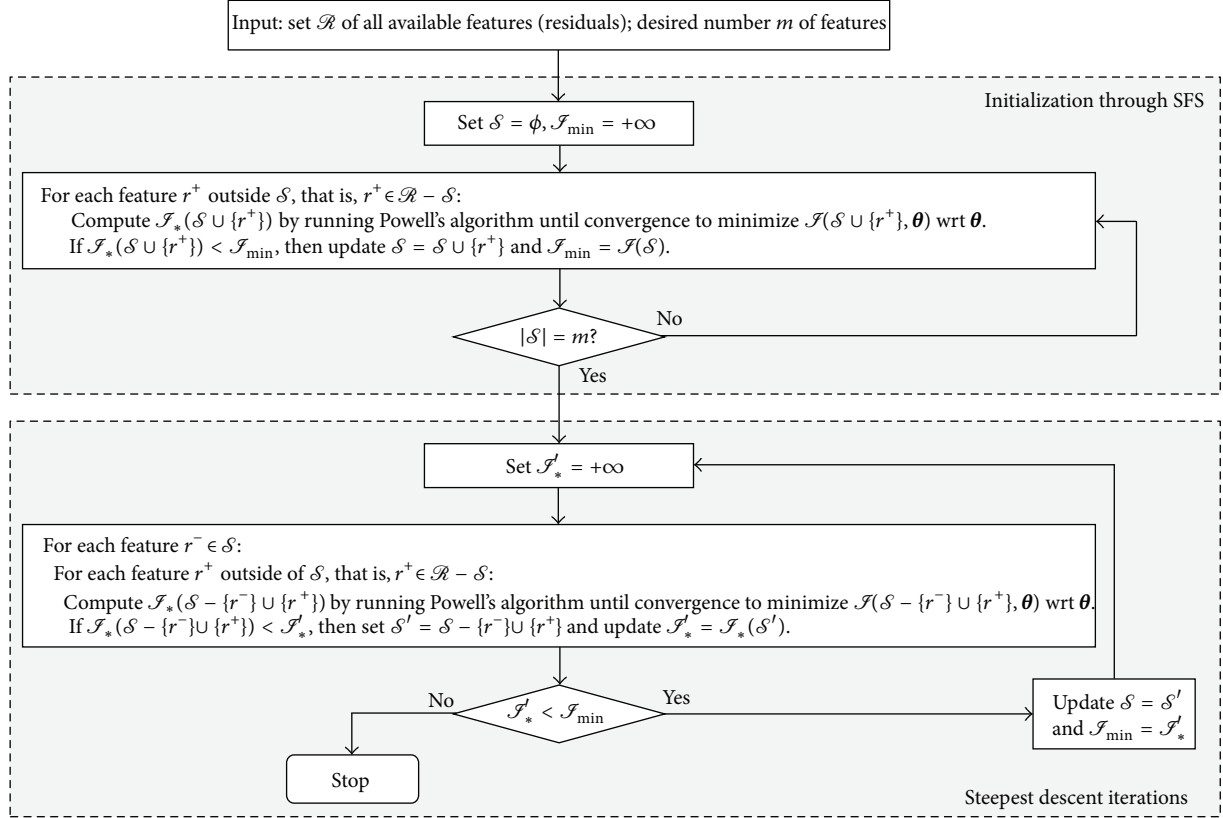


FIGURE 2: Flowchart of the proposed joint feature and model selection algorithm for FDI in SOFC systems.  $\mathcal{R}$ ,  $\mathcal{S}$ , and  $m$  denote the set of all available features (residuals), a feature subset, and the desired number of features to be selected, respectively.  $|\mathcal{S}|$  denotes the cardinality of  $\mathcal{S}$ .

$\mathcal{S}$  by one of the  $(d - m)$  features outside  $\mathcal{S}$  (i.e., in  $\mathcal{R} - \mathcal{S}$ ) by computing the corresponding value of  $\mathcal{J}_*(\cdot)$ , that is, by running Powell's algorithm until convergence (see (7)). Let  $\mathcal{J}'_*$  be the minimum span bound obtained across all these  $m(d - m)$  possible replacements. If  $\mathcal{J}'_* < \mathcal{J}_*(\mathcal{S})$ , the replacement is performed and  $\mathcal{S}$  is correspondingly updated. This procedure is iteratively repeated, while reductions in the span bound are feasible through some replacement of a feature inside by a feature outside the current subset.

The collection of the subsets of  $m$  features is finite, so finite-time termination is guaranteed. As discussed in [20], convergence to a local minimum of  $\mathcal{J}_*(\cdot)$  is also guaranteed, whereby the notion of the local minimum is interpreted by endowing the discrete space of the subsets of  $\mathcal{R}$  with a metric-space topology through the well-known Hamming distance. This property, together with the aforementioned convergence behavior of the Powell's algorithm, suggests that, at the least, local minima of the span bound functional are identified by the proposed method in the searches for both a feature subset and a parameter vector.

Initialization of the method is performed through the sequential forward selection (SFS) algorithm, that is, a well-known suboptimal approach to feature selection [17]. First, SFS starts from an empty subset of features, separately computes the values of  $\mathcal{J}_*(\cdot)$  associated with the  $d$  subsets composed of one feature each, and selects the feature corresponding to the smallest value of  $\mathcal{J}_*(\cdot)$ . Then, it evaluates

$\mathcal{J}_*(\cdot)$  for all the  $(d - 1)$  subsets of two features, which are obtained by separately pairing the previously selected feature with each other feature. Again, the resulting feature pair with the smallest value of  $\mathcal{J}_*(\cdot)$  is selected. Then, the procedure is repeated iteratively, progressively adding one feature at a time until the desired number  $m$  of features is reached. Figure 2 displays a flowchart of the proposed feature selection and parameter optimization algorithm. Further details on the SFS and steepest descent (ascent) algorithms can be found in [20, 36].

**2.4. SOFC System Description.** In this study, the model-based FDI scheme and SVM classification are applied to an electric generation system consisting basically of a reformer, an SOFC stack (formed by a number of planar cells superimposed to each other), and a post burner. The reformer contains a suitable catalyst that promotes the steam reforming reaction within the feeding mixture (3:1 vol. methane and steam), which is partially converted into hydrogen and carbon monoxide. This partially reformed fuel is then fed into the anode compartment of the SOFC stack, while air is fed into the cathode side. The SOFC stack (average operating temperature of 850°C) is composed of a number of rectangular planar cells superimposed onto each other, each of which develops an electrochemical reaction producing steam and carbon dioxide along with electrical power and heat. Nevertheless, the anode exhaust contains a significant

percentage of flammables. Thus, the anode exhaust is mixed with the cathode exhaust and burned in an off-gas burner to reduce the release of pollutants and increase the temperature of the flue gas for further utilization or energy recovery in subsequent components (not considered here). The system scheme is displayed in Figure 3; further details can be found in [37].

**2.5. Quantitative Model and Fault Classes.** The model of the electric generation SOFC system is a quantitative model, which embeds the physical equations of the phenomena occurring in the process, earning the classification of “first-principle” or “white-box” model. Overall, the model is obtained by coupling the quantitative models of the three components, that is, reformer, fuel cell stack, and burner. The SOFC stack model assumes all cells are identical along the stack. The single cell model is then developed according to a typical scheme applied to chemical reactors [38] and includes the equations of the local chemical and electrochemical reaction kinetics. In turn, the latter includes the evaluation of the Nernst voltage and of all the sources of losses (anodic activation, cathodic activation, and ohmic). The local kinetics is then coupled to local mass, energy, and momentum balances. A partial differential/algebraic system of equations is obtained, integrated using a relaxation method for the energy balance, and combined with a finite difference method to solve the other equations. Reformer and burner are simulated through macroscopic mass and energy balances. In the previous case, the steam reforming reaction is assumed to be at thermodynamic equilibrium. In the latter case, all the flammables are considered to be combusted completely. Further details can be found in [37].

In principle, the model is developed to simulate nonfaulty operating conditions, but it can also be extended to simulate faulty operating conditions by including suitable equations for the simulation of typical faults occurring in SOFC systems [37]. Thus, the following four main fault classes have been simulated [37].

**SOFC Stack Degradation.** A number of different faults can occur inside the SOFC stack, affecting the cell structure and, in particular, the electrolyte/electrodes coupling in different ways. A comprehensive overview is given in [37], in which it is also demonstrated that, for the purposes of plant simulation under faulty conditions, the effect of all these different faults is correctly simulated with an increase of the overall internal stack losses. Thus, the latter have been increased between 105% and 160% of their nominal value.

**Air Leakage.** In addition to providing the oxidant necessary for the electrochemical reaction, the cathode air flow allows the temperature of the stack to be controlled. A potential air leak between the air flow meter and the SOFC stack has been simulated by reducing the flow entering the stack to between 50% and 95% of its nominal rate.

**Fuel Leakage.** Inside the reformer, the methane/steam feed is converted into a mixture with a high percentage of hydrogen. Fuel leakage is likely to occur because of the low dimension

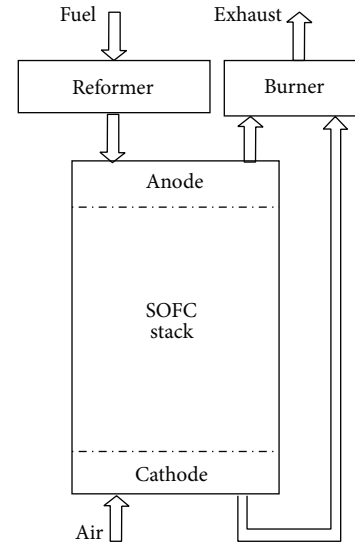


FIGURE 3: Schematic of the SOFC system.

and high diffusivity of the hydrogen molecule. A leak between the exit of the reformer and the entrance of the stack has been simulated by reducing the flow rate to between 75% and 95% of its nominal value.

**Reformer Degradation.** A reduced conversion of methane can be achieved in the reformer due to a number of faulty effects (e.g., catalyst degradation, carbon deposition, or sulfur poisoning). Several possible degrees of deviation from equilibrium have been simulated by reducing the equilibrium constant of the steam reforming reaction to between 30% and 95% of its thermodynamic value.

As indicated in Figure 3, the SOFC plant under consideration includes an SOFC stack, a methane steam reformer, a burner, a fuel feeding system, and an air feeding system. Given that the burner is a well-tested and mature technology, its faults are not taken into account. On the other hand, the faults of the other four plant components are all considered, one fault for each component. As mentioned above, the different faults that can occur in the SOFC stack end up giving similar effects [37]. Thus, they can be lumped together as one single fault class. Similar considerations hold for the steam reforming reactor. Consequently, the FDI procedure proposed here cannot be used to distinguish among the different types of faults that can occur in the SOFC stack or in the methane steam reformer. If necessary, further investigations (e.g., chemical or electrochemical tests) must be carried out to identify in detail the microscopic cause of the failure, as suggested in [37].

The reliability of the predictions obtained by the SOFC system model is assured by its validation against experimental data. This validation was performed under both steady-state and dynamic working regimes. Moreover, as described in [37], for these working regimes, different operating conditions have been considered. Circumscribed experimental validation under faulty operating conditions has been performed as well [39].

Even if our model of the SOFC system is able to simulate faults occurring during transient system operation, as discussed in [39], the development of an FDI procedure for application in transient conditions requires an analysis of the time-dependent behavior of residuals that is beyond the scope of the present paper. The latter is devoted to an investigation of faults occurring during steady-state operation of the system. Starting with the system working in an unfaulty steady-state operating condition, we simulate the occurrence of a fault, which triggers a transient behavior that is simulated by our model until a new (faulty) steady-state condition is reached. Residuals that we consider are those calculated as the difference between values of the observed physicochemical variables in the faulty and unfaulty steady states.

The experimental SOFC plant that provided the experimental data is identical to the plant described above (see Figure 3). The plant has been manufactured by Staxera GmbH (D) [40] and tested by EBZ GmbH (D) within the European project GENIUS [41].

*2.6. Computation of Residuals.* As discussed previously and according to [23], in this study, the real plant is replaced by a copy of the quantitative model, modified in view of simulating the effect of different faults of various size occurring in the plant (see Figure 1). Whereas ideal conditions were assumed in [9], here, the model uncertainty and measurement tolerance are considered by adding random errors to the values of the physicochemical variables simulated for the real plant (see Figure 1). This allows us to attain realistic residuals and to investigate the sensitivity of the FDI procedure by testing different error magnitudes.

To introduce the model uncertainty and measurement tolerance, each observed variable calculated by the model used in place of the real plant is multiplied by a random variable  $\gamma_\epsilon$ , uniformly distributed in  $[1 - \epsilon, 1 + \epsilon]$ , where  $100\epsilon$  represents the maximum percentage error. Therefore, the residual  $\delta_V$  related to a given monitored variable  $V$  is computed as follows:

$$\delta_V = V_m \gamma_\epsilon - V_p, \quad (8)$$

where  $V_m$  is the observed variable calculated by the (simulated) plant under faulty and nonfaulty conditions and  $V_p$  is the same variable predicted by the model for a nonfaulty plant. The value assumed by the random variable  $\gamma_\epsilon$  is updated each time the residual  $\delta_V$  is computed.

The residuals of the ten physicochemical variables of the SOFC system, listed in Table 1, are used as features for the classification algorithm. Although these ten variables are easy to access in numerical simulations, their measurement in a real plant raises some complexity concerns. Thus, we have classified them as easy to extremely difficult to measure, as reported in Table 1. The feature selection method proposed here makes it possible to assess the contribution provided by each of these variables toward a correct classification. This information, combined with the measurement difficulty, allows us to select the variables to be monitored in a real application of the FDI procedure.

TABLE 1: Residuals used for the FDI procedure with the related measurement difficulty.

Number	Residual	Measurement difficulty
1	Generated electric power	Easy
2	Air flow rate entering the stack	Easy
3	Fuel flow rate entering the stack	Easy
4	Air pressure loss between the inlet and outlet of the FC stack	Easy
5	Temperature at the burner outlet	Easy
6	Average stack temperature	Difficult
7	Anodic activation losses	Extremely difficult
8	Cathodic activation losses	Extremely difficult
9	Ohmic losses	Extremely difficult
10	Nernst voltage	Extremely difficult

*2.7. Control Strategies and Operating Conditions.* In this study, both typical control strategies employed in FC generation plants (i.e., constant-current and constant-voltage) have been considered. The generation plant is assumed to be equipped with a power inverter that, in addition to the task of converting the DC electrical power to AC electrical power, controls the power supplied by the plant and the operation mode of the stack. Thus, the inverter can force the stack to generate a constant voltage or constant current according to the  $V$ - $I$  characteristic curves of the SOFC stack.

The reference operating condition for the SOFC plant described above includes a constant electrical current of 26.2 A (or a constant SOFC stack potential of 42.5 V), a fuel utilization factor of 0.75, a reformer temperature of 650°C, and an average SOFC stack temperature of 850°C. In this condition, the plant generates an electrical power of approximately 1.1 kW. Starting from this reference operating condition, for each control strategy, different operating conditions are defined by tuning the values imposed for the constant current (or constant voltage) and the fuel utilization factor. During operation, the reformer is kept at fixed temperature (650°C) through an electrical heater, and the SOFC stack temperature is maintained at the desired level by regulating the air inlet flow rate. For the constant-current control strategy, ten operating conditions are considered by modifying the electrical current (ranging from 6 to 30 A) and/or fuel utilization factor (ranging from 0.35 to 0.75) with respect to their reference values. For the constant-voltage control strategy, ten operating conditions are considered as well. The stack potential is modified between 41 and 53 V, and the fuel utilization factor is modified between 0.35 and 0.75.

Further details regarding the control strategy and operating conditions of the SOFC generation plant under consideration are given in [37].

### 3. Results and Discussion

**3.1. Model Uncertainty.** As mentioned in Section 2.5, the SOFC system model has been validated experimentally. The maximum difference between the measured and predicted values of the monitored variables is approximately 3% [37]. On the basis of this value, the maximum magnitude for the random errors to be introduced when the measurement of the ten observed variables is simulated (see Figure 1) can be set. Here, the following three values are considered for the maximum percentage error: 2%, 4%, and 6%.

**3.2. Dataset Composition.** Due to a generalized lack of experimental faulty data in SOFC systems [41], which in turn is strictly related to their high cost, the simulated approach depicted in Figure 1 is used to assemble the dataset. Although the available experimental data are not sufficient to train and test an SVM classifier, they are adequate for validating a physics-based quantitative modeling tool, able to simulate unfaulty [37] and faulty [39] operating conditions, which can then produce the dataset pool necessary for training and validating the SVM classifier.

For each operating condition, ten different sizes of a given fault (inside the range defined in Section 2.5) are considered. Thus, for a given control strategy, 100 combinations of steady-state operating conditions and fault sizes are identified for each fault. After setting the maximum error magnitude, independent random errors are introduced for each monitored variable of each combination. As a result, for each control strategy, a dataset of approximately 500 feature vectors is available (5 classes are indeed considered: 4 faulty classes and the nonfaulty class). The hundred vectors for the nonfaulty class are generated by repeating the realization of the random errors for each operating condition ten times.

Subsequent realizations of the independent random errors enable the generation of an arbitrary number of datasets. Thus, we have produced a pool of datasets for each control strategy (i.e., constant-voltage and constant-current) and for each maximum percentage error (i.e., 2%, 4%, and 6%). Each dataset is composed of approximately 500 feature vectors, and each feature vector is composed of ten features (see Table 1). In each resulting dataset, the sets of training samples of the various classes have approximately the same size. A fuel cell will for the most part operate in a nonfaulty state, so the nonfaulty class is expected to have a larger prior probability than the individual faulty classes, a common situation in a detection problem. This may suggest using a larger training set size for “no-fault” than for the other classes. However, SVM-based classifiers are known to be generally sensitive to significantly unbalanced numbers of training samples per class. Therefore, the aforementioned approach was used to take benefit from the opportunity to actively generate the training set and make sure that balanced sets were constructed for the various classes. Indeed, if a different strategy was used and more training samples were available for the nonfaulty class than for the other classes, sample pre-selection algorithms such as [42] could be applied to make sure that strongly unbalanced classes are avoided.

All the features of a given dataset have been preliminarily normalized to ensure that each has a zero mean and unitary variance. This normalization is necessary because of the significantly different orders of magnitude of the measured residuals. It also helps preventing overflow and favors numerical stability in the solution of the QP problem for SVM training.

**3.3. Fault Detection and Isolation.** In real systems, the design of a classifier that, working with a given residual subset, provides a satisfactory performance when the error magnitude is not perfectly known and potentially varies over time has great relevance. To this end, a training set has been composed for each control strategy by joining three datasets together: one dataset for each maximum percentage error (i.e., 2%, 4%, and 6%). Here, this training set is used to train SVM classifiers in which the Gaussian RBF kernel in (3) is adopted. The joint feature and model selection method described in Section 2.3 provides the optimal feature subset, when the number of residuals  $m$  is increased from 1 to 10.

For each control strategy and optimal feature subset, the SVM classifier trained using the aforementioned mixture of error magnitudes is tested with several datasets (excluding those already used to compose the training set), characterized by given error magnitudes. The performance of the classifier is evaluated through the overall accuracy (OA), that is, the fraction of the correctly classified test samples (an estimate of the probability of correct classification). An average OA (referred to as  $OA_{avg}$ ) is introduced by averaging the three OA values obtained with regard to the 2%, 4%, and 6% error magnitudes. Finally, to evaluate the classifier performance for each specific class, the average producer accuracy ( $PA_{avg}$ ) is introduced; that is, the fraction of the test samples belonging to a given class that are correctly classified, averaged over the three error magnitudes (2%, 4%, and 6%).

The  $OA_{avg}$  value of the classifiers, trained with the mixture of error magnitudes, with the number of adopted features increasing from 1 to 10, is reported in Table 2 for the constant-voltage case and in Table 3 for the constant-current case. The subset of residuals obtained by the feature selection technique and the value of OA for each error magnitude are also listed. For the sake of brevity, the corresponding parameter configurations obtained by the proposed joint model and feature selection algorithm are not listed. However, as detailed in [19, 29], the parameter vector obtained by minimizing the span bound through Powell’s algorithm typically yield classification accuracies very similar to those obtained by time-expensive grid searches for the minimum cross-validation error rate over a predefined grid in the parameter space. Details on this aspect can be found in [19, 29] with regard to SVM for classification and regression, respectively.

Except for  $m = 1$ , the classification performance decreases as the error magnitude increases, as expected, and the OA values obtained for the constant-voltage control are higher than the related values obtained for the constant-current control.

The performance behavior as a function of the number of features  $m$  is more complex. For both control strategies,

TABLE 2: Residuals and OAs, with the number of features  $m$  increasing from 1 to 10, for the constant-voltage case. Training set including a mixture of error magnitudes.

$m$	Residual subset	Overall accuracy (OA)			
		Test-set max. error			$OA_{\text{avg}}$
		2%	4%	6%	
1	9	0.41	0.42	0.42	0.42
2	1, 2	0.90	0.88	0.82	0.87
3	2, 3, 8	0.95	0.89	0.80	0.88
4	2, 3, 4, 8	0.97	0.92	0.84	0.91
5	1, 2, 3, 4, 8	0.97	0.90	0.83	0.90
6	1, 2, 3, 4, 8, 9	0.98	0.89	0.80	0.89
7	1, 2, 3, 4, 7, 8, 9	0.98	0.88	0.79	0.89
8	1, 2, 3, 4, 5, 7, 8, 9	0.98	0.92	0.82	0.91
9	1, 2, 3, 4, 5, 6, 7, 8, 9	0.98	0.92	0.86	0.92
10	1, 2, 3, 4, 5, 6, 7, 8, 9, 10	0.98	0.92	0.86	0.92

TABLE 3: Residuals and OAs, with the number of features  $m$  increasing from 1 to 10, for the constant-current case. Training including a mixture of error magnitudes.

$m$	Residual subset	Overall accuracy (OA)			
		Test-set max. error			$OA_{\text{avg}}$
		2%	4%	6%	
1	2	0.61	0.59	0.58	0.59
2	2, 3	0.76	0.76	0.72	0.75
3	2, 3, 4	0.83	0.83	0.79	0.82
4	2, 3, 4, 7	0.90	0.84	0.75	0.83
5	1, 2, 3, 4, 7	0.90	0.81	0.72	0.81
6	1, 2, 3, 4, 7, 8	0.90	0.83	0.72	0.82
7	1, 2, 3, 4, 5, 7, 8	0.92	0.81	0.73	0.82
8	1, 2, 3, 4, 5, 7, 8, 9	0.92	0.80	0.73	0.82
9	1, 2, 3, 4, 5, 6, 7, 8, 9	0.69	0.68	0.63	0.67
10	1, 2, 3, 4, 5, 6, 7, 8, 9, 10	0.76	0.75	0.72	0.74

the value of  $OA_{\text{avg}}$  monotonically increases moving from  $m = 1$  to  $m = 4$ . In the constant-current case, for  $4 \leq m \leq 8$ , the  $OA_{\text{avg}}$  value is nearly constant, exhibiting small oscillations that do not exceed 0.02. For  $m > 8$ , the  $OA_{\text{avg}}$  value sharply decreases. In the constant-voltage case, for  $m \geq 4$ , the  $OA_{\text{avg}}$  value is nearly constant, exhibiting small oscillations that do not exceed 0.02. Concerning the residuals that are selected when the value of  $m$  is increased, we can observe that, in the constant-current case, the residuals selected for a given  $m$  are those selected for  $m - 1$  plus one new residual. This behavior is not forced by the feature and model selection method presented in Section 2.3. In fact, in the constant-voltage case, this behavior is observed only for  $m > 3$ , where the performance approaches its maximum.

Because the use of a number of residuals larger than four does not increase or increases negligibly the performance, in the following sections of this paper, we focus on the performance achieved for  $m = 4$  and the related residuals.

TABLE 4: OA when two subsets of easy-to-measure residuals are adopted. The training set included a mixture of error magnitudes.

Control str.	Residual subset	Overall accuracy (OA)			
		Test-set max. error			$OA_{\text{avg}}$
		2%	4%	6%	
Constant-voltage	2, 3, 4	0.87	0.78	0.70	0.78
	1, 2, 3, 4	0.97	0.89	0.82	0.89
Constant-current	2, 3, 4	0.83	0.83	0.79	0.82
	1, 2, 3, 4	0.90	0.82	0.74	0.82

In the constant-voltage case,  $OA_{\text{avg}}$  is equal to 0.91 and OA decreases by 0.13 when increasing the error magnitude from 2% to 6%. The selected residuals are those numbered with 2, 3, 4, and 8 in Table 1. In the constant-current case,  $OA_{\text{avg}}$  is equal to 0.83, and the OA decreases by 0.15 when increasing the error magnitude from 2% to 6%. The selected residuals are those numbered with 2, 3, 4, and 7. We note that residuals 2, 3, and 4 are selected for both control strategies. These residuals are considered easy to measure in Table 1 (as opposed to residuals 7 and 8, which are extremely difficult to measure). Moreover, when  $m$  increases from 4 to 5, the feature that is selected is residual 1, which is easy to measure. We can conclude that among the easy-to-measure residuals, those numbered with 2, 3, and 4 are the most informative for both control strategies. In addition, the residual numbered with 1 is potentially useful.

**3.4. Performance of Easy-to-Measure Residuals.** The results obtained by the joint feature and model selection can be used to design a classifier that working with a limited number of easy-to-measure residuals provides performance close to the optimal one. In other words, we attempt to exclude the residuals that are not easy to measure, limiting the performance decrease.

On the basis of the considerations drawn in Section 3.3, we analyze the performance of the SVM classifiers that use the two following subsets of residuals, (2, 3, 4) and (1, 2, 3, 4), and are trained by the aforementioned mixture of error magnitudes (see Table 4). While the residual subset (2, 3, 4) is the optimum choice for the constant-current case with  $m = 3$  (see Table 3), all the three remaining combinations reported in Table 4 are surely suboptimal. To maximize the performance, for the four possible combinations between control strategy and residual subset, the model parameters of the SVM classifiers have been optimized by minimizing the span bound (computed for a given subset of features) through the Powell's algorithm, according to the description in Section 2.3.

Table 4 displays the performance of the four classifiers when tested with samples with a given error magnitude as well as the average figure  $OA_{\text{avg}}$ . Comparing Tables 2 and 4, we observe that for the constant-voltage case, the performance obtained with the residual subset (2, 3, 4) is significantly lower than that obtained with the optimum subset (2, 3, 8). Instead, when four features are adopted, the use of the easy-to-measure subset (1, 2, 3, 4) provides an  $OA_{\text{avg}}$

TABLE 5:  $PA_{avg}$  when two subsets of easy-to-measure residuals are adopted. The training set included a mixture of error magnitudes. Class number meaning: 0: nonfaulty system; 1: SOFC stack degradation; 2: air leakage; 3: fuel leakage; 4: reformer degradation.

Control str.	Residual subset	Average producer accuracy ( $PA_{avg}$ )				
		Class number				
		0	1	2	3	4
Constant-voltage	2, 3, 4	0.87	0.68	0.88	0.88	0.49
	1, 2, 3, 4	0.89	0.89	0.89	0.92	0.85
Constant-current	2, 3, 4	0.97	0.45	0.83	0.89	0.97
	1, 2, 3, 4	0.85	0.57	0.90	0.86	0.99

that is only marginally lower than that obtained with the optimum subset for  $m = 4$  (i.e., 0.89 against 0.91). In addition, in the constant-current case, the use of the easy-to-measure subset (1, 2, 3, 4) provides an  $OA_{avg}$  that is only marginally lower than that obtained with the optimum subset for  $m = 4$  (i.e., 0.82 against 0.83). However, this performance is equal to that obtained by using the optimum subset (2, 3, 4) composed of only three features. In the constant-current case, the choice between three and four features can be driven by the error magnitude that is expected in real applications. The subset (2, 3, 4) provides a higher OA when the maximum error tends to 6%; the subset (1, 2, 3, 4) is preferable when the maximum error tends to 2%. On the contrary, in the constant-voltage case, the results reported in Table 4 indicate that the subset (1, 2, 3, 4) is always preferable.

While  $OA_{avg}$  encompasses the results related to the five considered classes,  $PA_{avg}$  provides a performance evaluation for each specific class. Table 5 displays the  $PA_{avg}$  values for the four classifiers that work with a limited number of easy-to-measure residuals, that is, the classifiers considered in Table 4. We observe that in the constant-voltage case, the addition of the feature number 1 improves all the  $PA_{avg}$  values, especially those related to classes numbers 1 and 4. With the feature subset (1, 2, 3, 4), the nonfaulty status and all the considered faults are identified with an average accuracy higher than 85%. In the constant-current case, the addition of feature number 1 improves the  $PA_{avg}$  values for classes 1, 2, and 4 and worsens the  $PA_{avg}$  values for classes 0 and 3. Although the  $OA_{avg}$  does not change (see Table 4), better performance uniformity is obtained. All the considered faults except for SOFC stack degradation are identified with an average accuracy higher than 85%.  $PA_{avg}$  for SOFC stack degradation does not exceed 57% when the constant-current control is adopted, demonstrating that in this specific case the identification of this fault through four easy-to-measure residuals is critical. We also verified that the addition of the last easy-to-measure residual (i.e., feature number 5) to the subset (1, 2, 3, 4) does not improve this performance. A further investigation of this specific misclassification shows that the feature vectors for the SOFC stack degradation fault are sometimes assigned to the fuel leakage fault.

More generally, the addition of residual 5 to the subset (1, 2, 3, 4) does not provide any improvement in the obtained performance. In the constant-voltage case, the addition of

residual 5 slightly decreases the OA values, especially when the maximum error is equal to 6%.

Finally, it is worth noting that the PAs for the nonfaulty class (i.e., the class number 0) were generally high; that is, a few false alarms were generated by the proposed system, although the nonfaulty class is expected to have a larger prior probability than individual faulty classes. This confirms the discrimination capability of the SVM approach and suggests that the generation of balanced sets of training samples per class did not erroneously favor the faulty classes.

## 4. Conclusions

In the context of SVM classification, we propose an original technique for the joint feature and model selection. This technique is applied to an open research problem: the design of a model-based FDI procedure, integrated with a data-driven diagnosis, for an SOFC electric generation plant. The FDI procedure is demonstrated to perform properly in a wide range of steady-state operating conditions and fault sizes and for various statistics of the random errors affecting the model predictions.

The joint feature and model selection make it possible to evaluate the relative importance of the residuals used as features for the robust FDI procedure, assuring the optimum performance for every cardinality of the feature vector. Moreover, for a given residual subset, if the maximum prediction error is increased by a factor of 3 (from 2% to 6%), the related OA decreases by a factor that does not exceed 1.26. Thus, because the performance reduction is very gradual despite the wide range of operating conditions and fault sizes that are considered, the robustness of the FDI procedure against modeling and measurement errors is proven.

Joining the results achieved by the feature selection to the evaluation of the difficulty in measuring the different residuals, we conclude that the use of the easy-to-measure residuals numbered 1, 2, 3, and 4 altogether are sufficient to achieve an overall performance that is very close to the absolute maximum observed when the use of all the residuals is enabled. This holds for both constant-voltage and constant-current control strategies. The only exception is the identification of the SOFC stack degradation under constant-current control. The accuracy for this fault is significantly lower than those observed for other faults. Further electrochemical investigations will be devoted to individuate new residuals able to provide a better discrimination of the SOFC stack degradation fault.

When a large number of combinations between the operating conditions and fault sizes are considered (for both training and testing), the SVM classifier using the four aforementioned residuals provides an OA, averaged over three values for the maximum prediction error (i.e., 2%, 4%, and 6%) that is higher than 80% for the constant-current case and is close to 90% for the constant-voltage case.

## Conflict of Interests

The authors declare that there is no conflict of interests regarding the publication of this paper.

## Acknowledgments

This work has been supported jointly by the Departments DICCA, DIME, and DITEN of the University of Genoa, Italy.

## References

- [1] S. Srinivasan, *Fuel Cells: From Fundamentals to Applications*, Springer, New York, NY, USA, 2006.
- [2] N. Behling, *Fuel Cells: Current Technology Challenges and Future Research Needs*, Elsevier, Oxford, UK, 2012.
- [3] D. Marra, M. Sorrentino, C. Pianese, and B. Iwanschitz, "A neural network estimator of Solid Oxide Fuel Cell performance for on-field diagnostics and prognostics applications," *Journal of Power Sources*, vol. 241, pp. 320–329, 2013.
- [4] R. Petrone, Z. Zheng, D. Hissel et al., "A review on model-based diagnosis methodologies for PEMFCs," *International Journal of Hydrogen Energy*, vol. 38, no. 17, pp. 7077–7091, 2013.
- [5] R. Isermann and P. Ballé, "Trends in the application of model-based fault detection and diagnosis of technical processes," *Control Engineering Practice*, vol. 5, no. 5, pp. 709–719, 1997.
- [6] R. Isermann, "Model-based fault-detection and diagnosis—status and applications," *Annual Reviews in Control*, vol. 29, no. 1, pp. 71–85, 2005.
- [7] I. Arsie, A. Di Filippi, D. Marra, C. Pianese, and M. Sorrentino, "Fault tree analysis aimed to design and implement on-field fault detection and isolation schemes for SOFC systems," in *Proceedings of the ASME 8th International Conference on Fuel Cell Science, Engineering and Technology (FUELCELL '10)*, pp. 389–399, New York, NY, USA, June 2010.
- [8] N. Y. Steiner, D. Hissel, P. Moçotéguy et al., "Application of fault tree analysis to fuel cell diagnosis," *Fuel Cells*, vol. 12, no. 2, pp. 302–309, 2012.
- [9] L. Pellaco, P. Costamagna, A. de Giorgi et al., "Fault diagnosis in fuel cell systems using quantitative models and support vector machines," *Electronics Letters*, vol. 50, no. 11, pp. 824–826, 2014.
- [10] A. Sorce, A. Greco, and L. Magistri, "Solid oxide fuel cell systems fault detection and identification through hybrid model and explicit rules," in *Proceedings of the 5th International Conference on Fundamentals & Development of Fuel Cells*, pp. 1–9, Karlsruhe, Germany, 2013.
- [11] T. Escobet, D. Feroldi, S. de Lira et al., "Model-based fault diagnosis in PEM fuel cell systems," *Journal of Power Sources*, vol. 192, no. 1, pp. 216–223, 2009.
- [12] A. Widodo and B.-S. Yang, "Application of nonlinear feature extraction and support vector machines for fault diagnosis of induction motors," *Expert Systems with Applications*, vol. 33, no. 1, pp. 241–250, 2007.
- [13] J.-D. Son, G. Niu, B.-S. Yang, D.-H. Hwang, and D.-S. Kang, "Development of smart sensors system for machine fault diagnosis," *Expert Systems with Applications*, vol. 36, no. 9, pp. 11981–11991, 2009.
- [14] O. Ondel, E. Boutleux, E. Blanco, and G. Clerc, "Coupling pattern recognition with state estimation using Kalman filter for fault diagnosis," *IEEE Transactions on Industrial Electronics*, vol. 59, no. 11, pp. 4293–4300, 2012.
- [15] J. Yu, "Local and nonlocal preserving projection for bearing defect classification and performance assessment," *IEEE Transactions on Industrial Electronics*, vol. 59, no. 5, pp. 2363–2376, 2012.
- [16] X. Zhang, W. Li, J. Xi, Z. Zhang, and X. Fan, "Surface defect target identification on copper strip based on adaptive genetic algorithm and feature saliency," *Mathematical Problems in Engineering*, vol. 2013, Article ID 504895, 10 pages, 2013.
- [17] A. W. Whitney, "A direct method of nonparametric measurement selection," *IEEE Transactions on Computers*, vol. 20, pp. 1100–1103, 1971.
- [18] V. Vapnik and O. Chapelle, "Bounds on error expectation for support vector machines," *Neural Computation*, vol. 12, no. 9, pp. 2013–2036, 2000.
- [19] G. Moser and S. B. Serpico, "Combining support vector machines and Markov random fields in an integrated framework for contextual image classification," *IEEE Transactions on Geoscience and Remote Sensing*, vol. 51, no. 5, pp. 2734–2752, 2013.
- [20] S. B. Serpico and L. Bruzzone, "A new search algorithm for feature selection in hyperspectral remote sensing images," *IEEE Transactions on Geoscience and Remote Sensing*, vol. 39, no. 7, pp. 1360–1367, 2001.
- [21] F. B. Shin and D. H. Kil, "Full-spectrum signal processing using a classify-before-detect paradigm," *The Journal of the Acoustical Society of America*, vol. 99, no. 4, pp. 2188–2197, 1996.
- [22] A. Trucco, "Detection of objects buried in the seafloor by a pattern-recognition approach," *IEEE Journal of Oceanic Engineering*, vol. 26, no. 4, pp. 769–782, 2001.
- [23] L. H. Chiang, E. L. Russell, and R. D. Braaz, *Fault Detection and Diagnosis in Industrial Systems*, Springer, New York, NY, USA, 2001.
- [24] E. Sobhani-Tehrani and K. Khorasani, *Fault Diagnosis of Non-linear Systems Using a Hybrid Approach*, vol. 383 of *Lecture Notes in Control and Information Sciences*, Springer, New York, NY, USA, 2009.
- [25] J. Luo, M. Namburu, K. R. Pattipati, L. Qiao, and S. Chigusa, "Integrated model-based and data-driven diagnosis of automotive antilock braking systems," *IEEE Transactions on Systems, Man, and Cybernetics Part A: Systems and Humans*, vol. 40, no. 2, pp. 321–336, 2010.
- [26] V. N. Vapnik, *Statistical Learning Theory*, John Wiley & Sons, New York, NY, USA, 1998.
- [27] C.-W. Hsu and C.-J. Lin, "A comparison of methods for multiclass support vector machines," *IEEE Transactions on Neural Networks*, vol. 13, no. 2, pp. 415–425, 2002.
- [28] J. Cui, M. Shan, R. Yan, and Y. Wu, "Aero-engine fault diagnosis using improved local discriminant bases and support vector machine," *Mathematical Problems in Engineering*, vol. 2014, Article ID 283728, 9 pages, 2014.
- [29] G. Moser and S. B. Serpico, "Automatic parameter optimization for support vector regression for land and sea surface temperature estimation from remote sensing data," *IEEE Transactions on Geoscience and Remote Sensing*, vol. 47, no. 3, pp. 909–921, 2009.
- [30] P. Mantero, G. Moser, and S. B. Serpico, "Partially supervised classification of remote sensing images through SVM-based probability density estimation," *IEEE Transactions on Geoscience and Remote Sensing*, vol. 43, no. 3, pp. 559–570, 2005.
- [31] L. Debnath and P. Mikusinski, *Introduction to Hilbert Spaces*, Academic Press, New York, NY, USA, 1990.
- [32] R.-E. Fan, P.-H. Chen, and C.-J. Lin, "Working set selection using second order information for training support vector machines," *Journal of Machine Learning Research*, vol. 6, pp. 1889–1918, 2005.

- [33] J. Guo, N. Takahashi, and T. Nishi, "An efficient method for simplifying decision functions of support vector machines," *IEICE Transactions on Fundamentals of Electronics, Communications and Computer Sciences*, vol. E89-A, no. 10, pp. 2795–2802, 2006.
- [34] O. Chapelle, V. Vapnik, O. Bousquet, and S. Mukherjee, "Choosing multiple parameters for support vector machines," *Machine Learning*, vol. 46, no. 1–3, pp. 131–159, 2002.
- [35] W. H. Press, S. A. Teukolsky, W. T. Vetterling, and B. P. Flannery, *Numerical Recipes in C++*, Cambridge University Press, New York, NY, USA, 2nd edition, 2002.
- [36] S. B. Serpico, M. D'Inca, F. Melgani, and G. Moser, "Comparison of feature reduction techniques for classification of hyperspectral remote sensing data," in *8th Image and Signal Processing for Remote Sensing*, vol. 4885 of *Proceedings of SPIE*, pp. 347–358, Crete, Greece, September 2002.
- [37] A. Sorce, A. Greco, L. Magistri, and P. Costamagna, "FDI oriented modeling of an experimental SOFC system, model validation and simulation of faulty states," *Applied Energy*, vol. 136, 908, no. 894, 2014.
- [38] H. S. Fogler, *Elements of Chemical Reaction Engineering*, Prentice Hall, New York, NY, USA, 4th edition, 2006.
- [39] A. Greco, A. Sorce, R. Littwin, P. Costamagna, and L. Magistri, "Reformer faults in SOFC systems: experimental and modelling analysis, and simulated fault maps," *International Journal of Hydrogen Energy*, vol. 136, pp. 894–908, 2014.
- [40] *Technical Documentation Integrated Stack Module (ISM)*, Staxera GmbH, Dresden, Germany, 2010, [http://www.fuelcellmarkets.com/content/images/articles/00864\\_AS\\_Dokumentation\\_ISM.pdf](http://www.fuelcellmarkets.com/content/images/articles/00864_AS_Dokumentation_ISM.pdf).
- [41] European Union, "Generic diagnosis instrument for SOFC systems (GENIUS)," Collaborative Project FCH JU 245128, 2010, <http://www.fch-ju.eu/project/generic-diagnosis-instrument-sofc-systems>.
- [42] G. Moser and S. B. Serpico, "Contextual remote-sensing image classification by support vector machines and Markov random fields," in *Proceedings of the IEEE International Geoscience and Remote Sensing Symposium (IGARSS '10)*, pp. 3728–3731, Honolulu, Hawaii, USA, July 2010.

## Research Article

# Vacuum Large Current Parallel Transfer Numerical Analysis

Enyuan Dong,<sup>1</sup> Shengkai Hou,<sup>1</sup> Xiang Zheng,<sup>2</sup> Taotao Qin,<sup>1</sup> Guixin Liu,<sup>1</sup> and Bing Zhao<sup>1</sup>

<sup>1</sup> College of Electrical Engineering, Dalian University of Technology, Dalian 116024, China

<sup>2</sup> School of Electronics and Information Engineering, Dalian Jiaotong University, Dalian 116028, China

Correspondence should be addressed to Enyuan Dong; [dey@dlut.edu.cn](mailto:dey@dlut.edu.cn)

Received 17 April 2014; Revised 19 May 2014; Accepted 19 May 2014; Published 3 August 2014

Academic Editor: Peng Shi

Copyright © 2014 Enyuan Dong et al. This is an open access article distributed under the Creative Commons Attribution License, which permits unrestricted use, distribution, and reproduction in any medium, provided the original work is properly cited.

The stable operation and reliable breaking of large generator current are a difficult problem in power system. It can be solved successfully by the parallel interrupters and proper timing sequence with phase-control technology, in which the strategy of breaker's control is decided by the time of both the first-opening phase and second-opening phase. The precise transfer current's model can provide the proper timing sequence to break the generator circuit breaker. By analysis of the transfer current's experiments and data, the real vacuum arc resistance and precise correctional model in the large transfer current's process are obtained in this paper. The transfer time calculated by the correctional model of transfer current is very close to the actual transfer time. It can provide guidance for planning proper timing sequence and breaking the vacuum generator circuit breaker with the parallel interrupters.

## 1. Introduction

With the rapid development of the power system and the increase of the transmission capacity, it requires safer and more stable environment. The fault current's breaking capacity and the longevity of high voltage circuit breaker that controls and protects power system are essential to the reliable operation of electric power systems. It can effectively reduce the average arcing time and peak arc current to use synchronous technology [1] to control the separate moment of breaker's contacts through the zero point and it is useful to improve the breaking capacity of circuit breaker and reduce contact's wear [2].

The rated current of single vacuum circuit breaker is less than 5 ka. And the single breaker is unable to burden the high rated continuous current and break the large short-circuit current [3–6]. In order to improve the vacuum circuit breaker's rated current and the capacity of the breaker, two parallel interrupters are used to share a large current especially for the generator circuit breaker and the occasion that needs to break the large current [7, 8]. However two pairs of contacts are impossible to absolutely separate at the same time due to the manufacture of breakers, the dispersion of actuators, and the arrangement which leads to a failure to break the whole fault current [9].

The parallel vacuum interrupters are used to share the rated large current. When the fault current occurs, main vacuum interrupter (MVI) is opened firstly. The fault current gradually is transferred from MVI to AVI (auxiliary vacuum interrupter). At the same time, the current constantly decays.

At the end of the current-transfer process, the fault current through AVI is removed with phase-control technology [10–12]. But in the transfer process, the multiplication of AVI's inductance and the instantaneous current is greater than MVI's arc voltage, which leads to uncontrollable transfer process and the current cannot transfer from MVI to AVI. The successful breaking of the AVI depends much on the precise calculated transfer time. So an accurate model of the transfer current is needed.

In the paper [13], the mathematical model of transfer current is provided through the relevant theoretical derivation. It is helpful to analyze the transfer process. The arc resistance's value in the model is constant, which leads to a large deviation for transfer time. So this model cannot provide accurate timing sequence for using the phase-control technology [10–12]. The success rate of transferring is related to transfer current's value, the time of breaking MVI, and so forth. This transfer current's model needs to be corrected. In this paper, the vacuum arc resistance's formula is obtained by Matlab through the analysis of experimental data of transfer

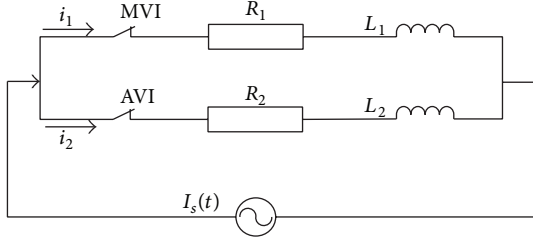


FIGURE 1: MVI and AVI share the large current.

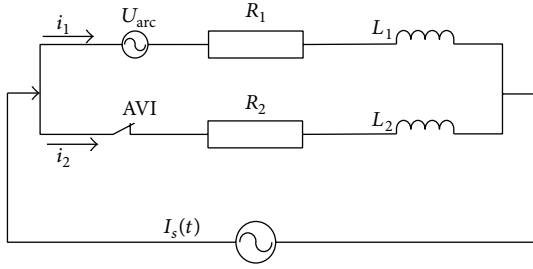


FIGURE 2: Equivalent circuit when MVI's contacts are opened.

current. The arc resistance changes with time and transfer current. Finally, the correctional model of transfer current is derived with the real arc resistance.

## 2. The Model of Transfer Current

At the beginning, the large rated current is shared by MVI and AVI as shown in Figure 1.

When the short-circuit fault occurs, MVI is opened firstly. The large current gradually is transferred from MVI to AVI. The equivalent circuit is shown in Figure 2.

Short-circuit current of the system [13]:

$$I_s(t) = \sqrt{2}I_e \sin(\omega t + \alpha - \varphi_d) + [I_e \sin(\alpha - \varphi) - \sqrt{2}I_e \sin(\alpha - \varphi_d)] e^{-t/\tau_{\text{sys}}}. \quad (1)$$

In (1),  $I_e$  is the effective value before short circuit occurring.  $\tau_{\text{sys}}$  is the decay constant of the system.  $\omega$  is the current's angular frequency.  $\alpha$  is the initial phase angle of power source's voltage when short circuit occurs instantly.  $\varphi_d$  is the impedance angle after short circuit occurring. And  $\varphi$  is the impedance angle before short circuit occurring.

The impedance of power source can be ignored when it is compared with the interrupter's resistance and the system capacity is much larger. Considering the constant arc voltage  $U_a$  when the MVI is opened, the transfer current in Figure 2 can be expressed with [9]

$$i_1 + i_2 = I_s(t),$$

$$L_1 \frac{di_1}{dt} + R_1 i_1 + U_a = L_2 \frac{di_2}{dt} + R_2 i_2 \quad (2)$$

$(T1 \leq t \leq T2).$

$T1$  is the moment of breaking MVI.  $T2$  is the moment of breaking AVI.  $R_1$  does not contain contact resistance between a pair of contacts when MVI is separated in (2) and it mainly consists of arc resistance and the resistance of internal conductive rod in MVI. So the differential equation (3) is derived from (2):

$$\frac{di_1}{dt} + \frac{(R_1 + R_2)}{(L_1 + L_2)} i_1 = \frac{L_2}{(L_1 + L_2)} \frac{dI_s(t)}{dt} + \frac{R_2}{(L_1 + L_2)} I_s(t) - \frac{U_a}{(L_1 + L_2)}. \quad (3)$$

$i_1$  is the instantaneous value of the transfer current [9] in the following:

$$i_1 = C e^{-((R_1 + R_2)/(L_1 + L_2))t} - \frac{U_a}{R_1 + R_2} + \sqrt{2}I_e \frac{L_2 - R_2 \tau_{\text{sys}}}{(L_1 + L_2) - (R_1 + R_2) \tau_{\text{sys}}} e^{-t/\tau_{\text{sys}}} - \sqrt{2}I_e \frac{\omega L_1 R_2 - \omega L_2 R_1}{(R_1 + R_2)^2 + \omega^2 (L_1 + L_2)^2} \sin(\omega t) - \sqrt{2}I_e \frac{(R_1 + R_2) R_2 + \omega^2 L_2 (L_1 + L_2)}{(R_1 + R_2)^2 + \omega^2 (L_1 + L_2)^2} \cos(\omega t). \quad (4)$$

In (4),  $\varphi_d$  is  $\pi/2$ .  $R_1$  is the equivalent resistance of MVI's branch.  $L_1$  is the equivalent inductance of MVI's branch.  $R_2$  is the equivalent resistance of AVI's branch.  $L_2$  is the equivalent inductance of AVI's branch.  $T_k$  is the moment at which MVI is opened. The differential constant  $C$  is shown in the following:

$$C = e^{((R_1 + R_2)/(L_1 + L_2))T_k} \times \left\{ \frac{U_a}{R_1 + R_2} - \sqrt{2}I_e \frac{L_2 - R_2 \tau_{\text{sys}}}{L_1 + L_2 - (R_1 + R_2) \tau_{\text{sys}}} e^{-T_k/\tau_{\text{sys}}} + \sqrt{2}I_e \frac{\omega L_1 R_2 - \omega L_2 R_1}{(R_1 + R_2)^2 + \omega^2 (L_1 + L_2)^2} \sin(\omega T_k) + \sqrt{2}I_e \frac{(R_1 + R_2) R_2 + \omega^2 L_2 (L_1 + L_2)}{(R_1 + R_2)^2 + \omega^2 (L_1 + L_2)^2} \cos(\omega T_k) + \sqrt{2}I_e \sin\left(\omega T_k + \alpha - \frac{\pi}{2}\right) + \left[ I_e \sin(\alpha - \varphi_d) - \sqrt{2}I_e \sin\left(\alpha - \frac{\pi}{2}\right) \right] e^{-T_k/\tau_{\text{sys}}} \right\}. \quad (5)$$

The emulational value is deviated from the actual value, because arc resistance is assumed to be constant and unchanged with time in the model of transfer current.



FIGURE 3: The two parallel breakers.

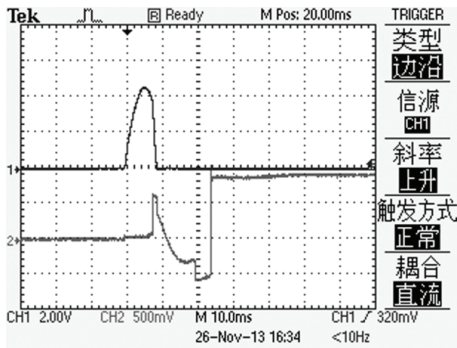


FIGURE 4: Transfer current of 5.2 ka and voltage.

### 3. Mathematical Model of Vacuum Arc Resistance

In the experiment, two parallel breakers are used to share the large current as shown in Figure 3. The interrupter's model is BD-12/1250-20A produced by the Kaisaier. The large current is generated by the Synthesis loop. Its half cycle is 12.5 ms and the current's value is adjustable.

The two breakers controlled by the controller are opened according to the timing sequence. The current signal of the two breakers is collected by Rogowski coil and the arc voltage is collected by the resistance-type voltage divider that is parallel with the MVI. In Figures 4 and 5, the current value of 1200 A corresponds to 1 V, which is the output of Rogowski coil. The curve 2 which is collected by resistance-type voltage divider amplified 22.6 times is the voltage between MVI. In this paper, the times of breaking MVI are 1.4 ms, 4.4 ms, 5.0 ms, 6.2 ms, 7.0 ms, and 8.3 ms. The transfer currents are 3.7 ka, 5.2 ka, 6.4 ka, 7.7 ka, and 9.6 ka. All current values are the peak of transfer currents.

The current that transfers from MVI to AVI is prevented by AVI's reactance. So the moment of breaking MVI needs to avoid the current's peak and it is better to choose the time in

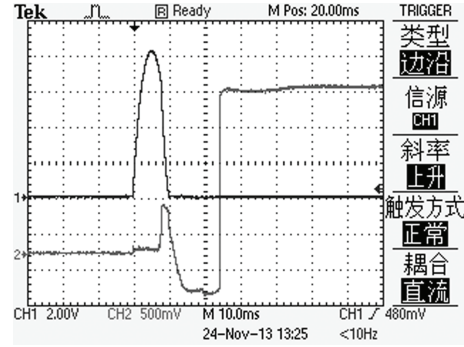


FIGURE 5: Transfer current of 9.6 ka and voltage.

which current's value is relatively low. In the moment that is close to current's zero crossing, the success rate of transferring is higher. The enough computation-time of the controller is required to break AVI with the phase-control technology and the result in the moment is more obviously and more representatively compared with all experimental data. So the time of breaking MVI is selected at 8.3 ms in this paper. The waveforms of the oscilloscope are only listed in 5.2 ka and 9.6 ka due to limited space. MVI's current (curve 1) and the voltage (curve 2) across the interrupter are shown in Figures 4 and 5.

In Figures 4 and 5, curve 2 is the voltage between MVI. At the beginning, the voltage is zero. When large current flows through MVI, its voltage has a slight uplift and maintains a stable value. At the moment at which MVI is opened, MVI's current drops rapidly and the arc is generated and the voltage pulse [14] increases immediately. The arc voltage is higher with the increase of transfer current. But the voltage's growth rate is low with the increase of transfer current. At the end of the transfer process, the arc is extinguished. The sinusoidal voltage is not the arc voltage but the voltage of AVI's branch in Figures 4 and 5. The voltage declines until AVI is opened. At the same time, the voltage pulse is the superposition of AVI's voltage and AVI's arc voltage in the negative half-cycle. Finally, the voltage is raised to the voltage of current source's capacitor and remains unchanged as shown in Figures 4 and 5.

It is shown how the MVI's and AVI's currents change in the first half-cycle when MVI is opened in Figures 6 and 7. MVI's current is 1.8 times larger than AVI's current before 8.3 ms. The large current of the MVI is transferred from MVI to AVI at 8.3 ms. In the transfer process, the MVI's arc voltage in 9.6 ka is shown in Figure 8. Figure 8 is the amplification of arc voltage in Figure 5.

The real vacuum arc resistance is calculated with transfer current and arc voltage as shown in Figures 9 and 10.

The vacuum arc resistance is close to exponential growth. The arcing time becomes longer with the increase of transfer current. At the beginning of the transfer process, arc resistance grows very slowly at a low level. On the contrary, the arc resistance increases rapidly to a high value when the arc is extinguished.

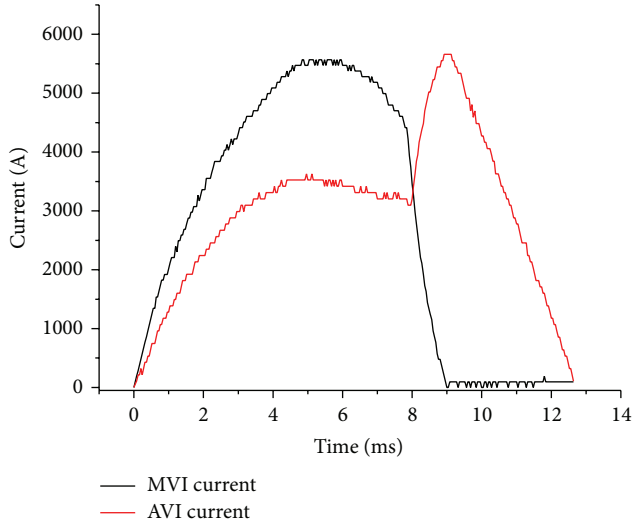


FIGURE 6: MVI's and AVI's currents in transfer current of 5.2 ka.

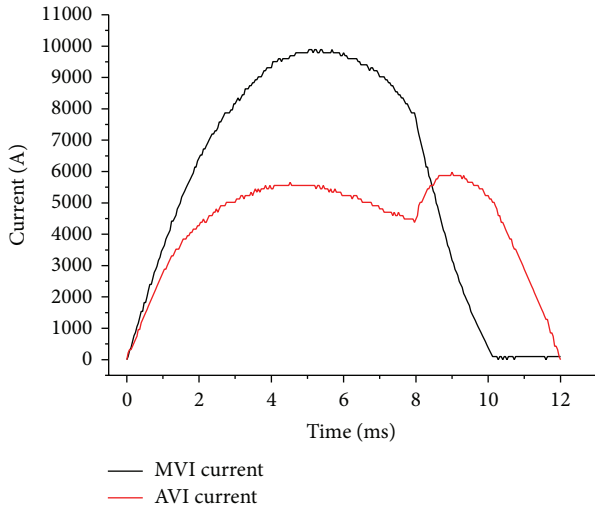


FIGURE 7: MVI's and AVI's currents in transfer current of 9.6 ka.

The mathematical formula of the arc resistance is expressed with (6) through the analysis of experimental data:

$$R_{\text{arc}(t)} = ae^{bt} + 600 \mu\Omega,$$

$$a = 2.794 \times 10^6 \times e^{[-3.024 \times 10^{-3} (2.892 \times 10^{-4} I_{\text{MVI}}^2 - 0.8731 I_{\text{MVI}} + 2729)]}$$

$$b = 2.124 \times I_{\text{MVI}} + 2376.$$

(6)

In (6),  $t$  is the arcing time.  $I_{\text{MVI}}$  is the transfer current.

The arc resistance is related with transfer current and arcing time. The arcing time becomes longer with the increase of the transfer current and the accumulation of heat becomes more and more. In (6),  $a$  becomes smaller and  $b$  becomes greater with the increase of the transfer current. In fact, arc resistance is related to contact material, the structure, the spacing of the contact, and so forth. The constants in (6) need to adjust in quite different experimental condition.

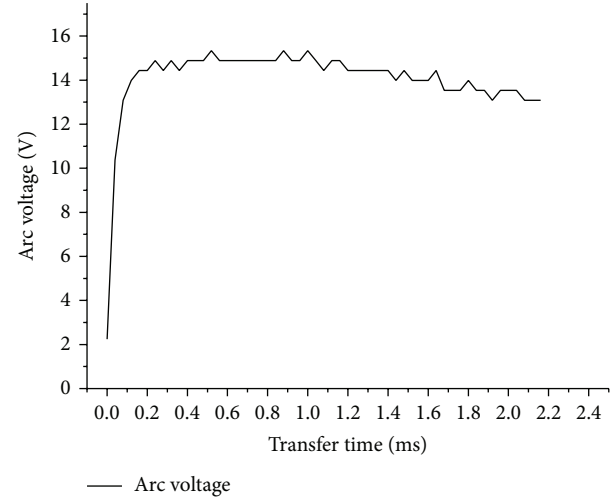


FIGURE 8: The arc voltage in the transfer process.

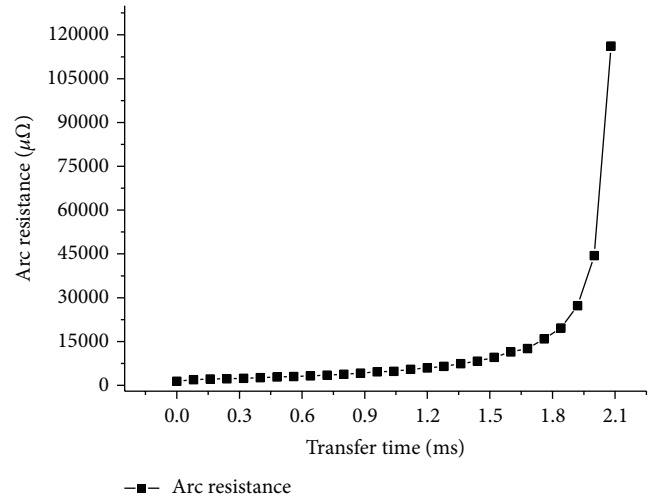


FIGURE 9: The vacuum arc resistance in transfer current of 9.6 ka.

The red points are the experimental data and the blue curve is the calculated value by the mathematical model of vacuum arc resistance. The calculated arc resistance is very close to the actual value with the model as shown in Figures 11, 12, 13, and 14.

#### 4. The Correctional Model of Transfer Current

The  $I_{(T1)}$  is the part of particular solution of differential equation (3). At this moment, the arc is not generated and the  $R_1$  remains constant. The constant  $R_1$  in other items of (4) is replaced with  $R_1 + R_{\text{arc}(t)}$  and the correctional model of transfer current is deduced as shown in the following:

$$I_{(T1)} = Ce^{-((R_1+R_2)/(L_1+L_2))t} - \frac{U_a}{R_1 + R_2} \quad (t = T1),$$

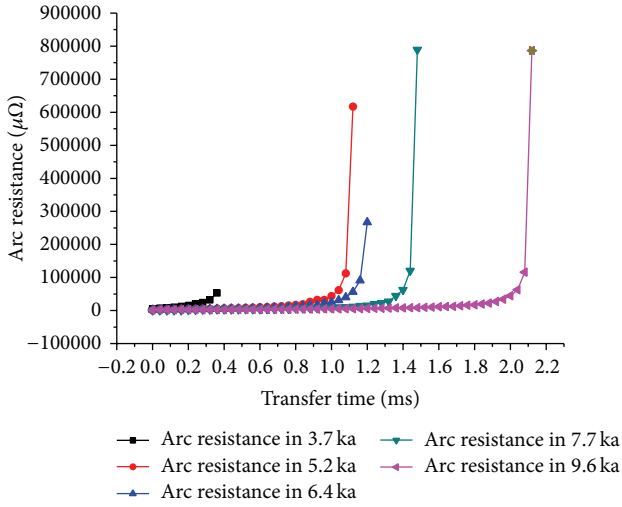


FIGURE 10: The vacuum arc resistance in all transfer currents.

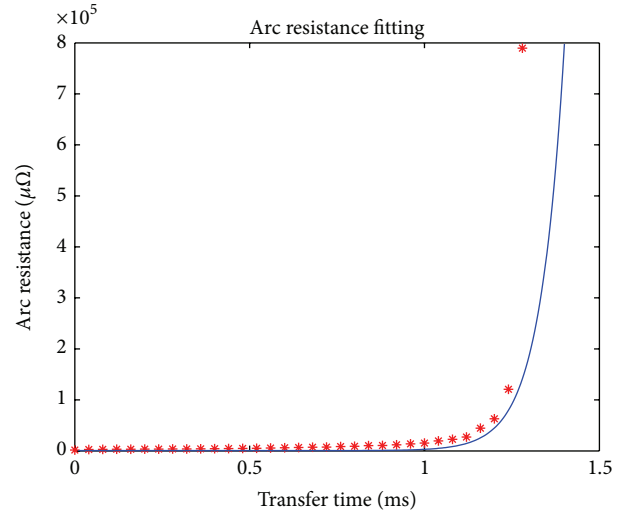


FIGURE 13: Arc resistance fitting in transfer current of 7.7 ka.

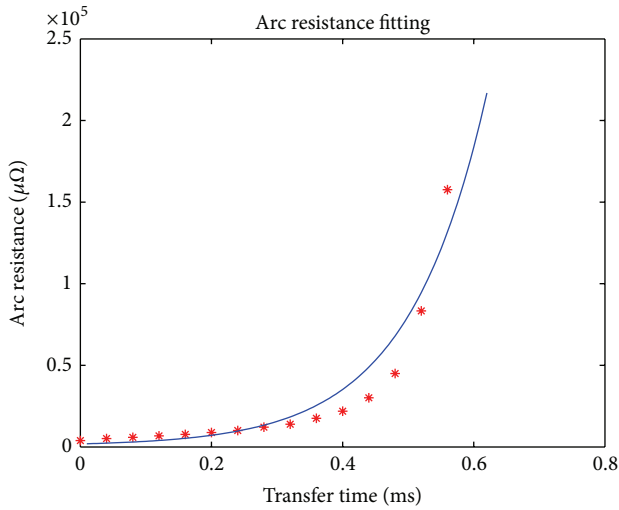


FIGURE 11: Arc resistance fitting in transfer current of 3.7 ka.

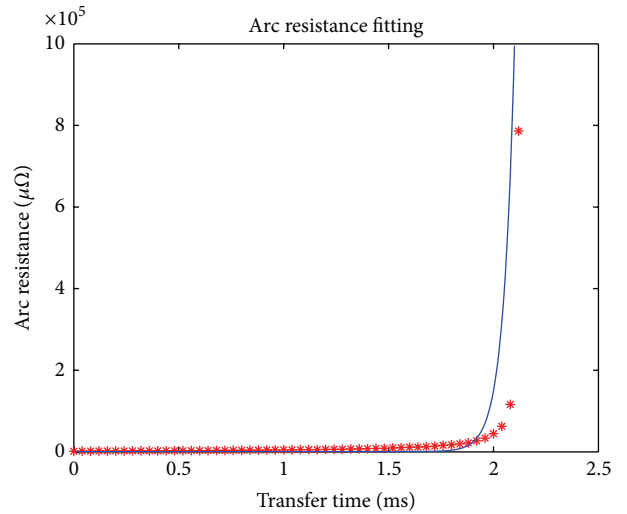


FIGURE 14: Arc resistance fitting in transfer current of 9.6 ka.

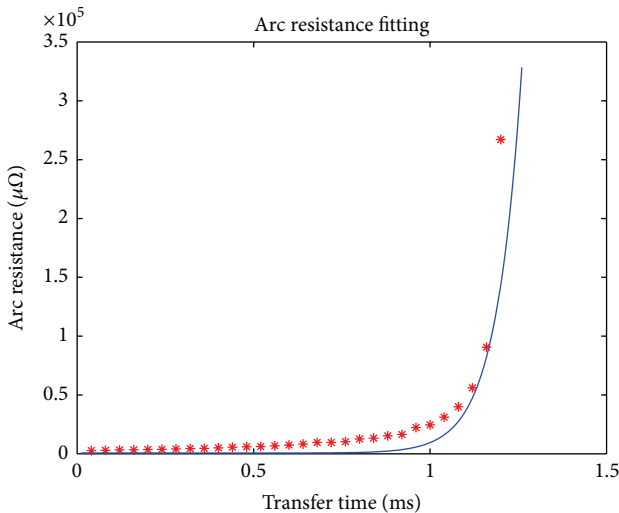


FIGURE 12: Arc resistance fitting in transfer current of 6.4 ka.

$$\begin{aligned}
 i_{1(t)} = & I_{(T1)} + \sqrt{2}I_e \frac{L_2 - R_2\tau_{sys}}{(L_1 + L_2) - (R_1 + R_{arc(t)} + R_2)\tau_{sys}} e^{-t/\tau_{sys}} \\
 & - \sqrt{2}I_e \frac{\omega L_1 R_2 - \omega L_2 (R_1 + R_{arc(t)})}{(R_1 + R_{arc(t)} + R_2)^2 + \omega^2 (L_1 + L_2)^2} \sin(\omega t) \\
 & - \sqrt{2}I_e \frac{(R_1 + R_{arc(t)} + R_2) R_2 + \omega^2 L_2 (L_1 + L_2)}{(R_1 + R_{arc(t)} + R_2)^2 + \omega^2 (L_1 + L_2)^2} \\
 & \times \cos(\omega t) \quad T1 < t \leq T2.
 \end{aligned} \tag{7}$$

The correctional transfer time is calculated with the correctional model of transfer current. The primary transfer time is calculated with the model of transfer current ((4)-(5)) in Figures 15 and 16. The actual transfer time is the experimental data.

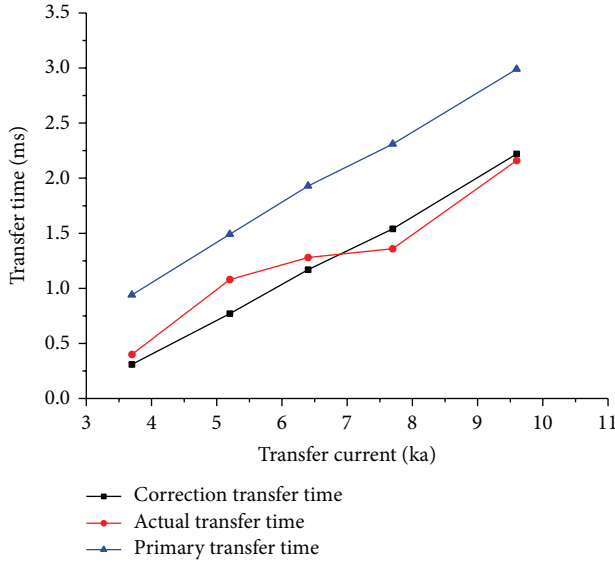


FIGURE 15: Three kinds of transfer time's comparison in different currents.

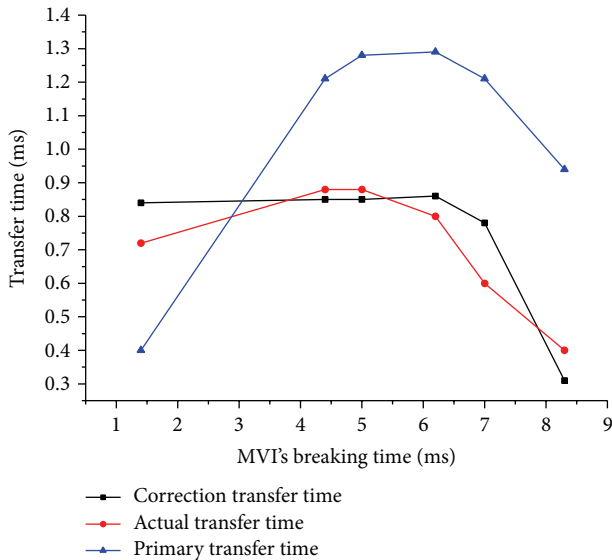


FIGURE 16: Three kinds of transfer time's comparison at different time of breaking MVT.

The comparison of the three kinds of transfer time in different current is shown in Figure 15 and the trend of transfer time at different times of breaking MVT is shown in Figure 16.

The correctional model of transfer current by analyzing experimental data with Matlab can accurately reflect the changing of the real vacuum arc resistance. The correctional model is more accurate and the correctional transfer time is closer to the actual transfer time. It can provide a proper timing sequence for breaking AVI with the phase-control technology.

So the correctional model can provide more accurate transfer time than the primary model for using the phase-control technology. The main contribution of the models can provide guidance for planning proper timing sequence and breaking a vacuum generator circuit breaker with the parallel interrupters.

Because the vacuum arc is affected by many factors, there is much work to research the more accurate vacuum arc's model.

## 5. Conclusion

The mathematical model of vacuum arc resistance and the correctional model of transfer current are established in this paper. By the analysis of experimental data and the results of simulation, the changing of real arc resistance is described and the real vacuum arc resistance is close to exponential growth. At the beginning of the transfer process, the arc resistance's growth rate is very low. But when the arc is extinguished, the real arc resistance increases rapidly to a high value. The arcing time becomes longer and the arc voltage is higher with the increase of the transfer current. At the same time, the duration of the low arc resistance's state maintains more time.

Although the mathematical model of vacuum arc resistance and the correctional model of transfer current are obtained under specific experimental condition, each of the important parameters in the models is adjustable according to specific circumstances. The real vacuum arc resistance's model and the correctional model of transfer current are widely applicable.

Because the transfer time calculated by the correctional model of transfer current is very close to the actual transfer time and the deviation is smaller, the models can provide proper guidance for breaking a large generator current with the phase-control technology.

As future work, there is much work to integrate the robust control algorithm [15] into the breakers and regulate the speed of breakers' movement. The authors plan to improve the scalability and fault tolerance [16] of the models at a satisfactory quality level and add the reciprocal determination process [17] where the models can take into account the speed of breakers and the type of fault current.

## Conflict of Interests

The authors declare that there is no conflict of interests regarding the publication of this paper.

## Acknowledgment

This work is supported by the National Natural Science Foundation of China (no. 51277019).

## References

- [1] CIGRE Working Group 13.07, *Controlled Switching of HV AC Circuit Breaker Guidance For Further Application Including*

*UnLoaded transformer Switching, Load and Fault Interruption and Circuit Breaker Uprating*, CIGRE, Chengdu, China, 1999.

- [2] A. Poltl and K. Frohlich, "A new algorithm enabling controlled short circuit interruption," *IEEE Transactions on Power Delivery*, vol. 18, no. 3, pp. 802–808, 2003.
- [3] X.-S. Chen and J. Zou, "Generator protection vacuum circuit breaker," *High Voltage Apparatus*, vol. 36, no. 1, pp. 34–37, 1998.
- [4] M. Homma, M. Sakaki, E. Kaneko, and S. Yanabu, "History of vacuum circuit breaker and recent development in Japan," in *Proceedings of the 21th International Symposium on Discharges and Electrical Insulation in Vacuum (ISDEIV '04)*, pp. 378–383, Yalta, Ukraine, October 2004.
- [5] P.-H. Zhou, M. Dai, Y. Lou, and M.-H. Xiu, "DC component time constant and zero off set phenomena of breaking current for 1000 kV circuit breaker," *High Voltage Engineering*, vol. 35, no. 4, pp. 722–730, 2009.
- [6] L.-J. Cao and J. Li, "Exploration on high capacity generate or outlet protection vacuum circuit breaker," *Electrical Device*, vol. 5, no. 9, pp. 84–85, 2004.
- [7] X.-S. Chen, J.-Y. Zou, and J.-J. - He, "Parallel high-current vacuum arc breaking," *High Voltage Apparatus*, no. 4, pp. 29–32, 1997.
- [8] M. Matsukawa, Y. M. Miura, T. Terakado et al., "Development of a vacuum switch carrying a continuous current of 36 kA DC," in *Proceedings of the 19th International Symposium on Discharges and Electrical Insulation in Vacuum*, vol. 2, pp. 415–418, 2000.
- [9] X.-S. Chen, Z.-W. Wang, J.-Y. Zou et al., "Experimental research on paralleled breaking process of vacuum circuit breaker," *High Voltage Apparatus*, vol. 33, no. 5, pp. 33–37, 1998.
- [10] X.-Y. Duan, M.-F. Liao, F.-H. Ding, and J.-Y. Zou, "Application and key technology analysis of controlled switching," *High Voltage Apparatus*, vol. 43, no. 2, pp. 113–117, 2007.
- [11] X. Duan, M. Liao, F. Ding, B. Liu, and J. Zou, "Controlled vacuum circuit breaker for shunt capacitor banks," *Transactions of China Electrotechnical Society*, vol. 22, no. 10, pp. 78–84, 2007.
- [12] F.-H. Ding, J.-Y. Zou, and X.-Y. Duan, "Research on optimum switching phase of phasing switches," *High Voltage Apparatus*, vol. 41, no. 6, pp. 408–411, 2005.
- [13] X. Zheng, J.-Y. Zou, and Z. Cheng, "Current transfer process of paralleled vacuum generator circuit breaker," *High Voltage Engineering*, vol. 35, no. 11, pp. 2709–2715, 2009.
- [14] Z.-Y. Liu, J.-M. Wang, Z.-Y. Wang, and S. Yuan, "Current transfer process in open operation between parallel breaks of a vacuum generator circuit breaker," *Proceedings of the Chinese Society of Electrical Engineering*, vol. 20, no. 12, pp. 20–23, 2000.
- [15] V. Veselly and D. Rosinova, "Robust MPC controller design for switched systems using multi-parameter dependent lyapunov function," *International Journal of Innovative Computing, Information and Control*, vol. 10, no. 1, pp. 269–280, 2014.
- [16] C. Dobre, "A cluster-enhanced fault tolerant peer-to-peer systems," *International Journal of Innovative Computing, Information and Control*, vol. 10, no. 2, pp. 417–436, 2014.
- [17] K. Harada and Y. Ishida, "Complex spatial-temporal patterns developed from an interaction of functions and data," *International Journal of Innovative Computing, Information and Control*, vol. 10, no. 1, pp. 405–416, 2014.